Structure – Property correlation in additive manufactured Ti-5553 components

by

Nivas Ramachandiran

A thesis

presented to the University of Waterloo

in fulfillment of the

thesis requirement for the degree of

Doctor of Philosophy

in

Mechanical and Mechatronics Engineering

Waterloo, Ontario, Canada, 2023

Examining Committee Membership

The following served on the Examining Committee for this thesis. The decision of the Examining Committee is by majority vote.

External Examiner	HATEM ZUROB Professor
Supervisor 1	EHSAN TOYSERKANI Professor
Supervisor 2	ADRIAN GERLICH Professor
Internal Member	JOHN WEN Professor
Internal Member	CLIFFORD BUTCHER Assistant Professor
Internal-external Member	WILLIAM WONG Professor

Author's declaration

This thesis consists of material all of which I authored or co-authored: see Statement of Contributions included in the thesis. This is a true copy of the thesis, including any required final revisions, as accepted by my examiners.

I understand that my thesis may be made electronically available to the public.

Statement of contributions

This thesis contains eight chapters, with Chapters 4 to 7 based on manuscripts written for publications. It should be noted that the main work in the laboratory including sample preparation, material characterization, mechanical testing and documentation were my contributions. The following co-authors have contributed to the current work as outlined below:

- **Prof. Ehsan Toyserkani:** Supervising the research, providing the original idea for the current thesis in the area of additive manufacturing, editing and reviewing papers, providing experimental facilities, providing funding.
- **Prof. Adrian Gerlich:** Supervising the research, providing the original idea for the current thesis in the area of material characterization, editing and reviewing papers.
- **Dr. Hamed Asgari:** Providing editorial feedback in the preparation of the individual manuscripts in Chapters 4 – 7 and carrying out the Archimedes density measurements.
- **Dr. Waqas Muhammad, Dr. Ali Keshavarzkermani and Mr. Henry Ma:** Providing technical training for carrying out EBSD analysis.
- **Mr. Francis Dibia and Mr. Roger Eybel:** Providing the support needed in statistical optimization of LPBF process parameters.

Abstract

A recently developed metastable β-titanium alloy, Ti-5Al-5V-5Mo-3Cr (Ti-5553), is a potential replacement to existing aircraft landing gear materials, offering a wider processing window along with excellent heat treatability. Laser powder-bed fusion (LPBF), a class of metal additive manufacturing (AM) known for building nearly fully dense parts with high geometrical complexity from 3D CAD data, could be a solution to eliminate the traditional difficulties faced in manufacturing titanium alloy parts. LPBF of Ti-5553 is a relatively new area, where any detailed investigations on the microstructural evolution and the corresponding mechanical properties achievable are not available in the open literature.

In the first part of this thesis, the processing parameters corresponding to the laser conduction mode melting were identified, resulting in near full-density parts consistently printed at scan speeds > 750 mm/s. On subsequent mechanical testing, even though the as-printed specimens reached a notable total elongation of 30±5 %, they exhibit poor tensile strength and poor impact toughness properties. The combination of an outstanding ductility coupled with poor impact toughness was attributed to the presence of intragranular non-lamellar α particles. Fracture surfaces examined under scanning electron microscopy indicate a bi-modal fracture mode.

In the second part, post-processing heat treatment was carried out to enhance the mechanical properties of the printed parts. LPBF-made Ti-5553 specimens were subjected to a wide range of heat treatment cycles to modify their corresponding microstructure in terms of the morphology and distribution of α particles. Solutionizing at the upper α+β region (800 °C) offered a good combination of finer grain size and a satisfactory α dissolution. On aging in the range of 500 to 700 °C for 0.5 to 4 hours, growth of α particles with different morphologies were observed. Subsequently, microhardness measurements ranged 300 to 500 HV depending on the applied heat

treatment cycle, and the corresponding tensile strength increased from 780±10 to 1640±6.29 MPa, compared to the as-printed specimens. Fracture surface revealed intergranular dominant and ductile dominant failures depending on the aging conditions.

The heat treatment study was extended to characterizing the detrimental α case caused by the diffusion of elemental oxygen into the material at high temperatures. Irrespective of the heat treatment parameters, a 20 to 50 µm α case followed by a 200 to 250 µm thick transition zone, comprising coarse α rich grain boundaries deleterious to the tensile performance were observed in Ti-5553 specimens. Microhardness measurements revealed a hard and brittle outer case whose depth approximately matched the α case and the transition zone identified earlier. Removing the α case and the transition zone by surface turning after heat treatment substantially improved the ultimate tensile strength by ~200 %, maintaining an acceptable ductility of ~10 %.

In the final part, the effect of anisotropy caused by directional solidification in LPBF-made Ti-5553 parts on its tensile properties was studied. Specimens printed normal (vertically printed), and parallel (horizontally printed) to the building direction were subjected to interrupted uniaxial tensile tests. In comparison, samples printed parallel to the building direction exhibit a significantly higher tensile strength of 846±6 MPa, whereas the specimens printed normal to the building direction reached 780±10 MPa. Electron backscatter diffraction results indicate that the grain boundaries act as favourable locations for fracture initiation, particularly when aligned perpendicular to the loading direction. Conversely, fracture in specimens printed parallel to the building direction were predominantly transgranular, which could be a major contributing factor for the higher tensile strength observed.

Acknowledgement

The completion of this research work involves help and support of several kind hearted people, to whom I wish to express my sincere gratitude.

My humble thankfulness to my supervisors, **Prof. Ehsan Toyserkani** and **Prof. Adrian Gerlich** for showing trust in me and offering a second chance. It is so kind of them to let me evolve at my own pace, understanding my strengths and being a strong support. Their recognition and appreciation of my work boosted my confidence tremendously and prepared me for tougher challenges. I feel so blessed to be working under the greatest research supervisors anyone could possibly imagine.

I thank the industry partners – Safran Landing System, especially **Mr. Roger Eybel** for the constant enthusiasm, appreciation and valuable feedbacks which guided the whole team in the right direction. I also acknowledge the support of Natural Sciences and Engineering Research Council of Canada (NSERC) for financially backing the research.

I thank my teammates in the Safran landing gear project – **Dr. Hamed Asgari**, **Dr. Paulo Russo**, **Mr. Francis Dibia**, **Mr. Soheil Bakshivash** and **Mr. Mahyar Hasanabadi** for being a constant source of motivation. A special thanks to **Dr. Behzad Behravesh**, **Dr. Ehsan Marzbanrad** and **Dr. Usman Ali** for providing the technical training required at various stages of mechanical testing.

Finally, a heartfelt thanks to my dearest of friends – **Dr. Pablo Enrique**, **Mr. Dileep Ramachandran**, **Mr. Rahul Ram Chandrasekaran** and **Mr. Arvind Kothandaraman Raghavan** for being my strong mental pillars.

Dedication

This is dedicated to my parents – **Mr. Ramachandiran Krishnasamy** and **Mrs. Dhanalakshmi Ramachandiran** for showering an unconditional love on me, since birth. To my sister, **Mrs. Dhivya Prakash Kumar** for being an upfront critic of my work. To my mentors, **Dr. Mainak Ghosh** and **Dr. Sivaprasad Katakam** for planting the drive in me to keep marching towards the light at the end of the tunnel. I am always indebted to my friends, who have been wholeheartedly celebrating my successes, mourning my failures and most important of all, exhibiting a strong belief in my abilities. Finally, to COVID-19 which was kind enough to stay away from me.

Table of Contents

List of figures

Chapter 1: Introduction

1.1 Background and motivation

Achieving weight reductions without compromising performance is one of the perennial objectives in the aircraft manufacturing sector. Replacing parts with a stronger material can offer more than a three-fold weight reduction in addition to a considerable improvement in stiffness and damage tolerance [1]. In particular, titanium (Ti) offers superior specific strength and has proven successful in replacing parts made of conventional materials in a variety of critical engineering applications [2]. A potential weight reduction of more than 200 kg was achieved by replacing the heavier steel and Ni-based compressor discs and fan blades with Ti-alloy blades which offer excellent creep resistance [3]. In another comparison, the higher specific strength of Ti compared to steel resulted in a two-thirds reduction in the weight of a spring, while maintaining the same load-bearing capacity [4]. For hydraulic tubing in modern aircrafts, Ti tubes provide up to a 40% weight reduction compared ones made of steel [1].

The materials used in an aircraft can be broadly classified into two groups as shown in Figure 1-1. Even though Ti alloys are being principally used in high temperature engine materials, its potential to be used as static and dynamic load bearing members in the airframe structure, is underutilized. As of 2009, Ti accounts only for 7 to 9 % of the Boeing 777s airframe structure, partly due to raw material cost, and the affinity of interstitial elements during welding which leads to difficulty in fabricating complex shapes [1,4,5]. It is noteworthy that a weight reduction of up to 60% is achievable by replacing aluminum (Al) with Ti, despite its higher density [6].

Replacement of 4340 or 300M conventional high strength low alloy (HSLA) steel by Ti-10V-2Fe-3Al (Ti-1023) forgings is a noteworthy example of materials substitution in landing gear application, and has resulted in a massive weight reduction of over 580 kg, accounting approximately 1.5% the operating empty weight of a Boeing 737 airframe [7]. However, the sensitivity of Ti-1023 to minor variations in temperature and strain rate is a disadvantage in achieving reliable products. Meanwhile, a recently developed metastable β Ti alloy, Ti-5Al-5V-5Mo-3Cr (Ti-5553) exhibiting mechanical properties comparable to Ti-1023 offers a wider processing window along with excellent heat treatability characteristics [8–10]. Yet, manufacturability of these metastable β Ti alloys is challenging, which restricts its widespread application in aircraft industry. Nonetheless, considering its superior mechanical properties over other materials, it is inevitable that with better manufacturing practices, Ti alloys can be utilized in a wider range of structural engineering applications by overcoming the limitations mentioned above.

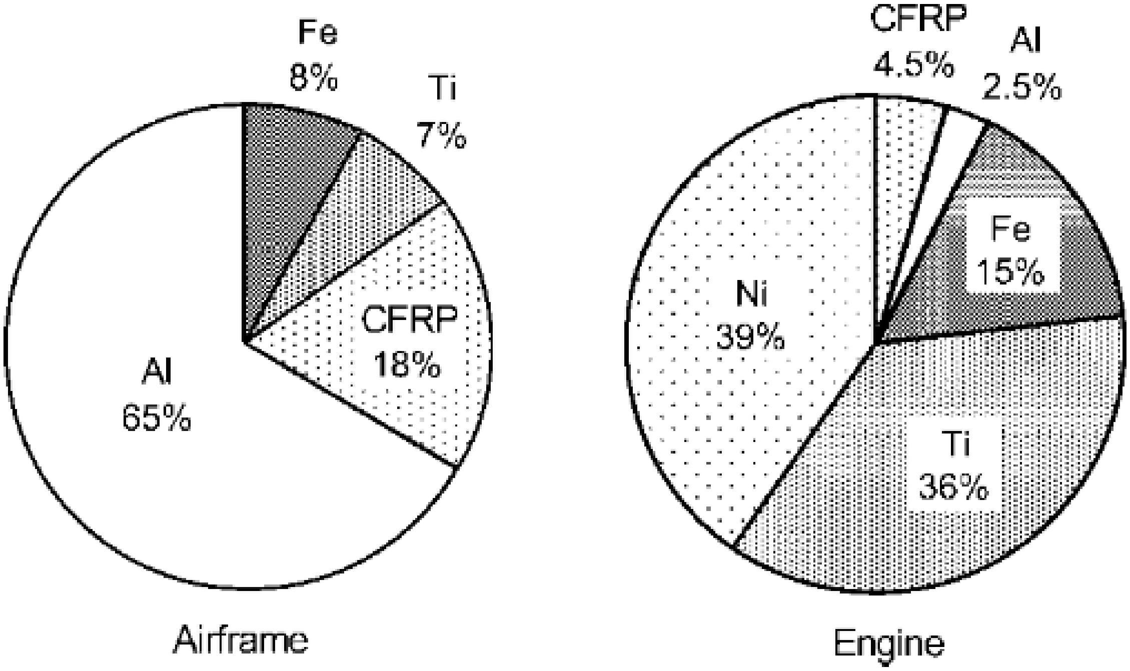

Figure 1-1: Percentage of different materials used in aircraft and gas turbine engines [1]

Additive manufacturing (AM), known as 3D printing, is a set of automated manufacturing processes that facilitates building physical 3-dimensional objects layer by layer from computer aided design (CAD) data. A variety of manufacturing processes categorised under AM, could process diverse class of materials. Laser powder bed fusion (LPBF) is an AM technique used to print metallic parts with complex geometries [11]. The automated laser-based printing which takes place in a controlled atmosphere eliminates or restricts the typical limitations experienced in Ti processing via traditional manufacturing routes. Higher utilisation of material or minimal wastage can be achieved compared to traditional or subtractive processes, which makes LPBF an excellent choice for processing expensive or sensitive materials. Most of the common structural alloys used in engineering applications including steel, titanium, stainless steel, aluminum, super-alloys can be processed through LPBF [12–15].

Although LPBF offers many advantages over traditional manufacturing, it involves its own set of engineering complications. Many process parameters (including laser energy, laser frequency, thermal conductivity, absorption factor, particle size distribution, reflectance and other similar physical characteristics) influence the quality of the printed parts [16]. Since the process does not involve the application of any externally applied pressure, and depends solely on thermal, gravitational and capillary forces, the fundamental challenge associated with optimizing an AM process is to achieve a consistently high relative density. The process optimized for a material is often not applicable to another one as the physical properties vary significantly. Often, the printed parts are subjected to sintering as a post processing step to improve the relative density [17]. A poor compaction density is commonly observed in multiple cases which might affect the geometrical precision of printed parts [18–20]. Additionally, if parameters are not optimized, it can result in distortion or an unstable melt pool resulting in balling defects being scattered on the surface [21,22]. The directional solidification involved in AM processes also tends to result in an overall microstructure that is quite different microstructures compared to conventionally processed materials [23–26]. The unique microstructure often exhibits distinctive mechanical properties which often more detailed analysis is required to confirm how these properties differ from conventionally manufactured components.

1.2 Problem statement

While some studies have confirmed the LPBF printability of Ti-5553, the corresponding tensile properties were inferior compared to the traditionally manufactured equivalents [27,28]. In another study, further optimization of LPBF process parameters was suggested as a remedy [29]. In most of the following research, in the aims to achieve 100% relative density, the laser scan speed was limited to 180 mm/s to minimize the chaotic fluid flow during the laser interaction. However, the ultimate tensile strength was still restricted to ≈ 800 MPa, whereas a minimum of 1147 MPa is expected by material specifications [29–32]. In addition, lower laser scan speeds would not be a long-term solution in implementing LPBF processed Ti-5553 in aircraft landing gear parts. Printing Ti-5553 parts at higher scan speeds (> 750 mm/s) have shown traces of the secondary α particles which are in contrast with slow speed prints (< 200 mm/s) [27–29]. Therefore, it is necessary to perform a comprehensive structure property correlation to understand the microstructural features affecting the tensile properties of LPBF printed Ti-5553 parts. High process parameters with scan speeds also need to achieve near full-density prints as well.

Moreover, post processing techniques to further enhance the tensile properties need to be formulated. The excellent heat treatability of Ti-5553 reported in the literature could be advantageous in achieving the desired mechanical properties. Yet, the LPBF-made Ti-5553 structures are composed of columnar grained grains, which are distinctive compared the epitaxial microstructures in Ti-5553 parts processed via traditional manufacturing routes. A few research papers have shown improved mechanical properties on post heating LPBF-made Ti-5553 [9,10]. However, they are preliminary, and demand a further comprehensive exploration to understand the mechanisms involved in the microstructural evolution. A thorough understanding of the phase transformations involved corresponding to the temperature and the duration of the heat treatment is essential. Precipitation of hard and brittle ω phase particles, which leads to an attendant loss of ductility needs to be carefully dealt with as well. The affinity of Ti for interstitial elements is higher at elevated temperatures which could lead to an undesired surface and sub-surface microstructural features deteriorating the mechanical properties. These issues provide a considerable scope for detailed research requiring several techniques and a comprehensive analysis of the corresponding results.

1.3 Objectives

The objective of the current work is to bridge the research gap in understanding the LPBF processed Ti-5553 microstructure and their corresponding mechanical properties. The five objectives derived based on the existing shortcomings discussed in the Sections 1.1 and 1.2 are:

- Identify the LPBF volumetric energy density (VED) window at which consistently high relative density prints (> 99.95%) can be achieved.
- Perform detailed microstructural investigation on as-printed Ti-5553 cross-sections to identify the features in LPBF microstructures which affect mechanical properties.
- Determine if the heat treatment for LPBF components are similar to conventionally manufactured components and identify the conditions to achieve improved tensile properties.

- Characterize the surface and sub-surface microstructural features in heat treated Ti-5553, to explain the formation of α case layer structures, and determine how this affects the corresponding mechanical properties.
- Assess the possibility of improving the tensile strength of as-printed Ti-5553 parts by engineering the printing direction with respect to the direction of loading.

1.4 Graphical abstract of the thesis

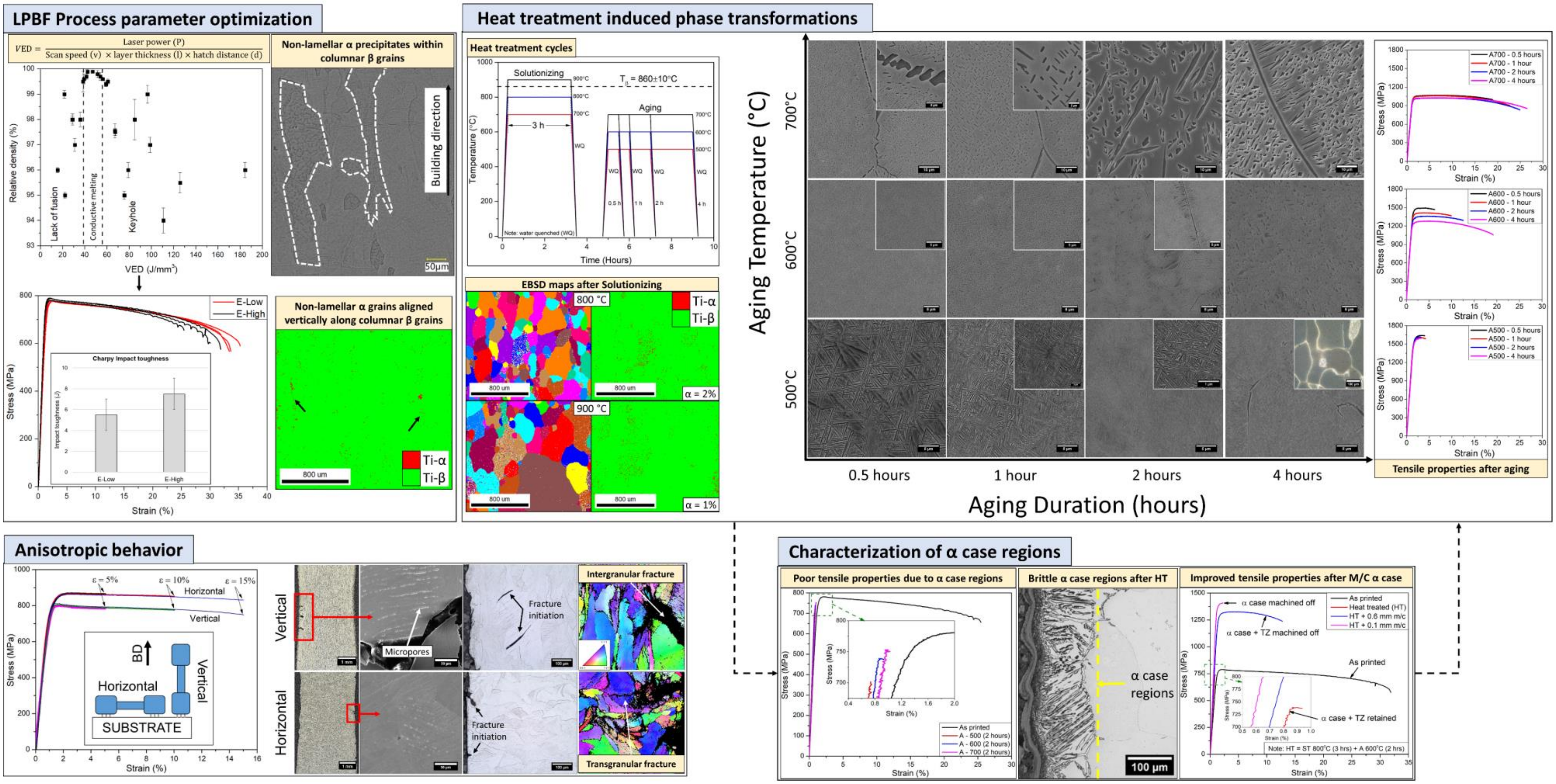

Figure 1-2: An overview of the key findings from the thesis

1.5 Flowchart of the procedure to achieve improved tensile properties

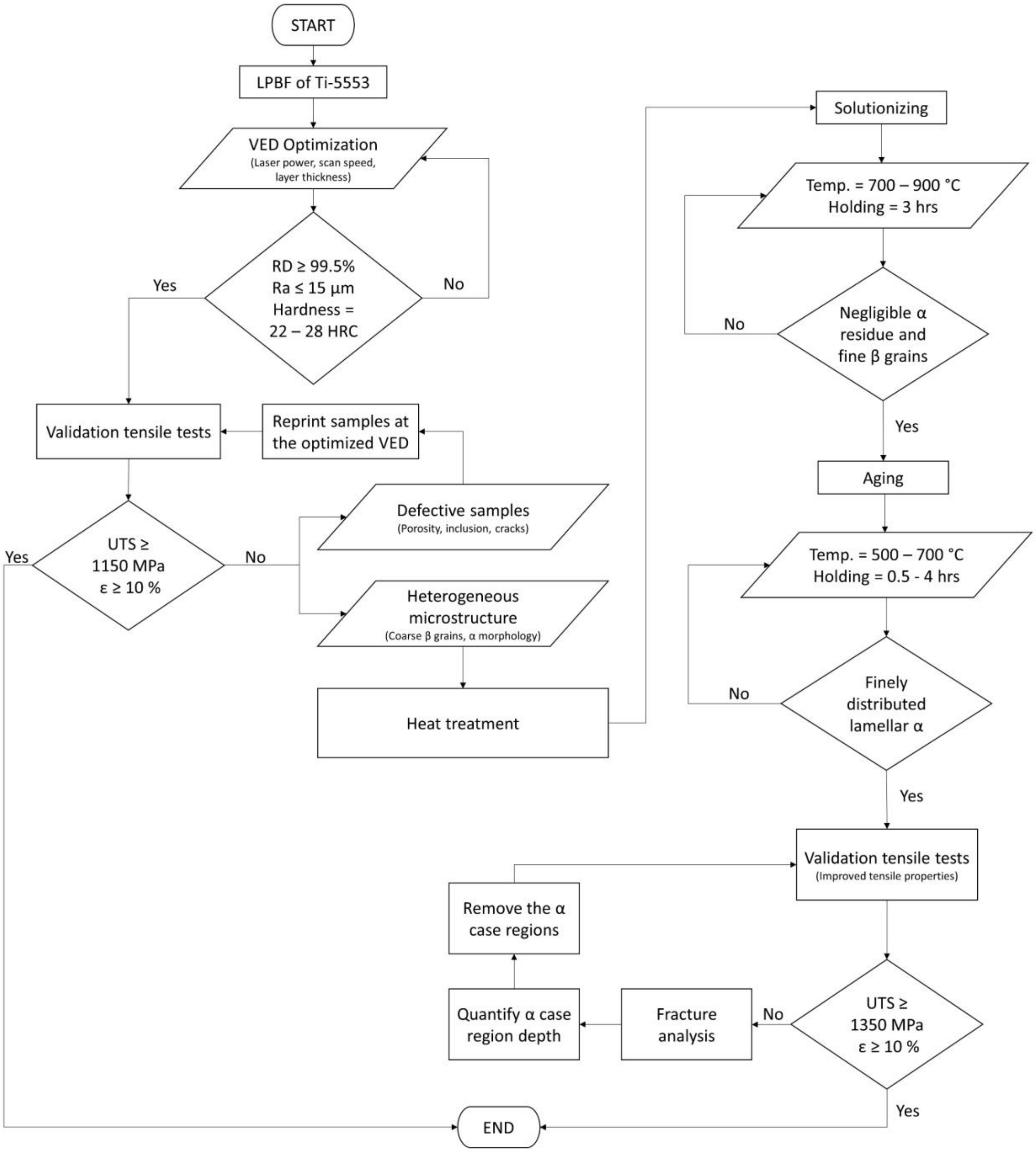

Figure 1-3: Recommendations to achieve acceptable tensile properties in LPBF-made Ti-5553

1.6 Thesis outline

This thesis consists of eight chapters including this one. The subsequent chapters and their contents are outlined as follows:

In Chapter 2, a comprehensive literature review regarding the metallurgy and in particular phase transformations in Ti is presented. Knowledge gathered from the previous reported works were discussed in detail and the existing research gap that thesis targets to address are logically laid out.

In Chapter 3, the methodology of the thesis are described. This chapter summarizes the experimental procedure carried out in order to attain the results discussed in the later chapters. It includes LPBF printing procedure, heat treatment cycles, metallographic practices followed by material characterization techniques employed and the corresponding mechanical tests to validate the effect of observed microstructural features.

In Chapters 4-7, the results are presented and the corresponding observations are discussed. In Chapter 4, the results from the screening phase of the systematic approach followed to identify the laser conduction mode VED range is presented. In addition, the microstructural characterization on the selected samples and their corresponding microhardness, tensile and impact test results are presented.

In Chapter 5, the microstructural changes effected by the heat treatment procedures carried out are discussed. Initially, the temperatures ranges corresponding to phase transformations are traced with the aid of Differential scanning calorimetry (DSC) followed by solutionizing and aging heat treatments covering a whole spectrum of 500 - 700°C up to 4 hours. A detailed Electron backscatter Diffraction (EBSD) for the 12 different aging conditions are used along with the optical images (OM) and scanning electron microscope (SEM) images to deduct the evolution of the second phase particles.

In Chapter 6, the effect of detrimental α case and the transition zone (TZ) on heat treated Ti-5553 are presented. Depth of the α case and the subsequent TZ are characterized and the factors influencing its growth are discussed. The observations are validated by comparing the tensile properties of heat treated components versus those heat treated with the α case removed.

In Chapter 7, the anisotropy effects in LPBF-made Ti-5553 are presented. Interrupted or partial tensile tests were performed to trace the fracture initiation and propagation on samples printed at two different mutually perpendicular directions. The differences in the tensile properties between them and the corresponding distinct fracture modes are presented.

Finally, in Chapter 8 a summary of the important findings related to the objectives in Section 1.3. Furthermore, a scope for future work is offered based on some of the select observations in experiments.

Chapter 2: Literature review

2.1 Titanium alloys

2.1.1 Extraction of titanium – an overview

Ti is one of the most abundant structural metals available, since its ores - Ilmenite ($FeTiO_3$) and rutile (TiO_2), account for 0.6% of the earth's crust [5]. Despite being abundant, Ti is 3 – 4 times costlier than Al, Mg and other commonly used engineering materials [33]. The high cost of Ti is due to the costs involved in maintaining an inert atmosphere, handling toxic chlorine gas, expensive Mg, long processing times, low productivity and high energy consumption during its extraction from ores [34]. The inert atmosphere is necessary to restrict Ti from reacting with interstitial elements (oxygen and nitrogen in particular) which would result in embrittlement [35–37]. Currently, reduction of Ti from its ores is carried out by using tetrachloride ($TiCl_4$) in the intermediate steps is the most economical route [38]. Through the Kroll process, $TiCl_4$ is treated with Mg ($TiCl_4 + 2Mg \rightarrow Ti + 2MgCl_2$) in an inert atmosphere to yield commercially pure porous Ti (titanium sponge) on a large scale. Several low cost Ti extraction technologies are being proposed, but an universal adaptation of any of these technologies are in their developmental years [33].

2.1.2 Initial industrial applications of titanium alloys

Despite its higher cost, Ti started gaining attention after the development of the $\alpha+\beta$ Ti alloys such as Ti-6Al-4V in 1954, which is still the most widely used Ti alloy [39,40]. Several other Ti alloys, including Ti-4Al-4Mo-2Sn-0.5Si and Ti-13V-11Cr-3Al were developed shortly to further improve the creep resistance and formability, respectively. In addition to the higher specific weight, corrosion resistance is one of the main features of Ti. Even though it is not among the noble metals, Ti offers excellent corrosion resistance as a result of a stable, protective oxide film

(TiO_2) similar to Al_2O_3 in aluminum and Cr_2O_3 in austenitic stainless steels. TiO_2 protective layer is highly effective in shielding the substrate, which allows Ti to be used in many salt solutions (including chloride, sulphate, sulphide, nitric, and chromic acid solutions).

Since then, a significant volume of research has resulted in the understanding of phase transformations in Ti, alloy development, fine-tuned production technologies, and characterization methodologies. This has led to many widespread applications including heat exchangers, cathodic protection systems in oil industry, surgical implants, desulphurisation plants (chimney lining) and many other engineering components demanding high performance.

2.2 Metallurgy of titanium alloys

Under equilibrium conditions, Ti exists in two different crystal structures (or allotropes) depending on the temperature as shown in Figure 2-1. The α – β allotropic phase transition from a hexagonal close-packed (HCP) to body centered cubic (BCC) structure is observed in Ti alloys, which occurs at 882°C for pure Ti [41,42]. Such a solid-state transformation is similar to the α – γ phase transformation from BCC to face centered cubic (FCC) structure in steels at the lower critical temperature (A1) on equilibrium cooling. Once an alloy system undergoes allotropic transition, often it can be subjected to a variety of heat treatments [3,8,38,43]. Through different combinations of heat treatments, the distribution and size of the second phase particles can vary, and subsequently the properties could be altered over a wide range to meet specific requirements [10,44–48]. An analogous situation is found in steels, which accounts for the widespread use of carbon and low alloy steels in engineering applications. Since Ti also responds to similar phase transformation, they are most suitable to replace ferrous alloys, especially in critical applications demanding superior performance.

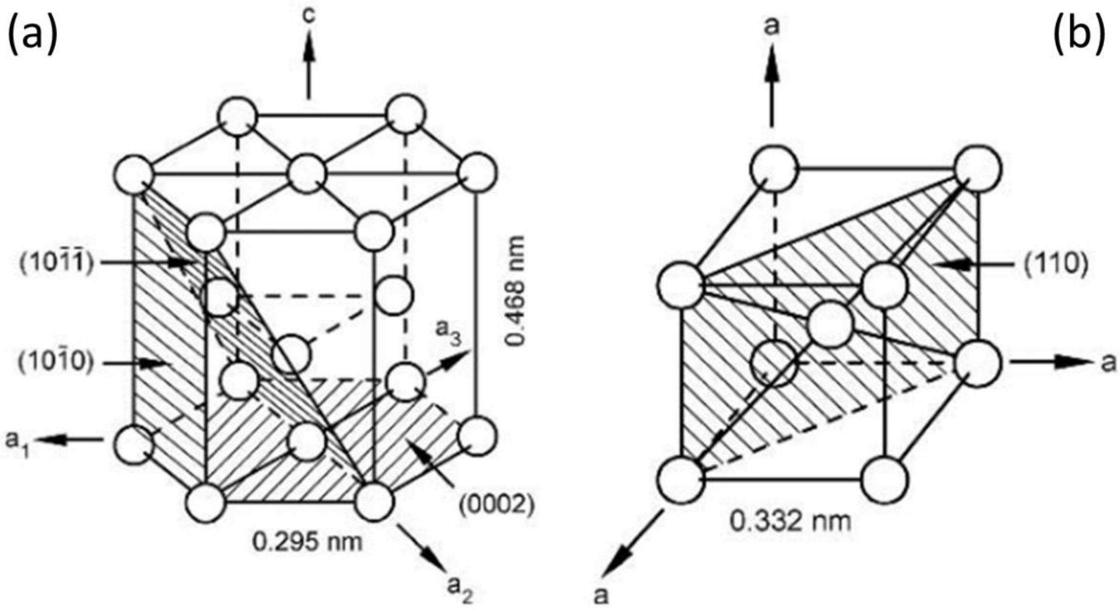

Figure 2-1: Crystal structure of Ti phases (a) α – HCP (b) β – BCC [5]

2.2.1 Effect of alloying elements

Since allotropic transformations occur in Ti alloys, the transition temperature limits the service temperature of α-Ti, although the value of the transition temperature varies with alloy chemistry as shown in Figure 2-2. By the addition of β stabilizers to the alloy chemistry, the high temperature β phase can be retained at room temperature.

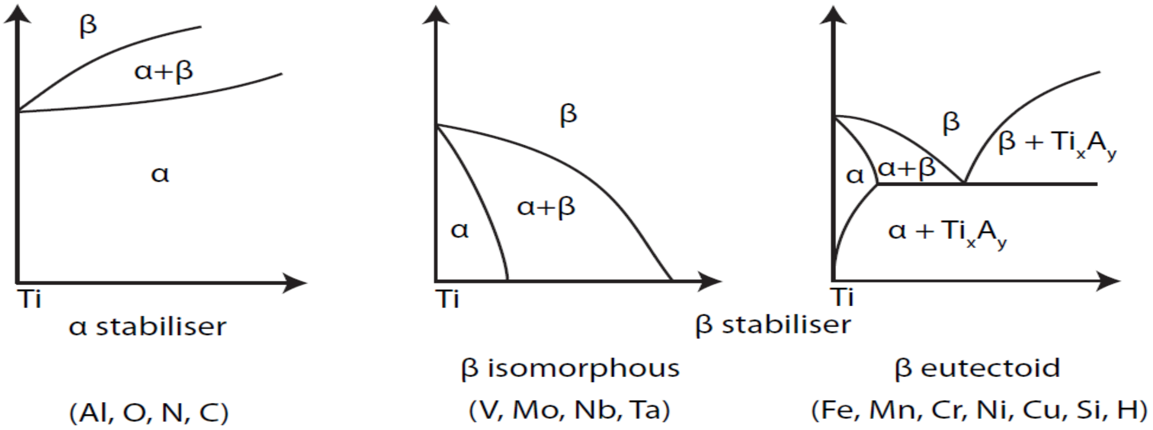

Figure 2-2: α and β stabilizers of Ti [5]

The main alloying additions that influence these transformations can be classified into the following categories as summarized in Table 2-1.

Table 2-1: Major phase stabilizing elements of Ti [8]

α – Stabilizing	**β – Isomorphous**	**β – Eutectoid**	**Neutral**
Aluminum	Vanadium	Copper	Zirconium
Gallium	Niobium	Silver	Hafnium
Germanium	Tantalum	Gold	Tin
Lanthanum	Molybdenum	Indium	
Cerium	Rhenium	Lead	
Oxygen		Bismuth	
Nitrogen		Chromium	
Carbon		Tungsten	
		Manganese	
		Iron	
		Cobalt	
		Nickel	
		Hydrogen	
		Silicon	

Alpha stabilizers – These are elements that are soluble in the α – phase, and these increase the β transus temperature. For example: as observed in Figure 2-4, with the addition of Al, the transformation temperature increases from 882 to 1285°C. In other words, Al stabilizes α phase.

Gallium (Ga), Germanium (Ge) and interstitial elements (oxygen, nitrogen, and carbon) could also stabilize the α phase.

Beta stabilizers – These are mostly BCC elements soluble in the β – phase and decrease the β transus temperature. They are further classified as β-isomorphous or β-eutectoid, as shown in Figure 2-2 [49]. High temperature β phase could be retained at room temperature by the addition of Vanadium (V), Molybdenum (Mb), Niobium (Nb), Tantalum (Ta), Chromium (Cr), Iron (Fe) and many other BCC elements.

Neutral additions – Elements such as Zirconium (Zr) and Hafnium (Hf) that are completely soluble in Ti, does not influence stabilising any phase in particular but still added as a strengthening agent or to slow down reaction kinetics.

Aluminum equivalency (Al-E) and Molybdenum equivalency (Mo-E) are parameters (similar to carbon equivalency in steel alloys) to quantify the α and β phase stabilities respectively of a Ti alloy. The parameter is a combined effect of α, β and neutral stabilizers towards β stability. Al and Mo are used as arbitrary baseline elements and the concentration (in weight %) of other elements are normalised as given below [8,38,50]:

$$\mathbf{Al\text{-}E = Al+0.17\,Zr+0.33Sn+10O}$$

$$\mathbf{Mo\text{-}E = 1Mo+0.67V+0.44W+0.28Nb+0.22Ta+2.9Fe+1.6Cr+1.25Ni+1.7Mn+1.7Co\text{-}1Al}$$

Al is a strong α stabilizer, and hence it is subtracted in Mo-E. With increase in Mo-E, the transus temperature (Tβ) decreases. Approximately, a Mo-E of 10 is necessary to retain the β phase during quenching.

2.2.2 Classification of titanium alloys

Ti alloys of commercial importance are classified as α, α+β, metastable β and stable β alloys as shown in Figure 2-3 [8,45]. Below the critical temperature (1285 – 882°C) Ti exists as α – HCP, as shown in Figure 2-4. The phase transition temperature is controlled by the concentration of alloying elements (Al in this example).

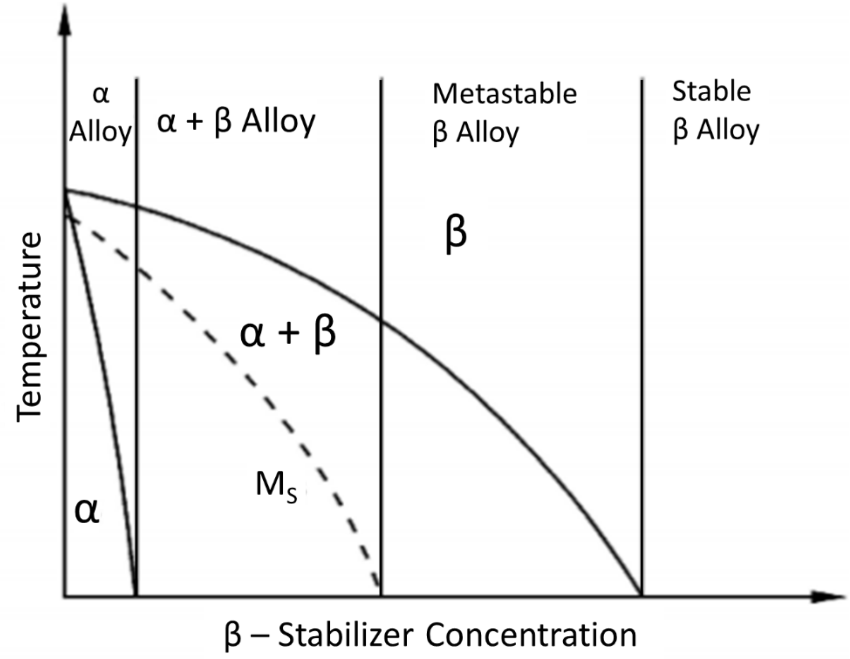

Figure 2-3: Pseudo binary phase diagram of Ti alloys [5]

α-Ti alloys are characterized by the absence or negligible presence of β particles at room temperature. They possess good weldability and corrosion resistance but lacks sufficient tensile strength. The denser and close packed nature of HCP crystal structure compared to BCC, as shown in Figure 2-1(a) aides in minimizing the undesired elemental diffusion. A ductile to brittle transition in mechanical properties does occur for this class of alloys, which makes them suitable for cryogenic environments [51]. They are extensively used in aero-engine gas turbines [52].

α+β Ti alloys are characterized by the significant presence of a stable mixture of both the phases (i.e., α and β). The combination gives a wide range of mechanical properties feasible through heat treatments. The size, distribution and morphology of the precipitates could be fine-tuned according to the design requirements. Ti-6Al-4V, the most commonly used Ti alloy (accounting for ~70% of Ti in current use) is based on the α+β category where the attributes of both α and β Ti alloys are extensively used in applications demanding an optimal combination of strength, fracture toughness and ductility. These alloys are more suitable for jet engines where high-temperature strength (up to a service temperature of 400°C) is mandatory [45,53–56].

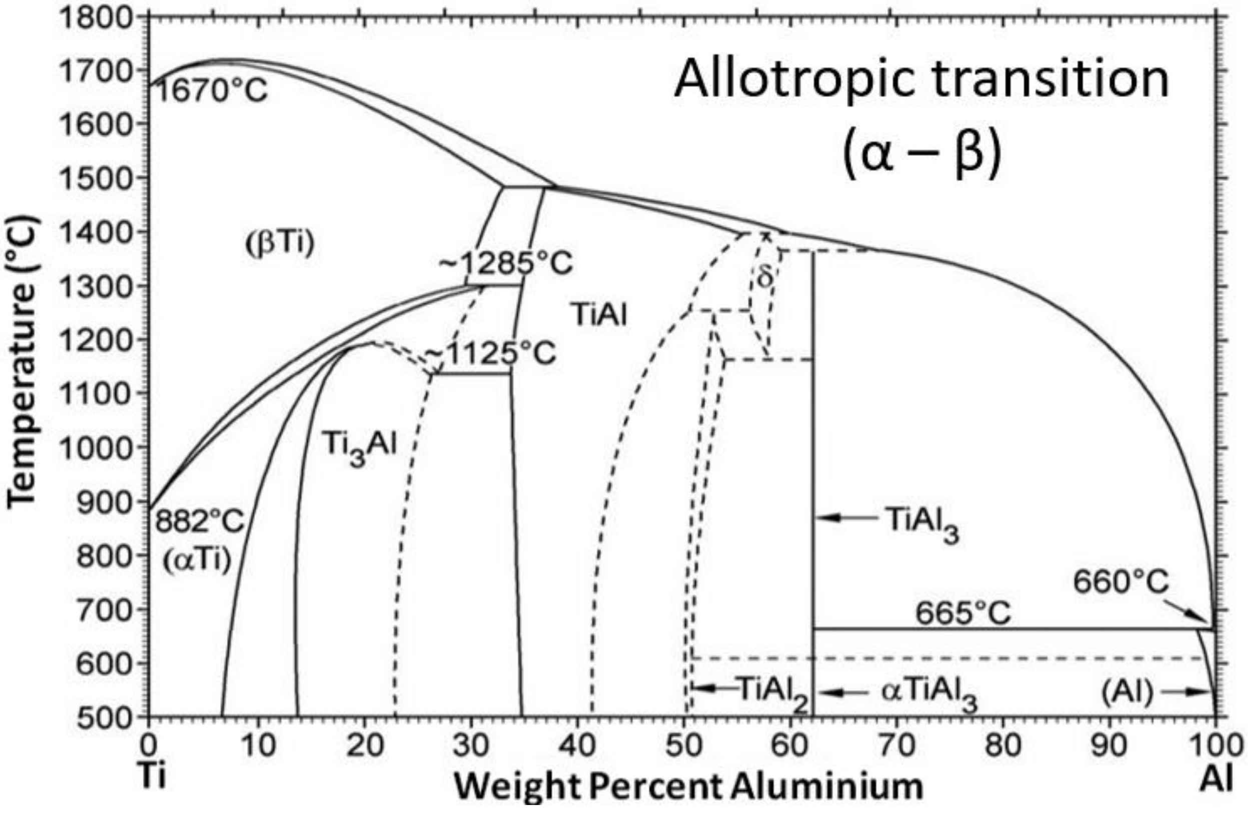

Figure 2-4: Ti-Al phase diagram [42].

On the other hand, BCC structured metastable β-Ti phase seen in Figure 2-1(b), has excellent formability, and hence, it is preferred for structural or airframe applications [8,29,47,48,57–65].

To retain the high temperature phase, alloying elements (β stabilizers) are added to enhance the properties, as will be explained in the next section.

2.3 Evolution of β-Ti alloys – an outline

Ti alloys are capable of retaining 100% β phase on quenching from the high temperature β phase field to room temperature [6], and retaining β phase is enabled by the addition of stabilizers or alloying elements as explained in Section 2.2.1. Based on the concentration of alloying elements added, these alloys are further classified as stable β alloys (containing >30%), metastable β alloys (with 8-30%) and β-rich α+β alloys (with <8%) [62] as shown in Figure 2-3.

Table 2-2: Mechanical properties after heat treatment of Ti-5553 [57]

Aging condition (°C)	Solution treated above β transus (885°C/ 4h)			Solution treated in upper α+β region (825°C/ 4h)			Solution treated in lower α+β region (800°C/ 4h)		
	UTS (MPa)	**True fracture strain**	**% RA**	**0.2% YS (MPa)**	**True fracture strain**	**% RA**	**0.2% YS (MPa)**	**True fracture strain**	**% RA**
450	1187	0	0	1379	0.05	4.5	1532	0.01	1.0
550	1341	0	0	1166	0.13	11.9	1285	0.03	3.0
600	1314	0.01	0.75	1028	0.21	19.1	1259	0.07	7.4
650	1147	0.02	2.0	1076	0.25	22.3	1239	0.13	12.1

Unlike the α+β alloys, metastable alloys do not transform into hard and brittle martensitic phase even on non-equilibrium cooling. Rather, the fine α particles that precipitate in metastable alloys occupy a high volume fraction in the β matrix and hinders the dislocation movement [5,10,65–67]. The distribution, size and geometry of these α particles could be tailored through heat treatment processes [9], resulting in a wide range of mechanical properties. One such example, Ti-5553 alloy exhibiting a wide range of tensile properties following different heat treatment cycles, as shown in Table 2-2. In addition to that, β-Ti alloys have better tolerance to resist hydrogen pickup, and can be processed at lower temperatures compared to α+β alloys [51]. Their corrosion resistance is also comparable to that of α+β alloys [6].

Table 2-3: Summary of β alloys with commercial importance [38]

Alloy	**Name**	**Application**	**Type**	**Mo-E**	**β-Transus (°C)**
Ti-13Nb-13Zr	-	Biomedical	Beta-rich	1.4	735
Ti-20Nb-10Zr-5Ta	TNZT	Biomedical	Near-Beta	5.0	-
Ti-5Al-5Mo-5V-3Cr	Ti-5553	Aircraft	Near-Beta	8.2	855-870
Ti-11.5Mo-6Zr-4.5Sn	TMA	Biomedical	Near-Beta	9.0	-
Ti-10V-2Fe-3Al	Ti-10-2-3	Aircraft	Near-Beta	9.5	790-805
Ti-35Nb-5Ta-7Zr	-	Biomedical	Near-Beta	9.7	-
Ti-29Nb-13Ta-4.6Zr	-	Biomedical	Metastable	10.2	-
Ti-15V-3Cr-3Al-3Sn	-	Aircraft	Metastable	10.9	750-770
Ti-15V-3Cr-3Al-3Nb-0.2Si	Beta 21S	Aircraft	Metastable	12.8	795-810
Ti-15Mo	-	Model Binary	Metastable	15.0	-
Ti-3Al-8V-6Cr-4Mo-4Zr	Beta C	Aircraft/ Oilfields	Metastable	16.0	715-740
Ti-12Mo-6Zr-2Fe	-	Biomedical	Metastable	16.8	-
Ti-13V-11Cr-3Al	B120VCA	Aircraft	Metastable	23.0	650
Ti-30Mo	-	Model Binary	Stable	30.0	-

Ti-40Mo	-	Model Binary	Stable	40.0	-
Ti-35V-15Cr	Alloy C	Aircraft	Stable	47.5	unknown

Shortly after the first demonstration of titanium in an airframe in 1954 with the X-3 [68], the first operational use of β-Ti alloys in an airframe was Ti-13V-11Cr-3Al (B120VCA) in 1966 on the SR-71 Blackbird military aircraft [69]. The combination of high strength forgings (>1170 MPa) and good thermal stability made it ideal for this application despite the difficulties encountered in melting and fabrication. However, the alloy lost significance because of its low elongation (<2%) which is not acceptable for critical aircraft applications. Later, in the 1980s Ti-15V-3Cr-3Al-3Sn alloy was extensively used in the Rockwell B-1B bomber military aircraft in the form of sheets and springs based on its better formability over Ti-6Al-4V [4].Table 2-3 summarizes the list of important β-Ti alloys, their molybdenum equivalence and the transition temperature.

On heat treatment, these β Ti alloys exhibit a minimum tensile strength of 1034 MPa, and is comparable to Ti-3Al- 8V-6Cr-4Mo-4Zr (β-C) alloy, with a strength of 1240 MPa and also used in springs [38]. Another alloy, Ti-14.7Mo-2.7Nb-3Al-0.27Si (β-21S) was developed to be used at high temperatures, offering excellent corrosion resistance and creep properties for resistance to attack by thermally decomposed hydraulic fluid, making it superior to Ti-6Al-4V [70]. Improved fatigue performance of Ti-10V-2Fe-3Al (Ti-1023) alloy compared to Ti-6Al-4V has justified it replacing α+β alloy components in more recent aircraft [60], and this trend is expected to grow. However, the sensitivity of Ti-1023 to minor variations in temperature and strain rate is a disadvantage.

2.3.1 Metastable β alloy: Ti-5553

As mentioned in Section 2.3, the sensitivity of Ti-1023 limits the processing window. Meanwhile, a modified version of the Russian alloy VT-22 was developed with mechanical performance comparable to that of Ti-1023 but with a wider processing window. The developed alloy, Ti-5Al-5Mo-5V-3Cr (Ti-5553) also posses more advantages allowing it to replace Ti-1023 in multiple applications including the truck beam parts of Boeing 7E7 and Airbus A-380 landing gears [4,60]. One such advantage is its superior response to heat treatability. Ti-5553 sections up to 152 mm could be easily heat treated followed by air cooling whereas the maximum section heat treatable is limited to 76 mm for Ti-1023 that also requires water quenching. Also, on heat treatment, a minimum tensile strength of 1240 MPa is achievable for Ti-5553, compared to 1192 MPa for Ti-1023 [71].

Figure 2-5 shows the superior tensile strength and fatigue behaviour of Ti-5553 compared to Ti-64 (the most common Ti alloy). The combination of higher strength and ductility of Ti-5553 (a near β-Ti alloy) results in 60% higher performance in the high cycle fatigue (107 cycles) environment [72]. The improved properties are a result of a difference in the β → α transformation between β-Ti and α+β Ti alloys. In β-Ti alloys, the α precipitation happens at a lower temperature and hence it is more sluggish. This sluggish precipitation combined with isothermal ageing of β phase results in a finer distribution of α particles, improving the fatigue performance [73,74].

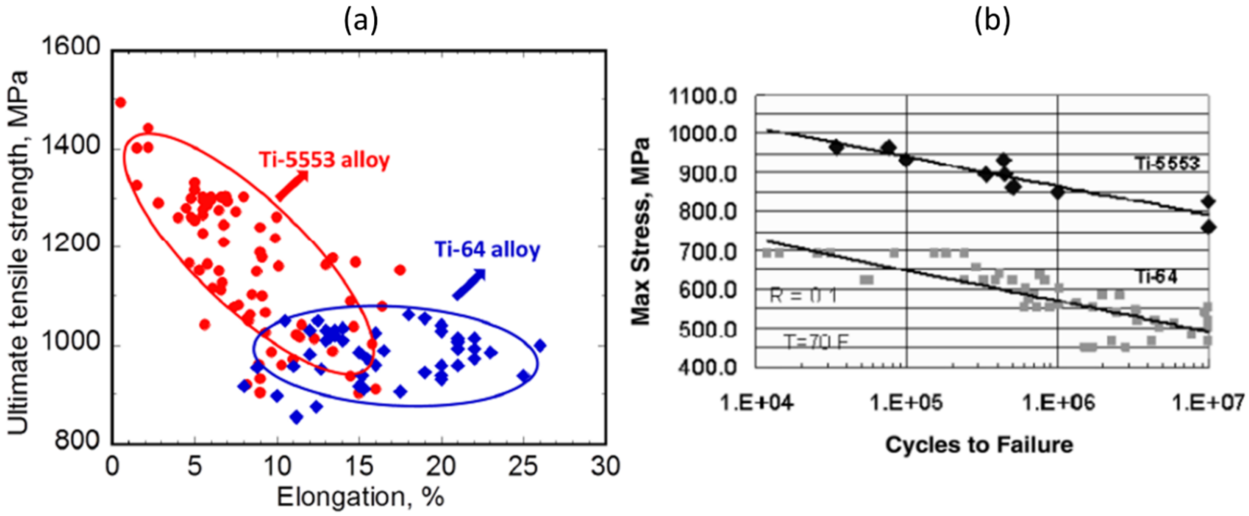

Figure 2-5: (a) Tensile properties of Ti-5553 compared with Ti-64 [71] (b) High cycle fatigue (HCF) behaviour of Ti-5553 compared with Ti-64 [72]

2.3.2 Limitations in traditional manufacturing of Ti alloys

Traditional manufacturing involves processing raw material or a semi-finished product into a final product through several steps, where each step is a value addition to the product being manufactured. Machining, welding, rolling, and casting are a few well known traditional manufacturing processes, each of which involve various complexities and challenges specific to the traditional manufacturing of Ti alloy parts [46,48,73,75–79].

2.3.2.1 Challenges in subtractive manufacturing of Ti alloys

Subtractive manufacturing processes is a division of traditional manufacturing processes where the final product is carved out by removal of undesired material to achieve the required geometry. Cutting, boring, drilling, grinding, milling are some of the subtractive manufacturing processes. Ti alloys are among the challenging materials to be subtractively manufactured. The high chemical reactiveness and poor thermal conductivity of Ti leads to a tendency to drastically reduced cutting tool life. Moreover, the superior high temperature strength and low modulus of elasticity of Ti impairs its machinability [80]. The one-third chip-tool contact area on the rake face during Ti-6Al-4V compared with that of steel at same feed rate and depth of cut was reported to result in 300 – 400% the higher stresses experienced on the tool while machining Ti alloy parts [81]. The low modulus of elasticity causes chatter which subsequently results in premature flank wear, vibration and higher cutting temperatures. The vibration reasons the high dynamic cutting forces ranging up to 30% of the static forces which often results in catastrophic thermoplastic shearing of the machined chips [82]. Tungsten carbide and cemented carbide are the best commercially cutting tool materials for machining Ti alloys. However, for industry-friendly high cutting rates and an excellent surface finish, new tool materials have been sought after for decades [83].

2.3.2.2 Challenges in welding of Ti alloys

Welding of Ti-5553 results in a heterogeneous microstructure across the weld with the fusion zone experiencing a loss of Al and a lower hardness values [48]. The localized heating involved in welding processes impart residual stresses as the weld contracts during the final stages of the joining process. In addition to the significant degree of distortion caused by the residual stresses, the fatigue properties are also severely affected [84,85]. Various preventive measures including reduction of heat input, following an optimized welding and machining sequence, stress relief heat treatments, specialized jigs and a training heat sink were trailed resulting in limited improvements [86]. Moreover, the welded regions are often the sites of fatigue crack initiations whereas, the use of pulsed current provides a marginal improvement to the as-welded mechanical properties which are further improved on heat treatment [87,88].

2.3.2.3 Challenges in rolling and casting of Ti alloys

Hot rolled Ti-5553 displays the finely distributed globular α precipitates within the β matrix. The texture in these specimens mainly consists recrystallized components, however a strong anisotropy exhibited affects the mechanical properties [64]. The full lamellar α morphology in vacuum arc melted and heat treated Ti-5553 followed transgranular shearing and a brittle dominant fracture. Correspondingly, the ductility was severely affected [77]. Ti alloy parts manufactured via investment castings exhibits a hard and brittle α case as a result of its reaction with ZrO_2 face coating and the residual oxygen in the shell mold [89,90].

To summarize, the prime limitations in processing Ti alloys through traditional manufacturing processes are listed below [4,62]:

- Severe alloy segregation in the cast form
- Poor fatigue properties of the weldment
- Negligible strengthening through work hardening
- High affinity for interstitial elements (O, N, C, H) that results in embrittlement
- Material wastage and manufacturing difficulties encountered during machining of Ti [39]
- Relatively high raw material cost compared to other structural alloys
- Narrow materials processing window and complicated processing routes
- Limited service temperature, ideally below 400°C

2.3.3 Additive manufacturing of Ti-5553

Additive manufacturing, as introduced in Section 1.1, is an automated manufacturing process capable of fabricating near net shaped products from 3D CAD data. Unlike traditional manufacturing which often requires multiple steps to manufacture complex geometries, products of any complexity could be made in a single step without human intervention via additive manufacturing techniques. For printing metallic parts aiming 100% relative density, laser beam and electron beam are the reliably preferred heat sources [91]. The heat energy could be projected on a bed of metallic powders - LPBF or applied on a spool of wire or on metallic powders fed through a nozzle, called as direct energy deposition (DED). Additionally, the pulsed mode of heat application offers further variants to the process. LPBF offers a higher resolution using smaller layer thickness, laser diameter and lesser number of support structures compared to DED. However, LPBF is limited by its slower build rate and hence for printing larger components, DED is generally preferred over LPBF [92–94]. The layer-by-layer printing in AM cause directional solidification which results in the growth of columnar grains aligned along the building direction. The recrystallized columnar grains introduce solidification defects and anisotropy in properties [43]. Therefore, metallurgy and hence the mechanical characteristics of AM fabricated parts are distinct compared to traditionally made counterparts.

2.3.3.1 Differences between traditionally and additively made Ti alloys

Rapid heating and cooling cycles involved in AM processes could introduce non-equilibrium phase transformations which were under certain degree of control in traditionally manufactured parts. The wear resistance of LPBF-made commercially pure Ti (CP-Ti) was reported to be better when compared with cast CP-Ti parts due to the martensitic microstructure (α’), finer grain size and superior hardness in AM specimens, as in Figure 2-6 [95].

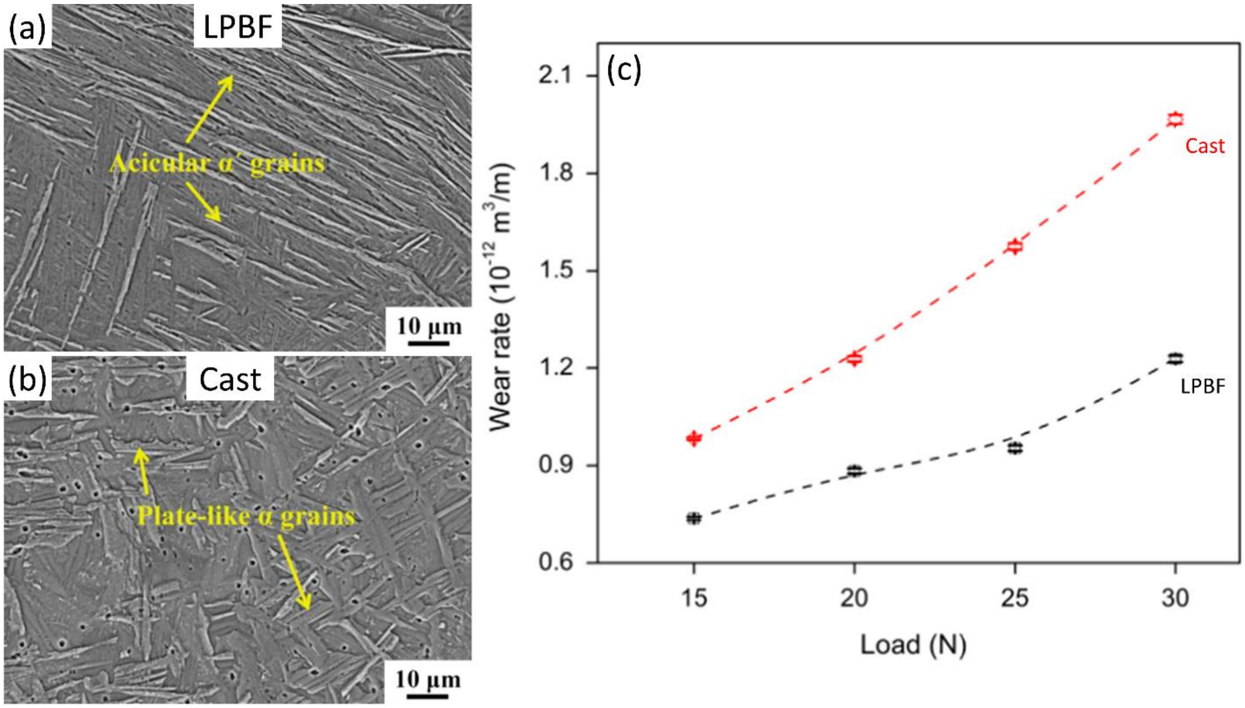

Figure 2-6: CP-Ti produced (a) exhibiting α' grains after LPBF process (b) exhibiting α grains after casting and (c) the corresponding sliding wear rate comparisons as a function of load [95]

Similar improved wear resistance is exhibited by LPBF processed Ti-64 compared with electron beam melted (EBM) and conventionally forged equivalents [96]. Grove *et al.* compared the machinability of Ti-5553 specimens fabricated under three methods - conventionally wrought, LPBF-made and LPBF-made with in-situ heat treatment. Highest tool load and the highest residual stresses were exhibited by the LPBF samples made with in-situ heat treatment owing to the hard and brittle ω phase precipitates in the microstructure [32].

2.3.3.2 LPBF process parameter tools

While optimal LPBF process parameter sets are established to improve the mechanical properties of the printed parts, it is essential to systematically identify the favorable processing window. Different methodologies have been reported in the literature aiming to detect the optimized process window [97–99]. Ansari *et al.* developed and applied a process model to couple the heat and mass transfer during the DED printing [97]. Within the identified optimal processing region in Figure 2-7, an 80% accuracy was demonstrated by the experimental validation results on comparison with the applied mathematical model [97]. Another widely popular process optimization approach is the regression analysis of the statistical data to derive a mathematical formulae that reveals the combined role of different processing parameters including laser power, scan speed, and layer thickness [98].

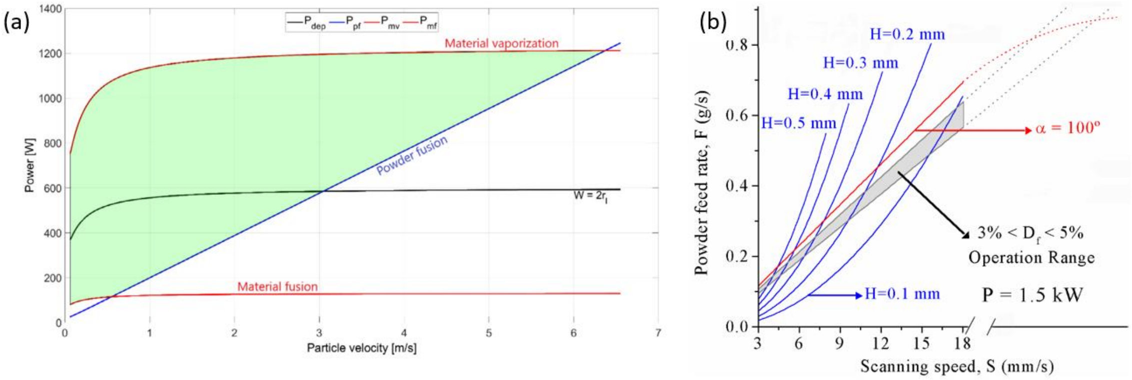

Figure 2-7: Identified AM process windows through (a) mathematical modelling [97] (b) statistical analysis [98]

2.3.3.3 LPBF process parameter optimization of Ti-5553

Since AM of Ti-5553 is currently in its formative years, only a limited volume of findings about its characteristics are available in open literature. Hence, predicting an optimal processing window using numerical models could involve several assumptions that might lead to a large magnitude of errors at an early stage of the research [27,97]. Initially reported preliminary studies on LPBF printability of Ti-5553 using a continuous laser achieved a rather high relative density in components by varying the process parameters, such as laser power, scan strategy and powder particle size [28,29]. Later, Bakhshivash *et al.* studied the possibility of LPBF printing Ti-5553 parts using a pulsed laser as the heat source [27]. In all of these cases, an acceptable relative density (>99.5%) is claimed at completely different ranges of process parameter sets. The applied LPBF process parameter set can also modify the surface roughness to a great extent, which could significantly affect the mechanical properties. Zopp *et al.* validated the LPBF process parameter sets developed for powder particles sized 10 to 63 μm and reported a relative density of 99.93%. Additionally, it was reported that the powder particles sized 25 to 32 μm resulted in the least surface roughness [28].

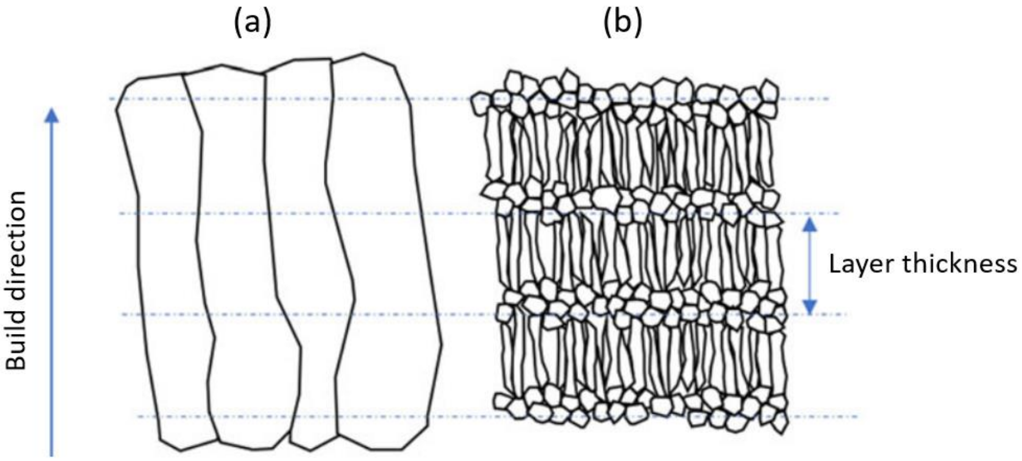

Figure 2-8: Schematic of columnar grain growth (a) with high VED (b) with low VED [94]

Volumetric energy density (VED), which is a quantitative measure of the thermal energy imparted on the metallic powders, is used to compare the consolidated effect of different LPBF process parameters $\left[\mathrm{VED} = \frac{\text{Laser power (P)}}{\text{scan speed (v)} \times \text{layer thickness (l)} \times \text{hatch distance (d)}}\right]$. Even though process parameter sets of different ranges were reported to exhibit good relative densities, the metallurgical features identified in them varied as in Figure 2-8. The columnar grains in low VED prints are relatively shorter and thinner compared to the high VED prints. Equiaxed grains were identified at the intersection of two subsequent layers for lower VED prints. Whereas, in high VED prints, the applied heat energy to sufficiently melt the previously deposited layer resulting in continuing the columnar gain chain [94]. Furthermore, as in Figure 2-9, low ranged process parameters (i.e. low laser power and low scan speed) exhibited 100% β microstructure whereas in high ranged process parameter sets (i.e. high laser power and high scan speed) traces of α precipitation were reported for Ti-5553 [27,29].

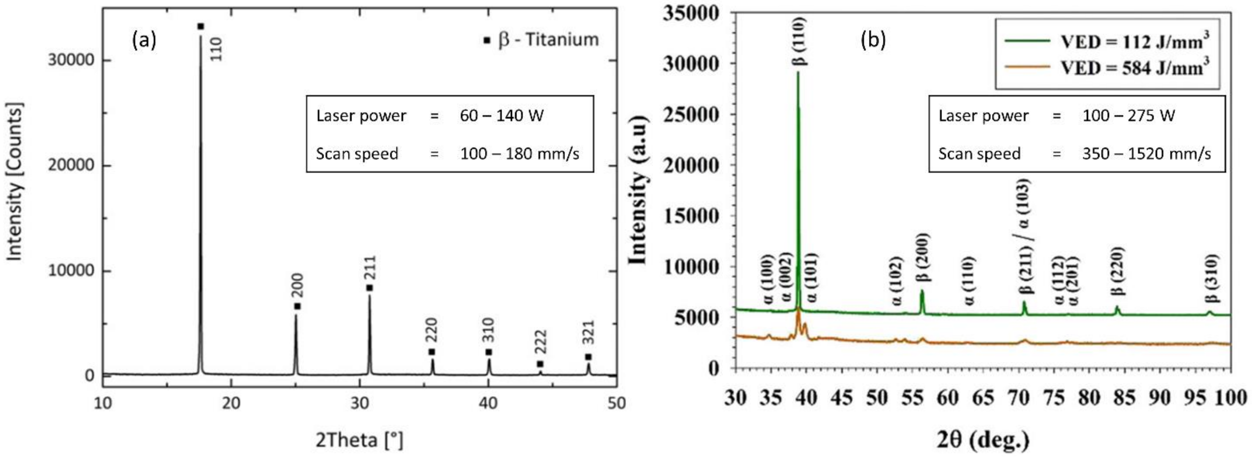

Figure 2-9: XRD patterns of LPBF processed Ti-5553 (a) 100% β microstructure (b) α precipitates in β matrix

In addition to the α precipitates, hard and brittle ω precipitates were also identified in the transmission electron microscope (TEM) images of high VED (VED = 584 J/mm^3) pulsed laser prints. Comparison between the microstructural features of samples taken from different heights of the printed parts reveal varying α needle sizes as in Figure 2-10 [27]. In similar research involving the characterization of LPBF-made Ti-5Al-5Mo-5V-1Cr-1Fe alloy, a 98.1% β microstructure encompassing a submicron cellular structure was reported. Furthermore, hatch spacing, which is the distance between two consecutive laser beams is also reported to be strongly correlated to the size of the columnar β grains [100]. A hatch spacing increment from 60 to 120 µm resulted in eliminating the continuous pore channel which existed throughout the Ti-5553 specimen [29].

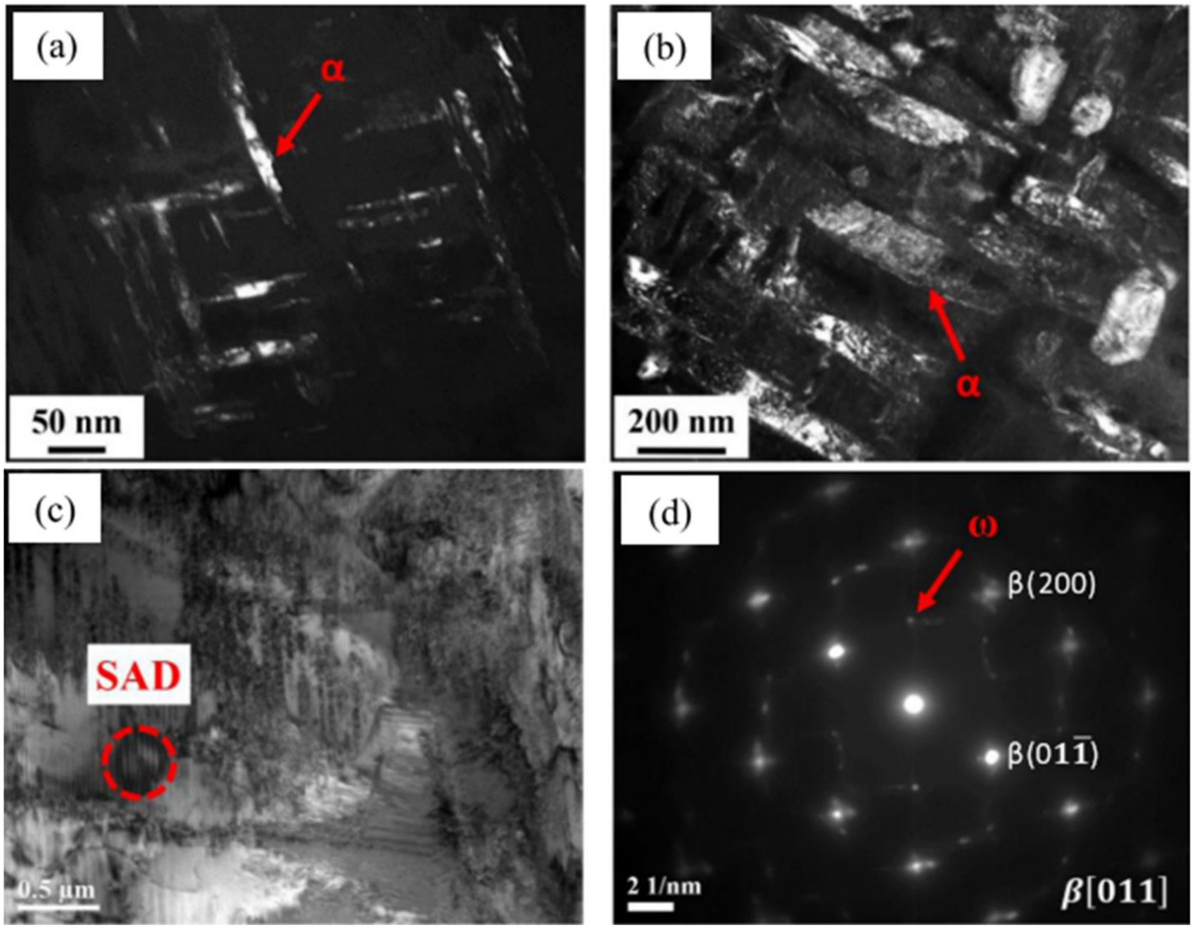

Figure 2-10: TEM images of VED = 584 J/mm^3 samples showing significant difference in α particle size at (a) top (b) bottom of the printed samples [27]

2.3.3.4 Tensile properties of additively manufactured Ti-5553

While microstructural characteristics unique to the AM processes observed in LPBF-made Ti-5553 were discussed above, certain similarities in the texture development with respect to the conventionally processed Ti-5553 were also reported. Therefore, it is of interest to evaluate the mechanical properties, especially the tensile properties of AM-fabricated Ti-5553. Even though the columnar grain growth is common to AM processes, the size of the β grains ranging 100 to 300 µm were comparable to forged Ti-5553 microstructures [60,101]. The grain growth preference of the β grains in the <100> direction is widely seen in traditionally processed Ti-5553 parts and preserved in LPBF as well [10,29]. The Rockwell hardness values reported for LPBF-made Ti-5553 are comparable to the conventionally made Ti-5553 specimens [102].

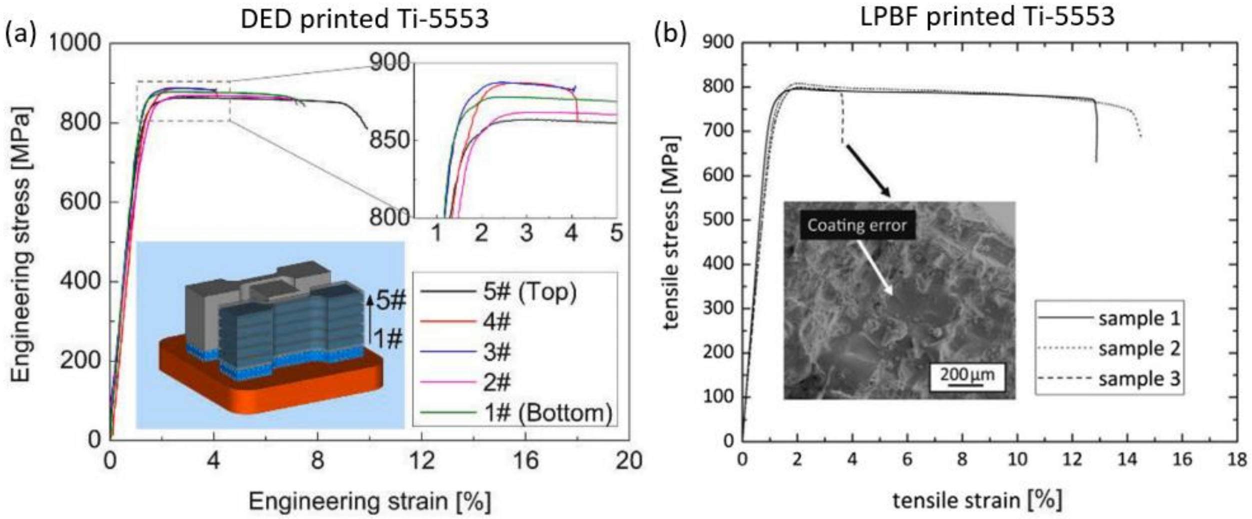

Figure 2-11: Tensile test curves of AMed Ti-5553 at optimized process parameter sets (a) DED printed rectangular Ti-5553 specimens (b) LPBF printed cylindrical Ti-5553 specimens [29,101]

Despite the acceptable relative densities and the hardness values achieved in LPBF or DED made Ti-5553, the ultimate tensile strength (UTS) reported is only a modest ≈ 800 MPa with a total elongation of 10 to 15 %, that is inferior compared to its traditionally manufactured counterparts (>1100 MPa) [100,101,103–105]. The need to further optimize the process parameters was reported as a pathway to achieve an improved set of tensile properties [29]. The lack of fusion (LOF) and porosity were anticipated to cause premature failures at lower than expected loads.

To limit the chaotic fluid flow interactions during laser printing, artificial neural network (ANN) algorithms were trialed to predict the relative densities for a given process parameter set. Even though the ANN-model is promising as in Figure 2-12, it needs to be trained with different materials which is required for a deeper phenomenological explanations of laser-material interactions [31].

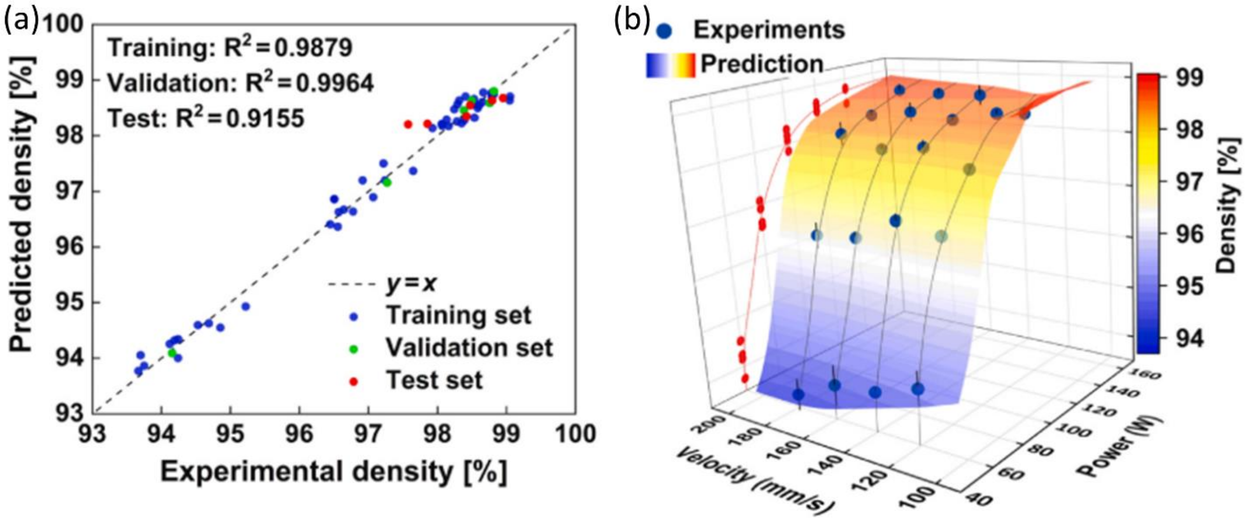

Figure 2-12: ANN model optimization (a) Predicted vs. experimental density values (b) density predicted by ANN for a 20% hatching distance [31]

The observed differences in phase distribution and the corresponding inferior tensile properties emphasise the necessity of a comprehensive study on optimizing the process parameter range including microstructural features, surface roughness and mechanical properties as evaluation criteria.

2.3.4 Heat treatment of β-Ti alloys

Heat treatability is one of the prime advantages of dual phased Ti alloys in fine tuning the mechanical properties over a wide range. As previously discussed in Section 2.2, BCC crystal structured β phase provides ductility and HCP crystal structured α phase provides strength to the alloy. Depending up on the heat treatment conditions, 12 α phase variants each with a different orientation to the parent β crystal could exist [106]. Also, depending up on the ratio, size, location and distribution of the α variants present in the microstructure, the corresponding mechanical properties differ.

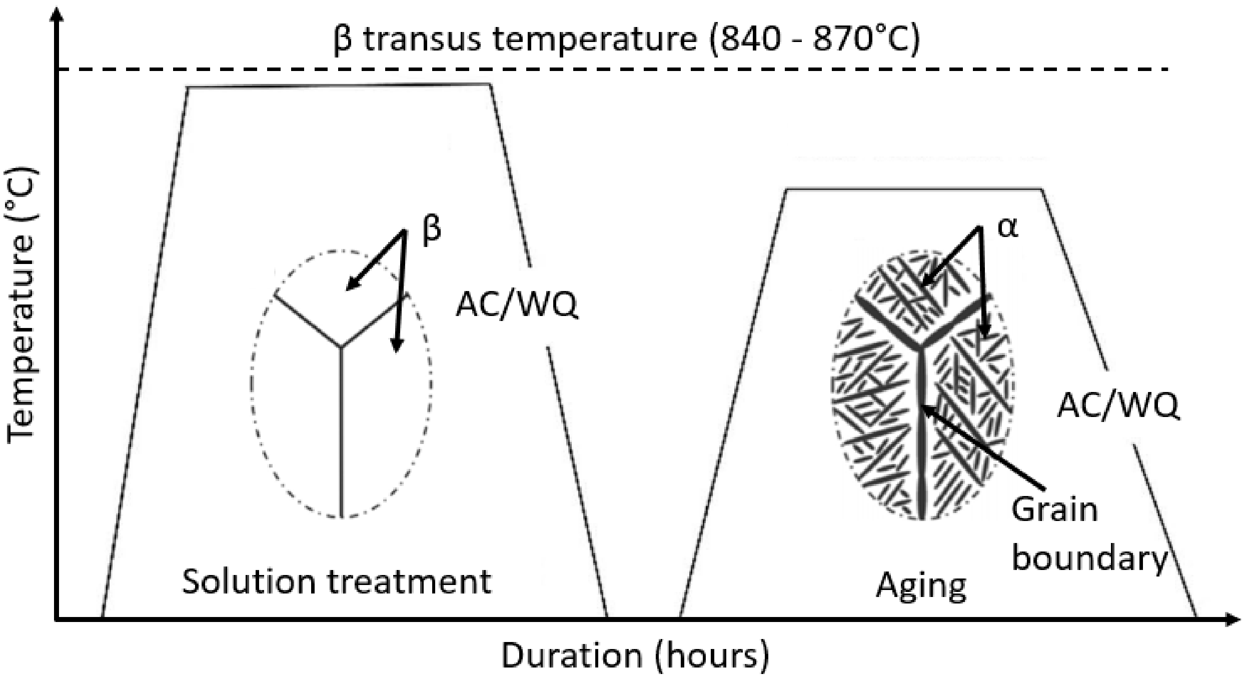

Figure 2-13: Schematic representation of the Ti heat treatment cycles and the corresponding microstructures [107]

Metastable β-Ti alloys are typically subjected to a two stage heat treatment cycle as in Figure 2-13. The two stages are solution treatment and aging. During solution treatment, the heterogeneously precipitated α precipitates are dissolved into the solid solution resulting in a nearly 100% β microstructure. While aging under inert atmosphere, growth of finely distributed thin secondary α needles are facilitated. Other heat treatment cycles including β annealing slow cooling and aging (BASCA) and duplex aging are claimed to result in a homogeneous α precipitate distribution in Ti-5553 but thickens the grain boundaries [108]. Thus, the unique grain structure developed in AM-fabricated Ti-5553 structures may require different heat treatment cycles than the conventionally manufactured alloy.

2.3.4.1 Solution Treatment of β-Ti alloys

Solution treatment could be further sub-divided into three steps as heating to the solution treatment temperature, soaking and cooling. The solution treatment temperature is decided based on the β-transus temperature (β_T), which is the minimum critical temperature at which 100% β microstructure exists in that alloy. The duration of soaking is critical as it needs to be long enough to achieve microstructural homogenization but not too long to facilitate coarsening of the homogenized grains. The cooling rate varies based on the medium of cooling. Furnace or air cooling, water or oil quenching are some of the commonly preferred cooling options for Ti after solution treatment reported in literature. The specimens subjected to solution treatment exhibit low strength and high ductility as the microstructure is composed of nearly 100% β phase. In a few cases, solution treatment is also applied as an intermediate step to soften the material for cold working [49,79,109].

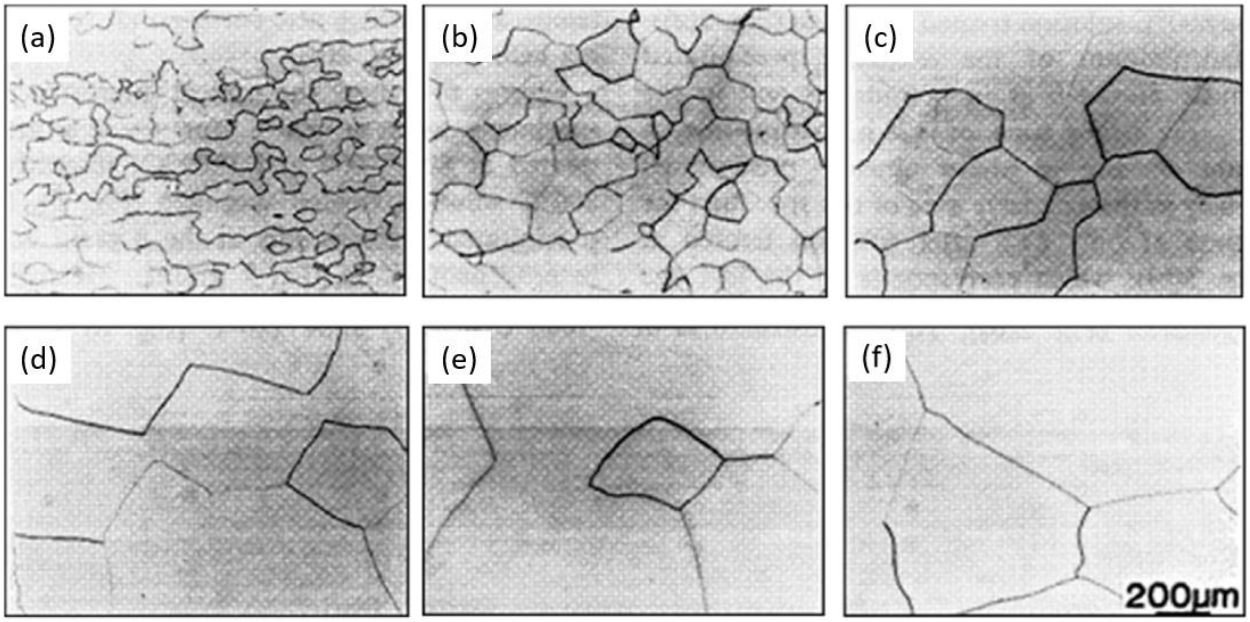

Figure 2-14: Effect of solution treatment temperature on grain size of a β-Ti alloy (Ti-15V-3Cr-3Sn-3Al) (a) 800°C (b) 900°C (c) 1000°C (d) 1100°C (e) 1200°C (f) 1300°C [110]

To design a heat treatment procedure, it is essential to map the temperature dependent phase transformations. Differential Scanning Calorimetry (DSC) and Thermogravimetric analysis (TGA) are the techniques generally employed to trace the phase transformations with temperatures. In these techniques, lattice parameter changes induced by the crystal structure transformations are linked to estimate the phase transformations. Typically, 840 to 870°C is reported as β_T for Ti-5553 with minor variations in the temperature range [111–113]. Solution treatment is carried out either at temperatures higher than β_T (super-transus) or below β_T (sub-transus). Even though the sub-transus solution treatment could result in residual α particles in the microstructure, it is effective in arresting the coarsening of β grains compared to the super-transus solution treatment. Smaller β grains are favourable in achieving finely distributed secondary α needles [114]. Microstructure developed during sub-transus (α+β) solution treatment of Ti-5553 revealed finer grains compared to super-transus (β) solution treatment and subsequently, a better combination of UTS and ductility was exhibited after sub-transus solution treatment [57]. Similar better tensile properties were exhibited for several other β-Ti alloys after sub-transus solution treatment as shown in Figure 2-14 [110,114,115]. Devaraj *et al.* studied different sub-transus solution treatment temperatures and reported that the temperature closest to β_T attributed to the highest concentration of finely scaled α needles distributed in β matrix which results in the best combination of yield strength (YS) and UTS [116]. The bimodal distribution of α is also a contributing factor for the improved tensile properties.

2.3.4.2 Aging Treatment of β-Ti alloys

Aging of the solution treated material improves its tensile strength accompanied by a considerable loss in ductility. During aging, α phase precipitation is facilitated accompanied by the simultaneous decomposition of β phase. A systematically optimized selection of aging parameters (temperature, time, cooling rate) could provide the finely distributed α precipitates in the microstructure. The precipitated α particles in the β matrix increase the α/β interfaces which subsequently decreases the effective shear band length of the dislocations resulting in increasing the tensile strength of the Ti alloy [117,118].

2.3.4.3 Effects of heat treatment process parameters

Heating rate, aging temperature and duration, cooling rate are considered to be fundamental process parameters of aging treatment. Variations in heating rate tend to alter the precipitation kinetics in β-Ti alloys as shown in Figure 2-15. Experiments carried out on comparing the effect of heating rate on Ti-5V-5Mo-1Cr-1Fe-5Al at different heating rates revealed that a low heating rate of 0.25°C/s results in a fine and uniform distribution of α phase. However, high heating rates of 20°C/s results in non-uniform and coarse precipitates [119].

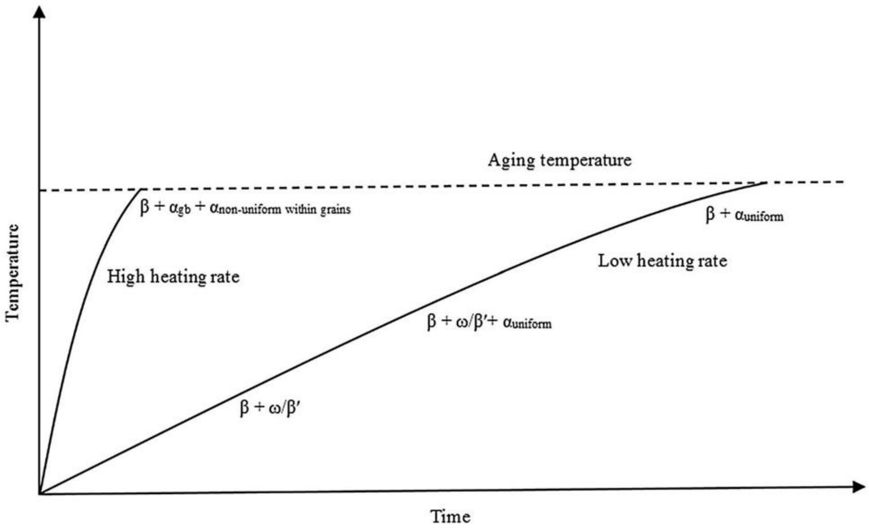

Figure 2-15: Schematic representation of α phase precipitation at different heating rates [120]

Morphological differences in the α precipitates caused due to different heating rate at 600°C is proven to have a significant difference in the hardness measurements of Ti-15-3 alloy [121]. Wain *et al.* reported a substantial refinement of the α precipitates in Ti-5553 when the heating rate was maintained low [122].

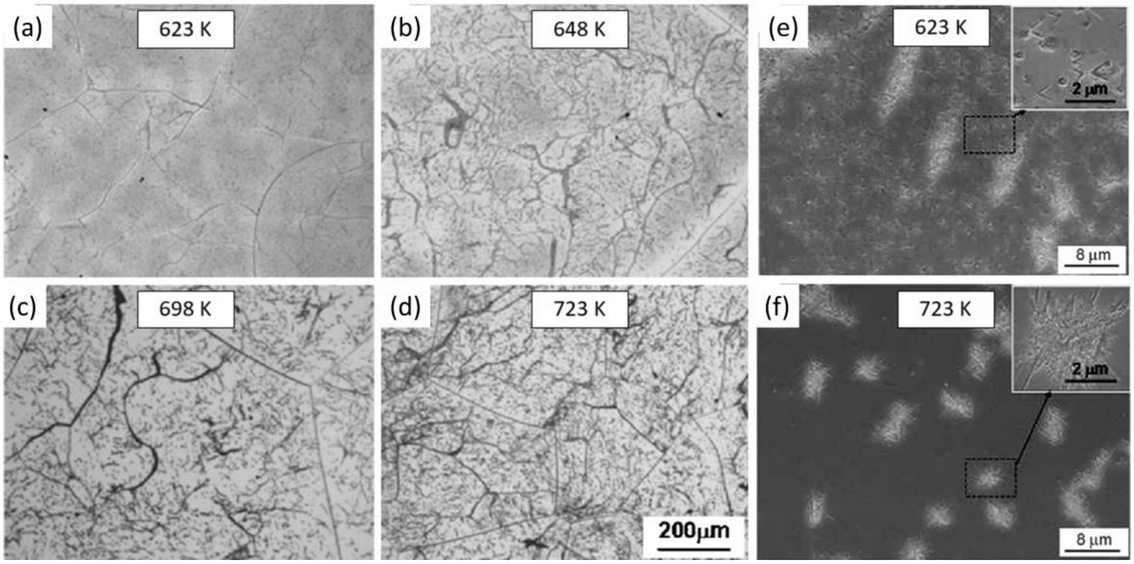

Figure 2-16: Isothermally treated Ti-5553 for 60 minutes (a-d) Optical images showing increase in volume fraction of α precipitates with temperature (e-f) SEM images showing two different α morphologies observed depending on temperature [73]

Temperature and ageing time significantly control the growth of second phase precipitates and it is detailed in several articles [8–10,57,66,73,123,124]. One such example is shown in Figure 2-16 and Figure 2-17. Microstructures of Ti-5553 samples subjected to heat treatment at different temperatures for a fixed time of 60 minutes is presented. As seen, the volume fraction of α particles (dark regions) is higher with an increase in temperature. Morphology of the α precipitates can vary from triangular to lamellar alignments based on the heat treatment temperature as in Figure 2-16.

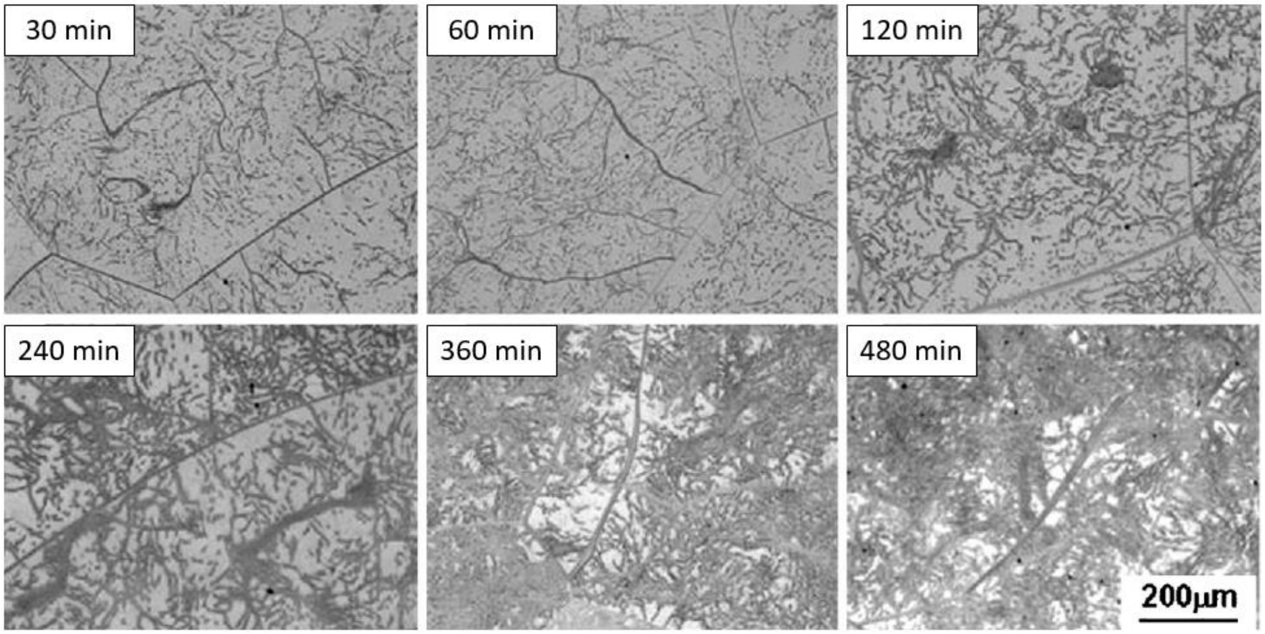

Figure 2-17: Optical images of Ti-5553 showing difference in volume fraction of α particles heat treated at 673 K for different durations [73]

Bai *et al.* reported a 1.6 μm to 21.8 μm increase in the width of the α needles in Ti-64 when the aging temperature was increased from 850°C to 1020°C. The corresponding changes in the mechanical properties are given in Table 2-4 [125]. Furthermore, the electron microscopy images shown in Figure 2-16 (e & f) reveal a shift in the geometry of precipitated α particles from V-shaped or triangular shaped to star shaped morphology with increase in temperature.

Table 2-4: Mechanical properties of Ti-64 after heat treatment at different temperatures [125]

Sample	**YS (MPa)**	**UTS (MPa)**	**Elongation (%)**	**KIC (MPa $\sqrt{m}$)**
As-printed	1065±6.8	1152±11.3	6.1±0.8	-
850°C	943±5.2	989±6.1	10.2±0.1	84.9±0.4
950°C	835±3.8	887±7.1	11.9±0.1	90.8±2.1
1020°C	742±13.5	839±6.2	15.3±0.3	58.7±4.6

Initial research on the heat treatment of LPBF-made Ti-5553 also resulted in the precipitation of α needles which coarsen with temperature as shown in Figure 2-18 (a-c) [9]. The corresponding phase transformation changes and changes in tensile properties are in Figure 2-18 (d &e) respectively, which confirm that ω precipitates form at 300 - 500°C aging temperatures to increase strength [9]. However, the severe embrittlement observed at 400 - 500°C is also related to the precipitation of ω particles. At higher temperatures the morphology and volume fraction changes result in high ductility when a α/β mixed microstructure forms with coarser particles.

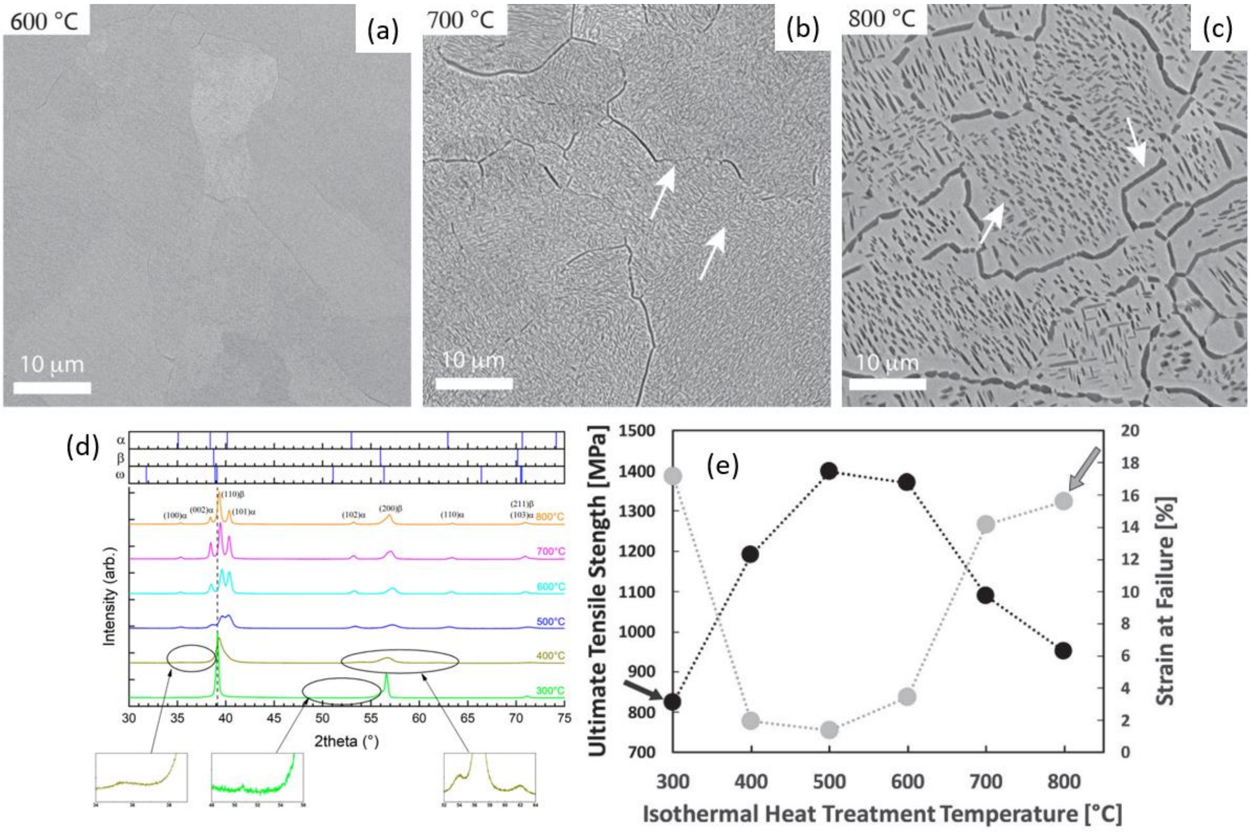

Figure 2-18: Characterization results of LPBF-made and post heat treated Ti-5553 (a-c) SEM images of 600°C, 700°C and 800°C aged microstructures (d) XRD spectrum at 300 - 800°C aging (e) Tensile strength and strain to failure as a function of aging temperature [9]

2.3.4.4 ω phase

ω and β' are the undesired intermediate non-equilibrium phases that may occur as a result of the heat treatment cycles in Ti alloys. In solute-lean β alloys (Mo-E < 10), ω phase is expected to form either during quenching, upon aging, or as a result of deformation [126]. Whereas, in solute rich β alloys (Mo-E > 10), β' is expected. Ti-5553 (Mo-E ≈ 8.2), being a solute lean β alloy, the hard and brittle ω phase exists.

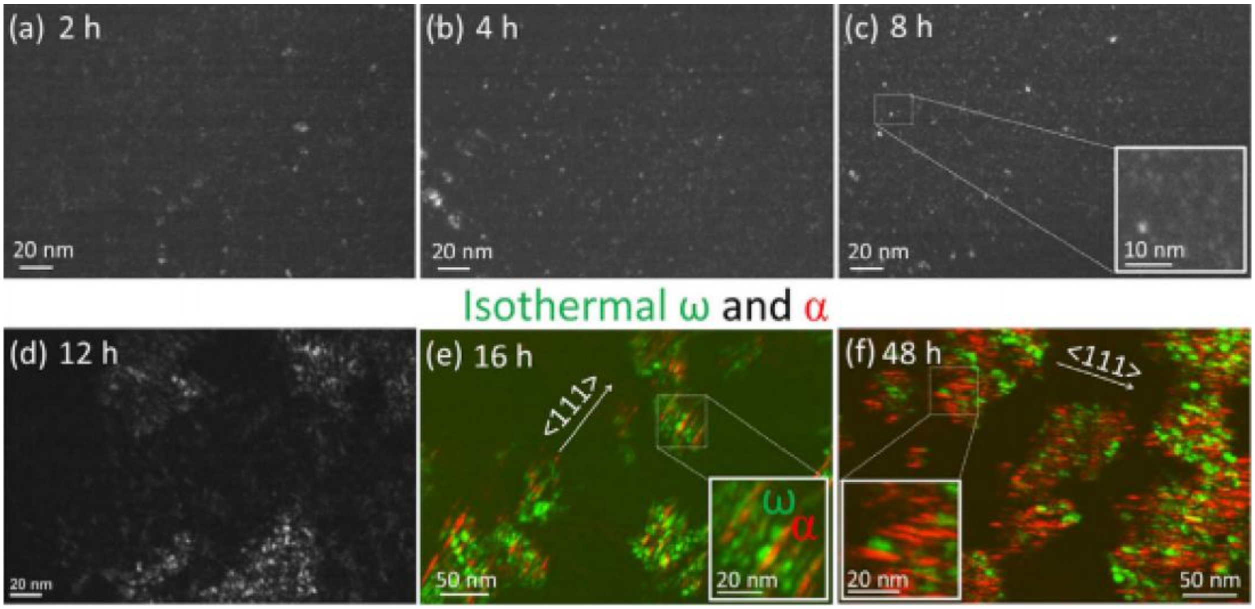

Figure 2-19: Precipitation and gradual growth of ω_{iso} phase at 300°C aging with time (a) 2 hours (b) 4 hours (c) 8 hours (d) 12 hours (e) 16 hours (f) 48 hours [127]

ω phase precipitates can occur in different forms and denoted as ω_{lath}, ω_{iso} or ω_s phases. ω_{lath} is a diffusion-free martensitic transformation formed below 1500°C, ω_{iso} is the precipitation that happens during aging treatment at 150 - 450°C and ω_s is the phase appears due to external strains. The mechanism of β → ω transformation is controlled by the alloying elements. An increased Al content decreases the upper limit of ω_{iso} transformation temperature. Ti alloys with lower Mo-E exhibit a lower ω_{iso} transformation temperature. Even though precipitation of ω_{iso} phase is instantaneous, the growth of the precipitates is time dependent. Grain boundaries are the most preferred locations of ω_{iso} precipitation. The growth of ω_{iso} phase facilitated by long-term aging treatments decrease the ductility of Ti alloys [128]. In another study dealing with low temperature aging at 300-350°C, a simultaneous increase in both the tensile strength and the ductility was reported with aging up to 10 hours and a sudden decrease in ductility afterwards [129].

Mechanical properties of heat treated LPBF-made Ti-5553 in open literature are limited to a few articles. The heat treatment temperature has a significant effect on the mechanical parameters as given in Table 2-5. With an increase in temperature, the YS and UTS increases up to 600°C and then decreases. The initial increase in strength is facilitated by the precipitation and growth of ω particles. Stress relieving at 300°C followed by heat treatment at 400-500°C resulted in severe embrittlement. The presence of α particles and the ω – α transformation is suspected to be the cause but not confirmed [9].

Table 2-5: Mechanical properties of LPBF-made Ti-5553 after isothermal heat treatments [9]

Heat-treatment temperature	**Hardness**	**Young's modulus**	**YS**	**UTS**	**Strain to failure**
(°C)	**(HV)**	**(GPa)**	**(MPa)**	**(MPa)**	**(%)**
300	291±4	48±1	801±14	824±13	17.2±1.5
400	432±26	66±3	1178	1190±80	1.9±0.1
500	475±20	98±4	1397	1397±36	1.4±0.1
600	416±16	97±1	1332±32	1371±21	3.5±0.6
700	362±14	92±1	996±17	1088±11	14.2±4.0
800	340±12	78±4	895±39	951±23	15.6±4.5

In another study, in-situ heat treatment where the powder bed was preheated and maintained at 500°C was evaluated [10]. The preheating is claimed to be an effective alternate to post ageing heat treatment. Compressive stresses were applied on the printed specimens. Microstructural characterization revealed the growth of lamellar α particles. The in-situ heat treated samples failed at a compressive stress of 1500 MPa and 20-25% strain (Figure 2-20), but this result is not comparable with the previously reported tensile stress values of as-printed Ti-5553 samples to justify an improvement. Additionally, the improvement in hardness caused by heat treatment has a negative effect on the subsequent machining process [32].

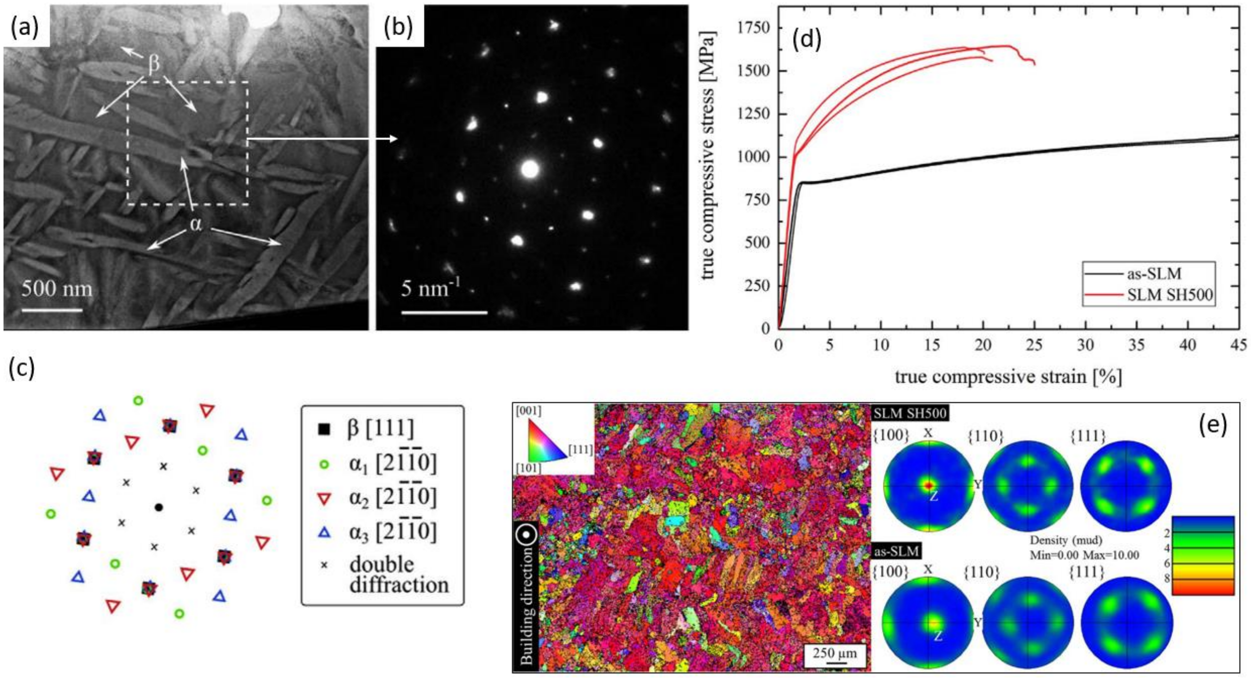

Figure 2-20: In-situ heat treated LPBF-made Ti-5553 (a) Bright field scanning TEM image of Ti-5553 specimen preheated at 500°C (b) SAD pattern of the selected region (c) Corresponding diffraction pattern (e) EBSD map along with pole figures compared to as printed specimens [10]

2.3.4.5 Unfavourable side effects of heat treatment in Ti alloys

When properly engineered, the phase transformations encountered due to heat treatment of Ti alloys can exponentially improve the mechanical properties. However, when necessary precautions were ignored or an optimal set of heat treatment process parameters were unknown, mechanical properties may deteriorate due to a variety of undesired phase transformational effects. The effects include an oxidized outer layer, brittle α case, and grain boundary coarsening.

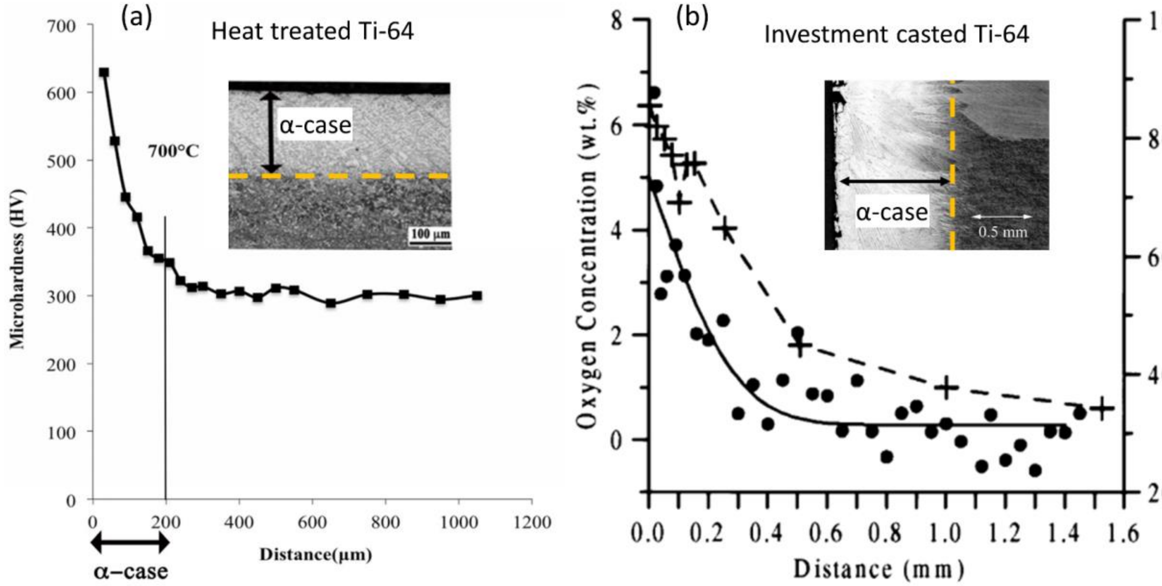

Figure 2-21: α case identified in Ti-64 alloy subjected to high temperature processing (a) α case and its corresponding high hardness after heat treatment [130] (b) α case and the corresponding oxygen diffusion after investment casting [89]

The high affinity of Ti for interstitial elements is well known, which is particularly crucial during the quenching stage of heat treatment from temperatures in the range of 600 to 1000°C, as this enables diffusion of oxygen atoms resulting in an oxygen-enriched surface layer. Oxygen is a strong α stabilizer as discussed in Section 2.2.1, and so the α phase concentration at the surface may be extremely high compared to the rest of the specimen. Thus, a 100 to 300μm thick hard and brittle α rich outer layer can form after heat treatment, which is referred to as α case (Figure 2-21). The presence of an α case affects the structural integrity of titanium alloy and drastically impacts the tensile strength and fatigue properties.

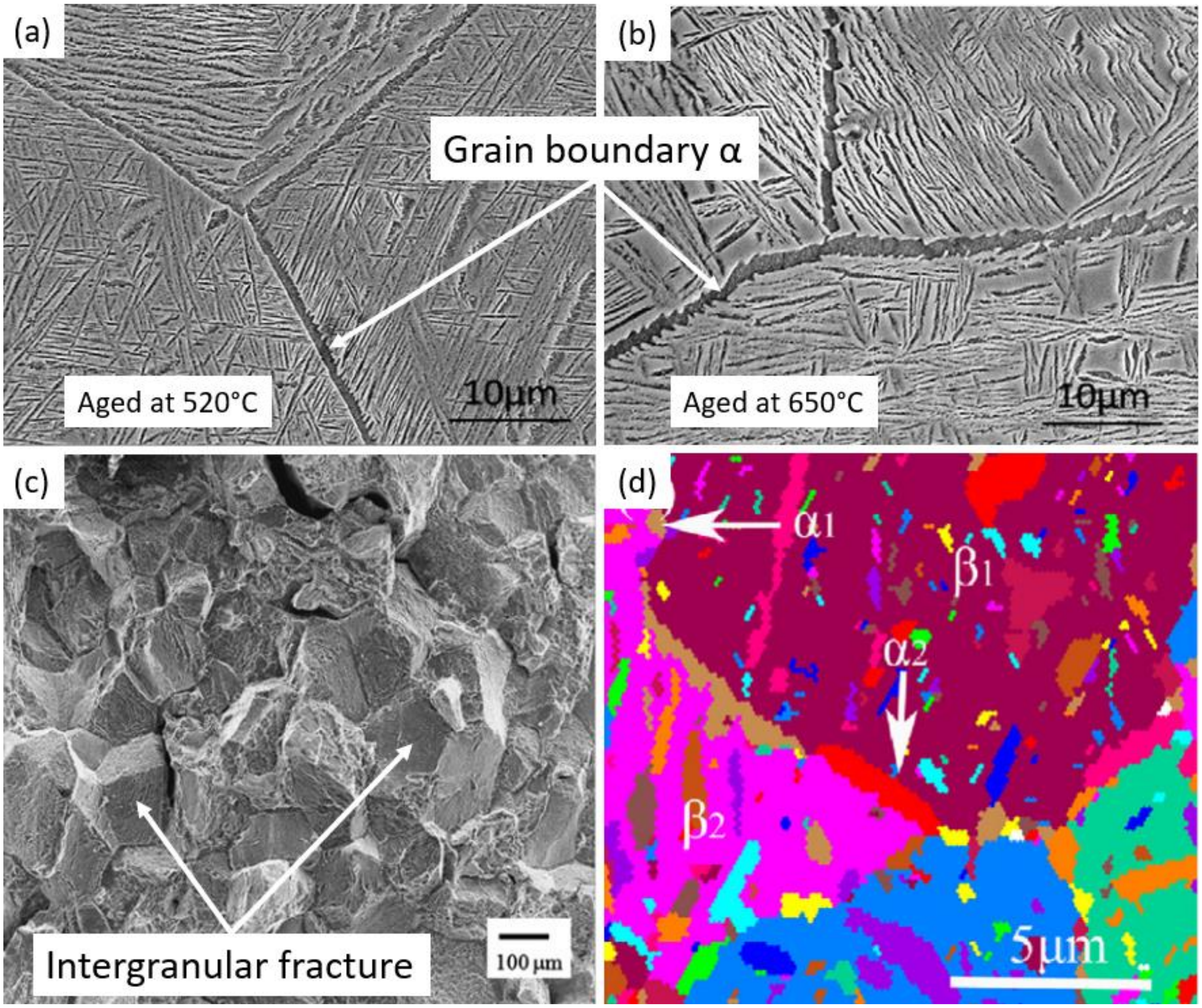

Figure 2-22: Grain boundary coarsening during heat treatment (a & b) coarser grain boundary is observed due to higher temperature aging (c) Intergranular fracture due to coarse and weak grain boundaries (d) EBSD maps depicts different α variants at grain boundaries

Removal of the α case have been reported through chemical, electrochemical, thermal or mechanical methods. Chemical milling involves the usage of hydrofluoric and nitric acid solutions [131]. The electrochemical deoxygenation technique is successful in removing α case from thin metallic strips with high surface area [132]. In some previous work, laser ablation to remove the α-case from Ti-6Al-4V (Ti-64) bulk forgings has been reported [133–135]. Nanosecond pulsed laser ablation can induce crack formation in the α-case layer, and could be used as a rapid detection technique to identify the presence of α-case [136].

Grain boundaries are the prime locations of α precipitation. During prolonged heat treatments, there is a possibility to produce thick grain boundary α layers, which severely deteriorate ductility. Under loading, these grain boundaries act as the favorable path for crack propagation.

2.4 Summary

Titanium alloys exhibiting superior mechanical properties are potential effective material replacements in structural aerospace applications. However, fabricating titanium parts through conventional manufacturing processes involves metallurgical limitations due to its affinity towards interstitial elements and the temperature-based phase transformations. Additive manufacturing technologies, known for printing parts layer-by-layer in a closed environment are promising in overcoming the above-mentioned limitations.

Since the introduction of additive manufacturing techniques to fabricate titanium alloy parts, the application of titanium parts in aircrafts have steadily grown. Ti-5553 is a metastable β-Ti alloy that exhibits improved tensile and fatigue properties compared to the most commonly used Ti-64 alloy. Laser powder bed fusion (LBPF) is an additive manufacturing technique that prints three-dimensional products in a powder bed. To reliably print high relative density products exhibiting satisfactory mechanical properties, it is essential to systematically optimize the LPBF process parameters. Volumetric energy density (VED) based optimization is considered as the most reliable approach especially as the LPBF printing of Ti-5553 is in its formative years.

In addition to the process parameter optimization, it is important to note the metallurgical differences between conventionally manufactured and additively made Ti-5553 microstructures. While a three-dimensional homogenized grain growth is typically seen in conventionally processed Ti-5553, the layer-by-layer printing in LPBF processed Ti-5553 results in directional solidification and hence the grain growth is columnar along the building direction. The as-printed microstructure being unique, the microstructural evolution on heat treatment is distinct.

In order to fine tune the microstructure and thereby achieve the best possible mechanical properties, it is essential to understand the mechanisms involved in the grain growth during printing and heat treatment stages. Thus, an in-depth understanding on the structure-property correlation of LPBF-made Ti-5553 is needed. This thesis is aimed to bridge the above mentioned research gap.

Chapter 3: Methodology

This chapter presents a brief description of the general LPBF printing, heat treatment and the subsequent metallurgical and mechanical characterization methodologies employed throughout the thesis. Wherever relevant, additional specific methodologies are presented in the corresponding chapters.

3.1 Materials and LPBF process

In this work, plasma-atomized Ti-5553 alloy powder was used with particles sized 15 to 45 µm, with the composition listed in Table 3-1. Powder particles were characterized by subjecting them to conventional metallographic preparation practices as described in Section 3.3.

Table 3-1: Chemical composition of Ti-5553 metallic powders used

Element	Al	V	Mo	Cr	Fe	O	Ni	Ti
Wt. %	5.14	4.98	4.97	2.91	0.37	0.09	0.01	Balance

LPBF printing was carried out using an EOS M290 (EOS GmbH, Krailling, Germany) equipped with a single-mode Ytterbium fiber laser (IPG Photonics, Oxford, Massachusetts, USA) operating in continuous mode capable of providing a maximum power of 400W. The laser spot size was 100 µm. The printing chamber, housing a high speed steel (HSS) recoater blade shown in Figure 3-1 was maintained at an argon inert environment to avoid any undesired chemical reactions with atmospheric gases. The cube shaped samples (length = 10 mm) printed for material characterization and the cylindrical dog-bone shaped samples printed for tensile testing are shown in Figure 3-2. Unless specifically mentioned, all the samples were printed vertically on the build plate following a 67 ° rotated stripe scan strategy.

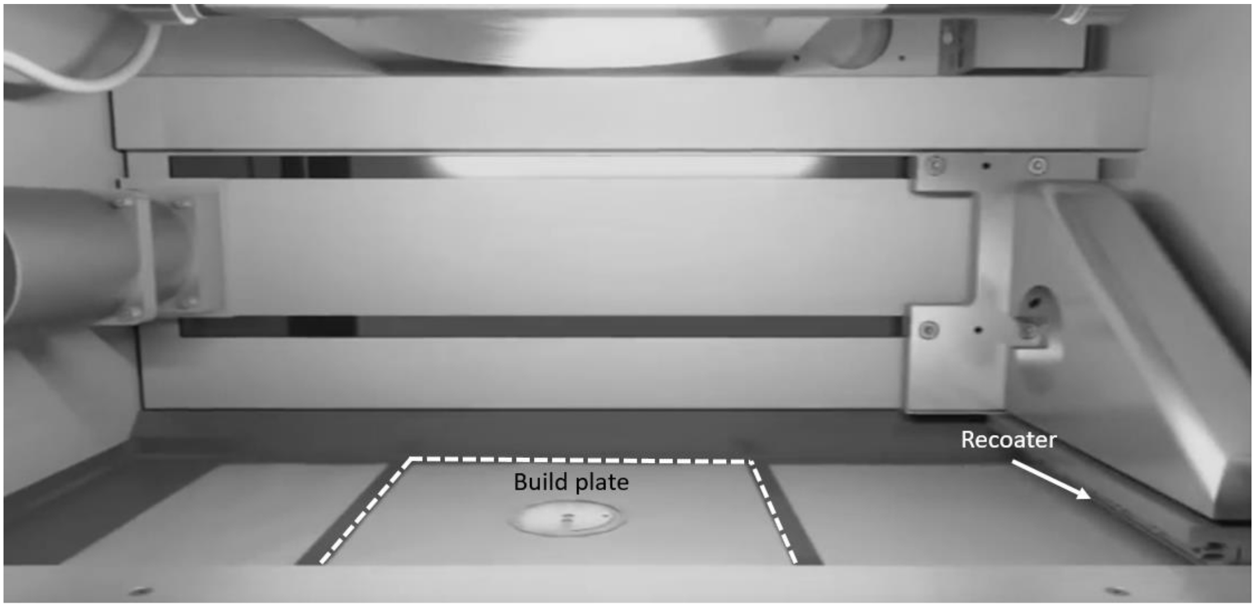

Figure 3-1: Process chamber of EOS M290

3.1.1 Preliminary process parameter screening – an overview

In the preliminary phase of the research, the laser conduction mode (LPBF processing window) was approximately traced based on Archimedes relative density, hardness, and surface roughness measurements which is presented in detail in Chapter 4. On further optimization, by applying Plackett-Burman fractional factorial design with the aid of Minitab statistical software, the continuously fine-tuned process parameter sets tabulated in Chapters 4 to 7 were achieved. A discrete set of process parameters were applied at core and contour regions of the prints. The core corresponds to the bulk of the sample, whereas the contour is the 0.2 to 0.3 mm thick outer ring in the samples. Contour parameters ensure a good surface finish and limit microstructural heterogeneities caused by different thermal gradient existing at the surface of the printed parts [25,137].

Figure 3-2: LPBF printed Ti-5553 samples on SS316 substrate plate

3.2 Heat treatment

The heat treatment experiments were carried out in an electric cold-wall retort furnace (Nabertherm VHT 40/18-KE), capable of sustaining up to 1800°C. The selected, nearly fully dense as-printed samples were subjected to a variety of isothermal heat treatment cycles under ultra-high purity argon atmosphere, as shown in Figure 3-3. Initially, the samples were subjected to solution treatment at temperatures of 700°C (corresponding to the lower α+β region), 800°C (the upper α+β region) and 900°C (which is above T_β temperature), each being held for three hours followed by water quenching (WQ). Following this solutionizing treatment, samples were subjected to aging at 500, 600 and 700°C for 0.5 to 4 hours. All the samples were water quenched both at the end of solution treatment and aging heat treatment cycles. Water quenching is preferred over air cooling, as metastable β-Ti alloys can restrict the formation of hard and brittle, mechanically detrimental α’ and α” non-equilibrium phases even with rapid cooling rates [5]. Finer grains are expected following water quenching compared to air cooling, likely improving tensile performance.

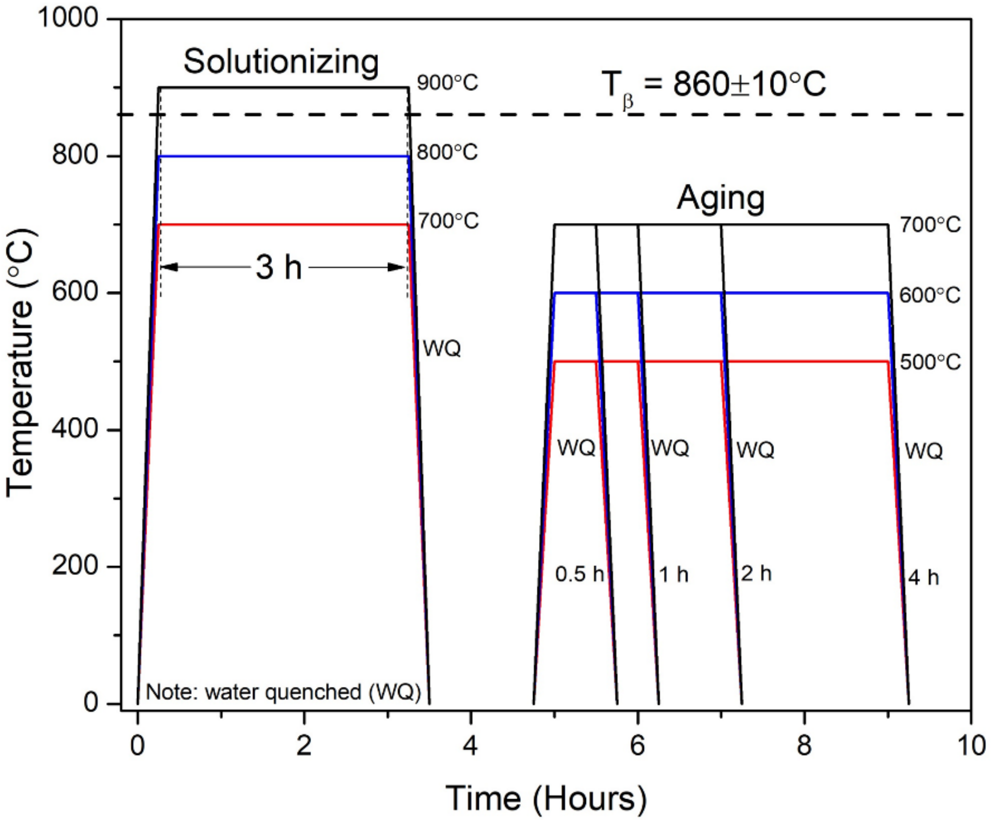

Figure 3-3: Schematic representation of the experimented heat treatment cycles

3.3 Material characterization

3.3.1 Optical microscopy and scanning electron microscopy

Metallography was performed on as-printed, solution-treated, and aged samples to obtain mirror-like surfaces through grinding (up to #4000 SiC paper) and polishing (up to 0.25 um diamond suspension) steps. Keller's reagent (a mixture of 190 mm H_2O + 5 ml HNO_3 + 3 ml HCl + 2 ml HF) was used as a chemical etchant by immersion for 20 - 50 seconds, depending up on the heat treated conditions and the freshness of the etchant. Microstructural investigations were carried out along the building direction using optical microscopes (Keyence VHX 7000 – Digital microscope and Zeiss Axio Vert.A1 MAT microscope) and scanning electron microscope (Tescan VEGA 3). Image J software was used for quantifying the observed microstructural features. Tescan

VEGA 3 scanning electron microscope (SEM) operated at a working voltage of 20 kV was used to examine the fracture surfaces.

3.3.2 Electron backscatter diffraction (EBSD) analysis

Energy Dispersive Spectroscopy (EDS) and Electron backscatter diffraction (EBSD) attachments with the Tescan VEGA 3 were employed to study the elemental composition and changes in grains characteristics (orientation and phase distribution) respectively. EBSD samples were prepared using a vibratory polisher (Buehler Vibromet 2). The accelerating voltage and step size during EBSD by Tescan VEGA 3 were 20 kV and 2.5 µm, respectively. ESpirit 2.2 analysis software was used integrate the EDS and EBSD results with the SEM.

3.3.3 X-ray diffraction (XRD) analysis

Crystal phase analysis was performed using a Bruker D8 advanced X-ray diffractometer with Cu Kα radiation ($\lambda = 0.154$ nm) at 40 kV, a 2θ scanning range of 30 - 80° and 30 mA for phase identification. The relative intensity peaks were used to trace the α particle precipitation in β matrix.

3.3.4 Relative density measurements

Using the Archimedes method and employing a Sartorious density kit YDK03, the density of the printed samples was measured. For each sample, five sets of dry and wet weights were recorded precisely to an order of 10^{-4} g, and the average values were considered for computing the resultant relative densities. To understand the location and distribution of different sized pores better, X-ray Computed Tomography (XCT) tests were carried out on selected samples using a ZEISS Xradia 520 Versa 3D X-ray microscope. The parameters used for the XCT scanning are listed in Table 3-2.

Table 3-2: X-ray Computed Tomography parameters.

Source-to-detector distance (mm)	222.0611
Voxel size (µm)	8.5
Voltage (kV)	140
Current (µA)	72
Source filter	Air
Exposure time (sec)	1
Optical magnification	0.4x
Camera binning	2
Number of projections	1601

3.4 Mechanical property evaluation

3.4.1 Vickers microhardness measurements

A Clemex CMT automated micro-hardness machine was used to conduct the Vickers hardness measurements as per ASTM E384 [138], by applying a load of 200 gf with a dwell time of 10 seconds. A minimum of 30 readings were taken for each of the samples aged under each condition, and the average values were reported.

3.4.2 Uniaxial tensile and Charpy impact tests

Uniaxial tensile tests were carried out as per ASTM E8 [139], using an Instron 8874 servo-hydraulic fatigue testing system equipped with an Instron 2630-120 extensometer with a gauge length of 8 mm, capable of recording up to ±4mm travel. The tensile load was applied in the displacement control mode at a rate of 0.45 mm/min. Charpy impact tests were carried out at 0°C according to ASTM E23-18 with a striker radius of 8 mm. The schematic diagrams of the tensile and impact test specimens with critical dimensions are given in Figure 3-4.

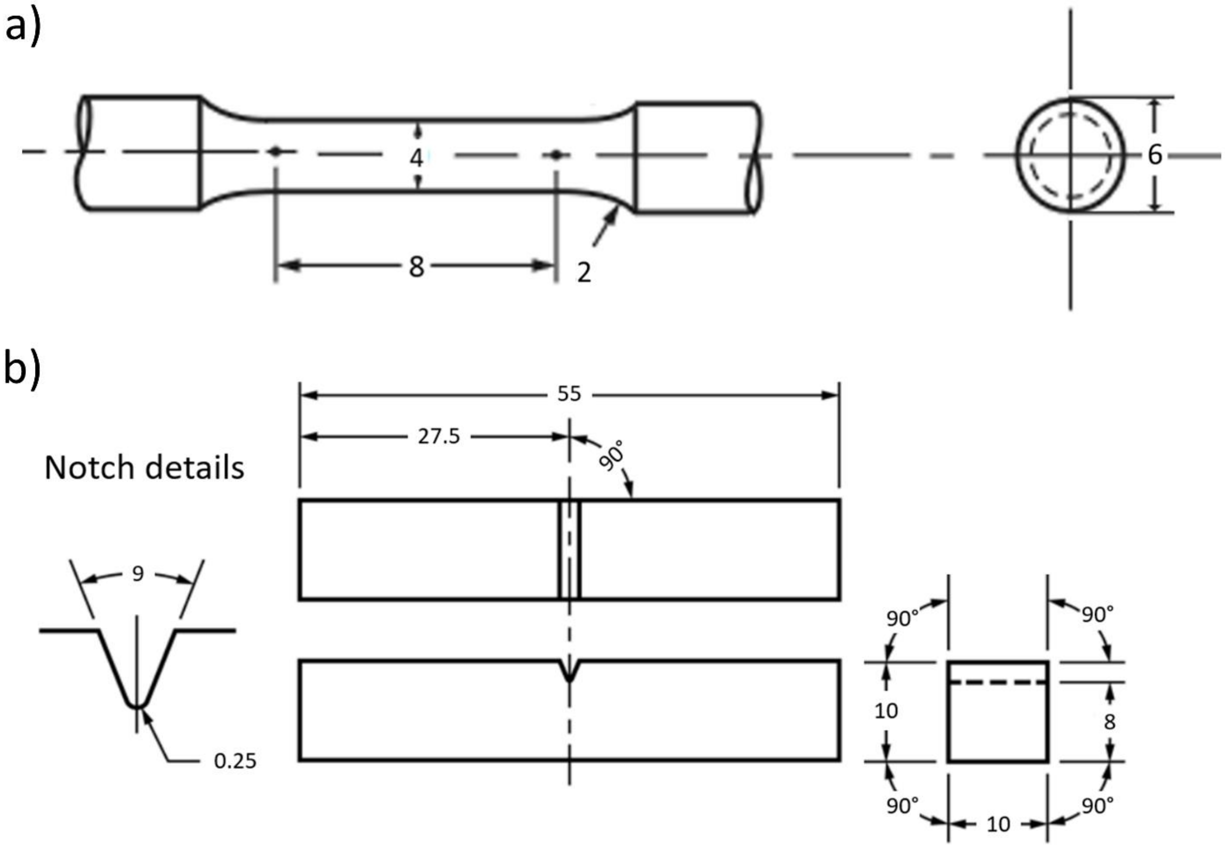

Figure 3-4: Schematic geometry of (a) tensile test samples [139] (b) Charpy impact test samples [140] (Note: all dimensions are in mm)

After the heat treatment, the tensile samples were surface turned to remove the detrimental α case [141]. A minimum of three tensile samples were tested for each condition and the average mechanical properties were reported along with a 95% confidence interval. The fractured surfaces were observed by SEM and analysed as mentioned in Section 3.3.

Chapter 4: Effects of non-lamellar α precipitate morphology on the mechanical properties of LPBF-made Ti5553 parts

This chapter covers the first two objectives by systematically determining the volumetric energy processing window for LPBF fabrication, and presenting the microstructural characterization results to elucidate the corresponding mechanical properties. The bulk of this chapter is based on the published manuscript: '*N. Ramachandiran, H. Asgari, F. Dibia, R. Eybel, A. Gerlich, E. Toyserkani, Effect of non-lamellar α precipitate morphology on the mechanical properties of Ti5553 parts made by laser powder-bed fusion at high laser scan speeds, Mater. Sci. Eng. A. 841 (2022). doi:10.1016/j.msea.2022.143039*'

4.1 Introduction

As mentioned in Section 2.3.3.3, information on the LPBF processing window for printing Ti-5553 parts is limited. Schwab *et al.* showed that the LPBF printability of Ti-5553 at low VED values was possible, but the printed parts were inferior in tensile strength compared to conventionally manufactured counterparts [29]. The slow scan speed employed (100 to 180 mm/s) was also a limitation when the printing is expected to be commercialized. Bakhshivash *et al.* identified the process window at high VED using a pulsed laser heat source [27]. Even though high relative density prints were achieved, a homogeneous microstructure was not possible and the effect of this was reflected in the subsequent microhardness measurements.

To date, a comprehensive structure-property correlation study to explain the significance of microstructural features in altering the mechanical properties of LPBF fabricated Ti-5553 alloy is needed. Consequently, in the first part of this chapter, two sets of LPBF process parameters that would closely represent the lowest and highest possible VEDs at high scanning speeds (>750 mm/s) within the processing window were identified. In the second part, a systematic and in-depth characterization of the two samples selected from the previous part revealed the presence of non-lamellar α precipitates. The corresponding mechanical properties were correlated with the microstructural features characterized using scanning electron microscopy (SEM), X-ray diffraction (XRD) and electron backscatter diffraction (EBSD) in detail. In the final part, differences in grain size between the core and contour of the printed samples are discussed and associated with the bi-modal fracture mode observed on the fractured surfaces of mechanically tested samples.

4.2 Experimental procedure

In addition to the methodologies elaborated in Chapter 3, a VED-based process optimization procedure followed during the initial pre-screening phase of this research is described here. A batch of 54 cylindrical specimens (sized 10 mm in diameter and 10 mm in height) covering 27 different process parameter (two samples for each process parameter set) sets were printed following a stripe scan strategy. The wide spectrum of chosen process parameter sets included different combinations of laser powers (100 to 275W) and scanning velocities (350 to 1520 mm/s) as listed in Table 4-1. The hatch distance and the layer thickness were maintained at 95 µm and 45 µm, respectively, to limit the process parameter set combinations. The calculated VED ranged from 15.4 to 184.3 J/mm^3.

Table 4-1: LPBF process parameters used for printing the pre-screening phase samples.

Sample No.	Laser Power (P)	Scan speed (v)	VED $= \frac{P}{vld}$ [27]
	(W)	(mm/s)	(J/mm^3)
1	100.0	1520	15.4
2	100.0	1090	21.5
3	100.0	1060	22.1
4	100.0	814	28.7
5	187.5	1520	28.9
6	100.0	758	30.9
7	100.0	652	35.9
8	100.0	610	38.3
9	187.5	1120	39.1
10	187.5	1060	41.4
11	275.0	1520	42.3
12	275.0	1357	47.4
13	100.0	455	51.4
14	187.5	814	53.9
15	187.5	781	56.1
16	275.0	1090	59.0
17	275.0	1060	60.7
18	100.0	349	67.0
19	187.5	652	67.3
20	187.5	581	75.5
21	275.0	814	79.0
22	275.0	758	84.9
23	187.5	455	96.4
24	275.0	652	98.7
25	275.0	581	110.7
26	187.5	349	125.7
27	275.0	349	184.3

Process parameter sets within the outlined processing window within the laser conduction mode are shown in Figure 4-3(a), and these resulted in the best densities are given in Table 4-2. Uniaxial tensile test and Charpy impact test samples examined in this research work were printed at these selected process parameter sets, and were labelled as ‘E-High’ and ‘E-Low’ based on their corresponding VED values. Contour, which is the outer ring segment of the sample, was printed at a lower VED (Table 4-2). This arrangement typically minimizes the microstructural differences caused by the variation in thermal dissipation across the cross-section after laser exposure. Three samples were printed for each of the selected parameter sets.

Table 4-2: Extreme process parameter sets identified from the conduction mode to print the mechanical test samples.

Sample ID		**Laser Power (P)**	**Scan speed (v)**	**Layer thickness (l)**	**Hatch Distance (d)**	$\mathbf{VED = \frac{P}{vld}}$
		(W)	**(mm/s)**	**(μm)**	**(μm)**	**(J/mm^3)**
Core	**E- High**	187.5	781	45	100	56.1
	E- Low	187.5	1120	45	100	39.1
Contour		163.7	900	45	110	36.7

The Z samples, printed vertically at a 0° orientation following a stripe scan strategy, are shown in Figure 4-1. To account for the possible metallurgical heterogeneity caused by repeated thermal cycles, samples for metallographic studies were taken along the transverse direction from the marked grip section after the tensile tests.

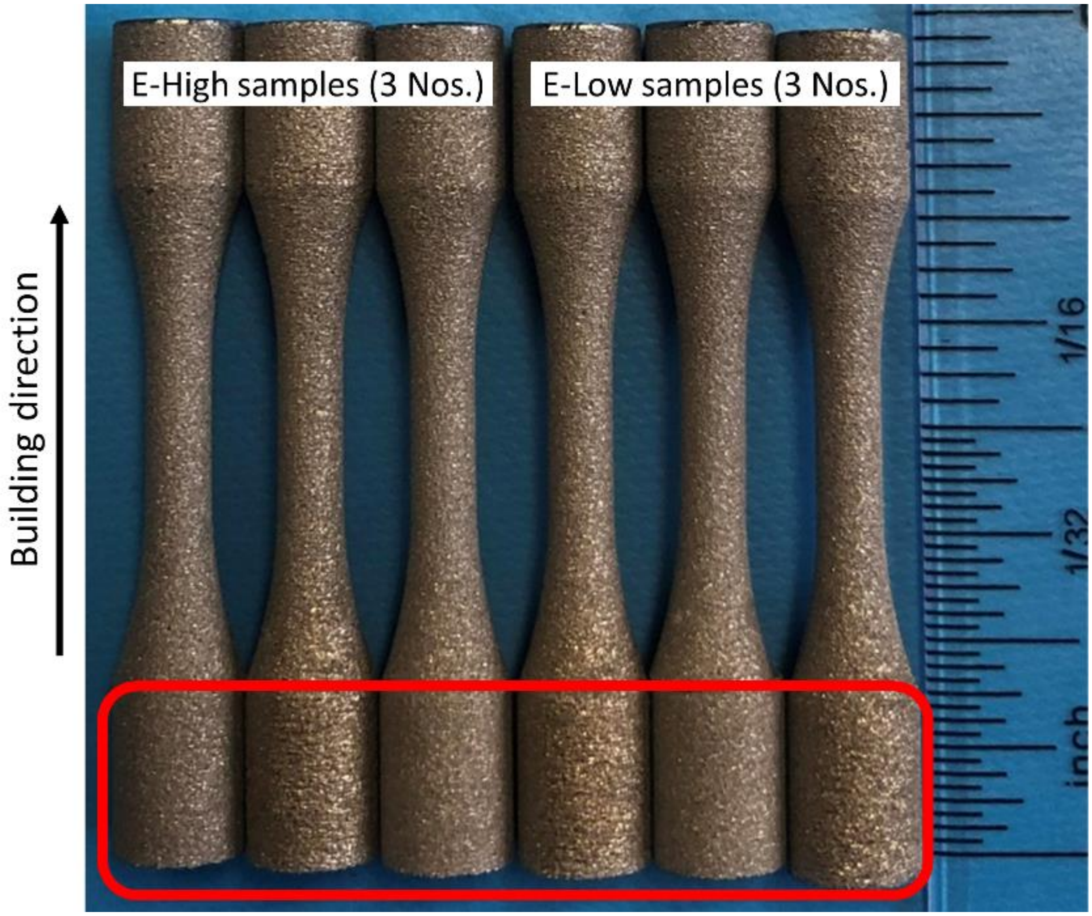

Figure 4-1: Vertically printed tensile samples with marked grip section showing the location from where samples used for characterization.

4.3 Results

4.3.1 Powder characterization

As seen in Figure 4-2(a), the powder particles exhibited a smooth surface with a mean sphericity factor of 0.95. The microstructure of the powder particles presented in Figure 4-2(b), reveals a dendritic structure owing to the high cooling rate encountered in the plasma atomization stage. A detailed characterization of the powder particles used in this research work is already discussed elsewhere [27].

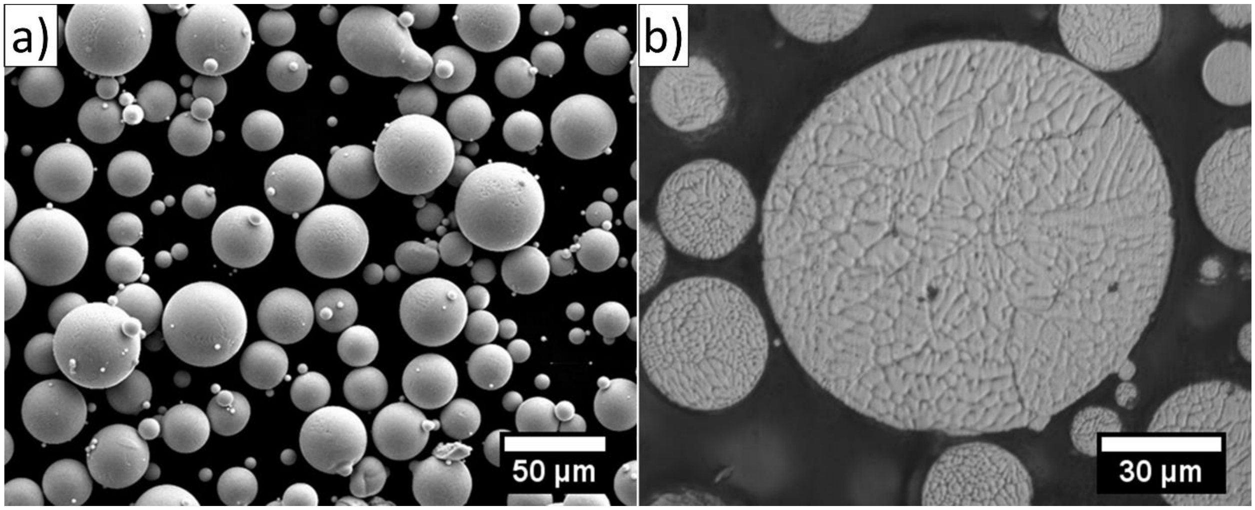

Figure 4-2: (a) SEM image of plasma atomized Ti-5553 virgin feedstock powder, and (b) OM image showing the dendritic microstructure of the Ti-5553 powder particles used in the present research.

4.3.2 Approximate identification of the laser conduction mode

The Archimedes density measurements are plotted as a function of VED in Figure 4-3(a). Based on the relative densities, lack of fusion (LOF), conduction and keyhole mode laser settings were identified. In Figure 4-3(b), the optical microscopy images of the samples from each of the identified bands are compared. Irregularly shaped discontinuities are present in the LOF sample and large spherical/near-spherical porosities are present in the keyhole mode sample. However, in the conduction mode sample, defects are rarely found, in addition to near-perfect semi-circle shaped melt pool boundaries, suggesting consistent fusion between the successive layers.

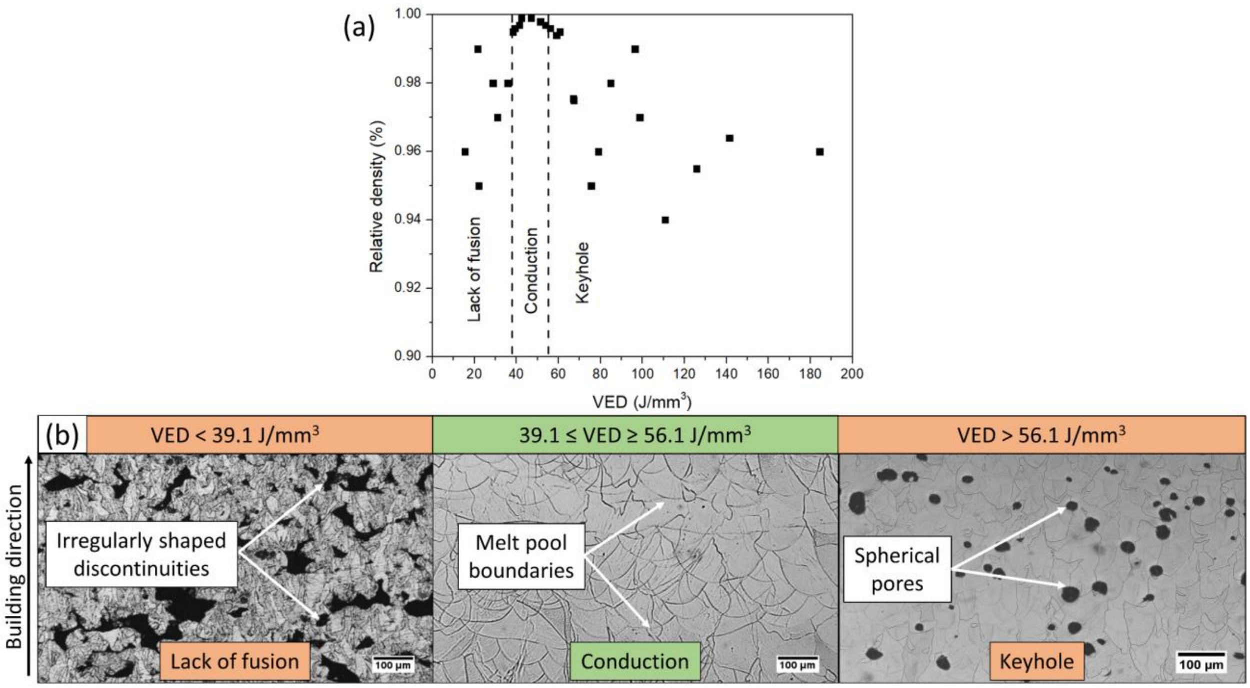

Figure 4-3: (a) Melting mode regions based on Archimedes relative density across the VEDs considered (b) OM images of samples printed in different VED ranges (Note: The depicted melting mode region boundaries are only approximate).

The XCT scan results of the two selected samples are presented in Figure 4-4. Both the samples exhibit relative densities greater than 99.98%, which is in accordance with the Archimedes relative density measurements seen in Figure 4-3(a). The pores, identified by different colors categorized based on their size, are represented by their respective scale below. The observed pores are randomly distributed across the volume, and do not follow any particular trend with process parameters. In comparison, more pores are observed in E-High samples and are larger in size. This observation matches with the expected keyhole-like pores expected in E-High sample. Similar large-sized pores were reported earlier for the LPBF printed Ti-5553 samples in VEDs in the keyhole mode [27,29].

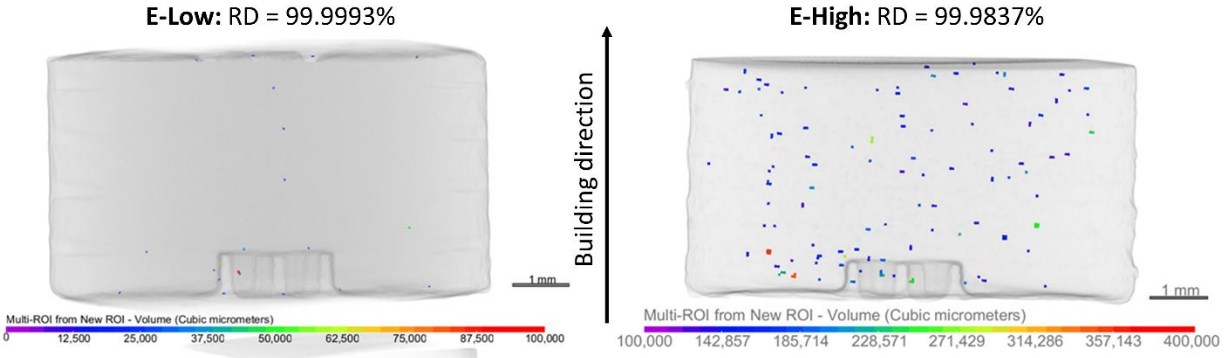

Figure 4-4: 3D visualization of porosities distributed throughout the volume of selected samples.

4.3.3 Microstructure of printed parts

The cross-sectioned surfaces along the transverse direction of printed tensile samples are shown in Figure 4-5(a). As noted in Figure 4-5(a), the surface is divided into core and outer contour surface. The contour region corresponds to the outer (0.2 to 0.8 mm) layer printed using process parameters given in Table 4-2. Figure 4-5(b & c) show the magnified images of selected regions from E-Low and E-High samples respectively. In Figure 4-5(b), lack of fusion defects such as irregularly shaped discontinuities are occasionally seen. In Figure 4-5(c), near-spherical discontinuities become apparent, which are usually observed in the keyhole processing condition.

The OM images indicate the microstructural difference between the outer and inner contour passes as shown in Figure 4-5(d). The outer sub-section contains a 0.1 to 0.2 mm thick layer of fine grains. The inner sub-section exhibited inward growing curved columnar lath grains as reported earlier [25]. The depth of the columnar lath grains varied from 0.5 to 0.8 mm. The measured contour layer depths are comparable to previously reported values for LPBF fabricated titanium alloys printed with optimized contour process parameters [25]. Figure 4-5(e) highlights the refined grains in the contour region as a consequence of using the contour printing parameters.

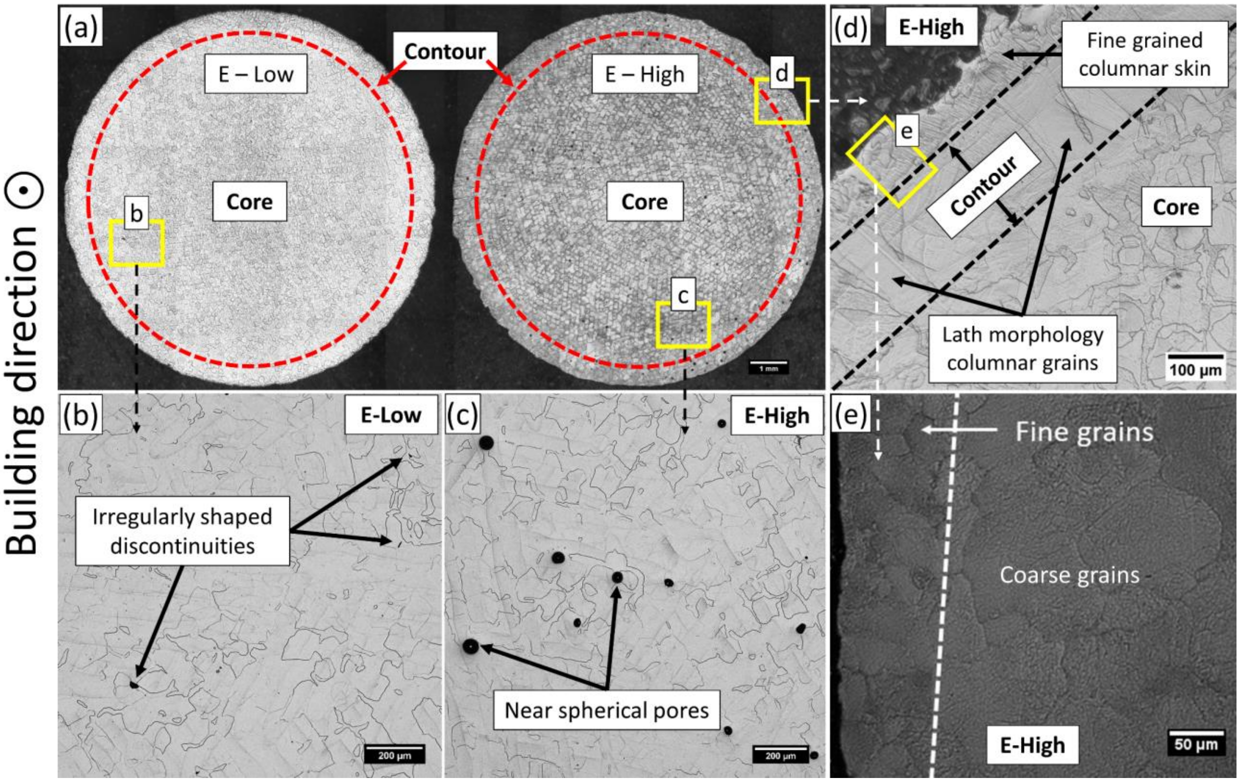

Figure 4-5: OM images of: (a) Transverse microstructural view of the printed samples (b) irregularly shaped discontinuities observed in E-Low (c) near spherical pores observed in E-High (d) core-contour interface exhibiting different microstructural features (e) Finer grains observed at the contour region in comparison with the core.

The core region of both the samples observed along the scanning direction is shown in Figure 4-6. They exhibit a near cubical/pentagon-shaped prior β grains (PBG), which are consistent and comparable for both VEDs considered. The size of the PBG ranged from 67 to 94 µm at the core, which is comparable to previously reported values [46,48,60,142].

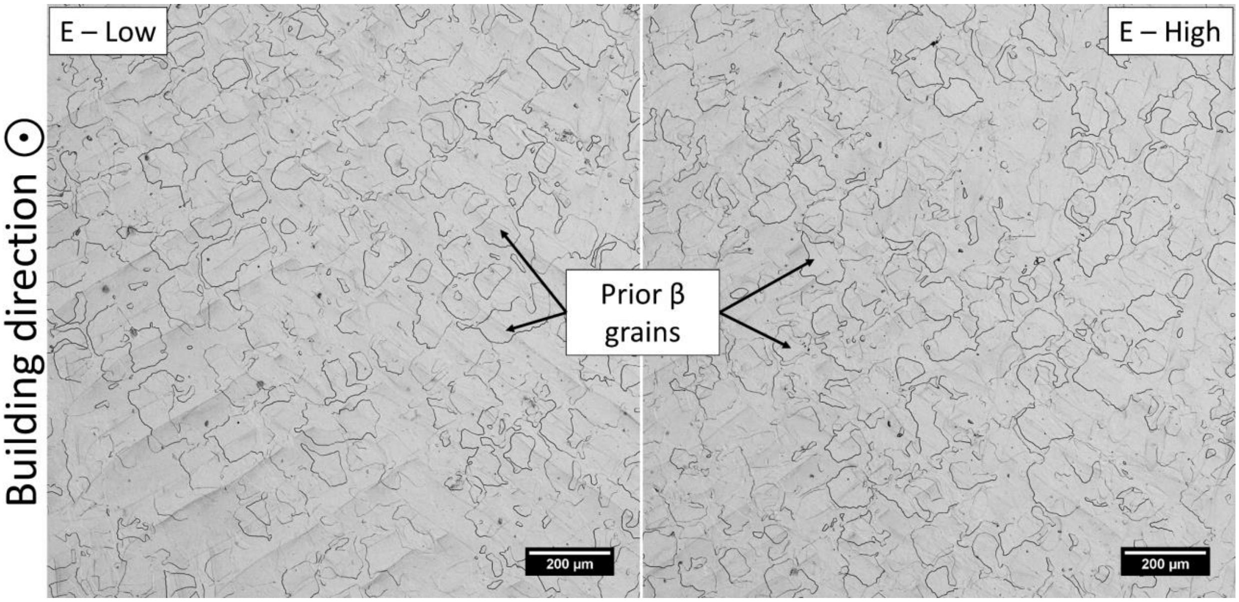

Figure 4-6: OM images showing the prior β grains along the transverse sectioned plane of E-Low and E-High samples.

The vertically aligned columnar grains found along the building direction are presented in Figure 4-7. The observed grains sized in the order of hundreds of microns, which is similar to previous reports [27,29]. On further comparison between the images in Figure 4-7, a number of sub-micron sized features, which are suspected to be α particles, are observed more vividly in the E-high sample.

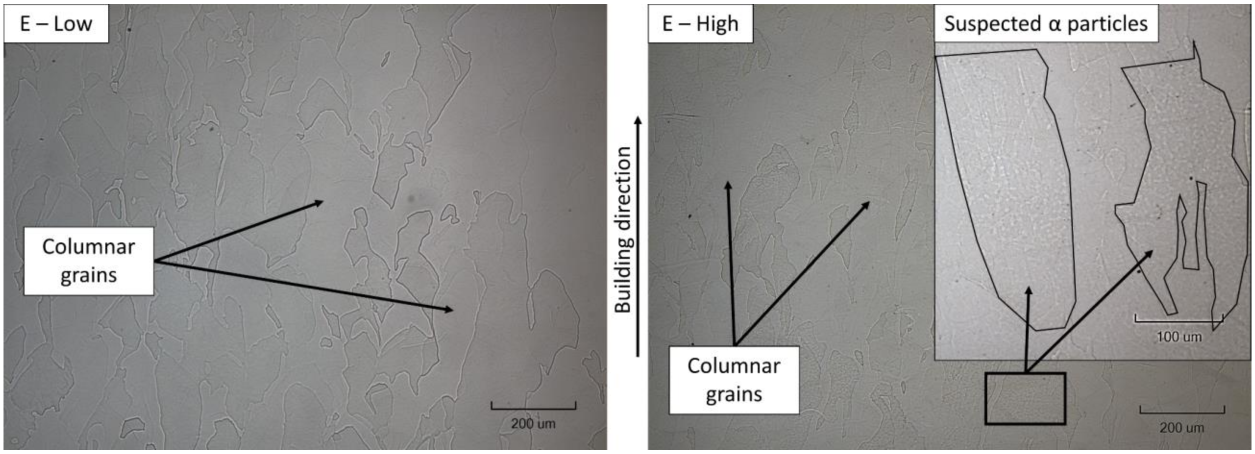

Figure 4-7: OM images of columnar grain growth along the building direction of E-Low and E-High samples (longitudinally sectioned).

4.3.4 Phase identification

Features observed within the columnar grains that were suspected as α precipitates in Figure 4-7(b) are captured at higher magnification and presented in Figure 4-8(a). The white dashed lines indicate columnar β grain boundaries and the presence of randomly shaped second phase particles are clearly visible within them. The XRD pattern of the as-printed E-high and E-Low samples are shown in Figure 4-8(b), which confirms the presence of α and β phases.

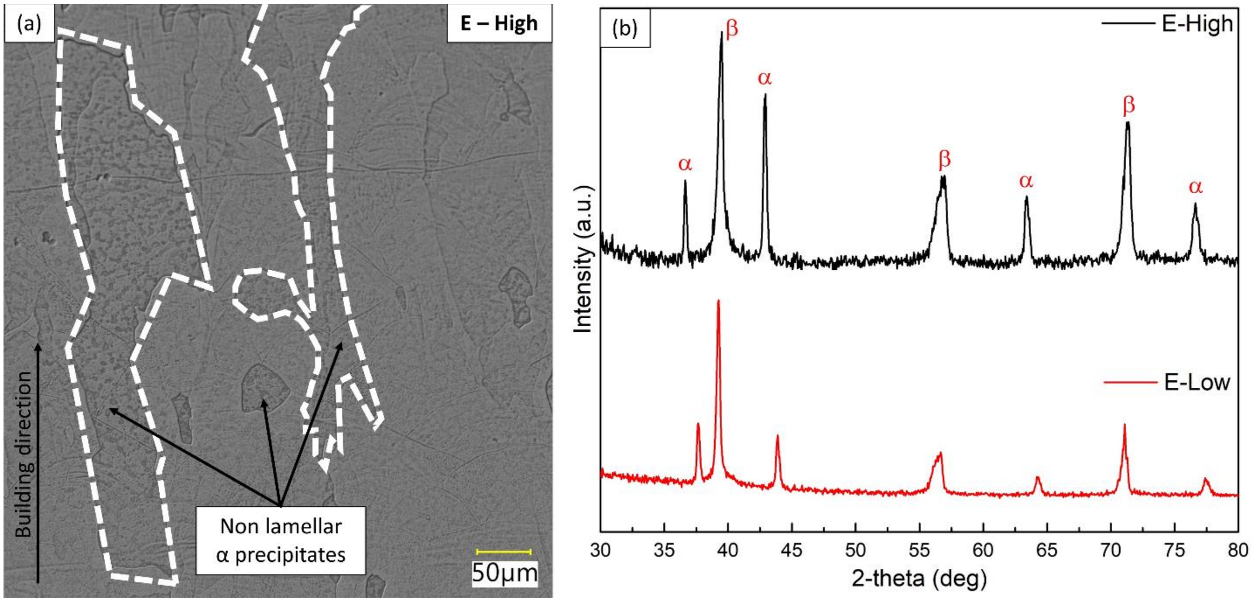

Figure 4-8: (a) Non lamellar α-like features observed predominantly within β-grain boundaries (b) XRD patterns of E-Low and E-High samples confirming the presence of α and β phases.

To understand the microstructural development during LPBF of Ti-5553 in detail, electron backscatter diffraction (EBSD) analysis was carried out. Figure 4-9 shows the crystallographic orientation analysis of E-Low and E-High samples in the scanning and building directions. Additionally, the phase distribution maps and pole figures along the building direction are also shown in Figure 4-9. On comparing the orientation maps along the scanning direction, a clear difference in the preferred grain growth direction is observed. The E-Low sample exhibits a <111> preferred growth direction and E-High shows <001> preference as indicated in Figure 4-9 (d, h), although these textures are relatively weak based on the peak intensities being up to 4.08. Secondly, in Figure 4-9 (b, f) along the building direction, there is little indication of a preferred direction for grain growth. Even though the grains are elongated along the building direction in both the cases, they are wider in the E-High sample, indicating this is promoted by the higher VED.

The green colored region in the phase distribution maps seen in Figure 4-9 (c, g) represent β phase and the red colored dots represent α precipitates grown in them. A significant area (2 × 2 mm) is covered to obtain a more confident approximation of the overall distribution of α grains, and it could be observed that the α particles are homogeneously distributed throughout the microstructure in both the cases. The arrow marks in the phase maps point out to those α particles which are aligned along the columnar β grains confirming that the features observed in Figure 4-8(a) are α precipitates.

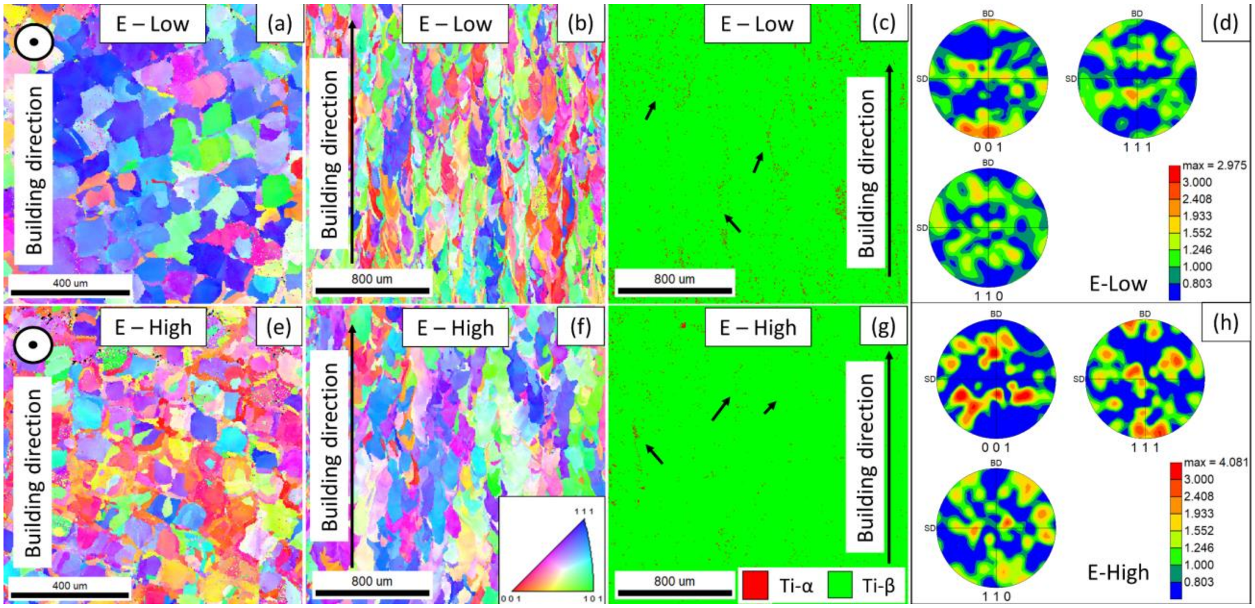

Figure 4-9: Crystallographic orientation maps (a & e) in scanning direction for E-Low and E-High samples respectively (b & f) in building direction for E-Low and E-High samples respectively (c & g) Phase distribution maps and (d & h) Pole figures of E-Low and E-High samples respectively.

4.3.5 Mechanical properties

4.3.5.1 Vickers microhardness measurements

Microhardness measurements across the cross section along the scanning direction are presented in Figure 4-10(a). The vertical dashed lines approximately segregate the core from their corresponding contour. The near ‘U’ shaped profile is roughly symmetrical along the vertical axis for both the samples. In the contour region at the sub-surface, a peak hardness of 315 to 340 VHN is observed, and a drastic decrease immediately adjacent to the peak hardness location is seen in both the samples. Deeper into the core, the hardness measurements taken at a regular interval of 200µm are more stable, varying within a narrow range of 260 to 300 VHN.

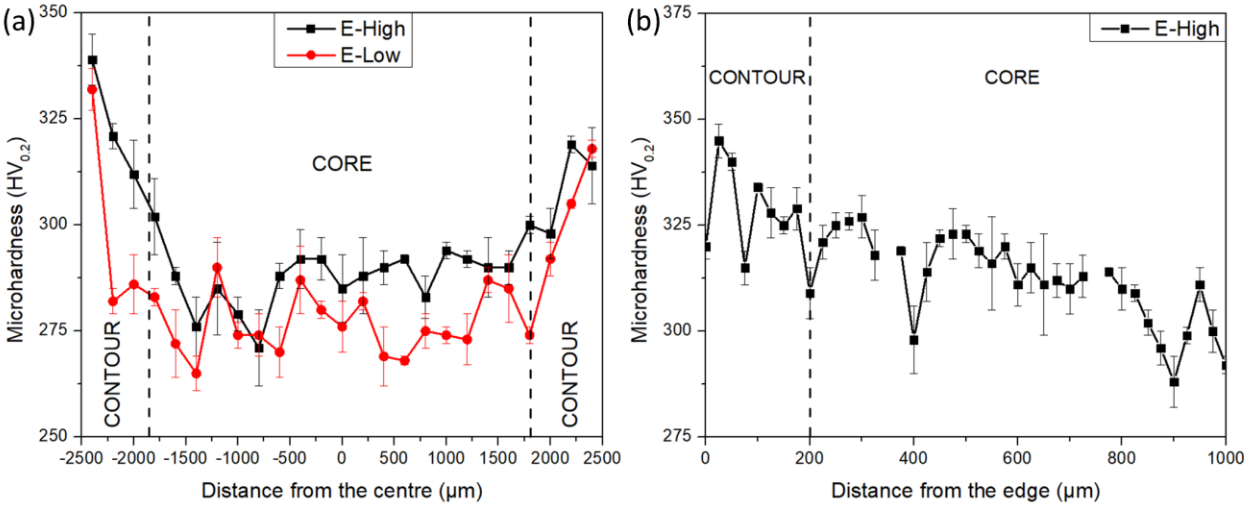

Figure 4-10: (a) Microhardness profile across the cross section along the scanning direction of E-Low and E-High samples respectively (b) Gradually decreasing microhardness trend from contour to core of E-High sample.

To better understand the contour-core microhardness hardness profile, another set of measurements, recorded at a periodic interval of 25µm more focussed at the interface was carried out, and the corresponding results are shown in Figure 4-10(b). A steady decrease in the microhardness values from the outer edge towards the core of the sample can be detected. This suggests that the microstructural differences observed in the core-contour interface could have a significant effect on the mechanical properties.

4.3.5.2 Tensile and impact tests

Uniaxial tensile test results of the samples shown in Figure 4-1, are presented in Figure 4-11 along with their corresponding impact toughness results. The engineering stress – strain curve in both the cases were comparable to the previously reported ones for Ti-5553, where the yield strength (YS) reached within 2% of the total strain with a similar slope and negligible work hardening [29,123], and hence an ultimate tensile strength (UTS) is not distinctly reported here.

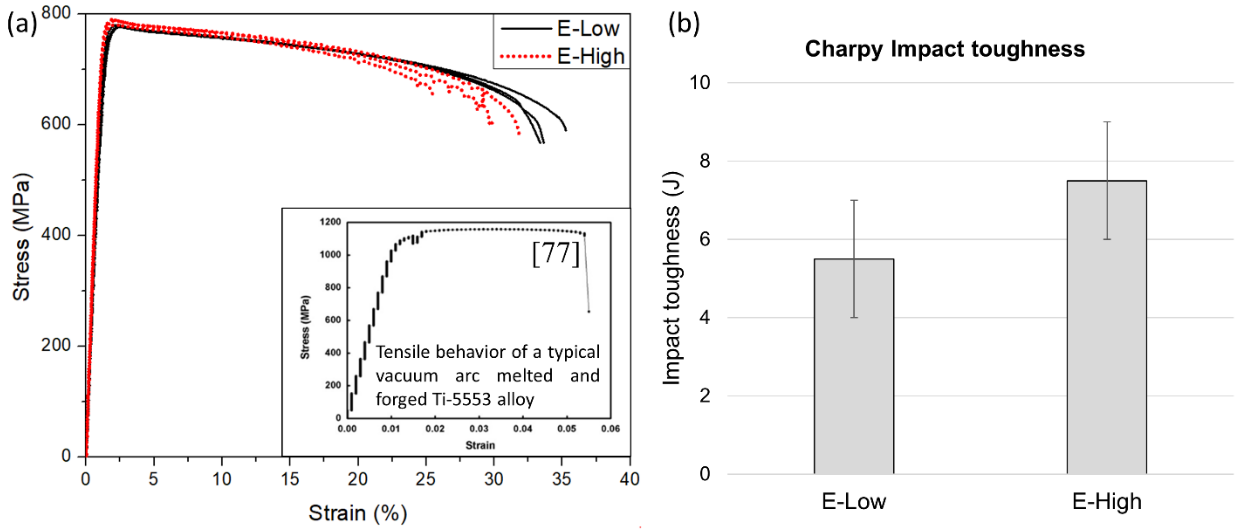

Figure 4-11: (a) Engineering stress-strain curves of LPBF printed E-Low and E-High samples, compared with VAM and forged Ti-5553 from literature(b) Charpy impact test results on printed samples tested at 0°C.

For comparison, the tensile behavior of a vacuum arc melted (VAM) and forged Ti-5553 alloy [77] exhibiting a UTS of 1160 MPa and an elongation of 5.5% is also shown in Figure 4-11(a). Even though the traditional elongation reported here in the example is just above 5%, there are certain cases where elongation values ranging 10 to 15 % are claimed [143].

The tensile tested samples exhibited a strength of 780±10 MPa, which is equivalent to the best reported tensile strengths for LPBF processed as-printed Ti-5553 [29,100], but with more than twice the traditionally reported elongation, reaching 30 ± 5%. On the contrary, the Charpy impact tested samples fractured by absorbing a trivial 4-9 Joules of energy, suggesting mainly brittle fracture occurred on impact.

4.3.6 Fractography

Fracture surfaces of tensile and impact tested samples are given in Figure 4-12 and Figure 4-13, respectively. In Figure 4-12 (a – c) correspond to E-Low and (d – f) represent E-High samples.

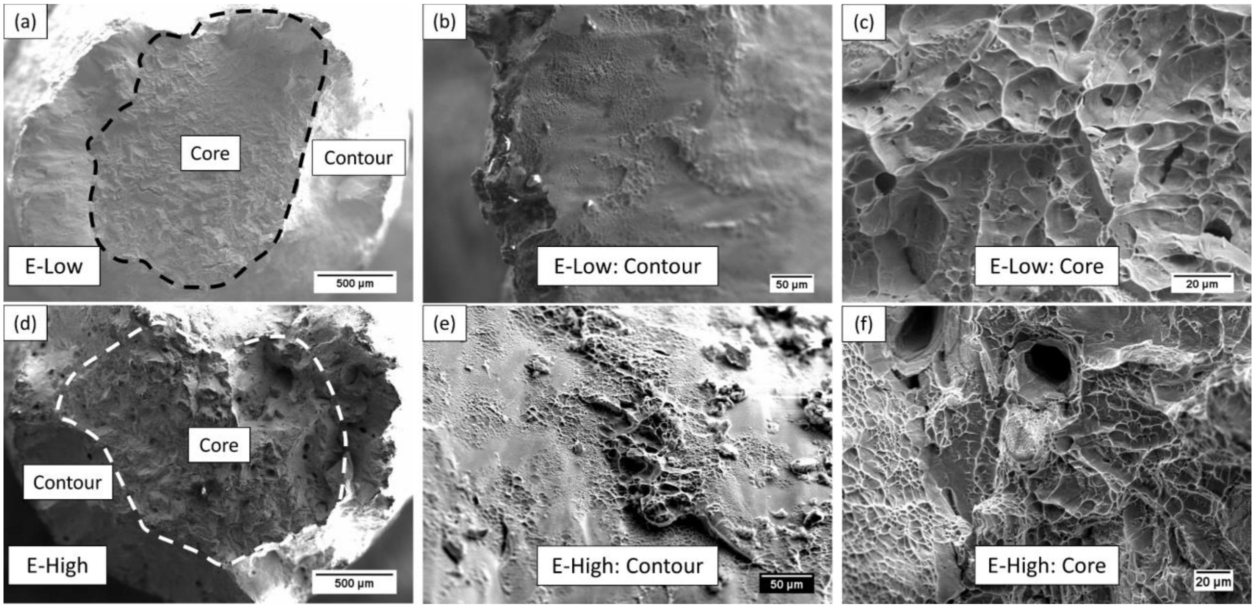

Figure 4-12: SEM images of (a - c) Tensile tested fracture surfaces of E-Low sample at core and contour sections (d – f) Tensile tested fracture surfaces of E-High sample at core and contour sections.

Two different fracture modes were identified on both the fracture surfaces. Figures labelled A1 and B1 represent the inner ductile fracture regions whereas (b) and (e) represent the outer predominantly brittle fracture regions. Such a bi-modal fracture surface was reported previously on forged and heat treated Ti-5553 samples exhibiting 1200 to 1300 MPa tensile strength and 7-13% total strain [57].The outer brittle region approximately overlaps with the contour section detailed in Figure 4-5 and Figure 4-11. The contour surfaces, as observed in Figure 4-12 (b and e), are flat with a sporadic honeycomb-like feature, suggesting a defect-free homogeneous fracture path with respect to the core.

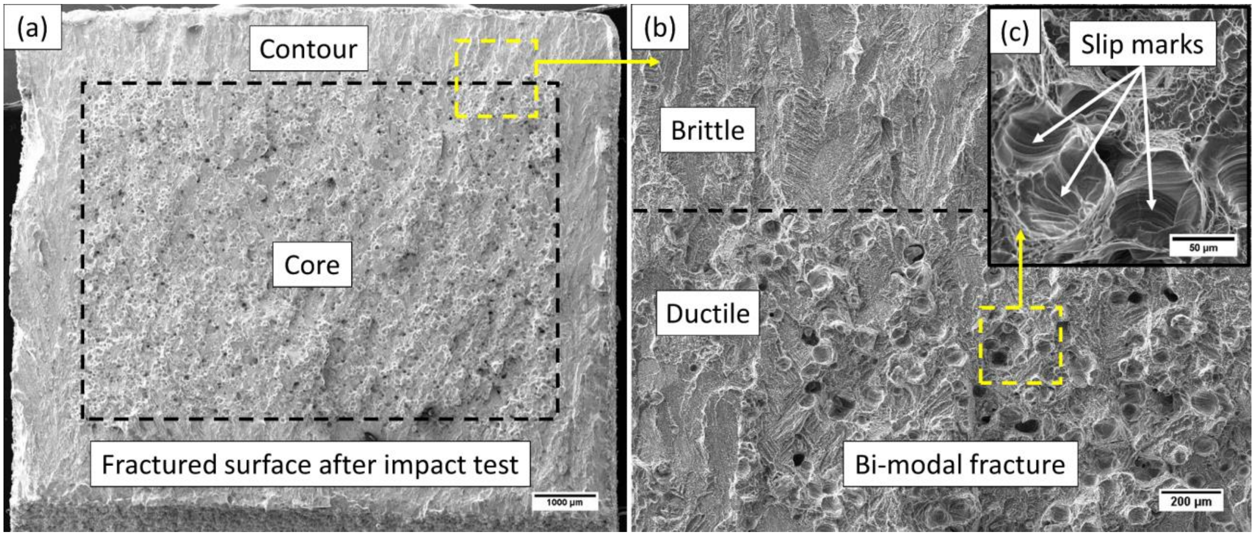

Figure 4-13: (a) Overall impact tested fracture surfaces (b) Fracture surface at contour-core interface exhibiting transgranular cleavage fracture at contour and (c) Higher magnification image from the core section displaying microvoid coalescence.

The transition from brittle to ductile fracture is more predominantly observed on the impact tested fracture surfaces as seen in Figure 4-13(a). In Figure 4-13(b), the transition from brittle to ductile dominant fracture is detailed at higher magnification. As seen, the fractured surface is brittle along the outer ring replicating the surfaces seen on tensile tested contour region. At the core of the impact tested sample surface, a large number of deep trenches with slip marks were observed as in Figure 4-13(c). Similar transition from transgranular cleavage at the contour to microvoid coalescence is already reported for electron beam welded Ti-5553 where the heat dissipation rates are comparable to that of LPBF process [48].

4.4 Discussion

The volumetric energy density (VED) range corresponding to the laser conduction mode is associated with specimens that achieve the highest relative densities. Boundaries of the traced bands are only approximate as they are limited by the number of samples tested. Additionally, considering the scope of this study, the transition zones that may exist at lack of fusion-conduction boundary and conduction-keyhole boundary are neglected. Within the identified laser conduction mode range, the lowest and the highest VEDs were chosen to print the tensile and impact test samples, as their consistency in mechanical properties was expected to represent the overall behaviour of all the process parameter sets within the conduction region.

XCT scans in Figure 4-4 quantified the size of internal defects in both the selected VED samples. Large defects in the E-High sample appear to be spherical porosities. The microstructures presented in Figure 4-5 (b, c) further confirm it as irregular discontinuities are identified in E-Low and spherical porosities in E-High. This behavior is consistent with the strong role of the process parameters on the relative density as estimated based on Figure 4-3 and Figure 4-4. The varying magnitude in the volume of the defects identified between the samples could be a result of their size and the neglected transition zones at the boundaries.

As detailed in Figure 4-5(a), the contour region is the outer layer printed with a different set of process parameters given in Table 4-2. Since the rate of heat dissipation is faster at boundaries compared to the centre of any printed geometry, such an arrangement to print the sample periphery with fine-tuned contour process parameters is necessary [24,144,145]. During cooling and solidification of the melted powder particles at the contour region, nucleation is initiated as heat is dissipated to the surrounding powder particles which were maintained at room temperature. The subsequent grain growth, which is nearly perpendicular to the building direction, will induce microstructural dissimilarities across the cross-section [25]. Additionally, optimized contour printing parameters set limits on the possibility of grain boundaries being rich in α phase and having an adverse effect on the resulting mechanical properties [146,147].

Typically, PBG influence the mechanical properties and are significantly affected by the thermal history experienced during the manufacturing process. Severe strain incompatibility among PBG on cooling below β transus temperature results in strong constraints to dislocation motion. With increasing PBG size, greater constrains exist and hence higher applied stress is needed to cause deformation [148]. Therefore, PBG strongly impacts the tensile strength and ductility in titanium alloys [141,149]. The implications of the LPBF process parameters on PBG growth in titanium alloys is rarely discussed in the open literature. In forged titanium alloys, during heat treatment cycles, PBG exponentially grows in size when heated above the β transus temperature for a considerable time period (> 30 minutes), and hence the major grain size differences are observed [141]. Alternatively, the rapid 10^4-10^5 K/s rapid cooling rates [150] experienced during LPBF may not significantly alter the β grain growth based on minor process parameter differences and this readily explains the similar sized PBG in Figure 4-6 for specimens printed with both VEDs.

Unlike the microstructures seen in forged or wrought Ti-5553, the additive manufactured ones have columnar β grains grown along the building direction as shown in Figure 4-7. Layer by layer deposition during the LPBF process results in directional solidification and it is typical to expect columnar grains along the building direction [151,152]. In the LPBF process, the previously deposited layer acts as a heat sink - dissipates a substantial portion of the applied heat energy through it and facilitates solidification of the just deposited layer. The directional heat dissipation assists heterogeneous nucleation, which causes the body centred cubic β grains to preferentially grow along the <100> direction and resulting in the columnar β grains [153].

The sub-micron features grown within the columnar β grains in Figure 4-7(b) and Figure 4-8(a) are suspected to be phase α precipitates. Huang *et al*. observed similar but locally distributed features in LPBF printed Ti-64 alloy, which corresponded to α precipitates since the alloy as enriched with strong α phase stabilizing elements [154]. It is well known that the grain boundaries are among the favorable sites for nucleation and recrystallization of second phase α precipitates in titanium alloys [52,100,155]. Similar, but not identical features dispersed within the β grains were reported as α precipitates by Carlton *et al*. on heat treating LPBF processed Ti-5553 at α+β region [9]. In this case, as the melted and solidified alloy cools down to room temperature, the surrounding powder particles will limit the cooling rate and indirectly facilitating the printed part to undergo an in-situ heat treating that would aid the growth of secondary phases. Schwab *et al*. has already reported the growth of α particles in LPBF processed Ti-5553 under the in-situ heat treatment [10].

The presence of these non-lamellar particles identified only in the E-high sample can be explained by their size being influenced by the energy input. It was reported that the difference in VED could influence the size of second phase particles [11,27] and higher VEDs are anticipated to result in coarser second phase particles. The higher VED that cause a lower thermal gradient and hence a slower cooling rate could facilitate elemental diffusion [5,27]. This might have resulted in a higher degree of α stabilizer elements accumulating at the nucleated sites of second phase particles assisting the further growth of the nucleated α particles.

The corresponding XRD patterns in Figure 4-8(b) and the EBSD phase distribution maps seen in Figure 4-9(c, g) further strengthens the claim that the observed features within the columnar grains must be α precipitates. Additionally, this finding is in good agreement with the previously published XRD patterns of forged or LPBF printed and heat-treated Ti-5553 samples [9,10,57,141,156]. However, the XRD patterns of as-printed Ti-5553 reported so far, which were printed at 60 to 140W, exhibit strong β phase peaks and only weak α phase peaks [27,29,32]. In another case, a set of weak XRD peaks indicate the minor presence of α phase [157]. The absence or negligible presence of α precipitates in previous reports could be ascribed to the lower laser power and hence lower thermal energy. The higher laser power employed in this study appears to promote in-situ heat treatment and precipitation of α particles from the solid solution.

The cubical/pentagon-shaped β grains observed in the EBSD orientation maps in Figure 4-9 (a, e) are equivalent to the optical microscopy images seen in Figure 4-6. Even though <100> direction is widely reported as the preferred orientation of β grain growth in several cases involving β-Ti alloys, no such preference is observed in any of the EBSD maps presented in Figure 4-9 (a, b, e, f). Alternatively, a preference towards <111> direction is witnessed in E-Low sample along the scanning direction. This observation is in contrast with the EBSD orientation maps of LPBF processed Ti-5553 reported so far where <100> direction is the preferred grain growth direction. In all those previously reported results, a near 100% retention of β phase might have contributed to such a preferred directional growth. However, based on a significant volume of α particles in the microstructure, the difference in the crystal texture is expected to have contributed to the random grain growth direction observed. Similar random texture caused by α particles is reported earlier for traditionally processed Ti-64 [158]. This randomness in β grain growth direction may also be attributed to the rather chaotic and fine grain structure, suggesting the primary solidification mode has been disrupted. This difference could be a result of the stripes printing pattern used where a 67° rotation is applied between successive layers of print as reported earlier [157,159]. Higher VEDs in the LPBF process with slower cooling rates could facilitate better elemental diffusion and could result in coarser grains as already reported [5,27,160]. The vertically aligned α particles in the phase distribution diagrams as denoted by the arrow marks and the weak texture seen in pole figures complement the above discussion.

The comparable hardness values between E-Low and E-High samples as in Figure 4-10(a) suggest similar mechanical properties. Similar ranged hardness values at contour and core are already reported for the LPBF processed Ti-5553[32]. The peak hardness could be a combined effect of finer and columnar grains observed at the inner and outer contour sub-sections respectively, as detailed earlier in Figure 4-5. On quantitative measurement, the grain size at contour varied from 37 to 52 µm, which is approximately one third the size of those grains observed at the core.

A prime observation from the tensile curves is the exceptional elongation to failure of 30±5%. To date, such a high elongation has never been reported in the available literature for LPBF-Ti-5553 alloy. However, formation of globular α particles within β grains is believed to result in the high elongation in β-Ti alloys [161]. It was reported previously that an increase in the volume fraction of globular α particles in the microstructure from 9% to 32% resulted in decreasing the yield strength from 1077MPa to 890 MPa but the corresponding elongation values were undisclosed [156]. Reduction in yield strength due to the presence of globular α particles may drastically affect the toughness. This is related to the fact that globular α particles are not as effective as compared to lamellar α particles in arresting the dislocation movement [4,161,162]. The inadequate impact toughness values of the samples tested at 0°C seen in Figure 4-11(b) confirm the impact of non-lamellar α particles on the mechanical properties.

Another striking observation from the tensile curves in Figure 4-11(a) is the lack of strain hardening. The negligible strain hardening commonly seen in BCC crystal structured materials is expected to be an outcome of low dislocation density [163]. It is drawn assuming that the grain boundaries are a source of new unpinned dislocations in these materials. The dislocations that are dissociated from solute atoms cause discontinuous yielding and resists strain hardening [163,164]. Secondly, simultaneous competing strengthening and softening mechanisms after yielding are also widely accepted theories to explain the negligible strain hardening. Saturation of twins in α and dislocation tangling in the β phase contribute to strengthening, whereas slip transfer through α/β interfaces, while deformation of α through twinning and slip promote softening behavior [75]. As the microstructure exhibited a strong presence of α precipitates distributed throughout, slip transfer through α/β interface must be governing over the twinning effect resulting in the observed softening in the plastic deformation region of the tensile curve.

The fracture surfaces presented in Figure 4-12 and Figure 4-13 reveal a mixed mode of fracture. The dimples indicate ductile fracture observed at the core section confirm that the fracture propagation was induced by homogeneous dimple nucleation and possibly the coalescence along the α/β interfaces. The diameter of these dimples are approximately comparable to the length of the identified non-lamellar α particles shown in Figure 4-8, with subsequent development of microvoids into secondary cracks support the high elongation observed under tensile loading. Even though secondary α precipitates are expected to induce plasticity and affect the mechanical properties adversely, it has been reported that the morphology of α particles can alter the mechanical behavior in titanium alloys [123]. Additionally, the presence of occasional facets seen in E-High sample indicate the traces of intergranular fracture suggesting an indirect in-situ heat treatment effect as similar facets were frequently reported in heat treated tensile samples after fracture [67,123].

Even though twinning is considered to be the preferred fracture mechanism in β-Ti alloys, slip can dominate if the microstructure is composed of large aspect ratio of α and a large area of semi coherent α/β interface [75]. The presence of these slip marks confirms the fracture mechanism is slip dominant. The large aspect ratio of α precipitates also supports the observations indicating they are non-lamellar.

4.5 Summary and conclusions

In this study, the mechanical properties of LPBF printed Ti-5553 samples at process parameters suitable to meet industrial production demands are evaluated. Two process parameters that yields high relative densities were selected based on the results of pre-screening phase of the project. In addition, microstructural characterization experiments were carried out to rationalize the findings. On the basis of the experimental results obtained through characterization techniques such as OM, XRD, microhardness, SEM and EBSD, in this research, the subsequent conclusions can be drawn:

1. Samples printed at VED = 39.1 J/mm^3 with a scan speed of 1120 mm/s and at VED = 56.1 J/mm^3 with a scan speed of 781 mm/s exhibited traces of LOF and keyhole defects starting to appear in the microstructure, but retained a high relative density (RD ≥ 99.9%)
2. At VED = 56.1 J/mm^3, the microstructure consists of non-lamellar α precipitates within columnar β matrix grains with <001> oriented in the building direction.
3. Subjected to uniaxial tensile load, the printed samples exhibited a yield or ultimate tensile strength of 780±10 MPa, with an elongation of 30±5% which is approximately twice higher than the usually reported elongation values for Ti-5553.
4. The higher than usual elongation is expected to be an outcome of the non-lamellar α particles, which is strongly supported by the poor impact toughness values recorded.

5. The transverse section of the printed Ti-5553 samples exhibited finer-grained microstructure along the contour, which gradually coarsened towards the centre. This resulted in preserving the strength despite higher elongation, which is proved by the bi-modal fracture observed.

Chapter 5: Effects of post heat treatment on mechanical properties of LPBF-made Ti5553 parts

This chapter addresses the third objective, which is investigating the possibility of fine tuning the morphology of second phase particles and thereby improving the tensile properties of LPBF-made Ti-5553 alloy. Majority of this chapter is adapted from the contents of the published manuscript: '*N. Ramachandiran, H. Asgari, F. Dibia, R. Eybel, W. Muhammad, A. Gerlich, E. Toyserkani, Effects of post heat treatment on microstructure and mechanical properties of Ti5553 parts made by laser powder bed fusion, J. Alloys Compd. 938 (2023). doi:https://doi.org/10.1016/j.jallcom.2022.168616.*

5.1 Introduction

In Chapter 4, it was established that the non-lamellar morphology of the α particles could be a prime reason for the poor tensile strength exhibited by the LPBF-made Ti-5553 parts. Recent works have confirmed the possibility of improving the tensile strength of LPBF-made Ti-5553 through heat treatment procedures [74,165]. However, the combined influence of aging temperature, duration, and cooling rate following heat treatment on LPBF-made Ti-5553 parts and their effects on mechanical properties are yet to be studied in detail. In this chapter, LPBF-made samples solution treated at super β-transus (900°C) and sub β-transus (700 & 800°C) temperatures were subjected to aging at 500 to 700°C for 0.5 to 4 hours. Heat-treated samples were water quenched to precisely control the size and shape of α particles. The corresponding microstructural observations were characterized, and their influence on the hardness and tensile properties were explored. Detailed characterization by optical and electron microscopy supported by electron back scatter diffraction (EBSD) maps to determine the microstructural evolution with heat treatment duration is discussed. The observed microstructural features are correlated to the corresponding microhardness and tensile properties.

5.2 Experimental procedure

Samples from the pre-screening phase of the project that resulted in the best relative density (RD ≥ 99.9%), acceptable hardness (23 to 25 HRC) and low surface roughness (Ra ≤ 10 μm) were chosen for the heat treatment analysis. As a part of the continued optimization, the process parameter set applied to obtain the above-mentioned density, hardness and surface roughness combination, is given in Table 5-1.

Table 5-1: LPBF process parameter set to obtain an optimal combination of density, hardness and roughness

Location	**Laser Power (P)**	**Scan speed (v)**	**Layer thickness (l)**	**Hatch Distance (d)**	$\mathbf{VED = \frac{P}{vld}}$
	(W)	**(mm/s)**	**(mm)**	**(mm)**	**(J/mm^3)**
Core	187.5	1089	0.06	0.11	26.08
Contour	175.6	841	0.06	0.11	31.64

In addition to the characterization methodologies mentioned in Chapter 3, differential scanning calorimetry (DSC) is used in this chapter. To identify the β-transus temperature (T_β), samples were heated from room temperature to 1100°C at heating rates of 20, 30 and 40°C/min in a simultaneous thermal analyzer (DTA, Netzsch STA 449) capable of maintaining a 25 ng resolution to weight capacity of 5 g. The corresponding phase transformations, observed as a function of temperature, were traced. Heating rates of 20 to 40°C/min were chosen here as they would closely replicate the heat treatment conditions dealt with in this research work.

5.3 Results

5.3.1 Phase transformations in Ti-5553

As phase transformations are a function of temperature, it is necessary to track down the corresponding phases present at respective temperatures, specifically prior to designing and optimizing a heat treatment routine. In Figure 5-1(a), differential scanning calorimetry (DSC) curves for Ti-5553 under three different heating rates are plotted. As it is observed, the changes are explicit at higher heating rates. On the curves, peaks represent endothermic reactions, whereas valleys represent exothermic reactions. The temperature range of 570 to 770°C is identified to facilitate α particle growth. Above 770°C, α particles start to dissolve into the solid solution, and 860±10°C is identified as the β-transus temperature (T_{β}), which is the temperature at which 100% of β phase can be reached. The identified T_{β} range is comparable to the previously reported values [75,156,166] for Ti-5553 alloy.

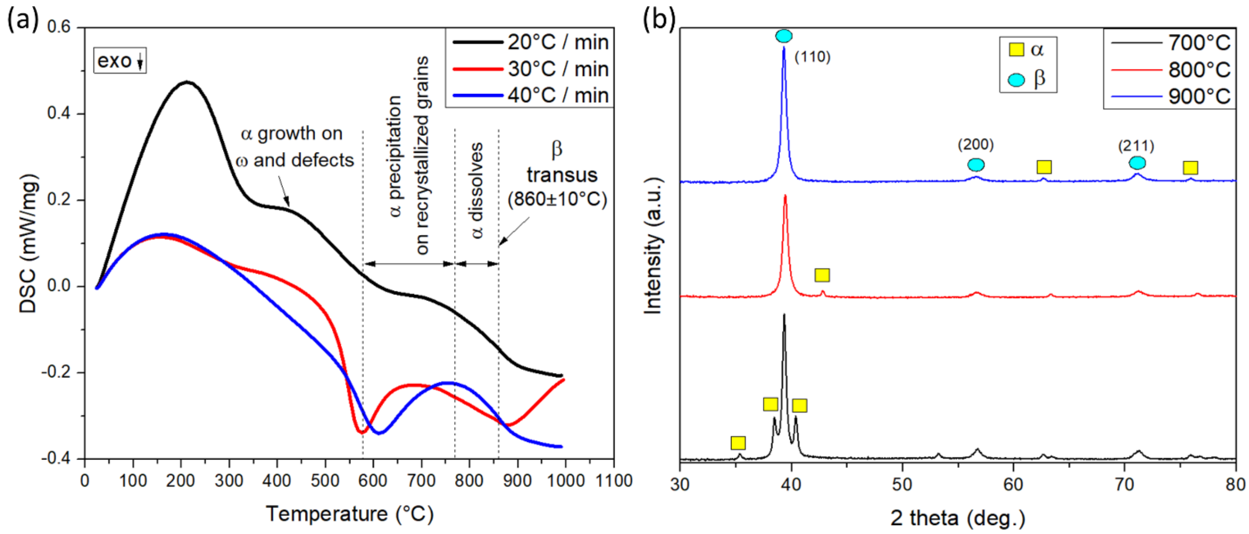

Figure 5-1: (a) Differential scanning calorimetry (DSC) curves for Ti-5553 (b) XRD spectra of LPBF-made Ti-5553 samples solution treated at 700, 800 and 900°C for 3 hours

Figure 5-1(b) shows the XRD spectra of samples solution treated at 700, 800 & 900°C for 3 hours. Strong α peaks identified at 700°C become weaker with increasing temperature, indicating their dissolution into the solid solution. Carlton *et al.* [9] also reported similar strong α peaks on heat treating LPBF-made Ti-5553 at 700°C. The trivial presence of α phase beyond T_β (at 900°C) is expected to be a side effect of the unavoidable minor drop in the temperature caused during sample handling while quenching, as this would inevitably induce some nucleation of α phase as the temperature drops into the α + β phase region.

5.3.2 Effect of solutionizing temperature

Solutionizing or solution treatment (ST) is carried out to dissolve the heterogeneously grown secondary phase precipitates back into the solid solution. Figure 5-2 shows the microstructural variations caused by three different ST temperatures on LPBF-made Ti-5553 relative to the as-printed microstructure. The results are presented in four sets of optical microscopy (OM) images, EBSD grain orientation maps, phase maps and pole figures. The OM images reveal the columnar β grains evident in the as-printed condition, which are a result of directional solidification in the LPBF process. The EBSD grain orientation maps highlight the retention or disruption of columnar β grains along with the typical subsequent changes in the grain size caused by corresponding thermal treatments. The matching EBSD phase maps project the distribution of α precipitates within the β matrix, while the corresponding pole figures highlight the differences in the crystal texture.

At 700°C, extensive growth of α precipitates within the columnar β grains (as depicted previously in Figure 5-1) is confirmed in Figure 5-2. The higher magnification SEM image given in Figure 5-2 – A2 shows the development of secondary α needles (α_S) and clearly segregates them from the residual primary α particles (α_P), which can provide nucleation sites for α_S

recrystallization. The average diameter of β grains shrank from 109.7 µm in the as-printed state (Figure 5-2 – B1) to 80.4 µm (Figure 5-2 – B2), and the area fraction of α precipitates increased from 7% to 26% (Figure 5-2 – C1 and C2). A strong <001> texture, along the building direction with an intensity of 4.765 mrd is observed in Figure 5-2 – D2 compared to the as-printed texture (Figure 5-2 – D1), is expected to be an effect of the nucleation of α particles at the unstable β grains [25]. These observations are in accordance with the DSC curves and XRD patterns in Figure 5-1, where 700°C is within the preferred temperature range for α phase growth.

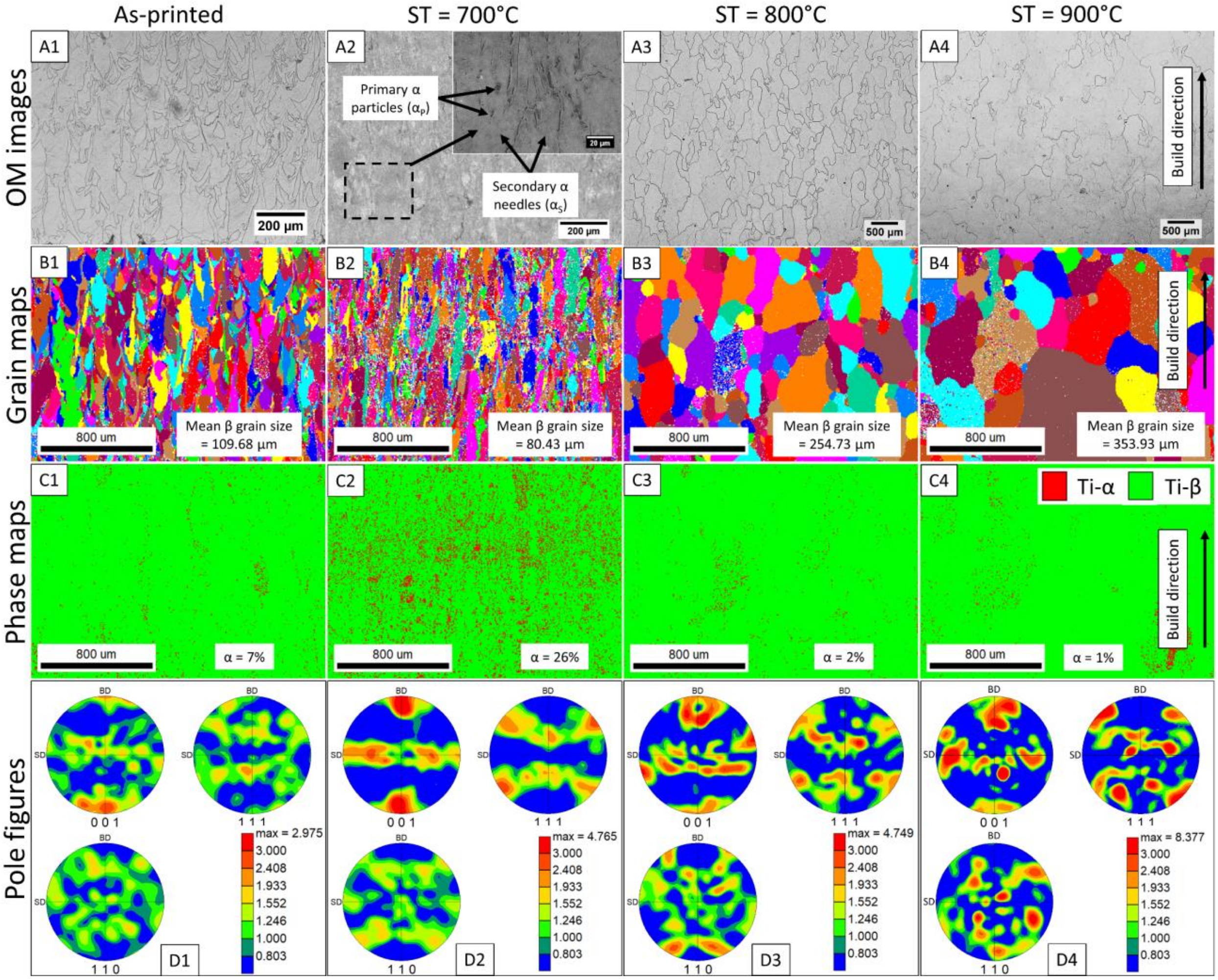

Figure 5-2: (A1-A4) OM images illustrating the microstructural changes in the columnar β grains caused by different ST temperatures (B1-B4); Corresponding changes in the β grain size (C1-C4); Area fraction of α particle distribution within the β matrix (D1 – D4); EBSD Pole figures exhibiting the increase in <001> texture intensity from D1 to D4

With a further increase in temperature beyond 770°C, dissolution of α particles into the solid solution concurrently with β grain growth is expected based on the DSC curve, and is evident in Figure 5-2. This observation is in good agreement with previous reports [57,112]. Up to 800°C, the columnar grains are retained (Figure 5-2 – A3). Analyzing the corresponding EBSD maps results in quantifying the average diameter of β grains to 254 µm (Figure 5-2 – B3) and a drastic reduction in α content in the microstructure to 2% (Figure 5-2 – C3). Additional increase in temperature, namely ST at 900°C, seems to break the columnar grain structure through extensive β grain coarsening (Figure 5-2 – A4). The corresponding β grain size measured to 354 µm (Figure 5-2 – B4) with a slender reduction in α content to approximately 1% (Figure 5-2 – C4). At 800°C, the α phase dissolves back into the solid solution, but the texture intensity is unchanged compared to that of 700°C sample (Figure 5-2 – D3). At 900°C, as the microstructure is nearly 100% β, an increased intensity up to 8.377 mrd is detected. Considering the ST heat treatment at 800°C for 3 hours that provides an appropriate combination of finer β grains coupled with a relatively insignificant second phase precipitation, it was chosen as the optimal ST condition for further experiments.

5.3.3 Effect of aging temperature and duration (time)

5.3.3.1 XRD spectrum at different aging conditions

XRD patterns obtained from LPBF-made Ti-5553 alloy subjected to an 800°C ST for 3 hours followed by aging at 500, 600 and 700°C for 30 minutes and 2 hours are given in Figure 5-3. As previously reported in many similar cases involving heat treatment of β-Ti alloys [167–169], α and β are the only identified phases across the investigated temperature range. Minor asymmetry in the $(110)_\beta$ peaks, particularly for the 500°C case reported previously, was speculated due to the effect of non-equilibrium ω phase [9]. For the cases of aging at 500°C and 600°C, a significant increase in the intensity of $(101)_\alpha$ peaks compared to $(110)_\beta$ peaks with aging duration could be an indicator of the increase in the α volume fraction with time as claimed previously [73]. In addition, $(103)_\alpha$ and $(211)_\beta$ peaks are more intense for the 600°C cases. This could be an effect of the high cooling rates caused by quenching that promotes the precipitation of ω phase, whose peaks are closely overlapped by the α and β phase peaks [73,170]. For the specimen aged at 700°C aged, a minor increase in the intensity of $(002)_\alpha$ and $(101)_\alpha$ peaks are noted, although the $(110)_\beta$ peaks are vastly stronger in intensity by comparison.

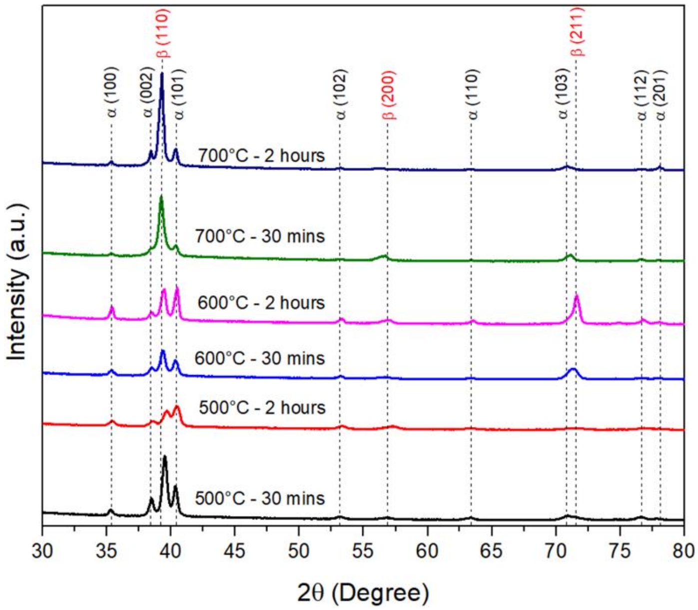

Figure 5-3: XRD Spectrum of LPBF-made Ti-5553 alloy aged at 500, 600 and 700°C for 30 minutes and 2 hours

5.3.3.2 Aging at 500°C

Aging treatments are carried out to facilitate the growth of second phase particles in Ti alloys. Figure 5-4 displays the microstructural changes of LPBF-made Ti-5553 alloy after ST at 800°C for 3 hours followed by aging at 500°C for time periods ranging from 30 minutes to 4 hours. As seen in Figure 5-4 (A1-A4), the morphology of the precipitated α particles varies with time. Initially (Figure 5-4 – A1), it is triangular morphology where the average β grain size measures to

106±14 μm (Figure 5-4 – B1). After 1 hour of aging (Figure 5-4 – A2), the triangular lamellae evolve into a Widmanstätten star-like morphology with a gradual reduction in the β grain size to 96±7 μm (Figure 5-4 – B2). The precipitation origin from where the three-dimensional α needle growth is expected to initiate is marked. The sizes of the spotted α lamellar particles ranged from 2.31 to 12.75 μm in length and 0.88 to 1.22 μm in width, respectively. Moreover, their corresponding pole figures, showing the overall texture of the samples, are presented in Figure 5-4 – C1 and C2. The isolated hotspots seen in Figure 5-4 – C1 could be due to a marginal increase in preferred grain growth along the <001> direction aligned with the building direction involving a random rotation between the scanning direction and the transverse direction. Generally, the <100> direction is reported as the easy-growth direction for BCC materials, but such a preference is not observed in Figure 5-4 (C1 – C4) due to the disrupted primary solidification, and a more complicated thermal gradient across the sample caused by the repeated melting and solidification cycles during the LPBF process [137]. Additionally, the grain structure appears to be fully crystallized compared to the as-printed condition seen in Figure 5-2 – D1 and might have contributed to the observed overall weak texture.

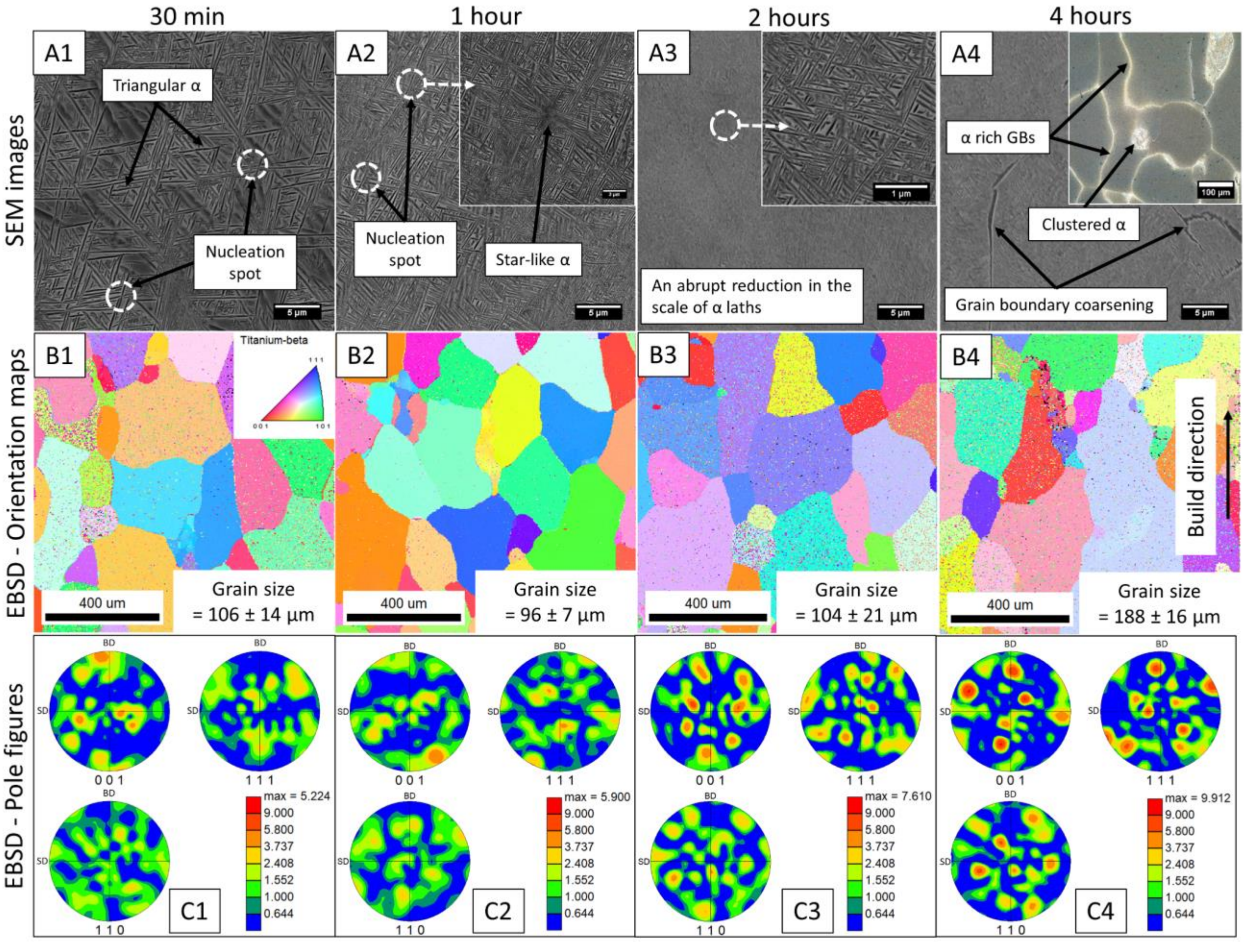

Figure 5-4: LPBF-made samples aged at 500°C (A1 – A4); SEM images detailing the transformations in α particle morphology, distribution and scale dictated by the duration of heat treatment (B1 – B4 & C1 – C4); Corresponding EBSD maps of the samples

Further increasing the aging duration (i.e., to 2 hours) caused the α needles to be finely dispersed within the solid solution, as seen in Figure 5-4 – A3. The α needles measured 0.183 to 0.398 µm in length, and 0.029 to 0.052 µm in width. Rarely, α needles measuring 1.4 to 1.6 µm in length were also seen. Simultaneously, a minor increase in the β grain size from 96±7 µm (Figure 5-4 – B2) to 104±21 µm (Figure 5-4 – B3) was noted as well. Figure 5-4 – B3 also suggests a minor increase in β grain growth preference towards the <111> direction. The corresponding pole figure (Figure 5-4 – C3) also confirms the preference for β grain growth, as a marginal increase in the maximum intensity from 5.9 mrd (Figure 5-4 – C2) to 7.61 mrd is observed but the texture is still relatively weaker compared to the previous publications [171–173].

With an additional increase in aging duration, as seen in the 4 hours case (Figure 5-4 – A4), the grain boundaries (GBs) start growing exponentially in size, indicating a heterogeneous α particle precipitation as previously reported [174–176]. An increase in the area fraction of α precipitates from 4% (Figure 5-9 – B1) to 32% (Figure 5-9 – B4) caused by the extended aging at 500°C confirms the widespread α precipitation. Furthermore, there are random locations of clustered α particles deep within the grains. The segregation of α particles at GBs can detrimentally affect the homogeneous distribution of the finely distributed second phase precipitates throughout the microstructure. An increase in β grain size (188±16 μm) is also observed (Figure 5-4 – B4). The overall texture remains almost unchanged up to 2 hours aging, and no grain growth occurs in a specific (preferred) direction. At 4 hours, with an increase in maximum intensity up to 9.960 mrd (Figure 5-4 – C4), traces of grain growth preferences in the <001> and <111> directions are seen. However, a strong texture component is not distinctively developed.

5.3.3.3 Aging at 600°C

Aging at 600°C is the most preferred condition for controlled lamellar α growth reported in the literature for conventionally manufactured Ti alloys [74,166,177–179]. Figure 5-5 presents the microstructural changes and their corresponding EBSD grain orientation maps and pole figures of LPBF processed and heat-treated samples. These samples were subjected to ST at 800°C for 3 hours followed by aging treatment at 600°C for time periods ranging from 30 minutes to 4 hours. As noted in Figure 5-5 (A1 – A4), the initially observed lenticular α particles gradually transformed into lamellar and then into a combination of spherical and cylindrical morphologies with time.

Aging at 600°C for 30 minutes results in the formation of finely distributed sub-micron-sized lenticular α precipitates (Figure 5-5 – A1) throughout the microstructure. The observed lenticular morphology could be an effect of the combined growth of nano-sized spherical ω precipitates and fine α laths [166]. At this temperature range, the phase kinetics promote ω precipitates to undergo massive swelling, which eventually leads to the quantifiable lenticular precipitates seen after 1 hour of aging (Figure 5-5 – A2). Along with the lenticular morphology, needle-like lamellar or acicular α particles were also witnessed throughout the microstructure. The EBSD grain orientation maps depicted a steep reduction in β grain size from 123±38 µm (Figure 5-5 – B1) to 79±56 µm (Figure 5-5 – B2). The length of the observed α particles ranged from 0.5 to 2 µm, which is also comparable to the previously reported values for forged Ti alloys under equivalent heat treatment conditions [73,180].

Two distinct features are prominent on samples aged at 600°C for 2 hours (Figure 5-5 – A3). Firstly, as a continuation of the previous case - decomposition of ω precipitates or a gradual dissolution of lenticular α particles resulting in a proportional increase of the lamellar α particles is observed. Image processing software quantified lamellar α particles occupying a 26±2 % of the total observed area. Secondly, the fixated presence of triangular α particles in the vicinity of GBs. The spherical or globular α particles marked near the GBs were previously reported as the precursors for nucleation and growth of intergranular α platelets [141]. An increase in the β grain size from 79±56 µm (Figure 5-5 – B2) to 104±41 µm (Figure 5-5 – B3) is noted. At 4 hours of aging (Figure 5-5 – A4), cylindrical α morphology (α particles with rounded edges) started to appear in the microstructure. The identified cylindrical α particles ranged 0.8 to 1.65 µm in height and 0.37 to 0.41 µm in diameter.

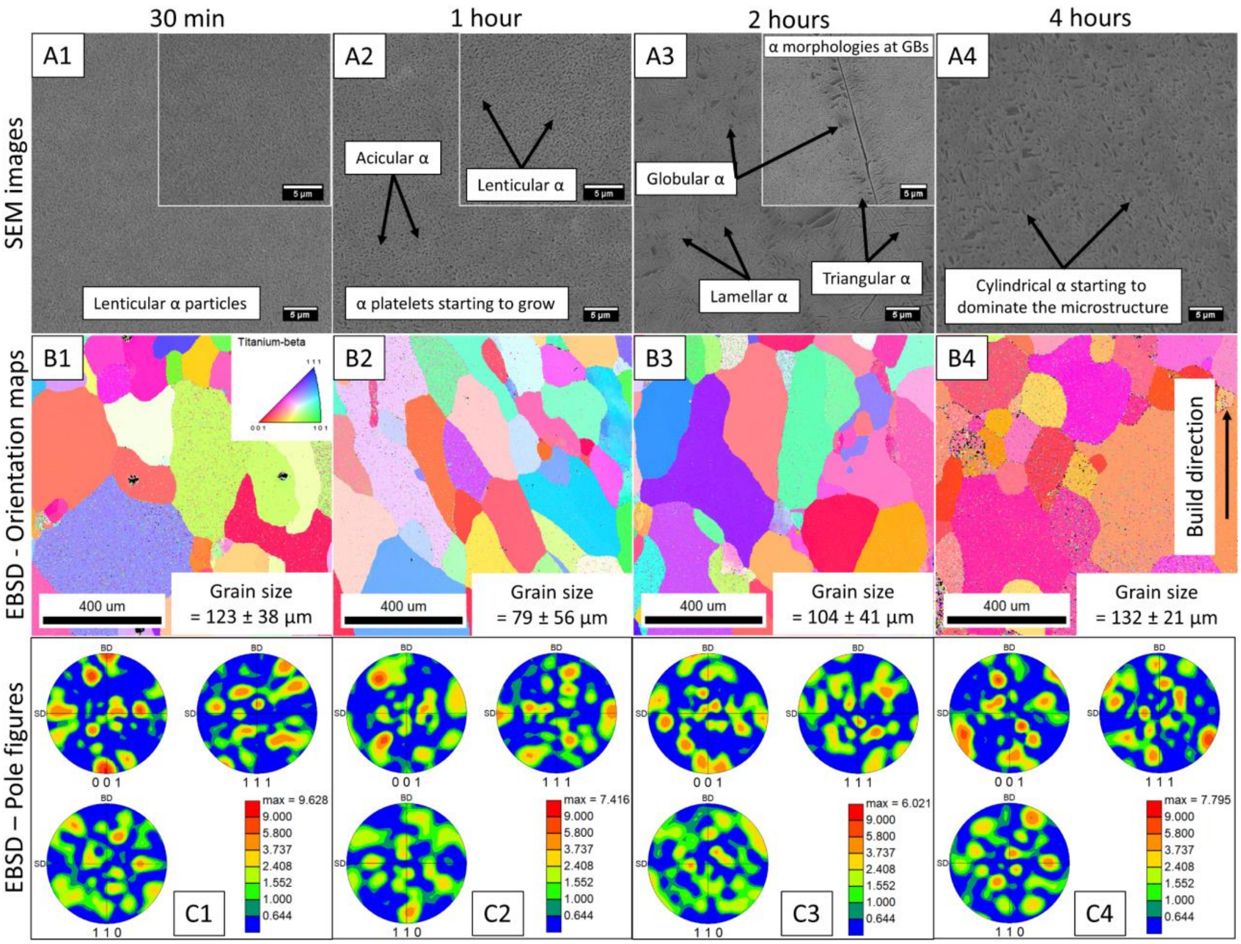

Figure 5-5: LPBF-made samples aged at 600°C (A1 – A4) SEM images detailing the step-by-step transformation of lenticular to cylindrical morphology α particles (B1 – B4) EBSD grain orientation maps of the samples & (C1 – C4) EBSD pole figures of the samples

Initially at 30 minutes of aging, a strong (9.628 mrd) texture persisted (Figure 5-5 – C1) as the <001> direction of the unit cells was aligned along the building direction. The initial strong texture is expected to be an outcome of the directional solidification caused by the layer-by-layer material deposition in the LPBF process [181]. For BCC crystals, <001> is the easy-growth direction [182], which is the preferred orientation observed in several titanium alloys produced by LPBF [29,183]. With an increase in aging time, the strength of the texture along the building direction deteriorates as a weak recrystallization texture is developed.

5.3.3.4 Aging at 700°C

Figure 5-6 presents the microstructural changes and their corresponding grain orientation maps and pole figures of samples subjected to ST at 800 °C for 3 hours followed by aging treatment at 700 °C for periods ranging from 30 minutes to 4 hours. As can be seen in Figure 5-6 (A1 – A4), the initially observed combination of fine α laths adjacent to the chevron-shaped GBs gradually transform into a combination of cylindrical and lamellar morphologies with time.

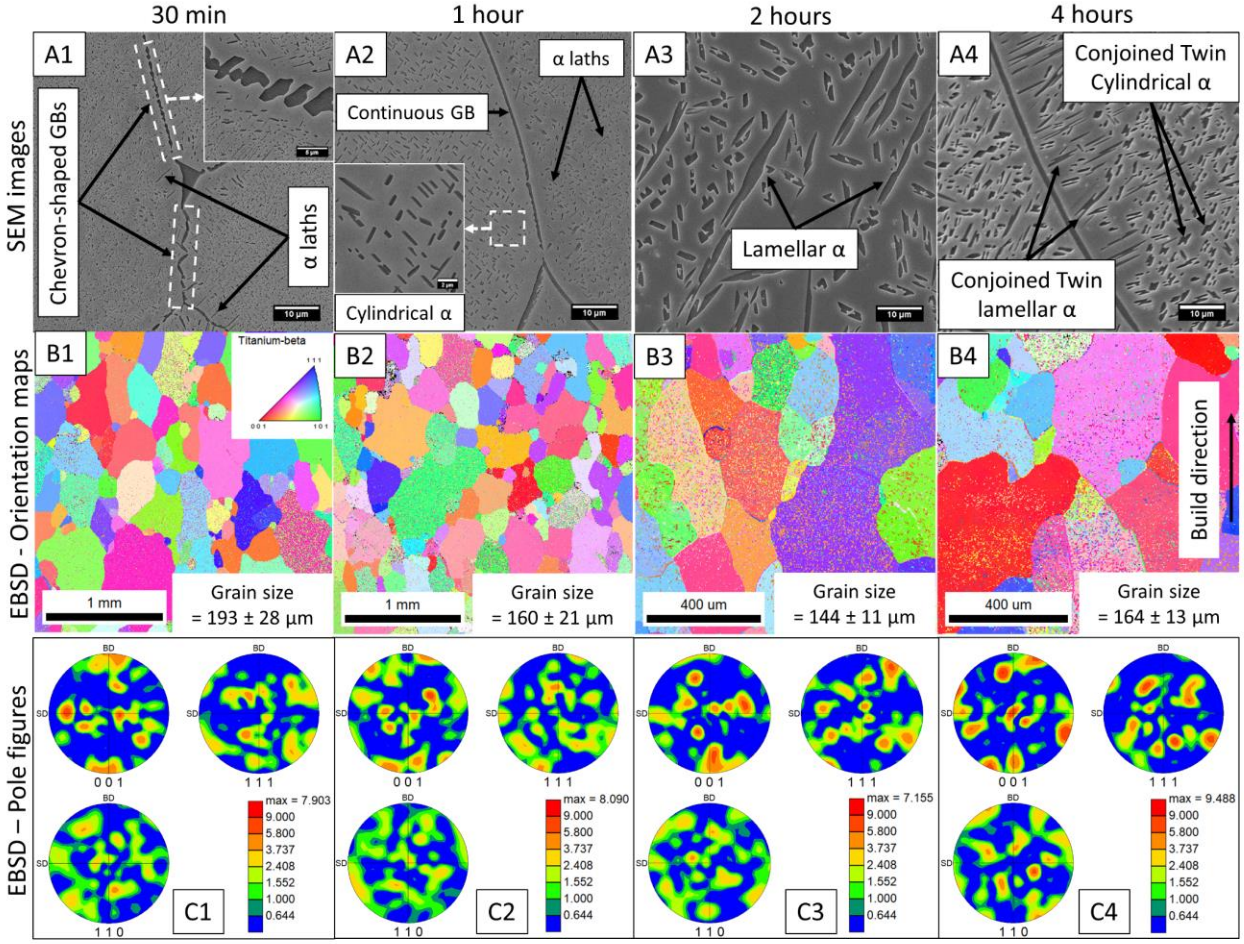

Figure 5-6: LPBF-made samples aged at 700 °C (A1 – A4) SEM images emphasizing the discontinuous chevron-shaped GBs transforming into continuous GBs with time and the α laths evolving into lamellar and cylindrical morphology precipitates (B1 – B4) EBSD orientation maps of the samples (C1 – C4) EBSD pole figures of the samples

Aging at 700 °C for 30 minutes resulted in chevron-shaped GBs surrounded by fine laths of α particles in the vicinity, as seen in Figure 5-6 – A1. Similar chevrons were found previously in conventionally manufactured Ti-5553 parts subjected to heat treatment procedures that induce the growth of isothermal ω particles [184]. The corresponding β grains measured 106±14 µm (Figure 5-6 – B1).

On continued aging at 700°C, a portion of the α laths developed into cylindrical morphology. Figure 5-6 – A2 presents the microstructure after 1 hour. The α morphology in one grain is predominantly cylindrical, whereas it is still fine laths in the adjacent grain, indicating the transformation is gradual and time-dependent. Alternatively, the variation in α morphologies between two adjacent β grains could be an effect of the difference in crystallographic relation between the α phase and the β phase from which it is formed [183]. Chevron GBs transform into typical continuous GBs seen in wrought-based processing, signaling the microstructural features caused by isothermal ω particles are possibly neutralized. Continuous GB α are detrimental to the mechanical properties, especially ductility [185]. A marginal reduction in the β grain size, as shown in Figure 5-6 – B2 (96±7 µm) is an outcome of the gradual thickening of the α laths.

With further aging, the α laths evolved into sharp lamellar α particles, as noted after 2 hours (Figure 5-6 – A3). The microstructure is predominantly lamellar, accounting for 12.4±0.5 % of the area fraction with the occasional presence of cylindrical α particles. Lamellar α needles extending up to 24 - 29 µm in length were identified. Such long α needles were rarely reported for heat-treated Ti-5553 anywhere in the open literature. Despite the enormous growth of α needles, the β grain size has increased to 144±11 µm (Figure 5-6 – B3). After 4 hours of aging, the long needles seen previously were understood to have undergone saturation and broken into several fragments (Figure 5-6 – A4). The length of the α needles observed in this condition ranges 2.4 to 15.8 µm.

Interestingly, these fragmented lamellar and cylindrical α needles were conjoined. Further investigation is required to understand the mechanism involved in fragmentation and conjoining.

The pole figures given in Figure 5-6 (C1 – C4) suggest traces of grain growth preference existing in the <001> direction along the building direction, maintaining an intensity level of 7.903 to 9.488 mrd. However, a strong texture towards a particular direction is absent. The minor angular displacements seen in Figure 5-6 – C2 and C4 should have been affected by the grain growth process activated by the heat treatment cycles. The existence of such grain growth preference, although the magnitude of intensities are different, is comparable to our previous results on LPBF processed Ti-5553 in the as-printed condition [137], where a higher than usual ductility (< 25%) was perceived.

5.3.4 Mechanical properties

5.3.4.1 Microhardness measurements

Microhardness values measured at different heat treatment temperature and duration combinations are presented in Figure 5-7. Within the range considered, as the aging temperature increases the microhardness values gradually decreases. At 500°C, the average microhardness ranged in the order of 380 to 390 HV up to 1 hour and 450 to 500 HV afterwards. Whereas it was 360 to 390 HV at 600°C and further dropped down to 300 to 315 HV at 700°C. This reduction in hardness measurements with temperature could be a cumulative effect of the α particle morphology variations, changes in the β grain size and the level of decomposition of isothermal ω precipitates with increasing temperature [9].

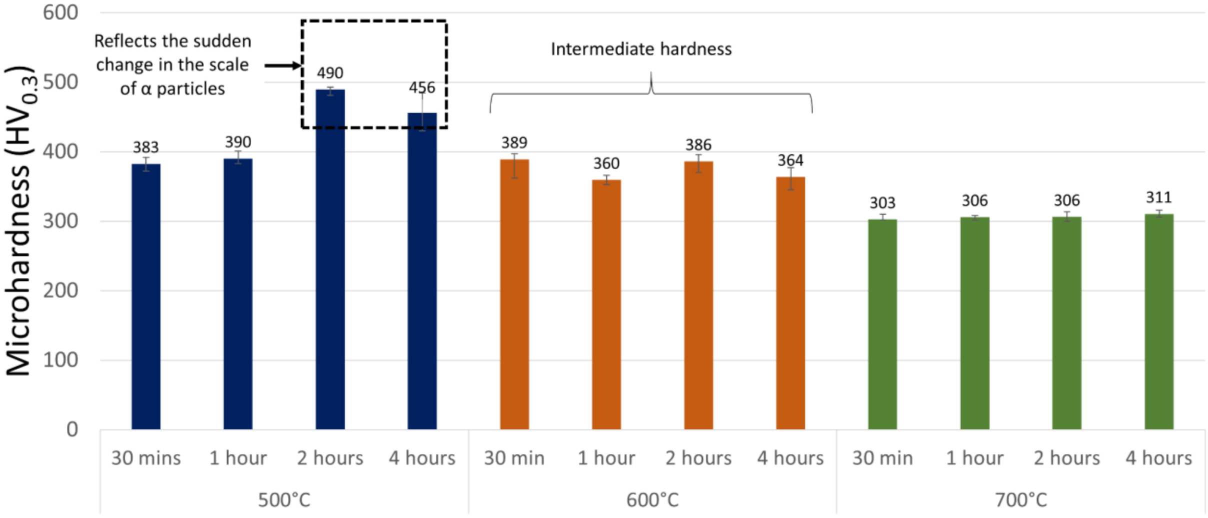

Figure 5-7: Microhardness measurements for different heat treating conditions

Another key observation to be noted in Figure 5-7 is the increase in hardness at 500°C at 2 hours. This increase perfectly synchronizes with the abrupt change in the scale of the α laths discussed in Figure 5-4 – A3. Similar hardness values were reported by Carlton *et al*. on aging at 500°C and predicted that the higher microhardness values observed could be an effect of the presence of ω particles in the microstructure [9].

5.3.4.2 Tensile test

The uniaxial tensile test results of LPBF-made samples subjected to post heat treatment are plotted in Figure 5-8. Figure 5-8(a) presents the results of aging at 500°C, Figure 5-8(b) corresponds to aging at 600°C and Figure 5-8(c) indicates the microstructure for 700°C aging at 0.5 to 4 hour time intervals respectively. The trend of the engineering stress – strain curves is analogous to the previously published results for Ti-5553, in which the elastic limit reaches within 2% of the total elongation and negligible hardening is witnessed in the plastic deformation region [29,123]. The slope of the curves follow a negative trend for Ti-5553 [137], and hence the yield strength (YS) and ultimate tensile strength (UTS) values are not too far apart and therefore they are not separately pointed out.

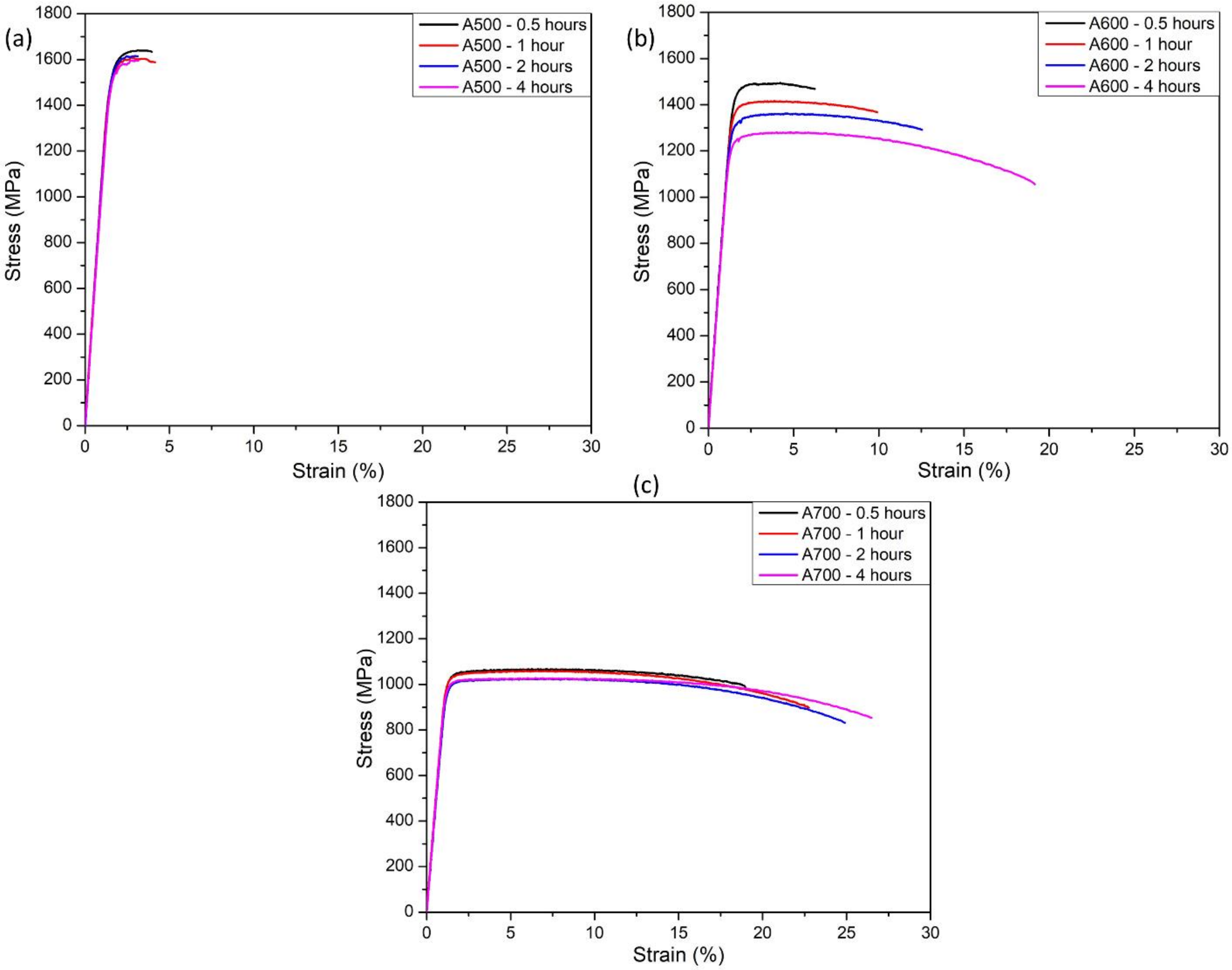

Figure 5-8: Engineering stress-strain tensile response of specimens (a) Aged at 500°C, (b) Aged at 600°C, (c) Aged at 700°C

The comprehensive outcomes of the measured tensile properties are consolidated in Table 5-2. As it is seen, the 500°C aging results in the highest UTS (1640±6.3 to 1614±15.4 MPa) of the samples, but the ductility is poor, as noted by the recorded total elongation values, which are limited in the range of 4.26±1.2 to 3.77±0.9%. In contrast, aging at 700°C leads to the lowest documented UTS values for the tested aging conditions, limited to 1075±16.0 to 1028±10.2 MPa but with a remarkable ductility as total elongation values range 18.18±5.5 to 23.2±4.2 %. However, aging at 600°C leads to an optimal combination of a high UTS (1487±19.2 to 1314±27.3 MPa) together with reasonable acceptable total elongation (6.5±0.8 to 11.5±6.2 %), indicating some ductility remains.

Even though the reduction in UTS with increasing aging duration was observed in all the temperature cases considered, the magnitude of this reduction is more prominent at 600°C aging. Alongside the reduction in UTS at this aging temperature, the ductility improved incredibly to approximately three folds (5.72 to 17.67 %).

Table 5-2: Comprehensive tensile test results of the heat-treated samples

Aging Tempera-ture	**Aging heat treatment duration**							
	0.5 hours		**1 hour**		**2 hours**		**4 hours**	
	UTS (MPa)	**Elongation (%)**	**UTS (MPa)**	**Elongation (%)**	**UTS (MPa)**	**Elongation (%)**	**UTS (MPa)**	**Elongation (%)**
500°C	1640 ±6.29	4.26 ±1.12	1608.67 ±2.82	4.55 ±0.12	1612.67 ±2.97	3.20 ±0.34	1614 ±15.38	3.77 ±0.95
600°C	1486.67 ±19.21	6.54 ±0.82	1413.33 ±15.85	10.72 ±1.17	1360.67 ±13.53	11.20 ±3.53	1314.3 ±27.32	11.49 ±6.18
700°C	1074.5 ±15.98	18.18 ±5.48	1063 ±12.7	18.06 ±3.95	1023.67 ±18.11	24.81 ±0.43	1028 ±10.16	23.19 ±4.15

5.3.4.3 Fractography

SEM micrographs of the fractured surfaces captured from the tested tensile samples aged at 500°C for 30 minutes to 4 hours are shown in Figure 5-9 – A1 to A4, respectively. As seen, the intergranular mode of fracture is predominant in all the four cases, irrespective of the heat treatment duration. Similar intergranular fracture, together with some microvoid coalescence, observed at high magnification is previously reported for heat-treated Ti-55531 alloy [46,186].

The EBSD phase maps of the equivalent samples before tensile tests are given in Figure 5-9 – B1 to B4. The red dots denote the precipitated α particles in the β matrix.

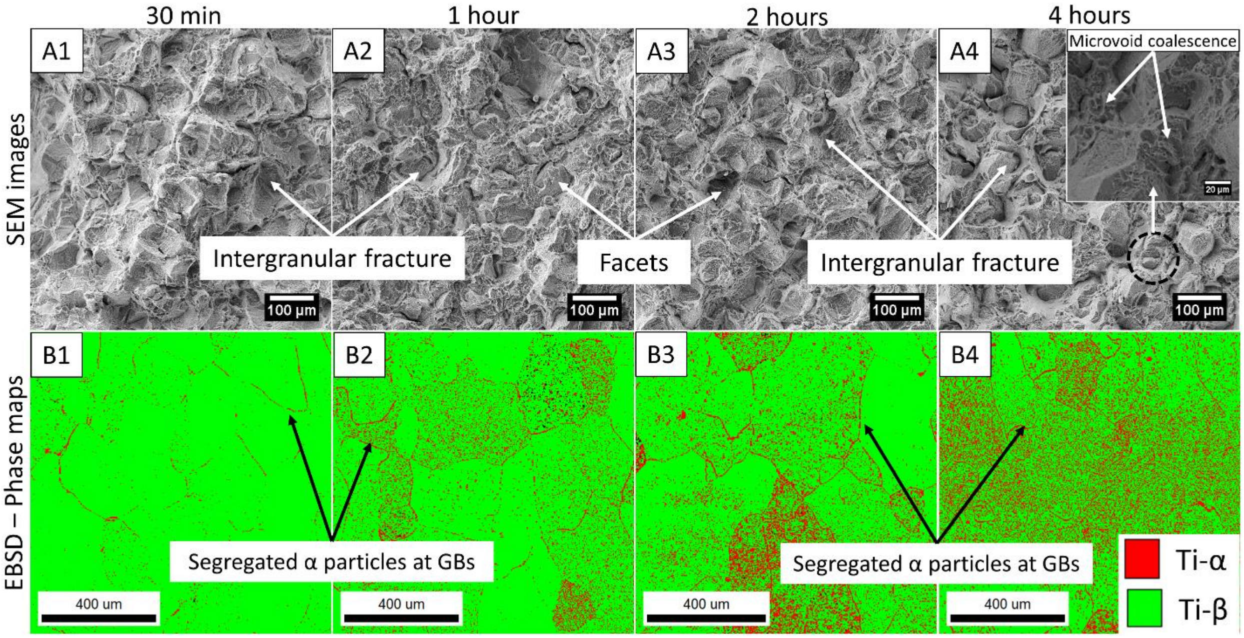

Figure 5-9: (A1 – A4) SEM images of fracture surfaces of tensile samples aged at 500°C revealing the dominant intergranular fracture (B1 – B4) EBSD phase maps of the equivalent non-deformed samples aged at 500°C showing the segregated α particles along the GBs

Three observations are critical to note in these phase maps and fracture surfaces. Firstly, the GBs are the most preferred locations for the precipitation of the HCP crystal structured α particles. Heat treatment procedure, causing the segregation of second phase particles, is a widely discussed phenomenon in Ti alloys, and considered to be a key factor in affecting the ductility [77,152,156,187–189]. Secondly, uniform precipitation of α particles takes place with time within the BCC crystal structured β grains. It is well known that the HCP crystal structure is brittle compared to BCC [190]. Hence, the segregated α particles with a HCP crystal structure located at the GBs could be detrimental to the overall mechanical properties, especially to the ductility. The formation of fine intragranular α particles with a uniform dispersion is much preferred for strengthening without a drastic deterioration of ductility. Finally, despite the dominance of intergranular failure throughout the fracture surface, dimples contributing to the ductile mode of fracture are witnessed (Figure 5-9 – A4) as well at higher magnifications.

Fracture surfaces of the tested tensile samples aged at 600°C are shown in Figure 5-10 – A1 to A4, and the EBSD phase maps of the equivalent samples at corresponding aging conditions examined before tensile testing are in Figure 5-10 – B1 to B4. Unlike the 500°C cases where the failure was intergranular irrespective of the duration of the heat treatment, here in the 600°C aging cases the predominant fracture mode switched from intergranular dominant to ductile dominant mode with time. Up to 1 hour of aging, the failure is predominantly intergranular; at 2 hours, the fracture surface exhibit traces of both the intergranular and ductile modes of failure. For samples aged 4 hours, the fracture is predominantly ductile.

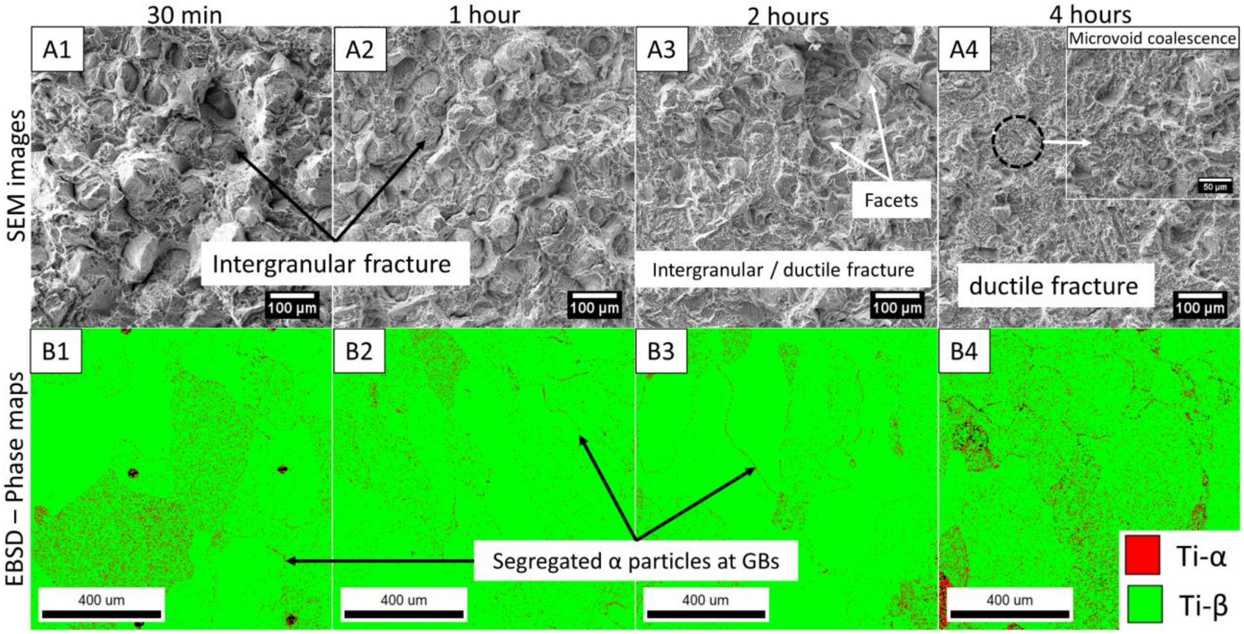

Figure 5-10: (A1 – A4) Fractured surfaces of tensile samples aged at 600°C revealing intergranular fracture (B1 – B4) EBSD phase maps of the samples aged at 600°C showing the segregated α particles along the GBs

The EBSD phase maps show that the segregation of α particles at GBs seen is not as prominent as seen previously in the 500°C case. The combination of a weak GB α segregation with the increasing area fraction of the uniformly distributed α particles throughout the microstructure with time must have contributed to the observed change in the failure mode.

For the 700°C aged conditions (Figure 5-11), the fracture surfaces recorded from the tested tensile samples are in Figure 5-11 – A1 to A4. The corresponding EBSD phase maps of the equivalent but non-deformed samples are given in Figure 5-11 – B1 to B4, respectively. The fracture is predominantly ductile irrespective of the heat treatment duration.

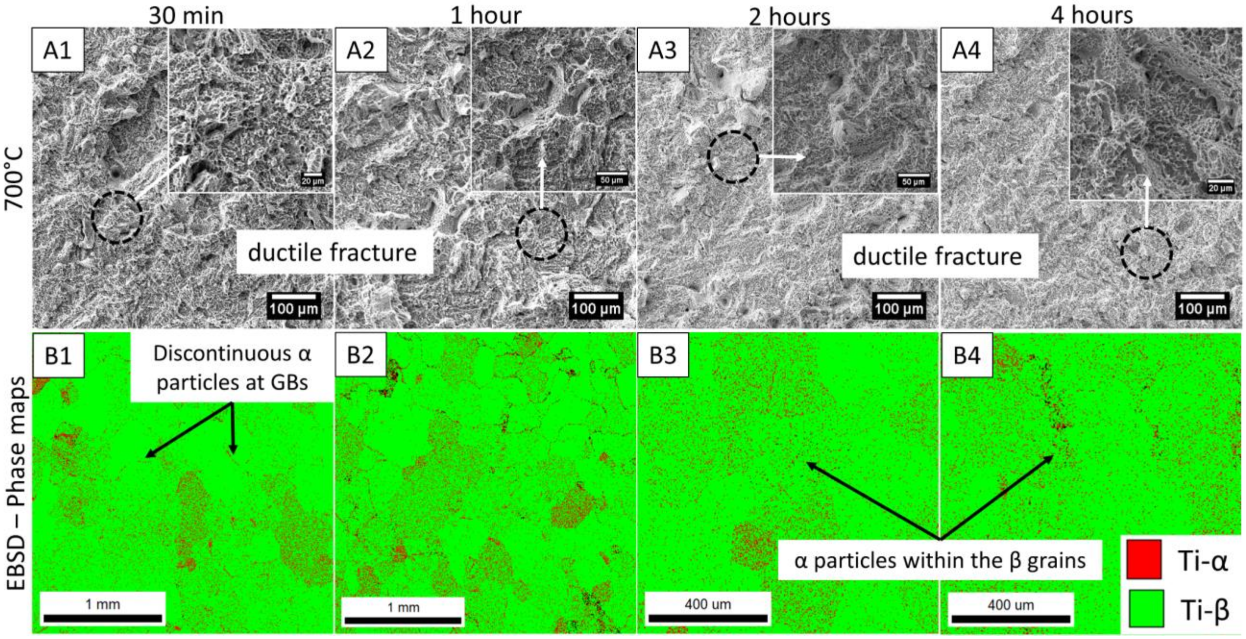

Figure 5-11: (A1 – A4) Fracture surfaces of tensile samples aged at 700°C (B1 – B4) EBSD phase maps of the samples aged at 700°C showing the uniform distribution of α precipitates

The phase maps display an isolated presence of a few discontinuous GB α particles. The widespread segregation of α particles at GBs throughout the microstructure is absent. In contrast to the 500°C and 600°C cases, the uniform distribution of α particles within the β grains is noted from the initial stages of aging itself. The discontinuities in the GB α could be an effect of the chevron-like α particles seen earlier in Figure 5-6 – A1. The absence or limited presence of GB α particles is expected to be a major factor in the observed predominantly ductile fracture mode.

5.4 Discussion

The current results show that ST at upper α+β region (800°C) can bring about the best microstructural combination of finer β grain size with negligible residual α precipitates. ST in the β region (900°C), even this further restricts the residual α content, it caused the columnar β grains to break, which is unfavorable for achieving improved mechanical properties. Similar rupture of columnar β grain chains in LPBF-made Ti-6Al4V alloy is previously testified on heat treatment at 1000°C accompanied by exponential grain coarsening [191]. Exponential grain coarsening is a result of the high migration rate of β grain boundaries (GBs) in the β region [112]. Furthermore, the ST process in β-Ti alloys above T_β (β-transus) temperature followed by quenching facilitates the formation of undesired athermal ω precipitates [166]. On subsequent isothermal aging, these ω precipitates assist the heterogeneous nucleation of α particles and thereby deteriorate mechanical properties [112,166,192]. Theoretically, at 900°C, a 100% β microstructure was expected but the residual α precipitates identified in Figure 5-2 - C4 appears due to the brief exposure to the atmosphere while quenching.

As shown in the Results (Section 5.3), the aging treatments carried out at 500°C, 600°C and 700°C facilitated the growth of different morphology α particles. The corresponding XRD patterns (Figure 5-3) showed that the growth of α precipitates in the β matrix took place by the aging treatments irrespective of the temperatures and the durations of heat treatment cycles. Although Carlton *et al.* [9] could not evidently discern the ω phase through XRD patterns, they were able to determine its role in affecting the ductility of LPBF-made Ti-5553 parts subjected to heat treatment at a similar heat treatment temperature range, namely 500 to 700°C. Moreover, the higher cooling rates caused by water quenching compared to typical air cooling is expected to encourage the formation of sub-micron sized ω precipitates [193]. Accordingly, besides the identified α and β phases, the possible presence of ω phase – which is often discussed as an intermediate phase that exists during β → α transformation, is also considered.

Aging at 500°C initially resulted in triangular α morphology, which evolved into Widmanstätten star-like morphology in 1 hour (Figure 5-4 – A2). Similar triangular and star-shaped particles reported in earlier publications were collectively categorized as fine meshes of Widmanstätten α platelets [46,73]. Triangular alignment of the α particles is rationalized as the natural tendency of second phase precipitates to accommodate the built-in and transformational strains dictated by the presence of ω-phase [194,195]. The Widmanstätten star-like morphology has been postulated as the three-dimensional growth of α platelets from a single nucleus [180,196–198]. The nucleation spots include prior β GBs and homogeneously distributed intergranular nucleation sites [166]. It was also previously reported that the triangular to Widmanstätten star-like morphology transformation could happen with an increase in the aging temperature [73].

Following continued aging at 500°C, a drastic reduction in the scale of α needles was noticed at 2 hours (Figure 5-4 – A3 and A4). A similar abrupt reduction in the scale of the triangular α precipitates was previously reported when the aging temperature at this range was raised by 50°C [195]. However, such a reduction caused by the aging duration has rarely been reported for Ti alloys. The observed reduction in the size of α needles is suspected to be a proportional effect of either the brittle ω phase growth or sub-micron scaled elemental partitioning of heavy atoms, which are expected at 400 to 600°C temperature range [9,199]. Such a reduction in the scale of α particles driven by the compositional fluctuations is described by the pseudo-spinodal mechanism [200]. The mechanism explains the influence of the local compositional fluctuations in thermodynamically stimulating the congruent transformation of β→ω→α. In several cases, the transformation is interrupted by the magnitude of local heterogeneity in composition resulting in a large volume of ω particles along with ultra-fine scaled α laths [195]. The high microhardness value (450 to 500 HV) measured (Figure 5-7) is consistent with the presence of a large volume ω precipitation. Previously, a microhardness range of 475±20 HV, UTS of 1397±26 MPa but a poor ductility of 1.4±0.1% was published for LPBF-made Ti-5553 alloy heat-treated at 500°C, where the presence of brittle ω phase was claimed [9,199]. It is, however, beyond the scope of this study to characterize for ω phase in detail at this stage of the research. After 4 hours of aging, clustering of α particles deep within the grains was noted (Figure 5-4 – A4). These clusters, which were characterized as α laths organized in a herring-bone pattern, have been previously reported as an effect of very long isothermal aging duration [73]. Moreover, coarsening of GBs with α precipitates were also widely observed [174].

A major observation in the tensile test results of the 500°C aged condition is the combination of high tensile strength with low ductility. Evidently, the observed second phase α morphologies have a significant role to play in achieving the tensile properties. Carlton *et al*. reported a UTS of 1397±36 MPa and an elongation of 1.4±0.1% on tensile testing post heat-treated LPBF-made Ti-5553 samples under furnace cooling [9]. A tensile strength of 1199 MPa with 5% elongation was previously reported for conventionally forged Ti-5Al-5Mo-5V-1Cr-1Fe alloy with Widmanstätten α platelet dominant microstructure [201]. The rather poor ductility is rationalized by the severe strain localization of shear bands influenced by the possible presence of hard and brittle ω phase in β grains experienced at this temperature range [202]. The heterogeneous growth of α particles along the GBs subsequently creates α depleted soft zones adjacent to the coarse Widmanstätten α colonies. On mechanical loading, these soft zones are expected to propel the fracture growth and hence drastically affect the tensile behavior compared to other α morphologies [201,203]. Segregation of α particles along the GBs shown in Figure 5-10 (B1 – B4) is clear evidence of the depleted soft zones formed as described earlier. The predominantly observed intergranular fracture on the tested tensile samples validates the loss in ductility caused by the segregation of α particles along the GBs.

Aging at 600°C initially resulted in finely distributed sub-micron sized lenticular α precipitates throughout the microstructure. The observed lenticular morphology is understood to be an effect of the combined presence of spherical ω particles with α needles in addition to the retained β phase. Similar lenticular α particles were observed previously on subjecting Ti-5553 to forging as well as equal channel angular extrusion (ECAE) processes [204,205] where the temperatures experienced are comparable to 600°C. After 1 hour of aging, a considerable increment in the size of the α precipitates is verified. The isolated presence of acicular α laths marked in Figure 5-5 – A2 suggests a significant volume of ω precipitates reaching saturation and ultimately undergoing decomposition. A steep reduction in the β grain size on continued aging, as seen in Figure 5-5 – B2 can be ascribed to the transformation of retained β phase into second phase particles. Such a transformation mechanism facilitating the precipitation of second-phase particles whose composition differ from the parent matrix is termed as sympathetic nucleation in the open literature [8,197,206]. Sympathetic nucleation in Ti alloys often results in plate-like α particle morphology at the interphase boundary following either an edge-to-edge or edge-to-face configuration [206]. The reduction in the microhardness measurements range for 600°C aged samples compared to the 500°C results (Figure 5-7) also supports the possible disintegration of ω particles in this aging condition. The significant reduction in tensile strength along with a subsequent increase in ductility with aging duration [Figure 5-8(b)], further strengthens the ω → α transformation aided by the aging condition. Observed lath morphology of the transformed α particles, which grow into plate morphology in time, can be ascribed to sympathetic nucleation.

After 2 hours of aging, the earlier observed lath/plate-like α particles were replaced by lamellar α within the grains and triangular α particles adjacent to the GBs. The presence of triangular α needles at the vicinity of GBs (Figure 5-5 – A3) suggests a strong pinning effect caused by the retained α particles that might delay ω particle decomposition [158]. Similar high concentrations of triangular α precipitates along the GBs were seen in multiple cases previously [176,196,204]. Cumulatively, such a microstructure combination resulted in a UTS ranging from 1180 to 1234 MPa with 10 to 12% elongation [207]. The cylindrical morphology α precipitates observed are previously reported as intragranular α laths and were claimed to substantially alter the tensile properties based on their dimensions [156,168]. Heat treatment cycles cause these intergranular α laths to grow in Ti alloys, and typically faster cooling rates result in finer precipitates [208].

Tensile test results of the samples subjected to aging at 600°C resulted in a wider range of properties with aging duration, as given in Figure 5-8 and Table 5-2. The negative trend seen, as an indication of a negligible strain hardening in the plastic deformation region, is a general trend observed for β Ti alloys [29,137]. The absence of strain hardening is rationalized by the low dislocation density characteristic of BCC materials [163]. Additionally, the slip transfer taking place through the α/β interface contributes to the softening behavior and might be suppressing the strengthening effect of twinning [75]. With increased aging duration, the α/β interfaces increase, giving rise to the observed reduction in tensile strength with a parallel increase in ductility. The hypothesized decomposition of the hard and brittle ω particles with extended aging, as described earlier, could have significantly subsidized the softening.

While a descending trend in the tensile test results (UTS: 1486±19.2 → 1413±15.8 → 1361±13.5 → 1314±27.3 MPa) is noted, this trend is not as clearly reflected in the microhardness results (389±13 → 360±5 →386±9 → 364±11 HV), and no particular trend can be found. This stable microhardness results suggest the overall microstructure to be fairly consistent throughout the aging treatments. The decreasing tensile strength trend is governed by the GB segregation of second-phase particles. The observed differences among the fracture surfaces of 600°C samples substantiates the GB segregation presumption. The intergranular dominant failure seen in the 30 minutes and the 1 hour aging conditions gradually turned into an intergranular/ductile mixed failure mode at 2 hours and then into a ductile dominant mode of failure at 4 hours (Figure 5-10). The corresponding phase maps explain the intergranularity nature of the fracture resulted from the GB segregation. The homogeneously distributed α particles, deep within the grains, have contributed to the ductile fracture behavior in the 4 hours case. It is then proposed that a combined effect of the GB α particles and the homogeneously distributed second phase particles is responsible for the observed mixed mode of failure in the 2 hours condition.

Aging at 700°C initially resulted in a fine α lath microstructure distributed throughout the β matrix. Chevron-like discontinuous α morphology was identified at GBs (Figure 5-6 – A1). These chevrons were characterized to incorporate a complex internal microstructure, and are proposed to have developed through multiple nucleation sites originating from the decomposing ω particles [184]. The presence of fine α laths in the vicinity of GBs (Figure 5-6 – A1) supports the premise of complete decomposition of ω particles in comparison to Figure 5-5 – A3, where triangular α particles were in large quantities. Heat treatment at temperatures higher than the critical monotectoid temperature (i.e.) ≥ 700°C for a β-Ti alloy (Ti-4Al-7Mo-3Cr-3V) developed from Ti-5553, led to the formation of large-sized chevrons of alpha phase [141]. These chevron-shaped discontinuous GB alpha phases were previously accounted for a higher toughness property in a β-Ti alloy (Ti-7Mo-3Nb-3Cr-3Al) compared to continuous GB α layer since crack propagation through discontinuous α precipitates are reported to be more complicated [168]. It is typical for these fragments of GB α particles to act as nucleation sites, and with prolonged aging develop into a continuous GB α layer in Ti alloys which can ultimately promote brittle grain boundary fracture [209], and thus a continuous GB α layer has a negative impact on the mechanical properties in Ti alloys [185]. As seen in Figure 5-11 (B1 – B4), the α precipitation is more uniform and homogeneously distributed throughout the microstructure. The segregation of α particles at GBs is limited compared to 500°C and 600°C aging conditions possible due to the absence of the ω particle influence in dictating the second phase particle precipitation. The stable microhardness readings, seen in Figure 5-7 (300 to 315 HV), also support the uniform microstructure. The limited presence of GB α particles resulted in high ductility (upto 27.3%), with mainly ductile fracture surfaces as confirmed by Figure 5-11 (A1 – A4).

5.5 Summary and conclusions

In this research, uniaxial tensile properties of LPBF-made Ti-5553 samples were improved by subjecting them to post heat treatment procedures. The Ti-5553 samples used in this research were printed using an optimized process parameter set proven to result in near full densities (RD ≥99.9%). The heat treatments were carried out in two stages, solutionizing and aging. Solutionizing was experimented in three temperature regions – in the lower α+β region (700°C), in the upper α+β region (800°C) and above T_β (900°C) for 3 hours. Aging was attempted at twelve heat treatment conditions involving three aging temperatures (500, 600 and 700°C) and four aging duration combinations (0.5, 1, 2 and 4 hours). The heat-treated specimens were water quenched. Microstructural characterization investigations were performed to rationalize the improved mechanical properties. Findings from the characterization techniques such as DSC, XRD, OM, SEM and EBSD were correlated with the microhardness measurements and tensile test results. On the basis of the mapped correlations, the subsequent conclusions could be drawn:

1. Based on the DSC measurements, three different temperature ranges for second-phase transformations were identified. In 570 to 770°C range, α particle growth was encouraged. At 770 to 850°C, α particles gradually dissolved into the solid solution, and 860 ± 10°C was identified as the β-transus temperature (T_β).
2. Solutionizing at temperatures higher than T_β (900°C) broke the columnar chain microstructure, which was present as a result of directional solidification in the as-printed condition. The breakage of the columnar grains resulted in an undesired exponential β grain coarsening. Whereas solutionizing at upper α+β region (i.e.) at 800°C for 3 hours, ensued in an optimal combination of fine β grain size (~250 μm) and negligible residual α particles (~ 2%) in the microstructure.
3. Aging at 500°C resulted in a triangular morphology α precipitates, which evolved into Widmanstätten (star morphology) α precipitates in 1 hour. After 2 hours, a sudden decrease in the scale of the α needles followed by grain coarsening were observed which reflected as high microhardness values (450 to 500 HV). On uniaxial tensile testing, high tensile strength of 1620 ± 22.2 MPa was recorded but with a low ductility value of 3.7 ± 0.9%. A dominant intergranular fracture was observed due to the grain boundary α segregation.
4. Aging at 600°C primarily gave rise to lenticular α precipitates at 0.5 and 1 hour of heat treatments. At 2 hours, the lenticular α particles transformed into lamellar α particles and at 4 hours the microstructure was largely composed of cylindrical α precipitates. On tensile testing, large differences were observed with respect to the aging duration. The highest

tensile strength of 1487 ± 21 MPa along with ductility of 6.54 ± 0.9% was recorded on 0.5 hours of aging.

5. Aging at 700°C led to finely distributed α laths surrounded by chevron-like grain boundaries at 0.5 hours. At 1 hour, the α laths evolved into cylindrical α particles and the chevrons transformed into continuous grain boundaries. At 2 hours, long lamellar α (24 – 29 µm) dominated the microstructures, which fragmented into conjoined lamellar and cylindrical twins at 4 hours. These sets of heat treatments resulted in a comparatively low tensile strength of 1004 to 1092 MPa but with an exceptional ductility of up to 23.19±4.5%.
6. The EBSD orientation maps and pole figures revealed a recrystallized microstructure on aging at 500°C aging, whereas on aging at 600°C and 700°C, a grain growth preference towards <001> is seen during shorter duration (30 minutes) heat treatments. On longer duration heat treatments (≥ 2 hours) a random-like texture indicating a three-dimensional homogeneous grain growth is identified.

Chapter 6: Characterization of α case regions on LPBF-made and heat treated Ti5553 parts

This chapter addresses the fourth objective, which is characterizing the surface and sub-surface microstructural features of LPBF-made and post heat treated Ti-5553 alloy. The majority of this chapter is adapted from the manuscript under review for publication: '*N. Ramachandiran, H. Asgari, F. Dibia, R. Eybel, H. Ma, A. Gerlich, E. Toyserkani, Influence of α case and transition zone microstructures on tensile properties in laser powder bed fused and heat-treated Ti5553 parts, (2023) under review*.

6.1 Introduction

Post heat treatment procedures of Ti alloys are proven to induce phase transformations and thereby achieve the desired lamellar morphology α precipitates in Ti alloys [9,57]. Furthermore, a methodically fine-tuned heat treatment procedure is capable of controlling the distribution and the size of lamellar α particles aiding in achieving the best combination of tensile properties. Nevertheless, at temperatures greater than 480°C, due to high affinity of Ti towards interstitial elements, which are strong α phase stabilizers, an α rich hard and brittle outer casing widely known as the α case, forms on the outer surface [130].

The presence of an undesired α case is detrimental to mechanical properties of Ti alloys. Sung *et al.* characterized Ti alloy investment castings and reported that, in addition to interstitial elements, Al_2O_3 also plays a key role in the α case formation mechanism [210]. In another endeavor, the reduction in tensile ductility caused by the α-case in Ti castings was predicted using the tensile ductility model [90]. Removal of the α case through chemical and electrochemical approaches were dealt with in a handful of publications [131,132]. Chemical milling involves the usage of highly corrosive hydrofluoric and nitric acid solutions which is not a long term preferred choice for components to be used in critical environments. The electrochemical deoxygenation technique is successful on thin metallic stripes but their effectiveness on real time structural components is unknown. In some previous researches, laser ablation to remove the α-case from Ti-6Al-4V (Ti-64) bulk forgings was experimented [133–135]. Nanosecond pulsed laser ablation resulted in crack formation in the α-case layer and could be used as a rapid detection technique to identify the presence of α-case [136]. In most of above cited publications, on removing 60 to 80 µm thickness of material, the α-case layer is claimed to be completely removed. But, in the same set of articles the typical thickness of α-case is mentioned as 100 to 300 µm. From our experience with Ti alloys, the 80 to 300 µm should correspond to a transition zone (TZ) that bridges the α-case with the core of the sample. TZ possesses distinctive microstructural characteristics and its significance on the mechanical properties are yet to be fully understood.

Recent studies have confirmed the possibility of removing the α-case through various methodologies with their own sets of advantages and limitations. However, a comprehensive knowledge about the gradual changes in the α-case - TZ - core microstructure and its effects on the mechanical properties are yet to be substantially explored. In the present research work, LPBF-made Ti-5553 specimens subjected to heat treatment cycles are characterized with a special focus on the α-case region and the TZ. The corresponding microstructural features are correlated with the mechanical properties.

6.2 Experimental procedure

The methodologies elaborated in Chapter 3 are used in this study. Furthermore, the listed process parameter set were derived from systematic statistical optimization using Plackett-Burman fractional factorial design. The process parameter set is capable of consistently delivering high relative density (RD ≥ 99.9%) Ti-5553 prints, if the typical LPBF printing precautions are adhered. Since the outer surface of the printed specimens would suffer oxidation due to post heat treatment, unique contour process parameters were not used to print the periphery.

Table 6-1: LPBF process parameters used to print the cylindrical and tensile specimens

Laser Power (P)	**Scan speed (v)**	**Layer thickness (l)**	**Hatch Distance (d)**	$\mathbf{VED = \frac{P}{vld}}$
(W)	**(mm/s)**	**(mm)**	**(mm)**	**(J/mm^3)**
187.5	1089	0.06	0.11	26.08

Cube shaped samples sized 10 mm in length per side, for material characterization and cylindrical tensile samples (gauge length = 8 mm; gauge diameter = 4 mm) for mechanical properties evaluation were vertically printed in the z direction following a 67 ° rotated stripe scan strategy. Dimensions of the printed cylindrical tensile samples were slightly revised from ASTM E-8 [139] specified standard sub-sized specimen measurements (gauge length = 10 mm; gauge diameter = 2.5 mm) to align with the available LPBF printing setup and tensile testing facilities. Previous research works have modified the tensile test sample dimensions for convenience and the modifications did not affect the results [192,211].

The LPBF printed specimens were subjected to heat treatment cycles in an electric cold-wall retort furnace (Nabertherm VHT 40/18-KE), capable of sustaining up to 1800°C under ultra-high purity argon atmosphere. Initially, solution treatment (ST) was carried out at 800°C for 3 hours. Finally, aging treatment to facilitate the growth of finely dispersed lamellar α needles was executed at 600°C for 1 hour. The ST and aged samples were water quenched at the end of their respective holding times. The ST and aging temperature and duration were chosen based on a variety of heat treatment cycles experimented, as discussed in our prior work [212]. Water quenching is preferred over air cooling to limit β grain coarsening and to avoid any possibility of prolonged diffusion of oxygen atoms.

Heat treated cubic samples were used for microstructural investigations after conventional metallographic grinding and polishing in gradual steps upto 0.25 µm diamond suspension. Keyence VHX 7000 – Digital optical microscope and Tescan VEGA 3 scanning electron microscope (SEM) were used to observe the α case, TZ and the core microstructures at high magnifications. The ancillary energy-dispersive spectrometry (EDS) attachment integrated with the SEM was employed for elemental mapping. Electron backscatter diffraction (EBSD) samples prepared by means of a vibratory polisher (Buehler Vibromet 2) was used to study the differences in the distribution, size and morphology of the α precipitates within the β matrix at regions of interest. The step size during EBSD by Tescan VEGA 3 was fixed at 1 µm. Beam intensity was varied between 15 and 18 depending on the size of the α needles in that region.

Table 6-2: Sample surface preparation and geometry versus treatment condition

Sample condition	**Depth of surface machining**	**Final diameter of the samples**
	(mm)	**(mm)**
As-printed	-	4 ± 0.1
Heat treated (HT)	-	4 ± 0.1
HT + α case machined	0.05	3.9 ± 0.02
HT + α case and TZ machined	0.3	3.4 ± 0.02

Vickers microhardness measurements as per ASTM E384 [138], was performed using a Clemax CMT automated micro-hardness machine. A load of 200 gf was applied and a dwell time of 10 seconds was given for each indentations. Measurements were taken at an interval of 50 µm from the surface towards the core of the specimen. Uniaxial tensile tests were carried out using an Instron 8874 servo-hydraulic fatigue testing system. The Instron 2630-120 extensometer, capable of recording up to ±4mm travel was coupled to continuously record the axial deformation. The test was carried out at 0.45 mm/min in displacement control mode as per ASTM E8 [139]. A minimum of three specimens were tested for each one of the as-printed, heat treated (HT), HT + α case machined and HT+ α case and TZ machined as given in Table 6-2. The depths of machining were decided based on quantitatively measuring the α case thickness from OM and SEM characterization. The corresponding fracture surfaces were examined using Tescan VEGA 3 SEM.

6.3 Results

6.3.1 Variation in α case thickness based on heat treatment parameters

Near surface microstructures in the LPBF printed Ti-5553 specimens along the building direction, after heat treatment are shown in Figure 6-1. The surface and the subsurface of the as-printed specimen is also shown as a reference for the absence of α case. On heat treatment, a hard and brittle oxygen enriched α case layer is clearly observed. The α case layers seen after ST for 3 hours and the following 2 hours of aging (A) are compared with each other. From quantitative measurements, it is understood that the collective thickness of the α case and the TZ is considerably altered based on the number of heat treatment cycles and temperature. For example, the α cases of aged specimens were relatively thicker than the ST specimens. Similarly, thickness of the α case increased with temperature. All the specimens were water quenched to avoid any differences in the α case thickness introduced by the effect of varied cooling rate.

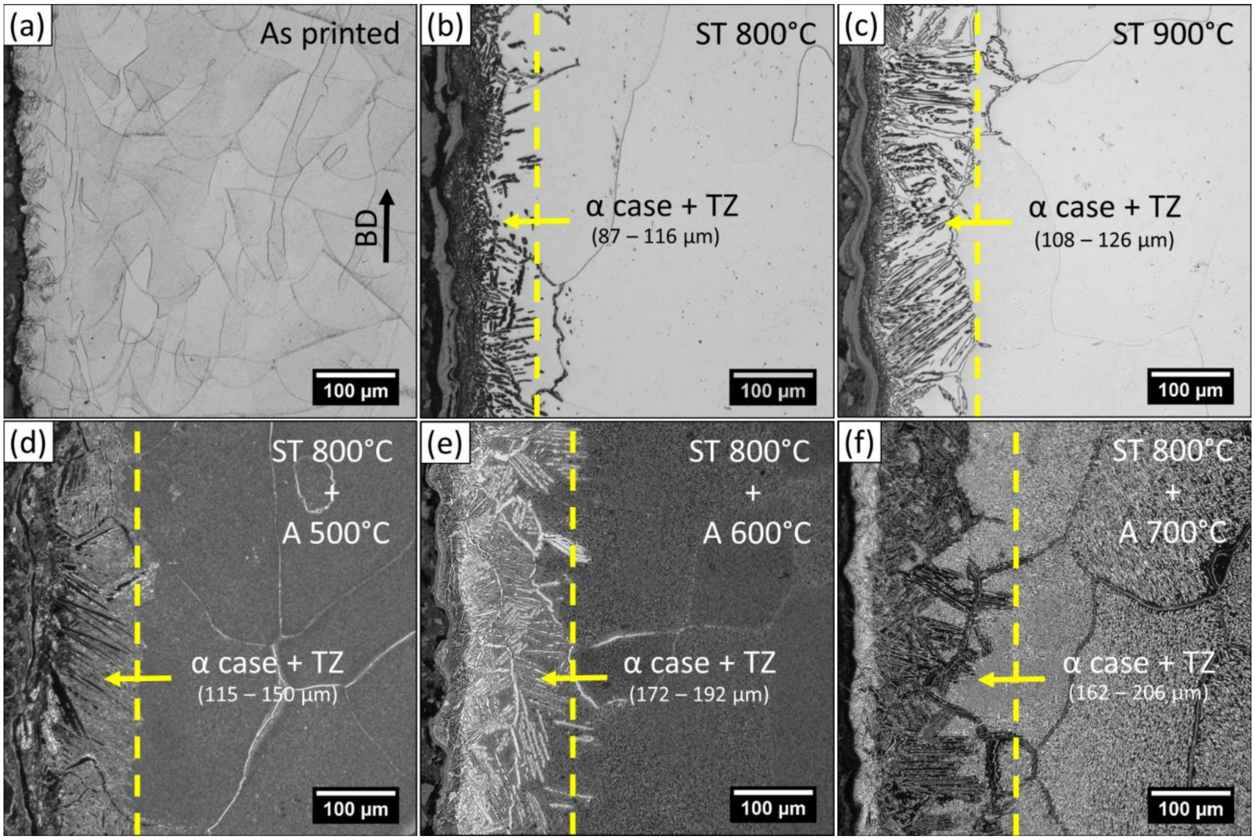

Figure 6-1: Peripheral microstructure of LPBF-made Ti5553 alloy along the building direction in (a) as-printed condition (b) ST for 3 hours at 800°C (c) ST for 3 hours at 900°C (d) aged for 2 hours at 500°C (e) aged for 2 hours at 600°C and (f) aged for 2 hours at 700°C

6.3.2 Microstructurally distinct α case regions

Microstructural differences between the core and the periphery of a heat treated specimen along the scanning or transverse direction is shown in Figure 6-2(a). The core microstructure is finely distributed lamellar α particles precipitated in β matrix, which is as expected after solutionizing at 800°C for 3 hours followed by aging at 600°C for 2 hours. However, the microstructure along the periphery is distinct, with a high volume of second phase particle precipitation as in Figure 6-2(b). At higher magnifications, the distinct peripheral microstructure could be further classified into four different regions as TiO_X film (8±3 µm), α case (27±5 µm), TZ – 1 (39±4 µm) and TZ – 2 (55±16 µm) based on the size, distribution and the morphology of the identified α precipitates.

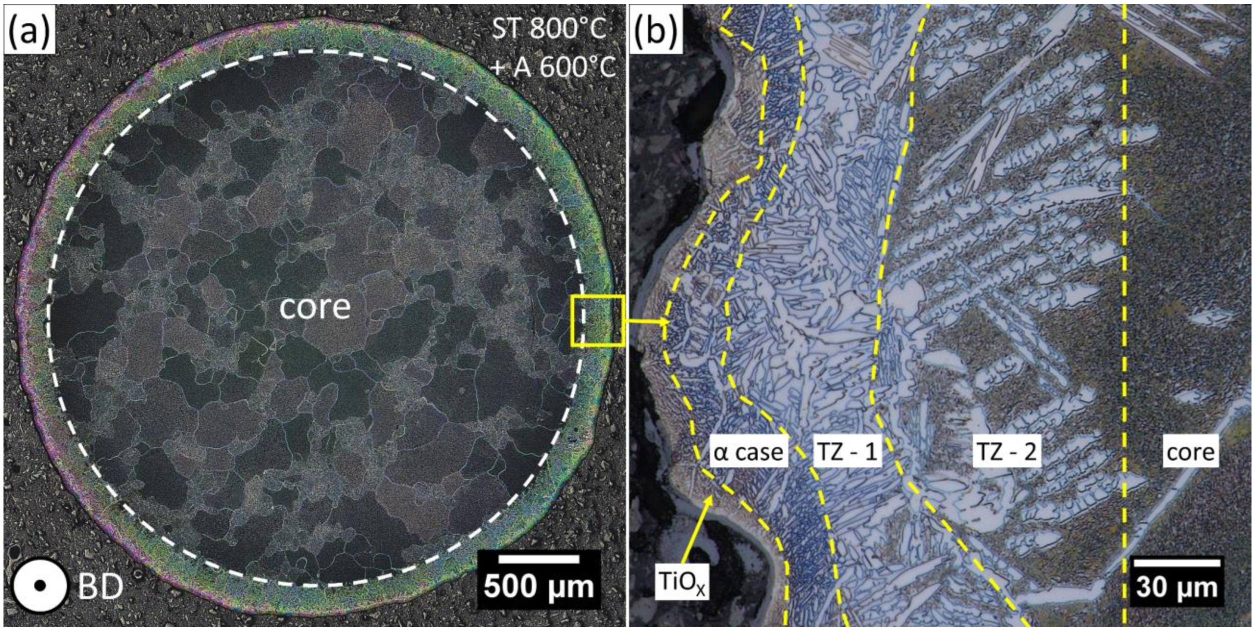

Figure 6-2: Cross-sectional microstructure of LPBF-made and heat treated Ti5553 alloy (a) overall microstructure (b) peripheral microstructure at high magnification

In the α case region, the identified second phase needles were extremely fine, short and closely packed. Length of each needle like particles in the α case region ranged 2.7±1 µm. Nonetheless, in TZ – 1 the observed α particles were thicker, longer and loosely packed compared to the outer α case region. Length of the α needles in TZ – 1 ranged 17±8 µm. In the TZ – 1 region, the identified α needles were mostly extended throughout the width of region. In certain cases, intermittently broken chevron-like α needles were also present. In TZ – 2, the α needles were the longest, ranging 67±24 µm, and predominantly broken into several segments. Similar fragmented α needles were previously hypothesized as a consequence of multiple site nucleation from ω particles [184].

6.3.3 Grain boundary dependency of α case regions

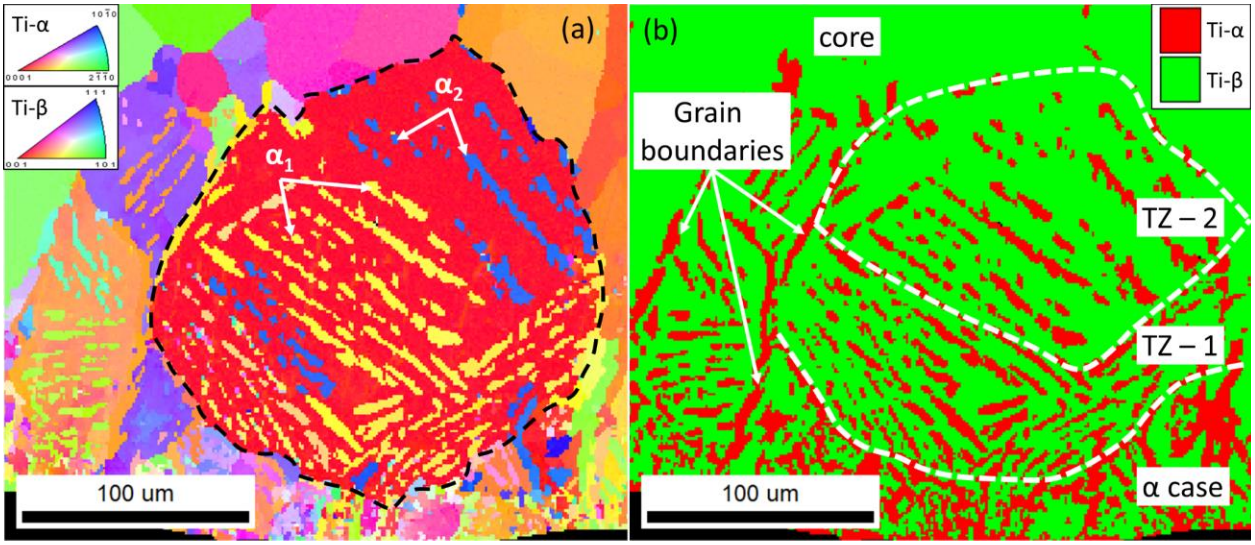

Figure 6-3: (a) Crystallographic orientation map (b) phase distribution map

EBSD analysis at the α case and TZ regions showing the insights of grain boundaries in α case precipitation kinetics is given in Figure 6-3. Lamellar α needles of two different variants (α_1 and α_2) identified in majority within a β grain is presented in Figure 6-3(a). The corresponding phase distribution map in Figure 6-3(b) shows the α precipitates accumulated at the grain boundaries, and the gradual transition in the morphology of α precipitates at the α case, TZ – 1, TZ – 2 and core regions. TZ – 2 region was distinctly identified from the dendrites-like intermittently broken α needles. It is to be noted that the α case boundaries are aligned nearly parallel to the grain boundaries and are not controlled by the surface boundary. The labelled α case boundaries not being parallel to the surface indicates the role played by the structure of the parent β grains in α precipitation. Area fraction of the α precipitates in the mapped region is 9±1%.

6.3.4 Microhardness and diffused oxygen measurements at the α case regions

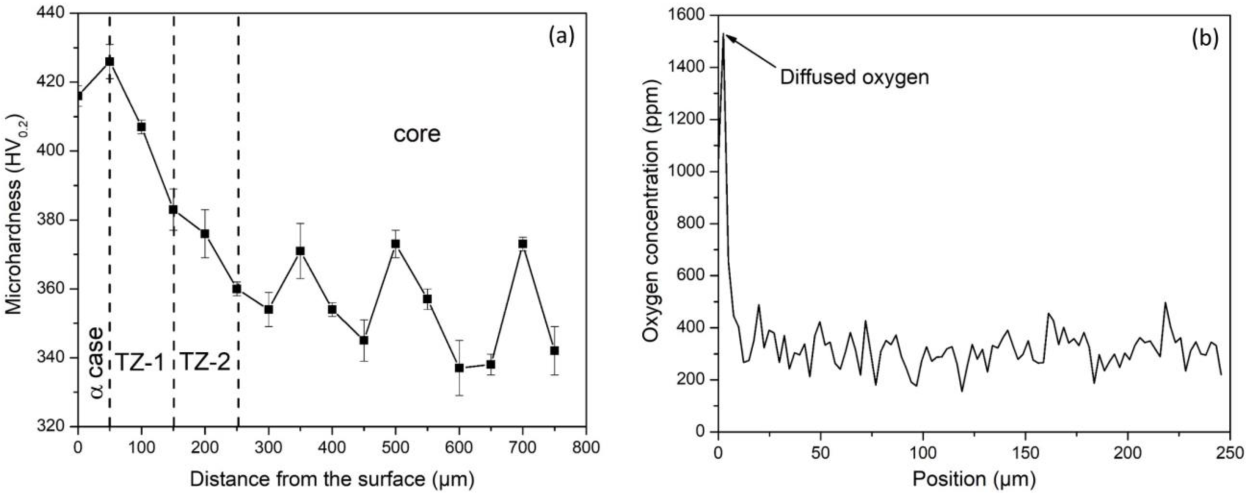

Figure 6-4: Observed changes across the peripheral cross-section after heat treatment cycles (a) Microhardness profile (b) elemental oxygen concentration profile

Vickers microhardness measurements taken across the contour – core interface is given in Figure 6-4(a). Except the oxidized TiO_X outer film, the remaining microstructurally distinct regions identified in Figure 6-2(b) are approximately discerned here. In the α case region, microhardness values are at its peak ranging 413 to 421 HV. In the adjacent TZ – 1 and TZ – 2 regions, the microhardness values are slightly lower, ranging 431 to 377 HV and 383 to 352 HV respectively. A similar trend in across the contour – core interface can be found in Ti alloys in which a high hardness at the α case region drastically decreases to a rather stable hardness within few hundreds of micrometers, reported elsewhere [130,210]. EDS analysis at the contour – core interface presented in Figure 6-4(b) showcases the spike in oxygen concentration near the surface. Similar presence of a high oxygen concentration in the α case region is well known [36,89].

6.3.5 Poor tensile test properties – with α case regions

Uniaxial tensile test results of the specimens subjected to solution treatment at 800°C followed by aging at 500 to 700°C for 2 hours encompassing the α case layers are compared with the as-printed specimen in Figure 6-5. Even though the elastic region of the heat treated specimens are similar to the as-printed specimen, the plastic deformation behavior is vastly different. When the as-printed specimen exhibit a superior ductility withstanding a total elongation of 23±8%, the heat treated specimens endured negligible plastic deformation. Tensile strength and ductility of the heat treated specimens, irrespective of the heat treatment temperature were severely affected despite the finely distributed lamellar α microstructure in the core section.

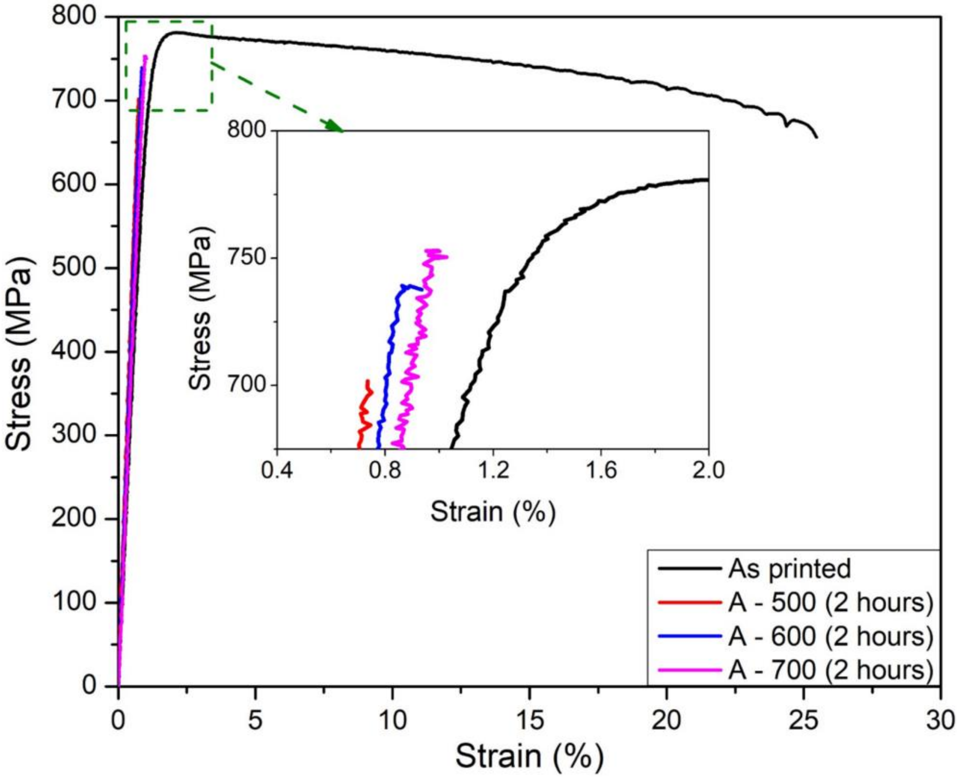

Figure 6-5: Tensile test results of LPBF-made Ti5553 alloy with α case regions

6.3.6 α case – fracture surface correlation

A direct comparison between the identified α case and TZ layers from the microstructural images with the fracture surface is in Figure 6-6. As the thickness of the α case regions is proportional to the heat treatment temperature, the highest temperature heat treatment cycle – ST at 800°C followed by aging at 700°C is chosen for characterization. The collective thickness of the α case and the TZ (179 to 248 µm) in Figure 6-6(a), approximately matches with the brittle outer region (220 to 305 µm) on the fracture surface in Figure 6-6(b).

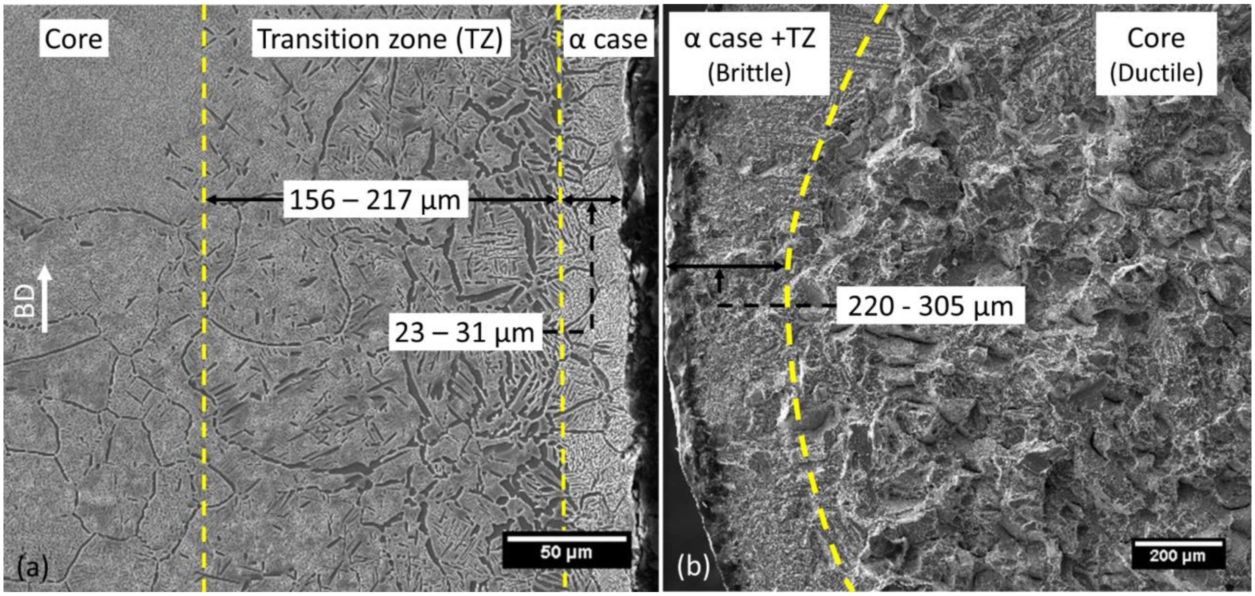

Figure 6-6: (a) SEM measurements of α case and TZ layers in ST specimen, (b) fracture surface exhibiting a brittle fracture at the outer region

Tensile properties exhibited by the LPBF printed and heat treated Ti-5553 specimens, with and without the α case and the TZ layers are compared with that of the as printed specimens in Figure 6-7. ST at 800°C for 3 hours and aging at 600°C for 2 hours is the applied heat treatment. Specimens were quenched at the end of ST and aging cycles. Surface turning 0.1 mm and 0.6 mm from the gauge section of the heat treated specimens corresponds to the α case machined off and α case + TZ machined off conditions respectively.

6.3.7 Improved tensile test properties – without α case regions

The as printed specimens exhibited an exceptional ductility of 30±5% but the tensile strength is limited to 780±10 MPa. The limited tensile strength is due to the absence of lamellar α precipitates as reported in our previous publication [137]. In the heat-treated condition, even though finely distributed secondary lamellar α needles were identified throughout the microstructure, the tensile strength (750±20 MPa) and the ductility (2±0.5%) were severely affected. The poor tensile properties in the heat treated condition could be a result of the hard and brittle α case layers [36]. On machining off the α case and the TZ layers (to a final diameter of 3.4 mm), a significantly improved ultimate tensile strength, reaching up to 1360±14 MPa along with an acceptable total elongation of 11±4% were observed. On machining off only the α case (to a diameter of 3.9 mm) a further increase in the UTS, reaching up to 1410±8 MPa is observed. However, the corresponding ductility is limited to 2±0.5% which is unacceptable.

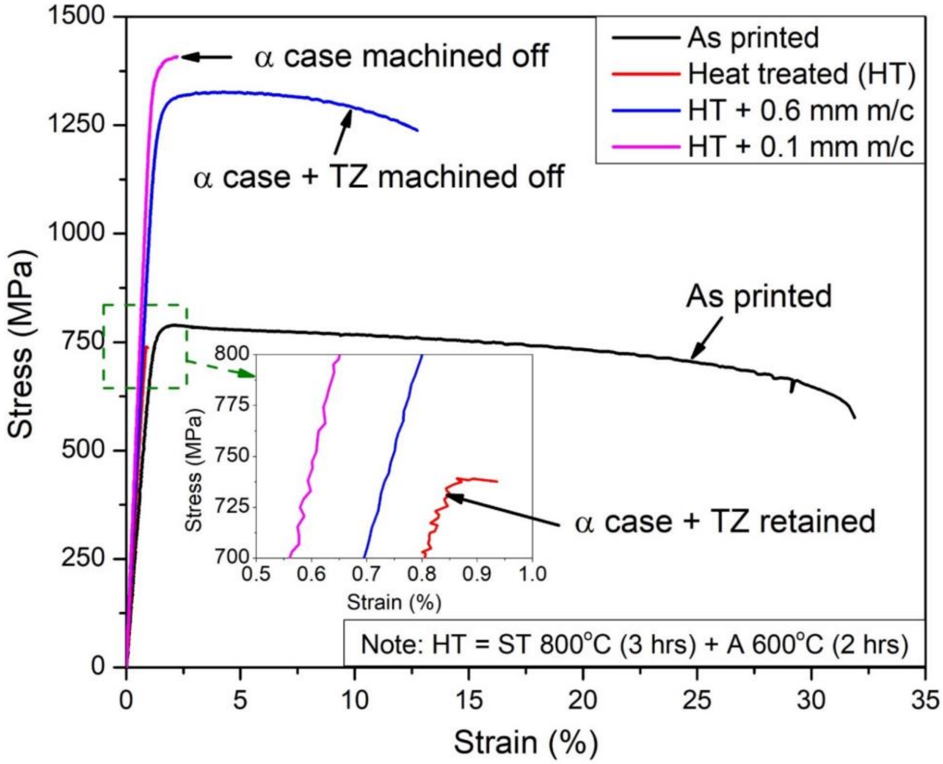

Figure 6-7: Tensile test results of LPBF-made and heat treated Ti5553 alloy at different levels of surface machining

6.3.8 Fractography

The fracture surfaces from the α case + TZ removed and the α case removed conditions are in Figure 6-8. In both the cases, the fracture is predominantly intergranular at the core region.

However, a major difference is observed between the contour regions. An extensive shearing on the α case + TZ removed fracture surface observed is absent in the α case removed condition.

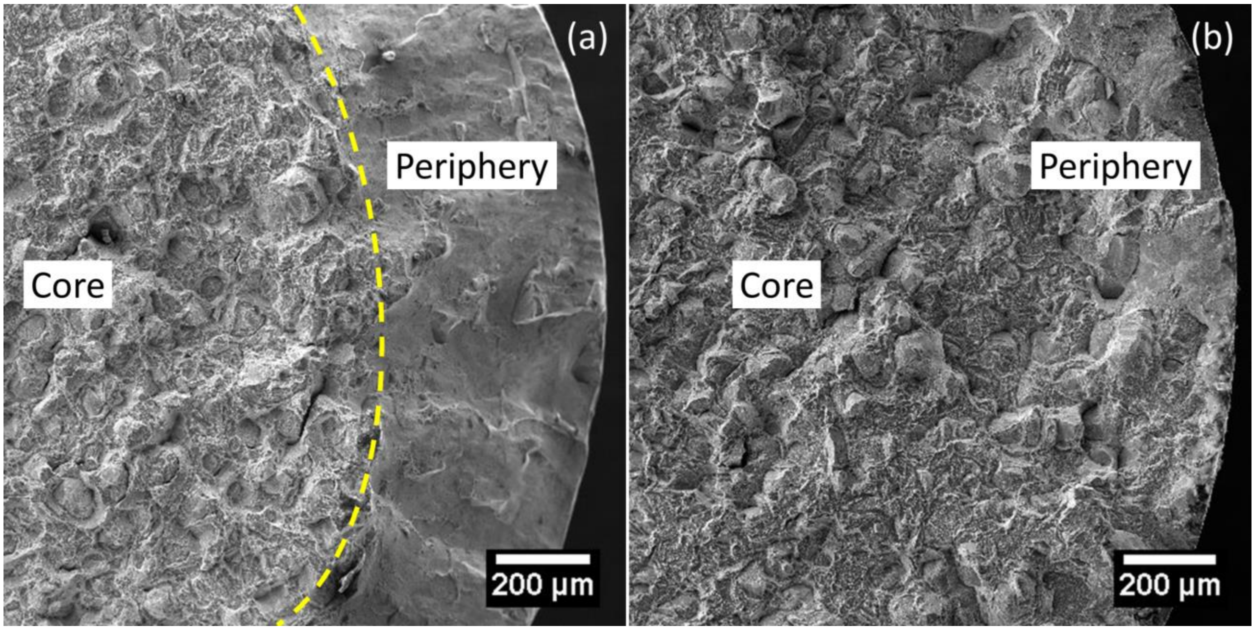

Figure 6-8: Fracture surfaces of heat treated, machined and tensile tested specimens (a) only α case removed (b) α case + TZ removed

6.4 Discussion

The current results show that isothermal heat treatment on LPBF-made Ti-5553 in the range of 500 to 900°C, causes the growth of α case at the periphery which severely affects the tensile properties. Thickness of the identified α case regions in Figure 6-1 depends on the heat treatment temperature, duration and the number of heat treatment cycles. A parabolic trend in the thickness of the α case as a function of heat treatment temperature and the duration is previously reported for Ti-64 alloy [213]. The well-known chemical affinity of Ti towards interstitial elements multiplies exponentially at higher temperatures resulting in the diffusion of elemental nitrogen and oxygen. Oxygen, being a strong α stabilizer, promotes development of a deleterious α case on heat treating Ti alloys at temperatures exceeding 480°C [130,214]. Beottinger *et al.* extracted the temperature-time data from the heat flow simulation of Ti-64 alloy investment castings and coupled it to a simple model that predicts the diffusion of oxygen into the β phase with a 95% accuracy [89]. The activation energy for the diffusion of oxygen in Ti-6Al-2Sn-4Zr-2Mo (Ti-6242) alloys is estimated as 203 to 244 kJ/mol [213,214]. Although this is a relatively high activation energy, the long heat treatment times at high temperature promote extensive oxygen diffusion to the surface.

The microstructural distinction between the four peripheral regions are shown in Figure 6-2. The outer oxide film is a result of the exposure to atmospheric gases at high temperature while quenching. Gaddam *et al.* characterized a similar oxide scale within the α case region, on heat treated Ti-6242 alloy as TiO2, and the EDS analysis suggested the presence of Al, O and similar α stabilizers near the surface [36]. Further characterization reported in several other articles has led to the observation of either a dense or a porous oxide scaled layer which were outcomes of different diffusion and cooling rates driven oxidation kinetics [214–217]. The presence of an oxide layer is reported to affect the tensile properties in Ti alloys, especially the ductility [218].

Next to the oxide layer, an extremely fine and closely packed α platelets rich region was observed in Figure 6-2(b). A high level of vanadium, which is a β stabilizer is detected through microprobe analysis at the α case region between the platelets [89]. The high concentration of alloying elements is expected to be an outcome of the localized elemental segregation caused by the rapid super saturation of α needles aided by the diffused oxygen atoms during quenching. The rapid cooling rate is also a cause for the short α needles in this region. However, in the TZ – 1 region, the longer and thicker lamellar α needles suggests a slower cooling rate on comparison with the α case region. The effect of cooling rate on the growth of α precipitates is well established [8]. Since the precipitation of second phase particles is better facilitated at lower cooling rates, an extended elemental segregation might be effected in this region resulting in the rather spaced out α needles. The intervals between the α needles in this region are Al depleted regions which would be rich in β stabilizing elements.

In the TZ – 2 region, α needles are even longer and distanced far apart from each other compared to the TZ – 1 region. Additionally, intermittent discontinuities were observed in the long α needles identified. Such fragmented plate morphology α precipitates are referred as blocky grain boundary α particles in open literature. The blocky grain boundary α precipitates are comparable to the grain boundary allotriomorphs observed in the precipitation of diffusion-controlled transformation of austenite to ferrite in carbon steels [8]. Simultaneous inhomogeneous nucleation of the second phase precipitates at high surface energy sites result in blocky grain boundary α needles. Similar blocky grain boundary α needles in Ti-7333 alloy are accompanied by an increased concentration of molybdenum. The slow diffusing character of Mo causes an increased precipitation driving force, which results in the nucleation of α phase by means of the defects such as dislocations and sub-grain boundaries [219].

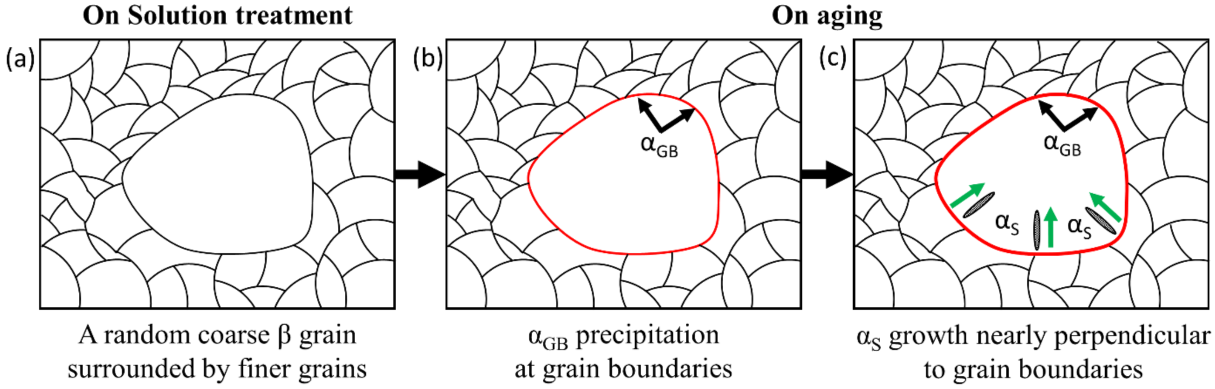

Figure 6-9: Schematic representation of the secondary α particle growth perpendicular to the grain boundaries

EBSD scanning at the α case region encompassing a coarse β grain, sized approximately 200 µm and surrounded by finer β grains is given in Figure 6-3. While the orientation of the α needles is observed in Figure 6-3(a), the morphology and the distribution of the α needles within the coarse grain of interest is of focus in Figure 6-3(b). Pang *et al.* identified different α variants distributed in a β grain and indicated the Burgers orientation relationship (BOR) between them as {011}β || {0001}α, <111>β || <11$\bar{2}$0>α [220]. The α2 variant in Figure 6-3(a), oriented in <10$\bar{1}$0> within the β grain oriented in <001> is expected to be an effect of the elemental diffusion of vanadium into the α precipitates. Bagot *et al.* examined α case formation in Ti-64 alloy with Atom Probe Tomography (APT) and characterized two different variants of lamellar α particles. It was claimed that one of the variants, α2 was rich in vanadium [216]. Furthermore, the precipitation mechanism of α needles established in the literature suggests the growth of α needles from the grain boundaries into the grain as represented in Figure 6-9 [221]. Initially, the α particles segregate at the grain boundaries, termed as αGB. Gradually, the growth of secondary α needles - αs is facilitated in the directions perpendicular to the grain boundaries as shown. An extended growth of the αs results in a basket weave pattern of secondary α cluster. As the growth of the α needles is in reference with the grain boundaries, the thickness of the α case layers were also relative to the grain boundaries as marked in Figure 6-3(b).

Microhardness measurements across the α case and TZ regions are given in Figure 6-4(a). Based on the changes in the slope of the microhardness curve combined with the measured thicknesses of each regions from Figure 6-2(b), the α case regions are marked. Compared to the core section, the α case and the TZ – 1 region exhibit a higher hardness range. The higher hardness is due to the higher area fraction of lamellar α needles in these regions. However, the hardness measurements at TZ – 2 are similar to the hardness readings at the core due to the effect of the spaced out α needles discussed previously. The elemental concentration of oxygen extracted from the EDS data at the periphery is given in Figure 6-4(b). A spike in the concentration of oxygen upto a thickness of 10 to 15 µm from the surface, which is relatable to the TiOx thickness quantified from Figure 6-2(b).

Several research works have reported the relationship between the diffused oxygen content and the microhardness values in Ti alloys. While earlier reports suggested a parabolic dependency between them, the recent reports have claimed a linear correlation [89,222]. Plate thickness, chemical affinity of the alloying elements also the factors that affect the oxygen content – microhardness relationship [90]. In addition to the near surface spike in oxygen concentration, it could be seen from Figure 6-4(b), that approximately 300 ppm of oxygen is present throughout the specimen. The source of this residual oxygen could be high temperature existed either during the plasma atomized powder manufacturing or the LPBF printing. Similar oxygen diffusion leading to a 500 µm thick α case was reported in Ti investment castings with Al2O3 mold [210]. Yet, as the α case was absent in the as-printed condition and no noticeable depletion is identified in the 300 ppm oxygen content, the influence of the residual oxygen in α case formation is considered to be negligible.

The uniaxial tensile test results shown in Figure 6-5 reveal a severe loss in ductility of Ti-5553 specimens on heat treatment. The corresponding peripheral microstructure and the fractured surface in Figure 6-6 observed under SEM, reflects the effect of hard α case regions discussed in Figure 6-4(a). Similar hard outer ring leading to brittleness under tensile or fatigue loading was previously encountered in several instances while thermally processing Ti alloys [67,210,223,224]. The mechanism of failure in Ti-5553 with lamellar α dominant microstructure is driven by localized strain [46]. The strain induced intrinsic damage of the α precipitates cause an exponential accumulation of micro-voids in the deformation band [225]. Poor surface characteristics leading to inferior mechanical properties is also well established in the literature

[36,135,216–218]. Under tensile stresses, the high area fraction of near sub-micron scaled α particles in the α case, undergoes severe localized strain which would activate multiple fracture initiations effecting in the inferior ductility observed in Figure 6-5. Thus, the fracture propagates at considerably lower stresses irrespective of the core microstructure, whereas the deformation mechanism in the TZ zones is marginally different. In TZ – 1 and TZ – 2 regions, due to a considerable presence of β phase particles in addition to the long α needles, the dislocation slipping must be the dominant deformation mechanism [226]. Therefore, even if the shearing direction of α platelets multiply, the slipping system of the β matrix would remain unique. Accordingly, the removal of α case improved the tensile strength, but not the ductility. Further removal of the TZ regions resulted in the improving both the tensile strength and the ductility as seen in Figure 6-7. The improved tensile properties are comparable to the properties expected in Ti-5553 with finely distributed lamellar α microstructure.

6.5 Summary and conclusions

In the present work, effect of α case on LPBF-made and isothermally heat treated Ti5553 is studied. Heat treatments were carried out at 500 to 900°C temperature range in Argon atmosphere followed by water quenching. The cross sectioned specimens were characterized using OM, SEM and EBSD. The effect of the identified microstructural features were correlated with the corresponding mechanical properties through microhardness and uniaxial tensile tests.

1. The thickness of the α case region is proportional to the heat treatment temperature and the number of cycles.
2. Four distinct microstructural regions were identified within the detrimental α case. They are the outer 8±3 µm thick TiO_X film, a region of sub-micron sized and closely arranged α

needles, a region of loosely packed continuous α needles in a β matrix and finally a region of widely spaced and intermittently broken lamellar α needles.

3. Energy dispersive spectroscopy (EDS) revealed the diffusion of oxygen up to a depth of 15 µm which could have resulted in the observed α case regions. Different ranges of microhardness readings across the distinct peripheral regions signify the presence of a hard, brittle and detrimental outer case.
4. Tensile properties were severely affected due to the presence of hard and brittle α case regions. On machining the α case and the transition zones (0.6 mm), the tensile strength improved to 1325±19 MPa with a total elongation of 12.7±0.8%, with uniform ductile fracture form edge to core.
5. Further improvement in the tensile strength up to 1402±11 MPa is achieved by removing only the α case (0.1 mm) but the total elongation was limited to 2±0.5%. The fractured surface reveled traces of brittleness at the periphery.

Chapter 7: Anisotropic behavior of LPBF-made Ti5553 parts

This chapter addresses the fifth objective, which is the possibility of improving the tensile properties by engineering the building direction with respect to the loading direction. The majority of this chapter is adapted from the manuscript: '*N. Ramachandiran, H. Asgari, F. Dibia, R. Eybel, A. Keshavarzkermani, A. Gerlich, E. Toyserkani, Anisotropic tensile behavior of laser powder-bed fusion made Ti5553 parts, Mater. Sci. Eng. A. 865 (2023) doi:10.1016/j.msea.2023.144633.*

7.1 Introduction

Rapid heating and cooling cycles in the LPBF process inevitably lead to directional solidification that promotes epitaxial grain growth, resulting in columnar prior β grains along the building direction [227]. Generally, <100> is reported as a preferred grain growth direction for LPBF processed metastable β-Ti alloys. Such a preference leads to anisotropic behavior, which leads to variation in properties when evaluated in different directions [30,228]. Anisotropy is undesired from a design perspective and could be a major influence in restricting the extensive use of the printed parts without post-processing [227,229]. Anisotropy is prominent in Ti alloys as the hexagonal close-packed (HCP) materials are highly prone to the crystallographic slip – deformation twinning interactions [230,231].

Nevertheless, by carefully engineering the building direction in reference to the loading direction, the adversely regarded anisotropy had been intended to improve the mechanical properties in several studies through different approaches [232]. The angle between the loading direction and the grain growth is vital in activating the respective slip systems. In vertically printed β-Ti samples, typically {110}<111> is the only dominant slip system resulting in work softening [233,234]. The horizontally printed Ti-5Al-5V-5Mo-3Cr-0.5Fe samples exhibit an enhanced work hardening ability, as slip band interactions are higher owing to additional {112}<111> slip systems being operative [104]. The added active slip systems enhanced work hardening behavior, leading to improved ductility. Porosity in the printed parts is another issue which leads to anisotropy, since voids can act as stress risers and are probable locations for failure initiation and hence inferior properties.

Recent studies have confirmed the possibility of achieving improved mechanical properties in LPBF-made Ti parts by horizontally printing the samples [30,177,228,232,233,235–238]. However, a comprehensive understanding of the microstructural features involved in fracture mechanics during uniaxial tensile testing is yet to be resolved. In this chapter, LPBF-made samples printed in vertical and horizontal directions were subjected to interrupted tensile tests, which were terminated at strain levels ranging between 5 to 15%. One set of samples is tensile tested until complete fracture. The partially strained samples were subjected to microstructural characterization, and the corresponding features significant to the fracture propagation were evaluated.

7.2 Experimental procedure

Using the plasma atomised Ti5553 powders and following the methodology described in Chapter 3, cylindrical tensile samples of 8 mm gauge length and 4mm gauge diameter were printed both vertically and horizontally, as shown in Figure 7-1(a). The geometrical measurements of the printed cylindrical tensile specimens is in Figure 7-1(b).

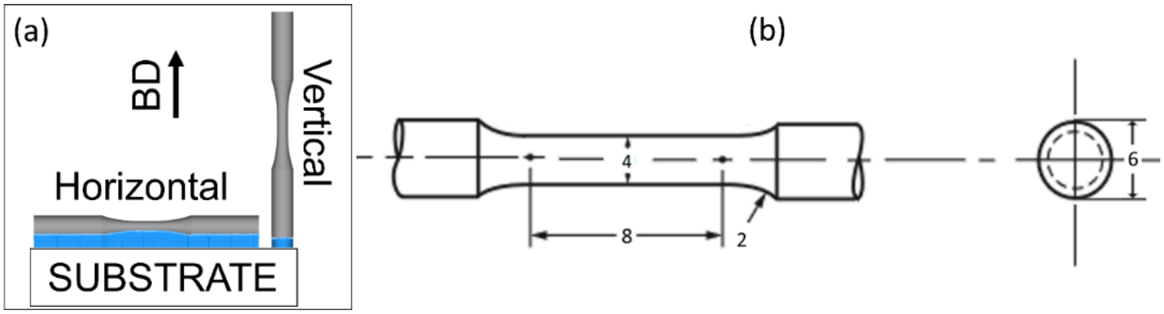

Figure 7-1: Schematic diagram showing (a) Horizontal and vertical printing directions (b) Geometry of the tensile specimens

Process parameter set used to print the specimens are listed in Table 7-1. Contour layer microstructures are found in the 0.2 to 0.3 mm thick surface region of the samples, where a distinct set of LPBF process parameters are applied to achieve a good surface finish and limit microstructural heterogeneities caused by different thermal gradients [25,137].

Table 7-1: LPBF process parameters used to print the specimens

Location	**Laser Power (P)**	**Scan speed (v)**	**Layer thickness (l)**	**Hatch Distance (d)**	$\mathbf{VED = \frac{P}{vld}}$
	(W)	**(mm/s)**	**(mm)**	**(mm)**	**(J/mm^3)**
Core	187.5	1089	0.06	0.11	26.08
Contour	175.6	841	0.06	0.11	31.64

Surface roughness measurements were carried out using a Keyence VK-X250K/X260K laser profilometer with an integrated VK-H1XME multifile analyzer package following JIS B0601:2001 standard. A minimum of five measurements were carried out at different locations within the gauge section of the printed tensile specimens.

Uniaxial partial tensile tests were carried out using an Instron 8874 servo-hydraulic fatigue testing system as per ASTM E8. The load was applied at a rate of 0.45 mm/min in displacement control mode. An Instron 2630-120 extensometer, with a maximum range of ±4mm travel, was used to record the displacement. The tests were prematurely terminated at three different strain levels (low, medium, and high) corresponding to 5, 10 and 15%. A minimum of three specimens were tested for each one of the strain levels for both horizontal and vertical printed conditions. A set of standard uniaxial tensile tests up to the complete failure was also carried out to analyze the fracture surface.

The deformed samples were axially dissected using wire electrical discharge machining (EDM) cutting followed by conventional metallographic preparation, chemical etching using Keller's reagent and microstructural characterization. The metallographic sample preparation involved grinding in steps up to #4000 SiC paper followed by diamond suspension polishing up to 0.25 µm. Finally, a Buehler Vibromet 2 polisher was used to attain strain-free surfaces required for advanced characterization. Microstructural examinations were carried out using Keyence VHX 7000 – digital optical microscope. The fracture initiation, growth and propagation were characterized using Tescan VEGA 3 scanning electron microscope. Electron backscatter diffraction (EBSD) analysis was carried out to correlate the grain characteristics with the fracture mechanics. A step size of 2.5 µm and an accelerating voltage of 20 kV were set during EBSD by Tescan VEGA 3 SEM system.

7.3 Results

7.3.1 Partial tensile tests

While analyzing fracture surfaces of tensile tested specimens, key information on the role played by various microstructural features on fracture initiation and growth might be overlooked. Alternatively, interrupted tensile tests, which are deliberately unloaded at different strain levels before fracture, could be a simple yet effective approach to preserve most of such fracture mechanics information. Previously reported findings from interrupted or in-situ tensile tests available in the open literature are highly revealing in terms of understanding the corresponding deformation mechanisms to a substantial extent [177,192,239,240]. In Figure 7-2, tensile plots generated from the partial tensile tests (three samples per strain level were tested) and one set of their respective cross-sectional microstructures provide some information regarding fracture initiation. The stress-strain response of these specimens are repeatable and comparable to the previous studies on LPBF-made Ti-5553 [9,29,64]. The elastic limit is reached within 1 to 2 % of the total strain, and the slope of the curves followed a negative trend after yielding, which is a common characteristic of most metastable β-Ti alloys [9,29,137]. Since work hardening is negligible, the yield strength (YS) and ultimate tensile strength (UTS) values are quantitatively similar and hence the YS is clearly distinguished from the UTS value. The vertical specimens exhibited a UTS of 780±10 MPa, whereas the horizontal specimens withstood higher stresses upto 846±6 MPa. On continued loading until complete fracture, the vertical specimens exhibited a marginally higher total elongation of 23±3 % compared to the 21±2 % exhibited by the horizontal specimens.

Cross-sectional microstructure of the strained specimens is shown in Figure 7-2(b). The major microstructural difference between them is the orientation of the columnar grains, caused by the difference in their building directions (BD). In the vertical specimens, columnar grains were parallel to the loading direction (LD), whereas, in the horizontal specimens, they were perpendicular to the LD. Necking is observed in both the specimens, consistent with the decreasing trend in stress level with strain at each of the 5% strain intervals. Multiple fracture initiation points are observed on both the specimens as marked. In the vertical specimen, most of the identified fracture initiation spots were at the surface and propagated nearly perpendicular along the cross-section. In the horizontal specimen, fracture initiation spots were also observed at the surface but the propagation seems to be suppressed even though the strain level is the same as in the vertical specimen. Microstructural defects, including porosities in the specimens, were least influential in prompting the fracture.

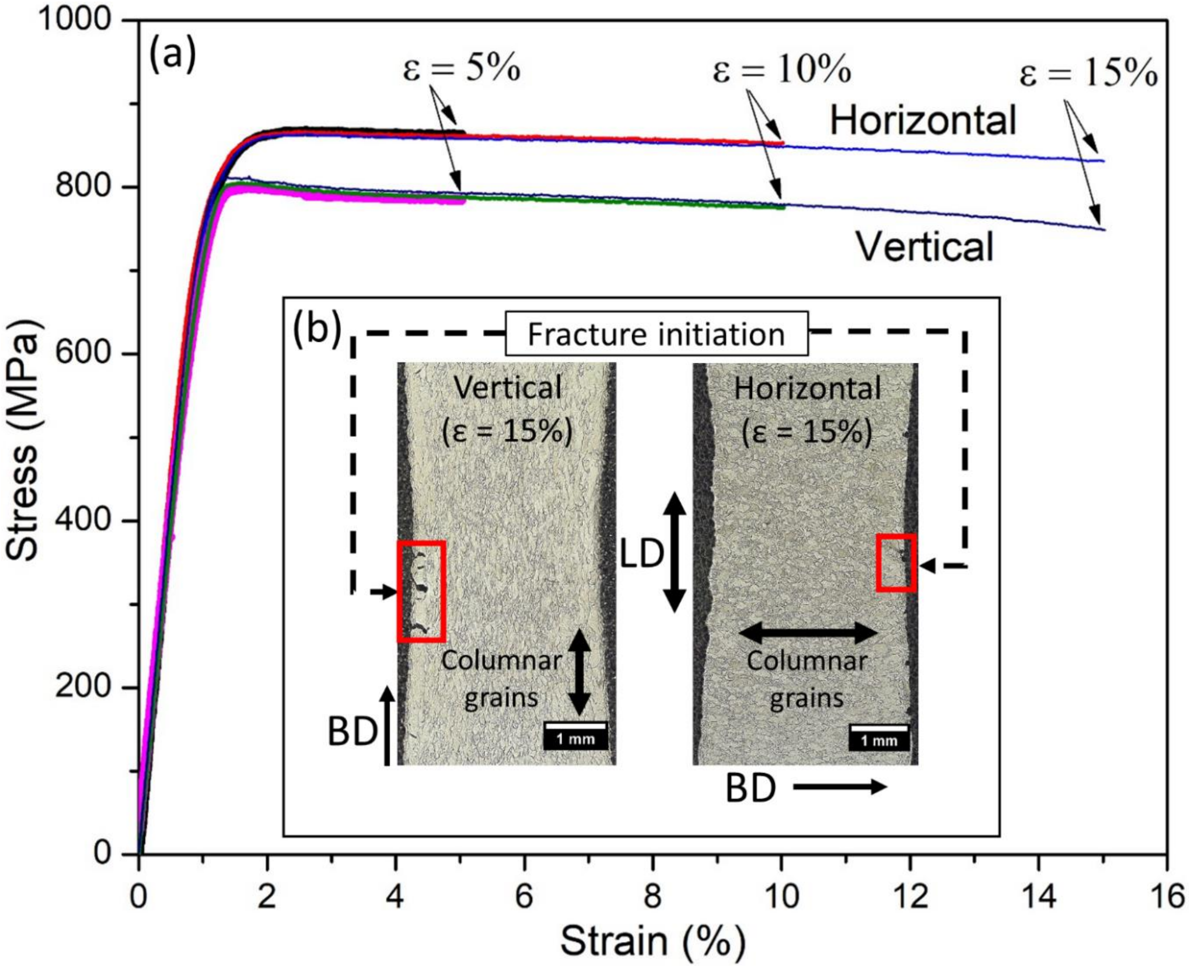

Figure 7-2: Interrupted tensile test results showing (a) partial engineering stress-strain curves (b) cross-sections of the gauge section indicating fracture initiation spots after 15% elongation

7.3.2 Surface roughness mapping

Surface condition is critical in controlling the tensile and fatigue properties. Surface roughness measurements taken at the gauge section of the specimens prior to the partial tensile tests are in Figure 7-3. In each one of these measurements, a 700 × 500 μm^2 surface area was covered. The results were analyzed to give an overall representation of the surface condition and quantitative surface roughness. As a result of the specifically fine-tuned contour process parameters given in Table 7-1, a smooth surface (with an arithmetical mean height of $R_a = 8 \pm 3$ µm) on both the specimens was achieved. However, as denoted by the arrows, several sharp protrusions ranging 80 to 130 µm in height were identified. These fine and sharp protrusions typically originate from partially melted powder particles that are superficially welded to the surface, and remain even after sand blasting the LPBF component. The corresponding peak to valley profile roughness, R_z was 90±30 µm. High R_z values in the as-printed condition is previously reported for Ti-5553 [32].

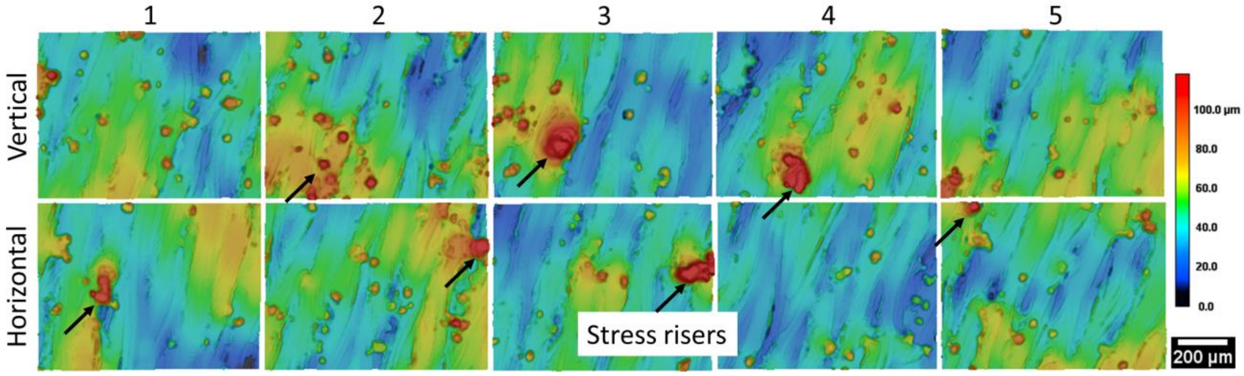

Figure 7-3: Surface roughness measurements at five different regions of the gauge section

7.3.3 Optical microscopy

The transverse section of the vertical and horizontal specimens focusing on the laser scan tracks are shown in Figure 7-4, corresponding melt pools and the subsequently solidified powder particles. The laser scan tracks are clearly evident on the vertical specimen and are comparatively more informative as its building direction is perpendicular to the plane of interest. The arbitrary boundary between the core and contour sections in the vertical specimen [Figure 7-4(a)] is marked in red colored dashed lines. Within the contour section, an optimized zig-zag pattern of laser track movement is clearly revealed. In the horizontal specimen, a smooth defect-free transition from the core to contour region can be noted.

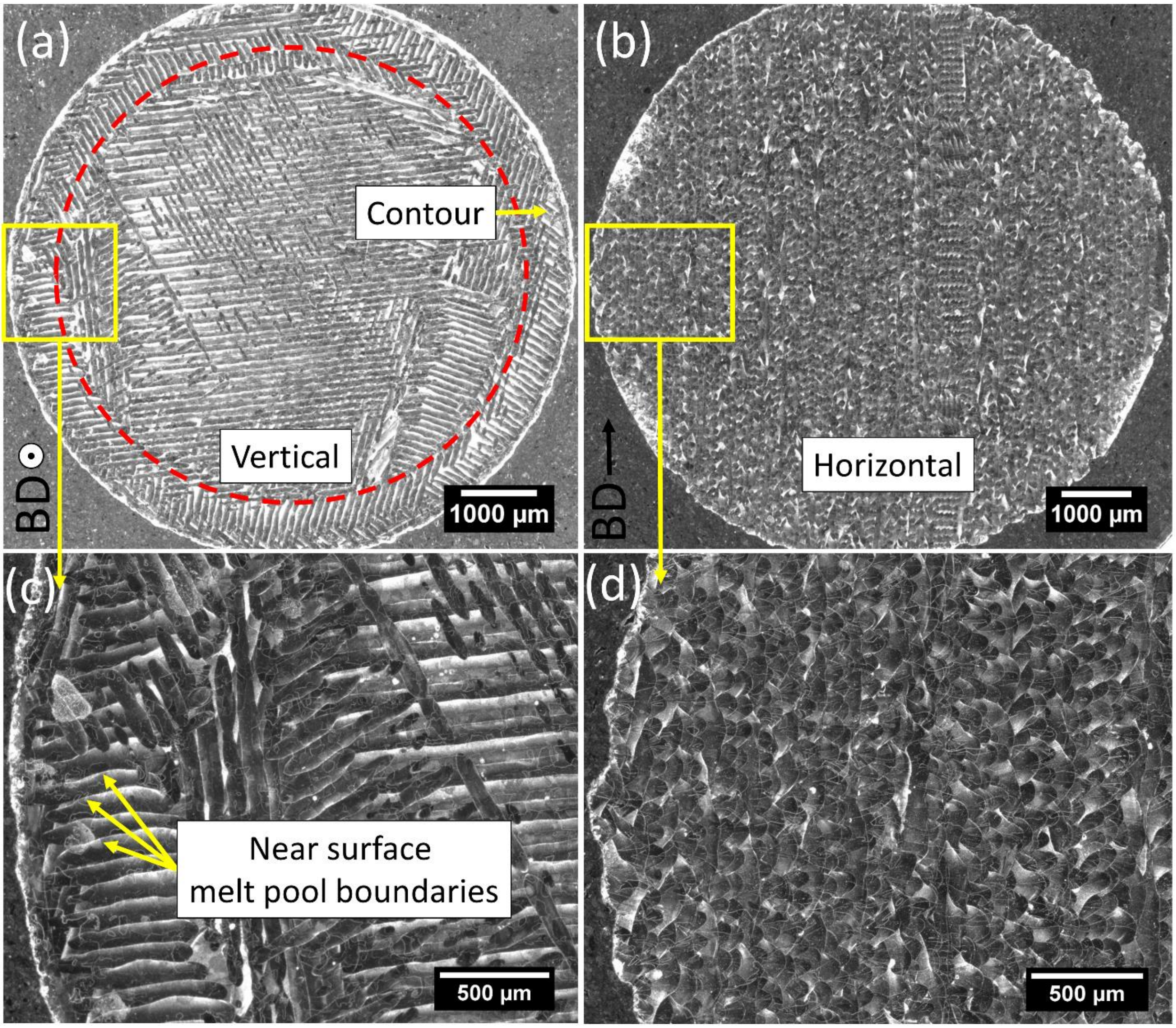

Figure 7-4: Optical microscopy images showing laser scan track impressions in (a & b) transverse direction of vertical and horizontal specimens respectively (c) Contour region of vertical specimens exposing melt pool boundaries at the surface (d) Melt pool boundaries unexposed in horizontal specimens

7.3.4 Stages of fracture initiation

Development of slip planes driven by plastic deformation was observed, and these evolved into a series of micropores and hence coalesce into cracks is illustrated in Figure 7-5. Depending upon the critically resolved shear stress levels, crystallographic texture, and the corresponding Schmid factor value - basal, prismatic, and pyramidal slip systems are expected at the α/β interfaces in titanium alloys [239]. Dislocation transmission affects slip transfer at the α/β interfaces, which is observed during the plastic deformation. The deformation bands with micropores ranging 1 to 3 μm in diameter are arranged nearly parallel to each other, as previously reported [241].

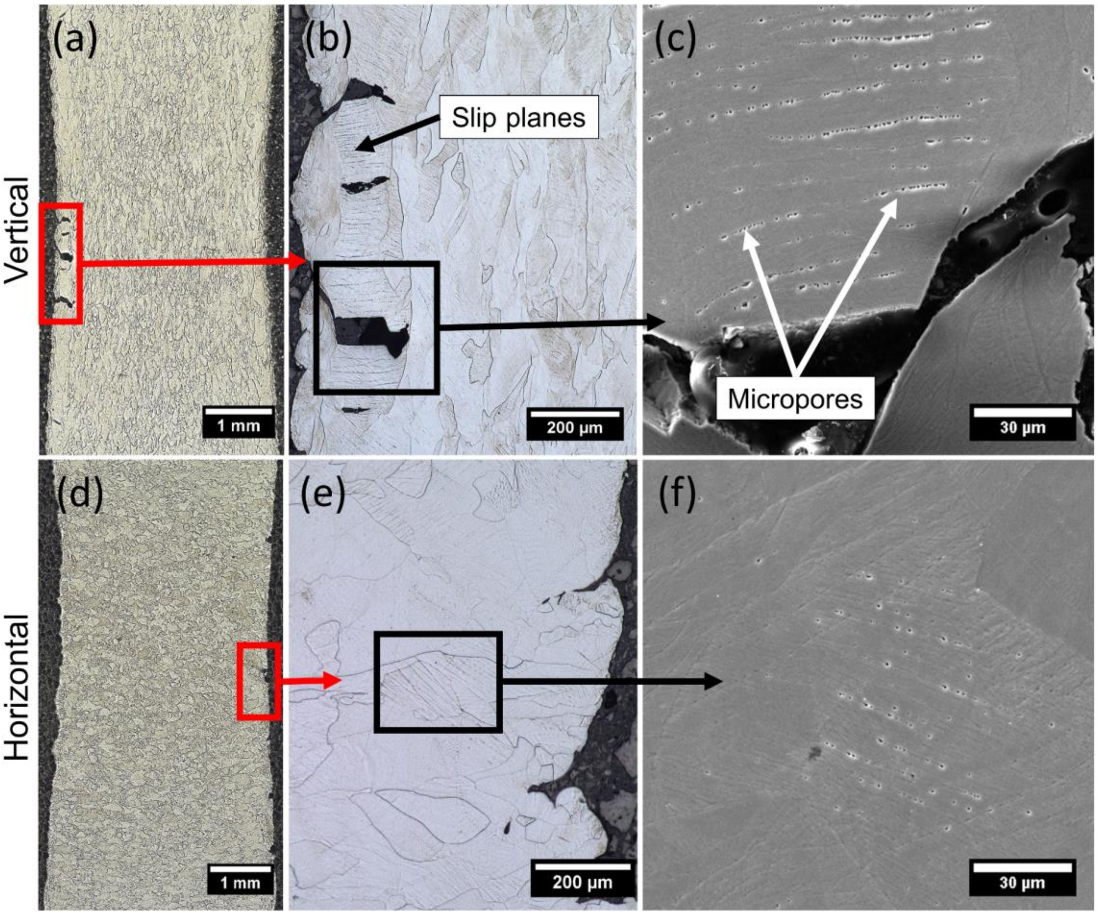

Figure 7-5: Cross sectioned interrupted tensile specimens where (a & d) Gauge section of specimens subjected to 15% elongation exposing fracture initiation spots (b & e) Identified slip lines revealing their role in fracture initiation (c & f) High magnification SEM images showing slip lines as series of micropores

7.3.5 Fracture mode comparison

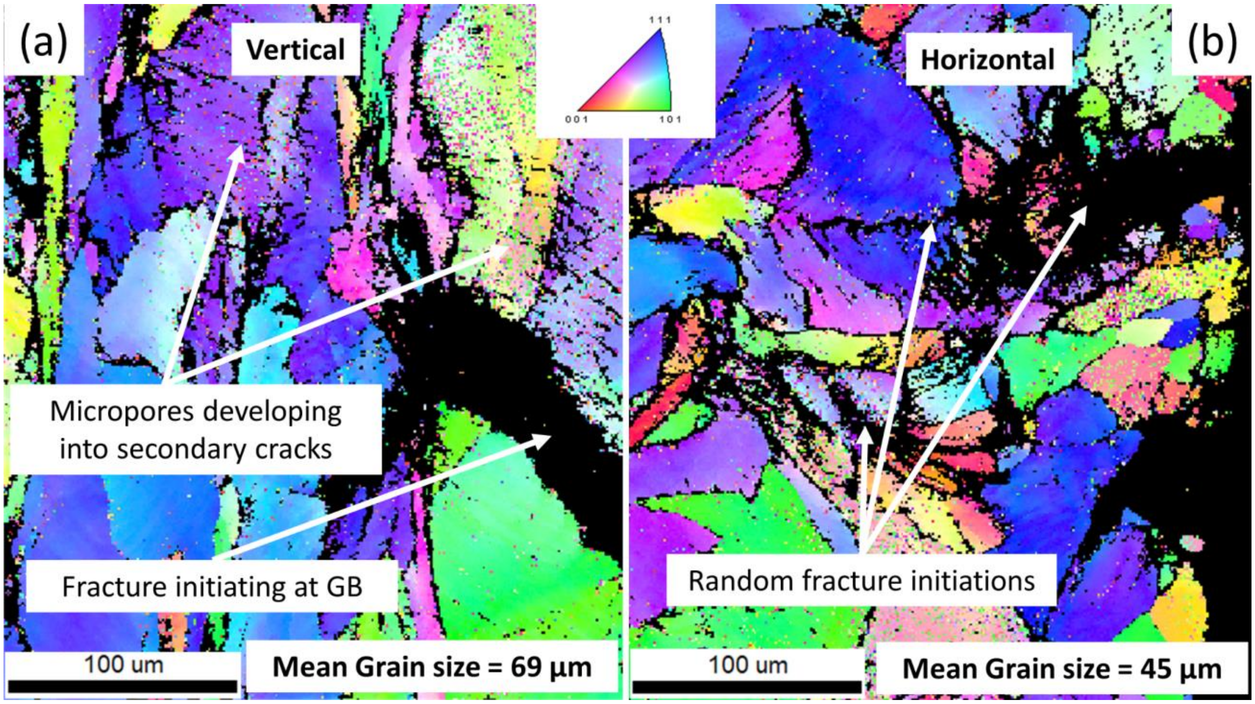

Figure 7-6: EBSD grain orientation maps showing (a) Intergranular dominant fracture mode in vertical specimens (b) Tansgranular dominant fracture mode in horizontal specimens

To understand the relationship between the microstructural features and fracture propagation, EBSD analysis was carried out on partially tensile tested samples along the length of the gauge section. The grain orientation maps of strained vertical and horizontal samples at fracture initiation spots are in Figure 7-6. Comparing the orientation maps, no directional preference was observed, which could be a combined effect of the 67° rotation between successive layers and the rapid heating-cooling cycles in LPBF process [137]. Most of the unindexed portions in the EBSD maps are grain boundaries, micropores or cracks. As seen in the vertical sample, the fracture is at the grain boundary indicating an intergranular fracture. However, in the horizontal sample, the fracture propagates through a grains suggesting a transgranular fracture. The grain size in vertical sample 69±12 µm is marginally higher than the grain sized 45±9 µm seen in the horizontal sample.

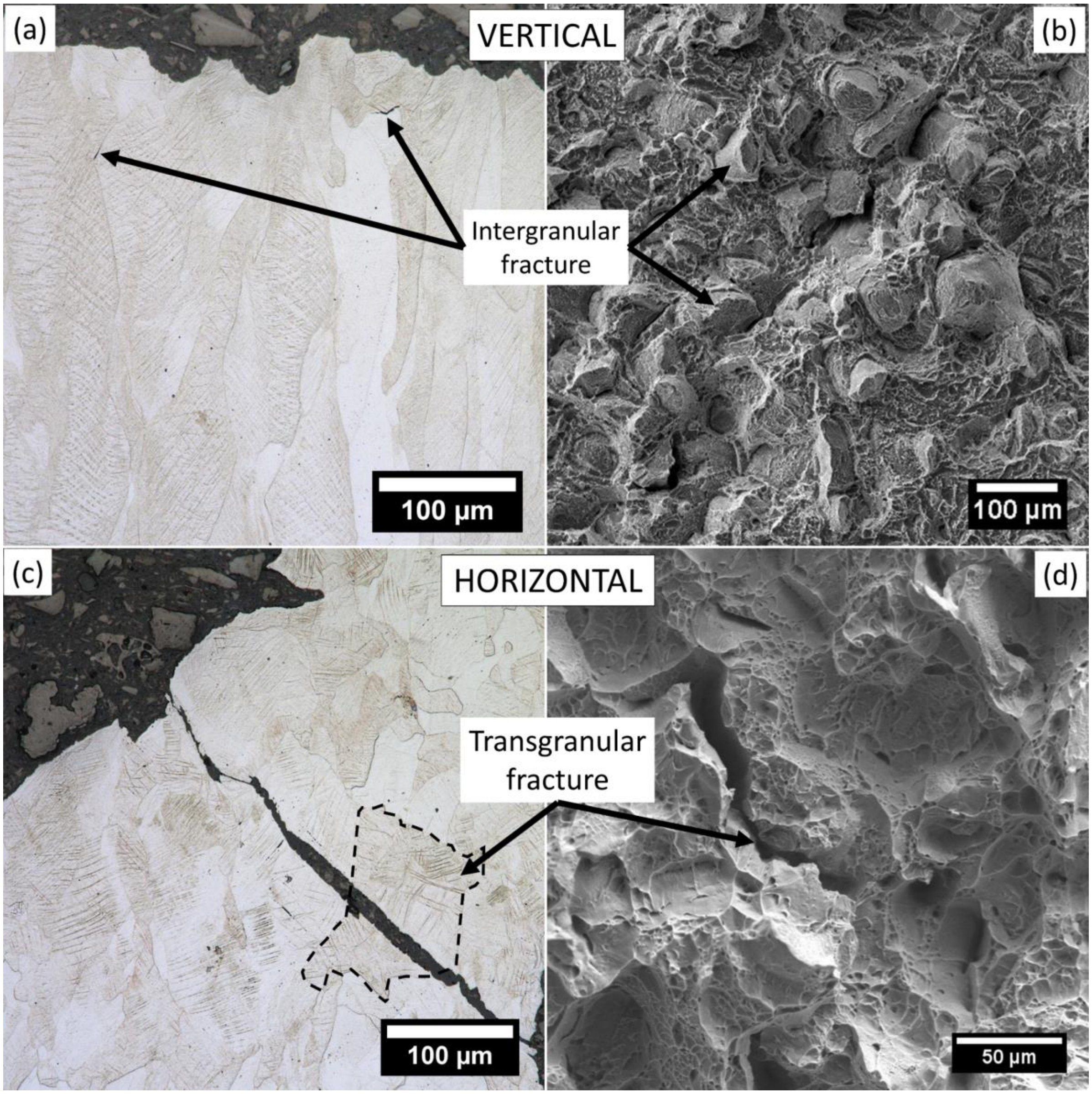

Figure 7-7: Fractured surfaces of vertical and horizontal specimens viewed from (a & c) Lateral direction after metallographic preparation and (b & d) axial direction after complete fracture

Figure 7-7 presents the cross-sectional and lateral views respectively of the completely fractured surfaces. The fracture propagation in the vertical specimen is along the grain boundaries resulting in an intergranular dominant fracture. In comparison, horizontally oriented specimens exhibit fracture propagation with a transgranular alignment based on the EBSD results in Figure 7-6. Both the fracture surfaces exhibited widespread evidence of microvoid coalescence, revealing ductile fracture characteristics. The fracture surfaces were free from any detrimental intermetallic compounds which could negatively affect the mechanical properties.

7.4 Discussion

The current results show that the horizontal samples are better than the vertical samples in resisting fracture growth and in withstanding higher tensile stresses. Previously, similar comparisons between vertically and horizontally printed specimens claimed mixed results. In a few instances, horizontally printed specimens have exhibited a higher elongation before fracture, but an increase in tensile strength is rarely seen in them [157,177,238]. The increased elongation in the horizontal specimens is claimed to be an effect of the lower stress concentration aided by the parallel alignment of the major axis to the loading direction [157]. Whereas, in certain publications, increased tensile strength is reported for horizontally printed specimens compared to the vertical specimens at the expense of ductility [227,228]. The greater hindrance to dislocation movement offered by a higher volume of grain boundaries in the horizontal specimens is attributed to be the cause for the observed higher strength, based on the well-known Hall-Petch mechanism [242–244]. A combination of several additional factors, including the differences in columnar grain growth direction, directional solidification in LPBF printing, existence of a strong texture and the subsequent grain orientation variations are influential in the observed assorted fracture growth behaviors.

The majority of the fracture initiations identified at the specimen surface could be a combined consequence of localized roughness on the surfaces (Figure 7-3) and the inwardly grown columnar lath grains (Figure 7-4). Rough surfaces affecting the tensile and fatigue strength of additive manufactured parts is well established in the literature [32,244–249]. Even though the overall surface roughness is within acceptable levels, the sharp projections caused by the partially melted powders on the surface are potential stress risers which limit ductility. Chan *et al.* reported a reduction in the fatigue life of additively manufactured Ti-64 alloy to the sharp projections on its surface acting as stress risers [250]. Melt pool boundaries are also viable sites of fracture initiation. The overall smooth surface discussed in Figure 7-3 is achieved by applying the contour LPBF process parameters. However, the printing pattern followed at the contour region shown in Figure 7-4(c), exposes a large volume of melt pool boundaries to the surface. Additionally, the solidification being nearly perpendicular to the cross section, these melt pool boundaries are potential sites of fracture initiations [157,251–253]. At the contour layer, heat dissipation is prominently facilitated through the circumference of the printed parts which is in the direction perpendicular to the building direction. Similar observations previously reported have shown the growth of columnar grains perpendicular to the building direction and are vulnerable to fracture under loading [25]. Moreover, finer grains at the contour region leading to higher hardness and hence localized brittleness is reported in our previous publication [137].

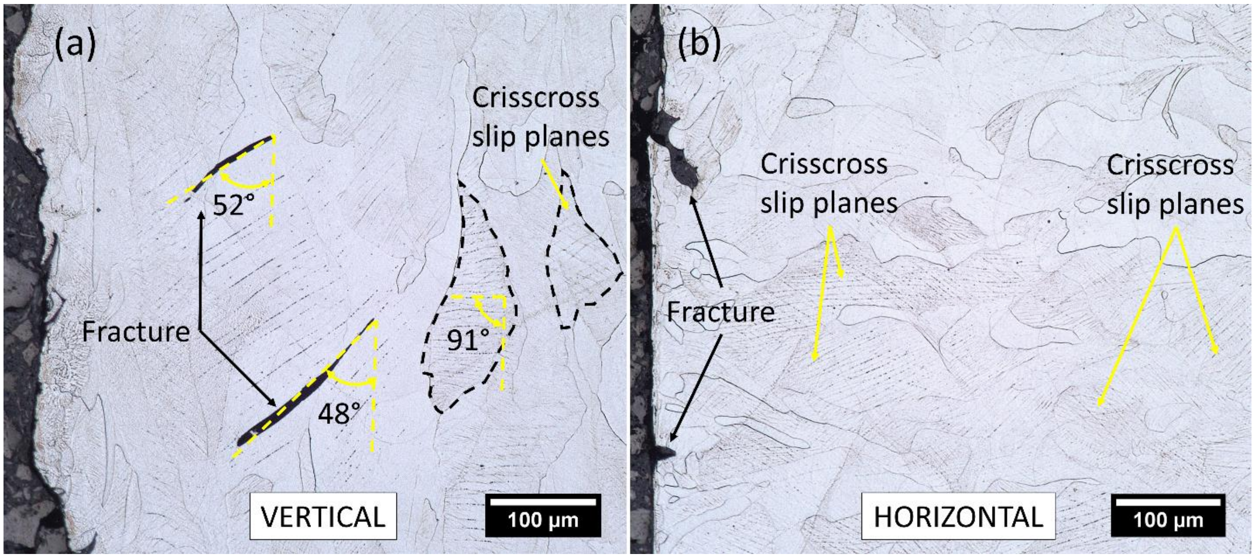

Figure 7-8: Optical microscopy images of plastically deformed specimens revealing (a) Three different slip plane orientations identified in vertical specimens (b) Identified crisscross slip planes in horizontal specimens

The evolution of fracture from the slip planes caused by the plastic deformation is illustrated in Figure 7-5. Even though the micropores identified on vertical and horizontal specimens were similar, their significance in causing the fracture appears to be vastly different. To understand the slip plane involvement in fracture initiation better, Figure 7-8 compares the orientation of the slip lines within grains for both orientations. The slip line structures in Figure 7-8 indicate that slip transfers are there in both the vertical and horizontal specimens. Three observations are critical to be noted in the vertical specimen. Firstly, alignment of slip planes within a short range follows a trend and several such distinct short ranged slip line groups were observed. In grains adjacent to the fracture initiation, slip planes were aligned 45 to 55° with respect to the loading direction. Similar 45° alignment of slip planes with respect to the tensile loading direction has been previously reported for β Ti alloys [254]. The typically strong {100} texture in β Ti alloys leads to maximum shear stress acting along {110} planes oriented at 45° to {100} due to the highest Schmid factor value experienced for {110}<111>. This will lead to the maximum shear stress being induced at 45° to the oriented slip planes, and thus promote fracture. A slight deviation (±5°) from the expected 45° slip plane could be a result of lattice rotation under deformation [104].

In a few cases involving β Ti alloys, an additional 30° alignment of the slip planes with respect to the loading direction, especially at the necking region caused by the activated {112} slip plane, is reported to result in a severe work softening [255,256]. However, neither a 30° slip plane alignment nor a severe work softening was observed in the present work. Moreover, away from the fracture sites, the alignment of the slip planes were at 85 to 95° in reference to the loading direction. Fractures are never initiated from these slip planes as they are the locations of zero shear stress. Secondly, irrespective of the alignment, the distance between successive slip planes is fairly constant ranging 8 to 12 µm. Finally, in a few grain sets, crisscross alignment of the slip planes was also seen. At higher magnification, the slip planes gradually develop into a series of micropores. Alternatively, in the horizontal samples, crisscross slip planes were widely present and did not significantly influence the fracture path. The interaction between multiple slip planes results in creating a kink, causing a dislocation entanglement at the junctions [104,257]. The entanglement of the dislocations adds stiffness to the joints, and hence they resist deformation under tensile load better.

Fracture surfaces in Figure 7-7 reveal different fracture modes between vertical and horizontal specimens. Furthermore, the EBSD maps in Figure 7-6, disclose the fracture path in vertical specimens being guided along the grain boundaries. Similar fracture path propagation through grain boundaries or melt pool boundaries on vertically printed specimens is widely reported [30,142,157]. Grain boundaries and melt pool boundaries are latent sites of manufacturing defects like gas pockets, improper fusion, and solidification cracks [258]. Alignment of the melt pools being perpendicular to the applied tensile load in vertical specimens, the stress concentration is extreme at these boundaries and subsequently may lead to premature fracture.

Figure 7-9 presents the differences observed in the energy per layer values of vertical and horizontal dog bone shaped cylindrical tensile specimens. The energy per layer values of vertical specimen are considerably lower compared to the horizontally printed counterparts. The energy per layer values of vertical specimens ranged 20 to 78 J due to the varying cross-sectional diameter between the grip and gauge sections. However, in the horizontal specimens, a wider range of energy per layer values (53 to 884 J) is recorded. The wider energy per layer values in horizontal specimens is caused by the cumulative effect of the simultaneously varying length and diameter values along the building direction. In addition to the above discussed metallurgical factors, differences in the energy per deposited layer caused due to the geometrical factors and the print orientations could have a significant influence on the mechanical properties.

$$E_l = VED \times l \times A_P \tag{1}$$

where, $\mathrm{E_l}$ – energy per layer (J)

VED – volumetric energy density (J/mm^3)

l – powder layer thickness (mm)

$\mathrm{A_P}$ – print area per layer (mm^2)

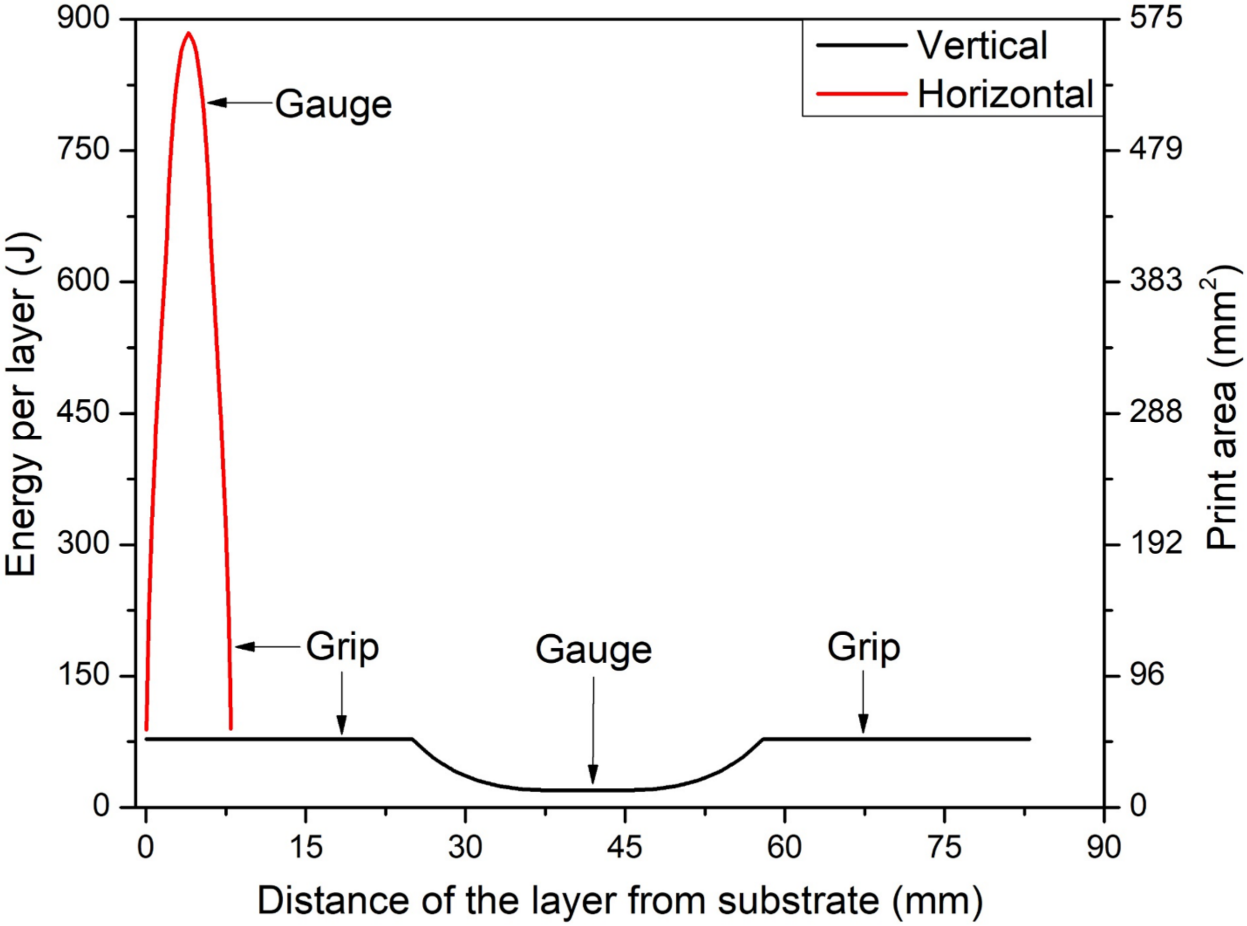

Figure 7-9: Variations in the energy per layer between vertical and horizontal specimens caused by the different print area per layer

Energy per layer plays an important role in minimizing the non-optimal process parameter set induced defects mentioned above. The optimal process parameters listed in Table 7-1 were determined based on the Archimedes relative density, Rockwell hardness and the surface roughness measurements analyzed from vertically printed standard cylindrical specimens, evaluated while the area of each deposited layer along the building direction is the same [27,137]. However, if the geometry of the printed parts involve varying areas of cross sections along the building direction, then the differences existing in the energy per layer, given in Eq. (1), could play a key role in the integrity of the printed parts. Because of the differences in the geometry along the building direction, the corresponding printing area per layer (A_P) and the layer thickness needs to be incorporated to precisely calculate the energy per layer, which is different from the VED. A wider range of energy per layer values in horizontally printed specimens resulted in inferior relative densities compared to the vertically printed specimens [259]. The inferior relative density parts are expected to affect the mechanical properties, especially the ductility. Additionally, In horizontal specimens, melt pool boundaries being parallel to the loading direction may not suffer the extremely high tensile stresses [157]. Hence the fracture path was random and primarily propagated through the grains.

7.5 Summary and conclusions

In this study, fracture propagation characteristics of vertically and horizontally printed Ti-5553 specimens are compared. Partial tensile tests (i.e.) tensile tests prematurely terminated in the plastic deformation regime at 5, 10 and 15% longitudinal strain were carried out. The cross sections of the strained specimens were examined through characterization techniques such as OM, laser profilometer, SEM and EBSD. Based on the findings, the subsequent conclusions could be drawn:

1. Horizontally-made specimens exhibited a higher strength (846±6 MPa) compared with the vertically-made specimens (780±10 MPa). Vertical specimens exhibited a slightly higher

total elongation of 23±3 % compared to the 21±2 % total elongation sustained by the horizontal specimens.

2. Most fracture initiations occur at the surface, which could be a combined effect of the surface roughness and the melt pool boundaries exposed to the surface.
3. The fracture mode in vertical specimens is predominantly intragranular, whereas in horizontal specimens, it is transgranular in nature.
4. Three different orientations of slip planes with respect to the loading - 45°, 90° and crisscross with unique responses to the loading were identified. The slip lines are a series of micropores which coalesce into cracks on continued loading.
5. The higher volume of crisscross slip planes representing dislocation entanglements and hence more stiffness caused the higher tensile strength in horizontally printed specimens.

Chapter 8: Summary of conclusions and future work

This chapter is divided into 2 sections. In Section 8.1, a summary of the conclusions derived from the chapters 4 – 7 are compiled. In Section 8.2, recommendations and opportunities for future research based on preliminary results of continued research are shared.

8.1 Conclusions

The work was focussed to study the microstructure of LPBF-made Ti-5553 alloy and its effect on the tensile properties. It was observed that the variation in size, area fraction, distribution and morphology of the α precipitates control the mechanical properties.

The LPBF printing at scan speeds > 750 mm/s at optimized process parameter set resulted in the precipitation of non-lamellar α particles within the columnar β grains. On tensile testing, the non-lamellar α precipitates in the microstructure caused an exceptional elongation of 30 ± 5%, which is nearly twice higher than the usually reported values for Ti-5553 alloy. However, the corresponding ultimate tensile strength is limited to 780 ± 10 MPa and the Charpy impact tested samples absorbed a trivial 4 to 9 J. The bi-modal fracture observed in the tensile tested and impact tested specimens is due to the difference in the β grain size between the contour and core sections.

In order to modify the morphology, size and distribution of the α precipitates, the LPBF-made specimens were subjected to post heat treatment proyocols. The β transus (T_β) temperature is experimentally identified at 860 ± 10°C. Solution treatment at above T_β, i.e. at 900°C showed traces of breaking the columnar chain but the subsequent β grains were exponentially coarser (> 350 µm). However, the solution treatment in the upper α+β region, i.e. at 800°C for 3 hours resulted in the best combination of negligible residual α precipitates (< 2%) and finer grain β grains (≈ 250 µm). On further aging at 500 to 700°C, a combination of multiple α morphologies, including

Widmanstätten, lenticular, cylindrical and lamellar were identified. The combination of α morphologies varied based on the heat treatment temperature and duration. The α needles were longer and wider with increasing aging temperature. At 700°C aging for durations beyond 2 hours, saturation in growth and hence fragmentation of lamellar α needles leading to the presence of conjoined lamellar α needles were noted. A recrystallized microstructure was revealed by the EBSD orientation maps and pole figures at 500°C aging. Whereas, at 600°C and 700°C aging a <001> texture was seen during 0.5 hours of aging. On longer duration aging, a random-like texture was identified, suggesting more uniform three-dimensional grain growth.

Microhardness measurements revealed a highest hardness of 490 ± 10 $HV_{0.3}$ at 500°C for 2 hours, which gradually lowered to 300 to 315 $HV_{0.3}$, at 700°C. A highest tensile strength of 1620±22.2 MPa with a ductility of 3.7±0.9% was recorded by 500°C aged specimens. On the specimens exhibiting high strength, a dominant intergranular fracture was observed due to grain boundary α segregation. At 600°C aging for 0.5 hours, an optimal combination of tensile strength (1487 ± 21 MPa) and a total elongation of 6.54 ± 0.9% was recorded. On 700°C aging, the tensile strength was limited to 1004 to 1092 MPa but with an exceptional ductility of 23.19 ± 4.5%. The corresponding fractured surfaces exhibited a predominantly ductile fracture mode.

As titanium is readily reactive with interstitial elements, irrespective of the aging condition, a 250 to 300 µm thick brittle outer ring is characterized on the heat treated specimens. The 20 to 50 µm part of the outer brittle ring is highly concentrated in finely distributed thin α needles and hence labelled as the α case. The rest of the brittle region is termed as the transition zone. The presence of an α case restricts the tensile strength to 620 to 858 MPa. On machining off the α case and the transition zone, the tensile strength improved to 1360 ± 14 MPa with a corresponding total elongation of 11 ± 4 %. Surface turning only the 20 to 50 μm thick α case, further improved the tensile strength to 1410 ± 8 MPa but the total elongation was limited to 2 ± 0.5 %.

The building direction dependent grain growth causes anisotropy in metal additive manufactured parts. It is possible to engineer the building direction with respect to the direction of the loading direction and improve the tensile properties. Ti-5553 specimens printed horizontally exhibited better tensile properties, with an UTS of 846 ± 6 MPa and a total elongation of 21 ± 2 % compared to the vertically printed specimens which failed at tensile stress of 780 ± 10 MPa and a total elongation of 23 ± 3 % in the as-printed condition. The difference in tensile strength caused by the printing direction is caused by the surface roughness, contour printing pattern and the orientation of slip planes which develop into a series of micropores and subsequently into cracks on continued loading.

8.2 Scope for future work

8.2.1 Normalized heat treatment parameters

While the results shared in Chapter 5 have shown the solution treatment at 800°C for 3 hours being effective in facilitating the dissolution of heterogeneously grown α precipitates, its effectiveness on varying cross sectional area is still an unknown. More comprehensive research involving heat treatment of specimens covering a reasonably wide range of cross-sectional diameters is necessary. The deliverable of such a research would be a normalized set heat treatment model that could suggest fine-tuned heat treatment process parameters to achieve precise microstructure irrespective of the size of the component.

8.2.2 Effect of cooling rate

In the current heat treatment research, only water quenching was experimented. However, β annealing slow cooling and aging (BASCA) and air cooling have been widely reported in the literature as recommended cooling options after aging cycle. The effect of different cooling mediums on the microstructural development of LPBF-made and heat treated Ti5553 with columnar grained initial as-printed microstructure is yet to be explored and would be a valuable addition to the existing knowledge in open literature.

8.2.3 Low temperature heat treatment

Heat treatment temperatures ranging 500 to 900°C resulting in the formation of hard and brittle α case regions is discussed in Chapter 6. However, according to the DSC curves in Figure 5-1(a), α particle growth can be also facilitated in 200 to 450°C range. It is to be noted that the α case growth is not expected at temperatures lesser than 480°C. The low temperature heat treatment of additively manufactured Ti alloys is one of the least explored avenues as it requires extended durations of aging and it is challenging to deal with the simultaneous growth of detrimental ω phase at this temperature range. A detailed study on overcoming the challenges could facilitate avoiding the currently recommended post machining to remove the deleterious α case regions.

8.2.4 Duplex aging

Two stage aging is widely reported in the literature to be capable of providing better mechanical properties compared to the single stage aging studied in this research. However, duplex aging introduces several unknowns including the optimal temperature, and the holding time in each stage of aging. Further exploration to improve the mechanical properties via duplex aging requires a broad investigation.

8.2.5 Fatigue performance

Aircraft structural components are repetitively subjected to fatigue stresses under service. It is important for these materials to exhibit a high fatigue life. Poor surface finish, internal porosities, improper fusion at the melt pool boundaries, brittle intermetallic compounds, heterogeneous microstructure along the building direction and other similar process induced defects are commonly faced problems in LPBF-made parts. Most of these issues, which might not highly influence the tensile properties can impart severe effects on the fatigue performance. Therefore, it is essential to evaluate the fatigue life of the specimens printed at the currently optimized process parameter set and if needed, fine tune the process parameters further to achieve reliable and repeatable printed parts that could consistently exhibit an acceptable endurance limit.

REFERENCES

[1] M. Peters, J. Kumpfert, C.H. Ward, C. Leyens, Titanium alloys for aerospace applications, Adv. Eng. Mater. 5 (2003) 419–427. doi:10.1002/adem.200310095.

[2] M.F. Ashby, Materials selection in mechanical design, Metall. Ital. 86 (1994) 475.

[3] P.M. Adrian, Introduction to Aerospace Materials, Woodhead Publishing, 2012. doi:10.1533/9780857095152.39.

[4] R.R. Boyer, R.D. Briggs, The use of β titanium alloys in the aerospace industry, J. Mater. Eng. Perform. 22 (2013) 2916–2920. doi:10.1007/s11665-013-0728-3.

[5] G. Lutjering, J.C. William, G. Lütjering, J.C. Williams, Titanium, 2nd ed., Springer Science & Business Media, Berlin, 2007.

[6] R.R. Boyer, An overview on the use of titanium in the aerospace industry, Mater. Sci. Eng. A. 213 (1996) 103–114. doi:10.1016/0921-5093(96)10233-1.

[7] R.R. Boyer, Aerospace applications of beta titanium alloys, JOM. 46 (1994) 20–23. doi:10.1007/BF03220743.

[8] R. Panza-Gios, The Effect of Heat Treatment on the Microstructure Evolution and Mechanical Properties of Ti-5Al-5V-5Mo-3Cr, and Its Potential Application in Landing Gears., 2009.

[9] H.D. Carlton, K.D. Klein, J.W. Elmer, Evolution of microstructure and mechanical properties of selective laser melted Ti-5Al-5V-5Mo-3Cr after heat treatments, Sci. Technol. Weld. Join. 0 (2019) 1–9. doi:10.1080/13621718.2019.1594589.

[10] H. Schwab, M. Bönisch, L. Giebeler, T. Gustmann, J. Eckert, U. Kühn, Processing of Ti-5553 with improved mechanical properties via an in-situ heat treatment combining selective laser melting and substrate plate heating, Mater. Des. 130 (2017) 83–89. doi:10.1016/j.matdes.2017.05.010.

[11] Y. Hagedorn, Laser additive manufacturing of ceramic components: Materials, processes, and mechanisms, Laser Addit. Manuf. Mater. Des. Technol. Appl. 6608 (2016) 163–180. doi:10.1016/B978-0-08-100433-3.00006-3.

[12] H. Attar, M. Bönisch, M. Calin, L.-C. Zhang, S. Scudino, J. Eckert, Selective laser melting of in situ titanium–titanium boride composites: Processing, microstructure and mechanical properties, Acta Mater. 76 (2014) 13–22. doi:10.1016/j.actamat.2014.05.022.

[13] L.C. Zhang, D. Klemm, J. Eckert, Y.L. Hao, T.B. Sercombe, Manufacture by selective laser melting and mechanical behavior of a biomedical Ti–24Nb–4Zr–8Sn alloy, Scr. Mater. 65 (2011) 21–24. doi:10.1016/j.scriptamat.2011.03.024.

[14] J.P. Kruth, P. Mercelis, J. Van Vaerenbergh, L. Froyen, M. Rombouts, Binding mechanisms in selective laser sintering and selective laser melting, 2005. doi:10.1108/13552540510573365.

[15] J.C. Fanning, R.R. Boyer, Properties of TIMETAL 555—A New Near-Beta Alloy for

Airframe Components, in: Proc. 10th World Conf. Titan., 2003: pp. 2643–2650.

[16] H. Fayazfar, M. Salarian, A. Rogalsky, D. Sarker, P. Russo, V. Paserin, E. Toyserkani, A critical review of powder-based additive manufacturing of ferrous alloys: Process parameters, microstructure and mechanical properties, Mater. Des. 144 (2018) 98–128. doi:10.1016/j.matdes.2018.02.018.

[17] M.K. Thompson, G. Moroni, T. Vaneker, G. Fadel, R.I. Campbell, I. Gibson, A. Bernard, J. Schulz, P. Graf, B. Ahuja, F. Martina, Design for Additive Manufacturing: Trends, opportunities, considerations, and constraints, CIRP Ann. - Manuf. Technol. (2016). doi:10.1016/j.cirp.2016.05.004.

[18] S. Sakata, N-dimensional Berlekamp-Massey algorithm for multiple arrays and construction of multivariate polynomials with preassigned zeros, Lect. Notes Comput. Sci. (Including Subser. Lect. Notes Artif. Intell. Lect. Notes Bioinformatics). 357 LNCS (1989) 356–376. doi:10.1007/3-540-51083-4_72.

[19] G. Jacob, A. Donmez, J. Slotwinski, S. Moylan, Measurement of powder bed density in powder bed fusion additive manufacturing processes, Meas. Sci. Technol. 27 (2016). doi:10.1088/0957-0233/27/11/115601.

[20] U. Ali, Y. Mahmoodkhani, S. Imani Shahabad, R. Esmaeilizadeh, F. Liravi, E. Sheydaeian, K.Y. Huang, E. Marzbanrad, M. Vlasea, E. Toyserkani, On the measurement of relative powder-bed compaction density in powder-bed additive manufacturing processes, Mater. Des. 155 (2018) 495–501. doi:10.1016/j.matdes.2018.06.030.

[21] S.W. Killi, Additive Manufacturing, CRC Press, 2017. doi:10.1201/b22510.

[22] A. Gusarov, I. Yadroitsev, P. Bertrand, I. Smurov, Heat transfer modelling and stability analysis of selective laser melting, Appl. Surf. Sci. 254 (2007) 975–979. doi:10.1016/j.apsusc.2007.08.074.

[23] M. Garibaldi, I. Ashcroft, M. Simonelli, R. Hague, Metallurgy of high-silicon steel parts produced using Selective Laser Melting, Acta Mater. 110 (2016) 207–216. doi:10.1016/j.actamat.2016.03.037.

[24] W.J. SAMES, Additive manufacturing of inconel 718 using electron beam melting: processing, post-processing, & mechanical properties, Texas A&M University, 2015.

[25] A.A. Antonysamy, J. Meyer, P.B. Prangnell, Effect of build geometry on the β-grain structure and texture in additive manufacture of Ti6Al4V by selective electron beam melting, Mater. Charact. 84 (2013) 153–168. doi:10.1016/j.matchar.2013.07.012.

[26] G.G. Yapici, I. Karaman, Z.-P. Luo, Mechanical twinning and texture evolution in severely deformed Ti-6Al-4V at high temperatures, Acta Mater. 54 (2006) 3755–3771. doi:10.1016/j.actamat.2006.04.007.

[27] S. Bakhshivash, H. Asgari, P. Russo, C.F. Dibia, M. Ansari, A.P. Gerlich, E. Toyserkani, Printability and microstructural evolution of Ti-5553 alloy fabricated by modulated laser powder bed fusion, Int. J. Adv. Manuf. Technol. (2019) 1–11. doi:10.1007/s00170-019-03847-3.

[28] C. Zopp, S. Blümer, F. Schubert, L. Kroll, Processing of a metastable titanium alloy (Ti-5553) by selective laser melting, Ain Shams Eng. J. 8 (2017) 475–479. doi:10.1016/j.asej.2016.11.004.

[29] H. Schwab, F. Palm, U. Kühn, J. Eckert, Microstructure and mechanical properties of the near-beta titanium alloy Ti-5553 processed by selective laser melting, Mater. Des. 105 (2016) 75–80. doi:10.1016/j.matdes.2016.04.103.

[30] Z. Liu, Z.B. Zhao, J. Liu, Q. Wang, Z. Guo, J. Wang, G. Yang, S. Gong, Anisotropy in microstructure and tensile properties of Ti–5Al–5Mo–5V–1Cr–1Fe produced via additive manufacturing, Mater. Sci. Eng. A. 798 (2020) 140093. doi:10.1016/j.msea.2020.140093.

[31] D.S. Shin, C.H. Lee, U. Kühn, S.C. Lee, S.J. Park, H. Schwab, S. Scudino, K. Kosiba, Optimizing laser powder bed fusion of Ti-5Al-5V-5Mo-3Cr by artificial intelligence, J. Alloys Compd. 862 (2021). doi:10.1016/J.JALLCOM.2020.158018.

[32] T. Grove, B. Denkena, O. Maiß, A. Krödel, H. Schwab, U. Kühn, Cutting mechanism and surface integrity in milling of Ti-5553 processed by selective laser melting, J. Mech. Sci. Technol. 32 (2018) 4883–4892. doi:10.1007/s12206-018-0936-8.

[33] R.G. Reddy, P.S. Shinde, A. Liu, Review—The Emerging Technologies for Producing Low-Cost Titanium, J. Electrochem. Soc. 168 (2021) 042502. doi:10.1149/1945-7111/abe50d.

[34] Y. Xia, H.D. Lefler, Z.Z. Fang, Y. Zhang, P. Sun, Extractive Metallurgy of Titanium, Amsterdam: Elsevier, 2020.

[35] K.S. Mcreynolds, S. Tamirisakandala, A Study on Alpha-Case Depth in Ti-6Al-2Sn-4Zr-2Mo, Metall. Mater. Trans. A. 42A (2011) 1732–1736. doi:10.1007/s11661-011-0710-3.

[36] R. Gaddam, B. Sefer, R. Pederson, M.L. Antti, Oxidation and alpha-case formation in Ti-6Al-2Sn-4Zr-2Mo alloy, Mater. Charact. 99 (2015) 166–174. doi:10.1016/J.MATCHAR.2014.11.023.

[37] H. Pang, J. Luo, C. Li, M. Li, The role of β phase in the morphology evolution of α lamellae in a dual-phase titanium alloy during high temperature compression, J. Alloys Compd. 910 (2022) 1–13. doi:10.1016/J.JALLCOM.2022.164901.

[38] R.P. Kolli, A. Devaraj, A Review of Metastable Beta Titanium Alloys, Metals (Basel). 8 (2018) 1–41. doi:10.3390/met8070506.

[39] B. Dutta, F.H. Froes, Additive Manufacturing of Titanium Alloys: State of the Art, Challenges and Opportunities, Butterworth-Heinemann, 2016. doi:10.1016/C2015-0-02470-4.

[40] G. Welsch, R. Boyer, E.W. Collings, Materials properties handbook: titanium alloys, ASM international, 1993.

[41] E.W. Collings, The physical metallurgy of titanium alloys, Met. Park Ohio. 3 (1984).

[42] J.C. Schuster, M. Palm, Reassessment of the Binary Aluminum-Titanium Phase Diagram, J. Phase Equilibria Diffus. 27 (2006) 255–277. doi:10.1361/154770306X109809.

[43] D. Herzog, V. Seyda, E. Wycisk, C. Emmelmann, Additive manufacturing of metals, Acta Mater. 117 (2016) 371–392. doi:10.1016/j.actamat.2016.07.019.

[44] L.C. Zhang, H. Attar, Selective Laser Melting of Titanium Alloys and Titanium Matrix Composites for Biomedical Applications: A Review, Adv. Eng. Mater. 18 (2016) 463–475. doi:10.1002/adem.201500419.

[45] J.P.D. C. Veiga A.J.R. Loureiro, Proprties and applications of titanium alloys, Rev. Adv. Mater. Sci. 32 (2012) 133–148.

[46] D. Qin, Y. Li, S. Zhang, L. Zhou, On the tensile embrittlement of lamellar Ti-5Al-5V-5Mo-3Cr alloy, J. Alloys Compd. 663 (2016) 581–593. doi:10.1016/j.jallcom.2015.12.158.

[47] N.G. Jones, R.J. Dashwood, D. Dye, M. Jackson, Thermomechanical processing of Ti-5Al-5Mo-5V-3Cr, Mater. Sci. Eng. A. 490 (2008) 369–377. doi:10.1016/j.msea.2008.01.055.

[48] J.C. Sabol, T. Pasang, W.Z. Misiolek, J.C. Williams, Localized tensile strain distribution and metallurgy of electron beam welded Ti-5Al-5V-5Mo-3Cr titanium alloys, J. Mater. Process. Technol. 212 (2012) 2380–2385. doi:10.1016/j.jmatprotec.2012.06.023.

[49] S. Ankem, C.A. Greene, Recent developments in microstructure/property relationships of beta titanium alloys, Mater. Sci. Eng. A. 263 (1999) 127–131. doi:10.1016/S0921-5093(98)01170-8.

[50] J.D. Cotton, R.D. Briggs, R.R. Boyer, S. Tamirisakandala, P. Russo, N. Shchetnikov, J.C. Fanning, State of the Art in Beta Titanium Alloys for Airframe Applications, Jom. 67 (2015) 1281–1303. doi:10.1007/s11837-015-1442-4.

[51] J. Gao, Understanding the Relationship between Microstructure and Mechanical Properties in HIPped Ti-5Al-5Mo-5V-3Cr, University of Birmingham, 2018.

[52] X. Gao, W. Zeng, S. Zhang, Q. Wang, A study of epitaxial growth behaviors of equiaxed alpha phase at different cooling rates in near alpha titanium alloy, Acta Mater. 122 (2017) 298–309. doi:10.1016/j.actamat.2016.10.012.

[53] S. Bontha, N.W. Klingbeil, P.A. Kobryn, H.L. Fraser, Effects of process variables and size-scale on solidification microstructure in beam-based fabrication of bulky 3D structures, Mater. Sci. Eng. A. (2009) 311–318. doi:10.1016/j.msea.2009.02.019.

[54] L.E. Murr, S.M. Gaytan, A. Ceylan, E. Martinez, J.L. Martinez, D.H. Hernandez, B.I. Machado, D.A. Ramirez, F. Medina, S. Collins, R.B. Wicker, Characterization of titanium aluminide alloy components fabricated by additive manufacturing using electron beam melting, Acta Mater. 58 (2010) 1887–1894. doi:10.1016/j.actamat.2009.11.032.

[55] P.A. Kobryn, S.L. Semiatin, Mechanical Properties of Laser-Deposited Ti-6Al-4V, n.d.

[56] P.A. Kobryn and S.L. Semiatin, The Laser Additive Manufacture of Ti-6Al-4V, JOM. Sep (2001) 40–42.

[57] S. Shekhar, R. Sarkar, S. Kumar Kar, A. Bhattacharjee, S.K. Kar, A. Bhattacharjee, S. Kumar Kar, A. Bhattacharjee, Effect of solution treatment and aging on microstructure and tensile properties of high strength β titanium alloy, Ti-5Al-5V-5Mo-3Cr, Mater. Des. 66

(2015) 596–610. doi:10.1016/j.matdes.2014.04.015.

[58] Y. Zheng, R.E.A. Williams, J.M. Sosa, Y. Wang, R. Banerjee, H.L. Fraser, The role of the ω phase on the non-classical precipitation of the α phase in metastable β-titanium alloys, Scr. Mater. 111 (2016) 81–84. doi:10.1016/j.scriptamat.2015.08.019.

[59] M. Jackson, R.J. Dashwood, L. Christodoulou, H.M. Flower, Application of novel technique to examine thermomechanical processing of near β alloy Ti–10V–2Fe–3Al, Mater. Sci. Technol. 16 (2010) 1437–1444. doi:10.1179/026708300101507433.

[60] A. Ghosh, S. Sivaprasad, A. Bhattacharjee, S. Kumar Kar, S.K. Kar, Microstructure-fracture toughness correlation in an aircraft structural component alloy Ti-5Al-5V-5Mo-3Cr, Mater. Sci. Eng. A. 568 (2013) 61–67. doi:10.1016/j.msea.2013.01.017.

[61] S.L. Nyakana, J.C. Fanning, R.R. Boyer, Quick reference guide for β titanium alloys in the 00s, J. Mater. Eng. Perform. 14 (2005) 799–811. doi:10.1361/105994905X75646.

[62] and R.W.S. D. Eylon, A. Vassel, Y. Combres, R.R. Boyer, P.J. Bania, Issues in the Development of Beta Titanium Alloys, Jom. 46 (1994) 14–15. doi:10.2307/j.ctt7s415.4.

[63] L.C. Campanelli, P.S.C.P. da Silva, A.M. Jorge, C. Bolfarini, Effect of hydrogen on the fatigue behavior of the near-β Ti-5Al-5Mo-5V-3Cr alloy, Scr. Mater. 132 (2017) 39–43. doi:10.1016/j.scriptamat.2017.01.028.

[64] P. Manda, U. Chakkingal, A.K.K. Singh, Microstructure, Texture and Mechanical Properties of hot Rolled Metastable β-Titanium Alloy Ti-5Al-5Mo-5V-3Cr, in: Mater. Today Proc., 2015: pp. 1118–1126. doi:10.1016/j.matpr.2015.07.018.

[65] T. Li, D. Kent, G. Sha, J.M. Cairney, M.S. Dargusch, The role of ω in the precipitation of α in near-β Ti alloys, Scr. Mater. 117 (2016) 92–95. doi:10.1016/j.scriptamat.2016.02.026.

[66] J. Fan, Microstructural study of the β → α phase transformation induced by thermo-mechanical treatments in metastable β Ti-5553 alloy, Materials (Basel). (2016).

[67] D. Qin, Y. Li, S. Zhang, L. Zhou, On the tensile embrittlement of lamellar Tie5Ale5Ve5Moe3Cr alloy, J. Alloys Compd. 663 (2016) 581–593. doi:10.1016/j.jallcom.2015.12.158.

[68] D.R. Bellman, E.D. Murphy, Lift and Drag Characteristics of the Douglas X-3 Research Airplane Obtained During Demonstration Flights to a Mach Number of 1.20, 1954.

[69] I. Weiss, S.L. Semiatin, Thermomechanical processing of beta titanium alloys—an overview, Mater. Sci. Eng. A. 243 (1998) 46–65. doi:10.1016/S0921-5093(97)00783-1.

[70] O.M. Ivasishin, P.E. Markovsky, Y. V. Matviychuk, S.L. Semiatin, C.H. Ward, S. Fox, A comparative study of the mechanical properties of high-strength β-titanium alloys, J. Alloys Compd. 457 (2008) 296–309. doi:10.1016/j.jallcom.2007.03.070.

[71] J. Baozhen, Effect of Severe Plastic Deformation on Microstructure in Metastable β - Ti Alloys, 2015.

[72] S. Veeck, D. Lee, R. Boyer, R. Briggs, The castability of Ti-5553 alloy: Its microstructure and properties, J. Adv. Mater. 37 (2005) 40–45.

[73] A. Dehghan-Manshadi, R.J. Dippenaar, Development of α-phase morphologies during low temperature isothermal heat treatment of a Ti-5Al-5Mo-5V-3Cr alloy, Mater. Sci. Eng. A. 528 (2011) 1833–1839. doi:10.1016/j.msea.2010.09.061.

[74] P. Manda, V. Singh, U. Chakkingal, A.K. Singh, Development of α precipitates in metastable Ti-5Al-5Mo-5V-3Cr and similar alloys, Mater. Charact. 120 (2016) 220–228. doi:10.1016/j.matchar.2016.09.005.

[75] M. Sen, S. Suman, T. Banerjee, A. Bhattacharjee, S.K. Kar, Tensile deformation mechanism and failure mode of different microstructures in Ti–5Al–5Mo–5V–3Cr alloy, Mater. Sci. Eng. A. 753 (2019) 156–167. doi:10.1016/j.msea.2019.03.003.

[76] Y. Cui, C. Li, C. Zhang, R. Li, Y. Ren, W. Zheng, Y. Wang, Effect of initial microstructure on the micromechanical behavior of Ti-55531 titanium alloy investigated by in-situ high-energy X-ray diffraction, Mater. Sci. Eng. A. (2020) 138806. doi:10.1016/j.msea.2019.138806.

[77] D. Qin, Y. Lu, Q. Liu, L. Zheng, L. Zhou, Transgranular shearing introduced brittlement of Ti-5Al-5V-5Mo-3Cr alloy with full lamellar structure at room temperature, Mater. Sci. Eng. A. 572 (2013) 19–24. doi:10.1016/j.msea.2013.02.029.

[78] T. Ali, L. Wang, X. Cheng, A. Liu, X. Xu, Omega phase formation and deformation mechanism in heat treated Ti-5553 alloy under high strain rate compression, Mater. Lett. 236 (2019) 163–166. doi:10.1016/j.matlet.2018.10.057.

[79] D. Li, X. Zhang, W. Zhao, H.D. Merrill, N.T. Meyer, S. Antonov, Y. Liao, Y. Zheng, The Role of High-Index Twinning on Hierarchical a Microstructure in a Metastable b Ti-5Al-5Mo-5V-3Cr Alloy, (n.d.). doi:10.1007/s11837-021-04757-0.

[80] H. Hong, A.T. Riga, J.M. Gahoon, C.G. Scott, Machinability of steels and titanium alloys under lubrication, in: Wear, 1993: pp. 34–39. doi:10.1016/0043-1648(93)90481-Z.

[81] W. Konig, K.H. Schroder, Meeting of AGARD Structural and Materials panel, in: Proc. 47th Meet. AGARD Struct. Mater. Panel, Florence, 1979: pp. 1.1-1.10.

[82] R. Komanduri, B.F. Von Turkovich, New observations on the mechanism of chip formation when machining titanium alloys, Wear. 69 (1981) 179–188. doi:10.1016/0043-1648(81)90242-8.

[83] E.O. Ezugwu, Z.M. Wang, Titanium alloys and their machinability - A review, J. Mater. Process. Technol. 68 (1997) 262–274. doi:10.1016/S0924-0136(96)00030-1.

[84] P.J. Withers, H.K.D.H. Bhadeshia, Residual stress part 1 - Measurement techniques, Mater. Sci. Technol. 17 (2001) 355–365. doi:10.1179/026708301101509980.

[85] P.J. Withers, H.K.D.H. Bhadeshia, Residual stress part 2 - Nature and origins, Mater. Sci. Technol. 17 (2001) 366–375. doi:10.1179/026708301101510087.

[86] A.B. Short, Gas tungsten arc welding of α + β titanium alloys: A review, Mater. Sci. Technol. 25 (2009) 309–324. doi:10.1179/174328408X389463.

[87] J. Oh, N.J. Kim, S. Lee, E.W. Lee, Correlation of fatigue properties and microstructure in

investment cast Ti-6Al-4V welds, Mater. Sci. Eng. A. 340 (2003) 232–242. doi:10.1016/S0921-5093(02)00176-4.

[88] J. Ault, J. Pillers, S. Veeck, The GTAW of Ti-6Al-4V Castings and Its Effect on Microstructural and Mechanical Properties, 2005.

[89] W.J. Boettinger, M.E. Williams, S.R. Coriell, U.R. Kattner, B.A. Mueller, Alpha Case Thickness Modeling in Investment Castings, Metall. Mater. Trans. B. 31B (2000) 1419–1427.

[90] K.S. Chan, M. Koike, B.W. Johnson, T. Okabe, Modeling of alpha-case formation and its effects on the mechanical properties of titanium alloy castings, Metall. Mater. Trans. A Phys. Metall. Mater. Sci. 39 (2008) 171–180. doi:10.1007/s11661-007-9406-0.

[91] M.T. Mohammed, V.G.S. Semelov, A.V.S. Sotov, SLM-built titanium materials: Great potential of developing microstructure and properties for biomedical applications: A review, Mater. Res. Express. 6 (2019). doi:10.1088/2053-1591/ab624c.

[92] S. Kumar, A.K.S. Choudhary, A.K. Singh, A.K. Gupta, A Comparison of Additive Manufacturing Technologies, Int. J. Innov. Res. Sci. Technol. 3 (2016) 147–152. http://www.ijirst.org/articles/IJIRSTV3I1093.pdf.

[93] T. DebRoy, H.L. Wei, J.S. Zuback, T. Mukherjee, J.W. Elmer, J.O. Milewski, A.M. Beese, A. Wilson-Heid, A. De, W. Zhang, Additive manufacturing of metallic components – Process, structure and properties, Prog. Mater. Sci. 92 (2018) 112–224. doi:10.1016/J.PMATSCI.2017.10.001.

[94] J. Kim, A. Wakai, A. Moridi, Materials and manufacturing renaissance: Additive manufacturing of high-entropy alloys, J. Mater. Res. 35 (2020) 1963–1983. doi:10.1557/jmr.2020.140.

[95] H. Attar, K.G. Prashanth, A.K. Chaubey, M. Calin, L.C. Zhang, S. Scudino, J. Eckert, Comparison of wear properties of commercially pure titanium prepared by selective laser melting and casting processes, Mater. Lett. 142 (2015) 38–41. doi:10.1016/J.MATLET.2014.11.156.

[96] W. Zhang, P. Qin, Z. Wang, C. Yang, L. Kollo, D. Grzesiak, K. Gokuldoss Prashanth, materials Superior Wear Resistance in EBM-Processed TC4 Alloy Compared with SLM and Forged Samples, (n.d.). doi:10.3390/ma12050782.

[97] M. Ansari, A. Martinez-Marchese, Y. Huang, E. Toyserkani, A mathematical model of laser directed energy deposition for process mapping and geometry prediction of Ti-5553 single-tracks, Materialia. 12 (2020). doi:10.1016/J.MTLA.2020.100710.

[98] L. Costa, I. Felde, T. Réti, Z. Kálazi, R. Colaço, R. Vilar, B. Vero, A simplified semi-empirical method to select the processing parameters for laser clad coatings, Mater. Sci. Forum. 414–415 (2003) 385–394. doi:10.4028/www.scientific.net/msf.414-415.385.

[99] T.R. Walker, C.J. Bennett, T.L. Lee, A.T. Clare, A novel numerical method to predict the transient track geometry and thermomechanical effects through in-situ modification of the process parameters in Direct Energy Deposition, Finite Elem. Anal. Des. 169 (2020). doi:10.1016/J.FINEL.2019.103347.

[100] H.-L. Huang, D. Li, C. Chao, R.-D. Li, X.-Y. Zhang, S.-C. Liu, Z. Ke-Chao(周科朝, K.-C. Zhou, Selective laser melted near-beta titanium alloy Ti-5Al-5Mo-5V-1Cr-1Fe : Microstructure and mechanical properties, J. Cent. South Univ. 28 (2021) 1601–1614. doi:10.1007/s11771-021-4720-z.

[101] J. Zhang, M. Bermingham, J. Otte, Y. Liu, M. Dargusch, Towards uniform and enhanced tensile ductility of additively manufactured Ti−5Al−5Mo−5V−3Cr alloy through designing gradient interlayer deposition time, Scr. Mater. 223 (2023) 115066. doi:10.1016/J.SCRIPTAMAT.2022.115066.

[102] M. Ahmed, M.A. Obeidi, S. Yin, R. Lupoi, Influence of processing parameters on density, surface morphologies and hardness of as-built Ti-5Al-5Mo-5V-3Cr alloy manufactured by selective laser melting, J. Alloys Compd. 910 (2022). doi:10.1016/J.JALLCOM.2022.164760.

[103] A. Zafari, P. Chandran, K. Xia, Superior tensile properties in additively manufactured Ti alloys, Aust. J. Mech. Eng. (2021) 1–7. doi:10.1080/14484846.2021.1979924.

[104] A. Zafari, E.W.C. Lui, M. Li, K. Xia, Enhancing work hardening and ductility in additively manufactured β Ti: roles played by grain orientation, morphology and substructure, J. Mater. Sci. Technol. 105 (2022) 131–141. doi:10.1016/j.jmst.2021.08.006.

[105] C. Hicks, G. Sivaswamy, T. Konkova, P. Blackwell, Anisotropic tensile properties and failure mechanism of laser metal deposited Ti–5Al–5Mo–5V–3Cr alloy before and after sub-transus heat-treatment, Mater. Sci. Eng. A. 825 (2021). doi:10.1016/J.MSEA.2021.141928.

[106] T. Furuhara, H. Nakamori, T. Maki, Crystallography of α Phase Precipitated on Dislocations and Deformation Twin Boundaries in a β Titanium Alloy, Mater. Trans. JIM. 33 (1992) 585–595. doi:10.2320/matertrans1989.33.585.

[107] N. Yumak, K. Aslantas, A review on heat treatment efficiency in metastable b titanium alloys: The role of treatment process and parameters, J. Mater. Res. Technol. 9 (2020) 15360–16280. doi:10.1016/J.JMRT.2020.10.088.

[108] L.C. Campanelli, P.S.C.P. da Silva, C. Bolfarini, High cycle fatigue and fracture behavior of Ti-5Al-5Mo-5V-3Cr alloy with BASCA and double aging treatments, Mater. Sci. Eng. A. 658 (2016) 203–209. doi:10.1016/J.MSEA.2016.02.004.

[109] L.E. Murr, S.A. Quinones, S.M. Gaytan, M.I. Lopez, A. Rodela, E.Y. Martinez, D.H. Hernandez, E. Martinez, F. Medina, R.B. Wicker, Microstructure and mechanical behavior of Ti-6Al-4V produced by rapid-layer manufacturing, for biomedical applications, J. Mech. Behav. Biomed. Mater. (2009) 20–32. doi:10.1016/j.jmbbm.2008.05.004.

[110] H. Fujii, H. Suzuki G., Effect of solutioning conditions on aging response in Tie15Ve3Cre3Sne3Al, Mater Trans, JIM. 34 (1993) 373–381. https://doi.org/10.2320/matertrans1989.34.373.

[111] H. Deng, L. Chen, W. Qiu, Z. Zheng, Y. Tang, Z. Hu, Y. Wei, Z. Xia, G. Le, J. Tang, X. Cui, Microstructure and mechanical properties of as-deposited and heat treated Ti–5Al–5Mo–5V–3Cr–1Zr (Ti-55531) alloy fabricated by laser melting deposition, J. Alloys

Compd. 810 (2019). doi:10.1016/J.JALLCOM.2019.151792.

[112] C. Wu, M. Zhan, Microstructural evolution, mechanical properties and fracture toughness of near β titanium alloy during different solution plus aging heat treatments, J. Alloys Compd. 805 (2019) 1144–1160. doi:10.1016/J.JALLCOM.2019.07.134.

[113] A.M. Anushree Kirthika, · M Nageswara Rao, G. Manivasagam, Duplex aging of metastable beta titanium alloys: A Review, 1 (n.d.) 3. doi:10.1007/s12666-022-02696-1.

[114] Z.X. Du, S.L. Xiao, Y.P. Shen, J.S. Liu, J.S. Liu, L.J. Xu, F.T. Kong, Y.Y. Chen, Effect of hot rolling and heat treatment on microstructure and tensile properties of high strength beta titanium alloy sheets, Mater. Sci. Eng. A. 631 (2015) 67–74. http://dx.doi.org/10.1016/j.msea.2015.02.030 (accessed October 18, 2022).

[115] C.L. Li, X.J. Mi, W.J. Ye, S.X. Hui, Y. Yu, W.Q. Wang, Effect of solution temperature on microstructures and tensile properties of high strength Ti-6Cr-5Mo-5V-4Al alloy, Mater. Sci. Eng. A. 578 (2013) 103–109. doi:10.1016/J.MSEA.2013.04.063.

[116] A. Devaraj, V. V Joshi, A. Srivastava, S. Manandhar, V. Moxson, V.A. Duz, C. Lavender, A low-cost hierarchical nanostructured beta-titanium alloy with high strength, Nat. Commun. 6 (2016). doi:10.1038/ncomms11176.

[117] D. Parkes, D. Westerbaan, S.S. Nayak, Y. Zhou, F. Goodwin, S. Bhole, D.L. Chen, Tensile properties of fiber laser welded joints of high strength low alloy and dual-phase steels at warm and low temperatures, Mater. Des. 56 (2014) 193–199. doi:10.1016/j.matdes.2013.10.087.

[118] K. Yue, J. Liu, S. Zhu, L. Wang, Q. Wang, R. Yang, Origins of different tensile behaviors induced by cooling rate in a near alpha titanium alloy Ti65, Materialia. 1 (2018) 128–138. doi:10.1016/J.MTLA.2018.06.005.

[119] O.M. Ivasishin, P.E. Markovsky, S.L. Semiatin, C.H. Ward, Aging response of coarse- and fine-grained β titanium alloys, Mater. Sci. Eng. A. 405 (2005) 296–305. doi:10.1016/J.MSEA.2005.06.027.

[120] R. Santhosh, M. Geetha, M. Nageswara Rao, Recent Developments in Heat Treatment of Beta Titanium Alloys for Aerospace Applications, Trans. Indian Inst. Met. 70 (2017) 1681–1688. doi:10.1007/S12666-016-0985-6.

[121] X. Wu, J. del Prado, Q. Li, A. Huang, D. Hu, M.H. Loretto, Analytical electron microscopy of C-free and C-containing Ti-15-3, Acta Mater. 54 (2006) 5433–5448. doi:10.1016/J.ACTAMAT.2006.07.002.

[122] N. Wain, X.J. Hao, G.A. Ravi, X. Wu, The influence of carbon on precipitation of α in Ti-5Al-5Mo-5V-3Cr, Mater. Sci. Eng. A. 527 (2010) 7673–7683. doi:10.1016/J.MSEA.2010.08.032.

[123] C. Huang, Y. Zhao, S. Xin, W. Zhou, Q. Li, W. Zeng, Effect of microstructure on tensile properties of Ti–5Al–5Mo–5V–3Cr–1Zr alloy, J. Alloys Compd. 693 (2017) 582–591. doi:10.1016/j.jallcom.2016.09.233.

[124] L.C. Campanelli, P.S.C.P. da Silva, C. Bolfarini, High cycle fatigue and fracture behavior

of Ti-5Al-5Mo-5V-3Cr alloy with BASCA and double aging treatments, Mater. Sci. Eng. A. 658 (2016) 203–209. doi:10.1016/j.msea.2016.02.004.

[125] H. Bai, H. Deng, L. Chen, X. Liu, X. Qin, D. Zhang, T. Liu, X. Cui, Effect of heat treatment on the microstructure and mechanical properties of selective laser-melted Ti64 and Ti-5Al-5Mo-5v-1Cr-1Fe, Metals (Basel). 11 (2021). doi:10.3390/MET11040534.

[126] B.S. Hickman, The Formation of Omega Phase in Titanium and Zirconium Alloys: A Review, 1969.

[127] Y. Mantani, Y. Takemoto, M. Hida, A. Sakakibara, M. Tajima, Phase transformation of α″ martensite structure by aging in Ti-8mass%Mo alloy, Mater. Trans. 45 (2004) 1629–1634. doi:10.2320/matertrans.45.1629.

[128] A. Gysler, G. Lütjering, V. Gerold, Deformation behavior of age-hardened Ti-Mo alloys, Acta Metall. 22 (1974) 901–909. doi:10.1016/0001-6160(74)90057-1.

[129] N. Yumak, K. Aslantas, W. Ahmed, Effect of aging treatment on the initiation and propagation of fatigue cracks in the Ti-15V-3Al-3Sn-3Cr metastable β titanium alloy, 2020 Adv. Sci. Eng. Technol. Int. Conf. ASET 2020. (2020). doi:10.1109/ASET48392.2020.9118214.

[130] R. Gaddam, B. Sefer, R. Pederson, M.L. Antti, Study of alpha-case depth in Ti-6Al-2Sn-4Zr-2Mo and Ti-6Al-4V, IOP Conf. Ser. Mater. Sci. Eng. 48 (2013). doi:10.1088/1757-899X/48/1/012002.

[131] B. Sefer, I. Dobryden, N. Almqvist, R. Pederson, M.L. Antti, Chemical milling of cast Ti-6Al-4V and Ti-6Al-2Sn-4Zr-2Mo alloys in hydrofluoric-nitric acid solutions, Corrosion. 73 (2017) 394–407. doi:10.5006/2277.

[132] G.Z. Chen, D.J. Fray, T.W. Farthing, Cathodic deoxygenation of the alpha case on titanium and alloys in molten calcium chloride, Metall. Mater. Trans. B Process Metall. Mater. Process. Sci. 32 (2001) 1041–1052. doi:10.1007/s11663-001-0093-8.

[133] T.M. Yue, J.K. Yu, Z. Mei, H.C. Man, Excimer laser surface treatment of Ti-6Al-4V alloy for corrosion resistance enhancement, Mater. Lett. 52 (2002) 206–212. doi:10.1016/S0167-577X(01)00395-0.

[134] C. Langlade, A.B. Vannes, J.M. Krafft, J.R. Martin, Surface modification and tribological behaviour of titanium and titanium alloys after YAG-laser treatments, Surf. Coatings Technol. 100–101 (1998) 383–387. doi:10.1016/S0257-8972(97)00653-1.

[135] Y.S. Tian, C.Z. Chen, S.T. Li, Q.H. Huo, Research progress on laser surface modification of titanium alloys, Appl. Surf. Sci. 242 (2005) 177–184. doi:10.1016/J.APSUSC.2004.08.011.

[136] L. Yue, Z. Wang, L. Li, Material morphological characteristics in laser ablation of alpha case from titanium alloy, Appl. Surf. Sci. 258 (2012) 8065–8071. doi:10.1016/J.APSUSC.2012.04.173.

[137] N. Ramachandiran, H. Asgari, F. Dibia, R. Eybel, A. Gerlich, E. Toyserkani, Effect of non-lamellar α precipitate morphology on the mechanical properties of Ti5553 parts made by

laser powder-bed fusion at high laser scan speeds, Mater. Sci. Eng. A. 841 (2022). doi:10.1016/j.msea.2022.143039.

[138] ASTM International, Standard Test Method for Microindentation Hardness of Materials, Am. Soc. Test. Mater. Handb. (2017) 281–293. doi:10.1520/E0384-17.

[139] ASTM E8, ASTM E8/E8M standard test methods for tension testing of metallic materials 1, Annu. B. ASTM Stand. 4. (2010) 1–27. doi:10.1520/E0008.

[140] ASTM International, ASTM E23 − 18, Standard Test Methods for Notched Bar Impact Testing of Metallic Materials, ASTM Int. (2018) 1–26. doi:10.1520/E0023-18.

[141] S. Sadeghpour, S.M.M. Abbasi, M. Morakabati, S. Bruschi, Correlation between alpha phase morphology and tensile properties of a new beta titanium alloy, Mater. Des. 121 (2017) 24–35. doi:10.1016/j.matdes.2017.02.043.

[142] M.K. Keshavarz, F. Sikan, C.E. Boutet, J. Milligan, A. Bois-Brochu, M. Brochu, Impact properties of half stress-relieved and hot isostatic pressed Ti–6Al–4V components fabricated by laser powder bed fusion, Mater. Sci. Eng. A. (2019). doi:10.1016/j.msea.2019.05.035.

[143] Gerday, Mechanical behavior of Ti -5553 alloy Modeling of representative cells, 2009. http://bictel.ulg.ac.be/ETD-db/collection/available/ULgetd-07142009-142010/unrestricted/THESE_AFGerday.pdf.

[144] I. Gibson, D. Rosen, B. Strucker, Additive Manufacturing Technologies - 3D printing, rapid prototyping, and direcct digital maufacturing, 2nd ed., Springer, New York, 2015.

[145] M. V Gerov, E.Y. Vladislavskaya, V.F. Terent'ev, D. V Prosvirnin, A.G. Kolmakov, O.S. Antonova, Fatigue Strength of a Ti-6Al-4V Alloy Produced by Selective Laser Melting, 2016 (2016) 14–20. doi:10.1134/S0036029516100049.

[146] J. Suryawanshi, K.G. Prashanth, U. Ramamurty, Mechanical behavior of selective laser melted 316L stainless steel, Mater. Sci. Eng. A. 696 (2017) 113–121. doi:10.1016/j.msea.2017.04.058.

[147] P. Kumar, U. Ramamurty, Microstructural optimization through heat treatment for enhancing the fracture toughness and fatigue crack growth resistance of selective laser melted Ti–6Al–4V alloy, Acta Mater. 169 (2019) 45–59. doi:10.1016/J.ACTAMAT.2019.03.003.

[148] Y.J. Liang, H.M. Wang, Influence of prior-β-grain size on tensile strength of a laser-deposited α/β titanium alloy at room and elevated temperatures, Mater. Sci. Eng. A. 622 (2015) 16–20. doi:10.1016/j.msea.2014.11.014.

[149] G.T. Terlinde, T.W. Duerig, J.C. Williams, and Fracture in Aged Ti 10V-2Fe-3AI, (1983) 2101–2115.

[150] S. Pauly, P. Wang, U. Kühn, K. Kosiba, Experimental determination of cooling rates in selectively laser-melted eutectic Al-33Cu, Addit. Manuf. 22 (2018) 753–757. doi:10.1016/j.addma.2018.05.034.

[151] B. Vrancken, L. Thijs, J.-P. Kruth, J. Van Humbeeck, Heat treatment of Ti6Al4V produced by Selective Laser Melting: Microstructure and mechanical properties, J. Alloys Compd. 541 (2012) 177–185. doi:10.1016/j.jallcom.2012.07.022.

[152] C.M. Liu, H.M. Wang, X.J. Tian, H.B. Tang, D. Liu, Microstructure and tensile properties of laser melting deposited Ti-5Al-5Mo-5V-1Cr-1Fe near β titanium alloy, Mater. Sci. Eng. A. 586 (2013) 323–329. doi:10.1016/j.msea.2013.08.032.

[153] L. Thijs, F. Verhaeghe, T. Craeghs, J. Van Humbeeck, J.-P. Kruth, A study of the microstructural evolution during selective laser melting of Ti-6Al-4V, Acta Mater. 58 (2010) 3303–3312. doi:10.1016/j.actamat.2010.02.004.

[154] Q. Huang, N. Hu, X. Yang, R. Zhang, Q. Feng, Microstructure and inclusion of Ti–6Al–4V fabricated by selective laser melting, Front. Mater. Sci. 10 (2016) 428–431. doi:10.1007/s11706-016-0354-8.

[155] T. Li, M. Ahmed, G. Sha, R. Shi, G. Casillas, H.W. Yen, Y. Wang, E. V. Pereloma, J.M. Cairney, The influence of partitioning on the growth of intragranular α in near-β Ti alloys, J. Alloys Compd. 643 (2015) 212–222. doi:10.1016/j.jallcom.2015.04.143.

[156] S.K. Kar, S. Suman, S. Shivaprasad, A. Chaudhuri, A. Bhattacharjee, Processing-microstructure-yield strength correlation in a near β Ti alloy, Ti-5Al-5Mo-5V-3Cr, Mater. Sci. Eng. A. (2014). doi:10.1016/j.msea.2014.04.113.

[157] H. Asgari, C. Baxter, K. Hosseinkhani, M. Mohammadi, On microstructure and mechanical properties of additively manufactured AlSi10Mg_200C using recycled powder, Mater. Sci. Eng. A. 707 (2017) 148–158. doi:10.1016/j.msea.2017.09.041.

[158] G.C. Obasi, S. Birosca, J. Quinta Da Fonseca, M. Preuss, Effect of β grain growth on variant selection and texture memory effect during α → β → α phase transformation in Ti-6 Al-4 v, Acta Mater. (2012). doi:10.1016/j.actamat.2011.10.038.

[159] H. Asgari, M. Salarian, H. Ma, A. Olubamiji, M. Vlasea, On thermal expansion behavior of invar alloy fabricated by modulated laser powder bed fusion, Mater. Des. 160 (2018) 895–905. doi:10.1016/j.matdes.2018.10.025.

[160] T. Nagase, T. Hori, M. Todai, S.H. Sun, T. Nakano, Additive manufacturing of dense components in beta-titanium alloys with crystallographic texture from a mixture of pure metallic element powders, Mater. Des. 173 (2019) 107771. doi:10.1016/j.matdes.2019.107771.

[161] R.R. Boyer, G.W. Kuhlman, Processing Properties Relationships of Ti-10V-2Fe-3AI, Metall. Trans. A. 18A (1987) 2095–103. https://link.springer.com/content/pdf/10.1007%2FBF02647081.pdf (accessed March 18, 2019).

[162] C.C. Chen, J.A. Hall, R.R. Boyer, Titanium'by H, Kimura O. Izumi. 457 (1980).

[163] L.X. Li, Y. Lou, L.B. Yang, D.S. Peng, K.P. Rao, Flow stress behavior and deformation characteristics of Ti-3Al-5V-5Mo compressed at elevated temperatures, 2002. https://ac.els-cdn.com/S0261306902000250/1-s2.0-S0261306902000250-main.pdf?_tid=55b7cb56-e305-4e06-a8bf-

c04efb6d07d3&acdnat=1552493870_f399a978aa482fcfcac4230b1791e2ae (accessed March 13, 2019).

[164] I. Philippart, H.J. Rack, High temperature dynamic yielding in metastable Ti-6.8Mo-4.5F-1.5Al, 1998.

[165] N.G. Jones, R.J. Dashwood, M. Jackson, D. Dye, β Phase decomposition in Ti-5Al-5Mo-5V-3Cr, Acta Mater. 57 (2009) 3830–3839. doi:10.1016/j.actamat.2009.04.031.

[166] S. Nag, R. Banerjee, R. Srinivasan, J.Y. Hwang, M. Harper, H.L. Fraser, ω-Assisted nucleation and growth of α precipitates in the Ti-5Al-5Mo-5V-3Cr-0.5Fe β titanium alloy, Acta Mater. 57 (2009) 2136–2147. doi:10.1016/j.actamat.2009.01.007.

[167] E. Aeby-Gautier, A. Settefrati, F. Bruneseaux, B. Appolaire, B. Denand, M. Dehmas, G. Geandier, P. Boulet, Isothermal α″ formation in β metastable titanium alloys, J. Alloys Compd. 577 (2013) S439–S443. doi:10.1016/j.jallcom.2012.02.046.

[168] J.K. Fan, J.S. Li, H.C. Kou, K. Hua, B. Tang, The interrelationship of fracture toughness and microstructure in a new near β titanium alloy Ti-7Mo-3Nb-3Cr-3Al, Mater. Charact. 96 (2014) 93–99. doi:10.1016/j.matchar.2014.07.018.

[169] N. Wain, X.J. Hao, G.A. Ravi, X. Wu, The influence of carbon on precipitation of in Ti-5Al-5Mo-5V-3Cr, Mater. Sci. Eng. A. 527 (2010) 7673–7683. doi:10.1016/j.msea.2010.08.032.

[170] K. Gu, B. Zhao, Z. Weng, K. Wang, H. Cai, J. Wang, Microstructure evolution in metastable β titanium alloy subjected to deep cryogenic treatment, Mater. Sci. Eng. A. 723 (2018) 157–164. doi:10.1016/J.MSEA.2018.03.003.

[171] K. Yamanaka, W. Saito, M. Mori, H. Matsumoto, A. Chiba, Preparation of weak-textured commercially pure titanium by electron beam melting, Addit. Manuf. 8 (2015) 105–109. doi:10.1016/j.addma.2015.09.007.

[172] C.L. Li, J.W. Won, S.W. Choi, J.H. Choe, S. Lee, C.H. Park, J.T. Yeom, J.K. Hong, Simultaneous achievement of equiaxed grain structure and weak texture in Pure Titanium via selective laser melting and subsequent heat treatment, J. Alloys Compd. 803 (2019) 407–412. doi:10.1016/j.jallcom.2019.06.305.

[173] W. Li, J. Liu, Y. Zhou, S. Wen, Q. Wei, C. Yan, Y. Shi, Effect of substrate preheating on the texture, phase and nanohardness of a Ti-45Al-2Cr-5Nb alloy processed by selective laser melting, Scr. Mater. 118 (2016) 13–18. doi:10.1016/j.scriptamat.2016.02.022.

[174] Y. Chen, Z. Du, S. Xiao, L. Xu, J. Tian, Effect of aging heat treatment on microstructure and tensile properties of a new β high strength titanium alloy, J. Alloys Compd. 586 (2014) 588–592. doi:10.1016/j.jallcom.2013.10.096.

[175] C.M. Liu, H.M. Wang, X.J. Tian, H.B. Tang, Subtransus triplex heat treatment of laser melting deposited Ti-5Al-5Mo-5V-1Cr-1Fe near β titanium alloy, Mater. Sci. Eng. A. 590 (2014) 30–36. doi:10.1016/j.msea.2013.10.002.

[176] D. Kent, G. Wang, W. Wang, M.S. Dargusch, Influence of ageing temperature and heating rate on the properties and microstructure of β Ti alloy, Ti-6Cr-5Mo-5V-4Al, Mater. Sci.

Eng. A. 531 (2012) 98–106. doi:10.1016/j.msea.2011.10.040.

[177] K. Wang, R. Bao, D. Liu, C. Yan, Plastic anisotropy of laser melting deposited Ti – 5Al – 5Mo – 5V – 1Cr – 1Fe titanium alloy, Mater. Sci. Eng. A. 746 (2019) 276–289. doi:10.1016/j.msea.2019.01.031.

[178] D. De Fontaine, N.E. Paton, J.C. Williams, The omega phase transformation in titanium alloys as an example of displacement controlled reactions, Acta Metall. 19 (1971) 1153–1162. doi:10.1016/0001-6160(71)90047-2.

[179] T. Vilaro, C. Colin, J.D. Bartout, As-fabricated and heat-treated microstructures of the Ti-6Al-4V alloy processed by selective laser melting, Metall. Mater. Trans. A Phys. Metall. Mater. Sci. 42 (2011) 3190–3199. doi:10.1007/s11661-011-0731-y.

[180] S.A. Mantri, D. Choudhuri, A. Behera, J.D. Cotton, N. Kumar, R. Banerjee, Communication Influence of Fine-Scale Alpha Precipitation on the Mechanical Properties of the Beta Titanium Alloy Beta-21S, Metall. Mater. Trans. A. 46 (2015). doi:10.1007/s11661-015-2944-y.

[181] T. Ishimoto, K. Hagihara, K. Hisamoto, S.H. Sun, T. Nakano, Crystallographic texture control of beta-type Ti–15Mo–5Zr–3Al alloy by selective laser melting for the development of novel implants with a biocompatible low Young's modulus, Scr. Mater. 132 (2017) 34–38. doi:10.1016/j.scriptamat.2016.12.038.

[182] R.W. Messler Jr, Principles of welding: processes, physics, chemistry, and metallurgy, John Wiley & Sons, 2008.

[183] B. Vrancken, L. Thijs, J.P. Kruth, J. Van Humbeeck, Microstructure and mechanical properties of a novel β titanium metallic composite by selective laser melting, Acta Mater. 68 (2014) 150–158. doi:10.1016/j.actamat.2014.01.018.

[184] N.G. Jones, R.J. Dashwood, M. Jackson, D. Dye, Development of chevron-shaped α precipitates in Ti-5Al-5Mo-5V-3Cr, Scr. Mater. 60 (2009) 571–573. doi:10.1016/j.scriptamat.2008.12.010.

[185] C.M. Liu, H.M. Wang, X.J. Tian, D. Liu, Development of a pre-heat treatment for obtaining discontinuous grain boundary α in laser melting deposited Ti-5Al-5Mo-5V-1Cr-1Fe alloy, Mater. Sci. Eng. A. 604 (2014) 176–182. doi:10.1016/j.msea.2014.03.028.

[186] C. Huang, Y. Zhao, S. Xin, W. Zhou, Q. Li, W. Zeng, Effect of microstructure on torsion properties of Ti–5Al–5Mo–5V–3Cr–1Zr alloy, Mater. Sci. Eng. A. (2017). doi:10.1016/j.msea.2016.11.049.

[187] K. Václavová, J. Stráský, P. Zháňal, J. Veselý, V. Polyakova, I. Semenova, M. Janeček, Ultra-fine grained microstructure of metastable beta Ti-15Mo alloy and its effects on the phase transformations, in: IOP Conf. Ser. Mater. Sci. Eng., Institute of Physics Publishing, 2017. doi:10.1088/1757-899X/194/1/012021.

[188] A. Pineau, A.A. Benzerga, T. Pardoen, Failure of metals I: Brittle and ductile fracture, Acta Mater. 107 (2016) 424–483. doi:10.1016/j.actamat.2015.12.034.

[189] R. Sabban, S. Bahl, K. Chatterjee, S. Suwas, Globularization using heat treatment in

additively manufactured Ti-6Al-4V for high strength and toughness, Acta Mater. 162 (2019) 239–254. doi:10.1016/j.actamat.2018.09.064.

[190] H. Ogi, S. Kai, H. Ledbetter, R. Tarumi, M. Hirao, K. Takashima, Titanium's high-temperature elastic constants through the hcp-bcc phase transformation, Acta Mater. 52 (2004) 2075–2080. doi:10.1016/J.ACTAMAT.2004.01.002.

[191] X. Yan, S. Yin, C. Chen, C. Huang, R. Bolot, R. Lupoi, M. Kuang, W. Ma, C. Coddet, H. Liao, M. Liu, Effect of heat treatment on the phase transformation and mechanical properties of Ti6Al4V fabricated by selective laser melting, J. Alloys Compd. 764 (2018) 1056–1071. doi:10.1016/j.jallcom.2018.06.076.

[192] R. Nivas, G. Das, S.K. Das, B. Mahato, S. Kumar, K. Sivaprasad, P.K. Singh, M. Ghosh, Effect of Stress Relief Annealing on Microstructure & Mechanical Properties of Welded Joints Between Low Alloy Carbon Steel and Stainless Steel, Metall. Mater. Trans. A. (2016). doi:10.1007/s11661-016-3840-9.

[193] R.G. Baggerly, Determination of omega phase volume fraction in single crystals of beta titanium alloys, Metallography. 8 (1975) 361–373. doi:10.1016/0026-0800(75)90006-3.

[194] T. Furuhara, T. Maki, Variant selection in heterogeneous nucleation on defects in diffusional phase transformation and precipitation, 2001. www.elsevier.com/locate/msea.

[195] S. Nag, Y. Zheng, R.E.A. Williams, A. Devaraj, A. Boyne, Y. Wang, P.C. Collins, G.B. Viswanathan, J.S. Tiley, B.C. Muddle, R. Banerjee, H.L. Fraser, Non-classical homogeneous precipitation mediated by compositional fluctuations in titanium alloys, (2012). doi:10.1016/j.actamat.2012.07.033.

[196] S.A. Mantri, D. Choudhuri, T. Alam, G.B. Viswanathan, J.M. Sosa, H.L. Fraser, R. Banerjee, Tuning the scale of α precipitates in β-titanium alloys for achieving high strength, (2018). doi:10.1016/j.scriptamat.2018.05.040.

[197] H.I. Aaronson, G. Spanos, R.A. Masamura, R.G. Vardiman, D.W. Moon, E.S.K. Menon, M.G. Hall, Sympathetic nucleation: an overview, Mater. Sci. Eng. B. 32 (1995). doi:10.1016/0921-5107(95)80022-0.

[198] E.S.K. Menon, H.I. Aaronson, Overview no. 57 Morphology, crystallography and kinetics of sympathetic nucleation, Acta Metall. 35 (1987). doi:10.1016/0001-6160(87)90179-9.

[199] S.Q. Wu, Y.J. Lu, Y.L. Gan, T.T. Huang, C.Q. Zhao, J.X.J. Lin, S. Guo, J.X.J. Lin, Microstructural evolution and microhardness of a selective-laser-melted Ti-6Al-4V alloy after post heat treatments, J. Alloys Compd. 672 (2016) 643–652. doi:10.1016/j.jallcom.2016.02.183.

[200] Y. Ni, A.G. Khachaturyan, From chessboard tweed to chessboard nanowire structure during pseudospinodal decomposition, Nat. Mater. 8 (2009) 410–414. doi:10.1038/nmat2431.

[201] G.Q. Wu, C.L. Shi, W. Sha, A.X. Sha, H.R. Jiang, Microstructure and high cycle fatigue fracture surface of a Ti-5Al-5Mo-5V-1Cr-1Fe titanium alloy, Mater. Sci. Eng. A. 575 (2013) 111–118. doi:10.1016/j.msea.2013.03.047.

[202] W. Zhu, Q. Sun, C. Tan, P. Li, L. Xiao, J. Sun, Tensile brittleness and ductility improvement

in a novel metastable β titanium alloy with lamella structure, J. Alloys Compd. 827 (2020). doi:10.1016/j.jallcom.2020.154311.

[203] N. Shamsaei, A. Yadollahi, L. Bian, S.M. Thompson, An overview of Direct Laser Deposition for additive manufacturing; Part II: Mechanical behavior, process parameter optimization and control, Addit. Manuf. 8 (2015) 12–35. doi:10.1016/j.addma.2015.07.002.

[204] D. Qin, Y. Lu, D. Guo, L. Zheng, Q. Liu, L. Zhou, On preparation of bimodal Ti-5Al-5V-5Mo-3Cr-0.4Si (Ti-5553s) alloy: α+β forging and heat treatment, Mater. Sci. Eng. A. 609 (2014) 42–52. doi:10.1016/j.msea.2014.04.056.

[205] E. Toyserkani, D. Sarker, O.O. Ibhadode, F. Liravi, P. Russo, K. Taherkhani, Metal additive manufacturing, John Wiley & Sons, 2021.

[206] E.S.K. Menon, H.I. Aaronson, Morphology, crystallography and kinetics of sympathetic nucleation, Acta Metall. 35 (1987) 549–563. doi:10.1016/0001-6160(87)90179-9.

[207] Heat-treatment induced microstructural evolution and enhanced mechanical property of selective laser melted near β Ti-5Al-5Mo-5 V-3Cr-1Zr alloy, J. Alloys Compd. 858 (2020). https://reader.elsevier.com/reader/sd/pii/S0925838820347149?token=94BF15F409C873E5EC38981508660D9DD3136BFBEF70835E784E08C97F84E0BB3DA02D0E9D81A1D44B804C83A90C634C (accessed January 12, 2021).

[208] S.K. Kar, A. Ghosh, N. Fulzele, A. Bhattacharjee, Quantitative microstructural characterization of a near beta Ti alloy, Ti-5553 under different processing conditions, Mater. Charact. 81 (2013) 37–48. doi:10.1016/j.matchar.2013.03.016.

[209] J.D.C. Teixeira, B. Appolaire, E. Aeby-Gautier, S. Denis, G. Cailletaud, N. Späth, Transformation kinetics and microstructures of Ti17 titanium alloy during continuous cooling, Mater. Sci. Eng. A. 448 (2007) 135–145. doi:10.1016/j.msea.2006.10.024.

[210] S.Y. Sung, Y.J. Kim, Alpha-case formation mechanism on titanium investment castings, Mater. Sci. Eng. A. 405 (2005) 173–177. doi:10.1016/j.msea.2005.05.092.

[211] R. Nivas, P.K. Singh, G. Das, S.K. Das, S. Kumar, B. Mahato, K. Sivaprasad, M. Ghosh, A comparative study on microstructure and mechanical properties near interface for dissimilar materials during conventional V-groove and narrow gap welding, J. Manuf. Process. 25 (2017) 274–283. doi:10.1016/j.jmapro.2016.12.004.

[212] N. Ramachandiran, H. Asgari, F. Dibia, R. Eybel, W. Muhammad, A. Gerlich, E. Toyserkani, Effects of post heat treatment on microstructure and mechanical properties of Ti5553 parts made by laser powder bed fusion, J. Alloys Compd. 938 (2023). doi:https://doi.org/10.1016/j.jallcom.2022.168616.

[213] K.S. McReynolds, S. Tamirisakandala, A study on alpha-case depth in Ti-6Al-2Sn-4Zr-2Mo, Metall. Mater. Trans. A Phys. Metall. Mater. Sci. 42 (2011) 1732–1736. doi:10.1007/s11661-011-0710-3.

[214] C.E. Shamblen, T.K. Redden, The Science, Technology and Application of Titanium, Pergamon, Oxford, 1966) P. 199 (1970).

[215] C. Leyens, M. Peters, Titanium and titanium alloys: fundamentals and applications, John

Wiley & Sons, 2003.

[216] P.A.J. Bagot, A. Radecka, A.P. Magyar, Y. Gong, D.C. Bell, G.D.W. Smith, M.P. Moody, D. Dye, D. Rugg, The effect of oxidation on the subsurface microstructure of a Ti-6Al-4V alloy, Scr. Mater. 148 (2018) 24–28. doi:10.1016/j.scriptamat.2018.01.015.

[217] H. Guleryuz, H. Cimenoglu, Oxidation of Ti-6Al-4V alloy, J. Alloys Compd. 472 (2009) 241–246. doi:10.1016/j.jallcom.2008.04.024.

[218] W. Jia, W. Zeng, X. Zhang, Y. Zhou, J. Liu, Q. Wang, Oxidation behavior and effect of oxidation on tensile properties of Ti60 alloy, J. Mater. Sci. 46 (2011) 1351–1358. doi:10.1007/s10853-010-4926-1.

[219] X. Zhang, H. Kou, J. Li, F. Zhang, L. Zhou, Evolution of the secondary a phase morphologies during isothermal heat treatment in Ti-7333 alloy, (2013). doi:10.1016/j.jallcom.2013.06.180.

[220] W.G. Burgers, On the process of transition of the cubic-body-centered modification into the hexagonal-close-packed modification of zirconium, Physica. 1 (1934) 561–586. doi:10.1016/S0031-8914(34)80244-3.

[221] K. Wang, M.Q. Li, Morphology and crystallographic orientation of the secondary α phase in a compressed α/β titanium alloy, Scr. Mater. 68 (2013) 964–967. doi:10.1016/j.scriptamat.2013.02.048.

[222] H.R. Ogden, R.I. Jaffee, The effects of carbon, oxygen and nitrogen on the mechanical properties of titanium and titanium alloys, Titan. Metall. Lab. XXXIII (2012) 81–87. http://www.ncbi.nlm.nih.gov/pubmed/15003161%5Cnhttp://cid.oxfordjournals.org/lookup/doi/10.1093/cid/cir991%5Cnhttp://www.scielo.cl/pdf/udecada/v15n26/art06.pdf%5Cnhttp://www.scopus.com/inward/record.url?eid=2-s2.0-84861150233&partnerID=tZOtx3y1.

[223] R.N. Shenoy, J. Unnam, R.K. Clarkt$, Oxidation and Embrittlement of Ti-6AI-2Sn-4Zr-2Mo Alloy, 1986.

[224] L. Bendersky, A. Rosen, The effect of exposure on fracture of Ti-6AL-4V alloy, Eng. Fract. Mech. 13 (1980) 111–118. doi:10.1016/0013-7944(80)90046-6.

[225] D. Qin, Y. Lu, D. Guo, L. Zheng, Q. Liu, L. Zhou, Tensile deformation and fracture of Ti-5Al-5V-5Mo-3Cr-1.5Zr-0.5Fe alloy at room temperature, Mater. Sci. Eng. A. 587 (2013) 100–109. doi:10.1016/j.msea.2013.08.055.

[226] D. Qin, Y. Lu, D. Guo, L. Zheng, Q. Liu, L. Zhou, Tensile deformation and fracture of Ti-5Al-5V-5Mo-3Cr-1.5Zr-0.5Fe alloy at room temperature, (2013). doi:10.1016/j.msea.2013.08.055.

[227] A. Keshavarzkermani, R. Esmaeilizadeh, P.D. Enrique, H. Asgari, N.Y. Zhou, A. Bonakdar, E. Toyserkani, Static recrystallization impact on grain structure and mechanical properties of heat-treated Hastelloy X produced via laser powder-bed fusion, Mater. Charact. 173 (2021). doi:10.1016/j.matchar.2021.110969.

[228] Y. Zhu, X. Tian, J. Li, H. Wang, The anisotropy of laser melting deposition additive manufacturing Ti-6.5Al-3.5Mo-1.5Zr-0.3Si titanium alloy, Mater. Des. 67 (2015) 538–542.

doi:10.1016/j.matdes.2014.11.001.

[229] A.N. Jinoop, J. Denny, C.P. Paul, J. Ganesh Kumar, K.S. Bindra, Effect of post heat-treatment on the microstructure and mechanical properties of Hastelloy-X structures manufactured by laser based Directed Energy Deposition, J. Alloys Compd. 797 (2019) 399–412. doi:10.1016/j.jallcom.2019.05.050.

[230] A.S. Khan, R. Kazmi, B. Farrokh, Multiaxial and non-proportional loading responses, anisotropy and modeling of Ti-6Al-4V titanium alloy over wide ranges of strain rates and temperatures, Int. J. Plast. 23 (2007) 931–950. doi:10.1016/j.ijplas.2006.08.006.

[231] D. Banerjee, J.C.C. Williams, Perspectives on titanium science and technology, Acta Mater. 61 (2013) 844–879. doi:10.1016/j.actamat.2012.10.043.

[232] M. Todai, T. Nakano, T. Liu, H.Y. Yasuda, K. Hagihara, K. Cho, M. Ueda, M. Takeyama, Effect of building direction on the microstructure and tensile properties of Ti-48Al-2Cr-2Nb alloy additively manufactured by electron beam melting, Addit. Manuf. 13 (2017) 61–70. doi:10.1016/j.addma.2016.11.001.

[233] L. Yan, Y. Yuan, L. Ouyang, H. Li, A. Mirzasadeghi, L. Li, Improved mechanical properties of the new Ti-15Ta-xZr alloys fabricated by selective laser melting for biomedical application, J. Alloys Compd. 688 (2016) 156–162. doi:10.1016/j.jallcom.2016.07.002.

[234] H. Xu, Z. Li, A. Dong, H. Xing, T. Zhang, D. Wang, G. Zhu, B. Sun, Study of superior strength in Ti15Mo alloy manufactured using selective laser melting, J. Alloys Compd. 885 (2021) 161186. doi:10.1016/j.jallcom.2021.161186.

[235] B.E. Carroll, T.A. Palmer, A.M. Beese, Anisotropic tensile behavior of Ti-6Al-4V components fabricated with directed energy deposition additive manufacturing, Acta Mater. 87 (2015) 309–320. doi:10.1016/j.actamat.2014.12.054.

[236] J. Yang, H. Yu, Z. Wang, X. Zeng, Effect of crystallographic orientation on mechanical anisotropy of selective laser melted Ti-6Al-4V alloy, Mater. Charact. 127 (2017) 137–145. doi:10.1016/j.matchar.2017.01.014.

[237] A.E. Wilson-Heid, Z. Wang, B. McCornac, A.M. Beese, Quantitative relationship between anisotropic strain to failure and grain morphology in additively manufactured Ti-6Al-4V, Mater. Sci. Eng. A. 706 (2017) 287–294. doi:10.1016/j.msea.2017.09.017.

[238] H. Huang, T. Zhang, C. Chen, S. Reza, E. Hosseini, J. Zhang, K. Zhou, Anisotropy in the Tensile Properties of a Selective Laser Melted Ti-5Al-5Mo-5V-1Cr-1Fe Alloy during Aging Treatment, Materials (Basel). 5493 (2022) 1–24. doi:https://doi.org/10.3390/ma15165493.

[239] F. Bridier, P. Villechaise, J. Mendez, Analysis of the different slip systems activated by tension in a α/β titanium alloy in relation with local crystallographic orientation, Acta Mater. 53 (2005) 555–567. doi:10.1016/j.actamat.2004.09.040.

[240] A. Serra, D.J. Bacon, R.C. Pond, Twins as Barriers to Basal Slip in Hexagonal-Close-Packed Metals, n.d.

[241] W. Chen, S. Cao, J. Zhang, Y. Zha, Q. Hu, J. Sun, New insights into ω-embrittlement in

high misfit metastable β-titanium alloys: Mechanically-driven ω-mediated amorphization, Mater. Des. 205 (2021) 109724. doi:10.1016/j.matdes.2021.109724.

[242] E. Brandl, B. Baufeld, C. Leyens, R. Gault, Additive manufactured Ti-6A1-4V using welding wire: Comparison of laser and arc beam deposition and evaluation with respect to aerospace material specifications, Phys. Procedia. 5 (2010) 595–606. doi:10.1016/J.PHPRO.2010.08.087.

[243] B. Baufeld, Effect of deposition parameters on mechanical properties of shaped metal deposition parts, (n.d.). doi:10.1177/0954405411403669.

[244] E. Liu, G. Xu, N. Wang, Analysis of Surface Morphology of Ti-5553 Based on Wavelet Transform, Integr. Ferroelectr. 217 (2021) 129–140. doi:10.1080/10584587.2021.1911304.

[245] M. Letenneur, V. Brailovski, A. Kreitcberg, V. Paserin, I. Bailon-Poujol, Laser Powder Bed Fusion of Water-Atomized Iron-Based Powders: Process Optimization, J. Manuf. Mater. Process. 1 (2017) 23. doi:10.3390/jmmp1020023.

[246] B. Song, S. Dong, B. Zhang, H. Liao, C. Coddet, Effects of processing parameters on microstructure and mechanical property of selective laser melted Ti6Al4V, Mater. Des. 35 (2012) 120–125. doi:10.1016/j.matdes.2011.09.051.

[247] M. Mazur, M. Leary, M. McMillan, J. Elambasseril, M. Brandt, SLM additive manufacture of H13 tool steel with conformal cooling and structural lattices, Rapid Prototyp. J. 22 (2016) 504–518. doi:10.1108/RPJ-06-2014-0075.

[248] N.M. Dhansay, R. Tait, T. Becker, Fatigue and Fracture Toughness of Ti-6Al-4V Titanium Alloy Manufactured by Selective Laser Melting, Adv. Mater. Res. 1019 (2014) 248–253. doi:10.4028/www.scientific.net/amr.1019.248.

[249] M. Rashid, J.B. Medley, Y. Zhou, Nugget formation and growth during resistance spot welding of aluminium alloy 5182, Can. Metall. Q. 50 (2011) 61–71. doi:10.1179/000844311X552322.

[250] K.S. Chan, M. Koike, R.L. Mason, T. Okabe, Fatigue Life of Titanium Alloys Fabricated by Additive Layer Manufacturing Techniques for Dental Implants, Metall. Mater. Trans. A. 44A (2013) 1010–1022. doi:10.1007/s11661-012-1470-4.

[251] A. Yadollahi, N. Shamsaei, S.M. Thompson, A. Elwany, L. Bian, Effects of building orientation and heat treatment on fatigue behavior of selective laser melted 17-4 PH stainless steel, Int. J. Fatigue. 94 (2017) 218–235. doi:10.1016/j.ijfatigue.2016.03.014.

[252] R.R. Dehoff, M.M. Kirka, W.J. Sames, H. Bilheux, A.S. Tremsin, L.E. Lowe, S.S. Babu, Site specific control of crystallographic grain orientation through electron beam additive manufacturing, Mater. Sci. Technol. 31 (2015) 931–938. doi:10.1179/1743284714Y.0000000734.

[253] D.D. Gu, W. Meiners, K. Wissenbach, R. Poprawe, Laser additive manufacturing of metallic components: materials, processes and mechanisms, Int. Mater. Rev. 57 (2012) 133–164. doi:10.1179/1743280411Y.0000000014.

[254] M.Y. Gutkin, T. Ishizaki, S. Kuramoto, I.A. Ovid'ko, N. V. Skiba, Giant faults in deformed

Gum Metal, Int. J. Plast. 24 (2008) 1333–1359. doi:10.1016/J.IJPLAS.2007.09.009.

[255] J.J. Bhattacharyya, S. Nair, D.C. Pagan, V. Tari, R.A. Lebensohn, A.D. Rollett, S.R. Agnew, Elastoplastic transition in a metastable β-Titanium alloy, Timetal-18 - An in-situ synchrotron X-ray diffraction study, Int. J. Plast. 139 (2021). doi:10.1016/J.IJPLAS.2021.102947.

[256] F. Mompiou, D. Tingaud, Y. Chang, B. Gault, G. Dirras, Conventional vs harmonic-structured β-Ti-25Nb-25Zr alloys: A comparative study of deformation mechanisms, Acta Mater. 161 (2018) 420–430. doi:10.1016/J.ACTAMAT.2018.09.032.

[257] M.J. Lai, C.C. Tasan, D. Raabe, Deformation mechanism of ω-enriched Ti-Nb-based gum metal: Dislocation channeling and deformation induced ω-β transformation, Acta Mater. 100 (2015) 290–300. doi:10.1016/J.ACTAMAT.2015.08.047.

[258] R. Hague, S. Mansour, N. Saleh, Material and design considerations for Rapid Manufacturing, Int. J. Prod. Res. 42 (2004) 4691–4708. doi:10.1080/00207840410001733940.

[259] R. Rashid, S.H. Masood, D. Ruan, S. Palanisamy, R.A. Rahman Rashid, J. Elambasseril, M. Brandt, Effect of energy per layer on the anisotropy of selective laser melted AlSi12 aluminium alloy, Addit. Manuf. 22 (2018) 426–439. doi:10.1016/j.addma.2018.05.040.